Detonation Induced Strain in Tubes

Thesis by

James Alan Karnesky

In Partial Fulfillment of the Requirements

for the Degree of

Doctor of Philosophy

California Institute of Technology

Pasadena, California

2010

(Submitted April)

© 2010
James Alan Karnesky
All Rights Reserved

Acknowledgments

I cannot imagine a better advisor than Joe Shepherd. His knowledge and guidance were constant and absolute necessities during my time as a graduate student. Had I been working under any other professor, I have my doubts as to whether I would have successfully completed my degree. Words are failing me, and I simply cannot thank him enough. I very nearly chose to include him as the sole person thanked in this section, since he certainly deserves the lion's share of the gratitude. Realizing that this may come off as lazy, and that there were several other individuals to whom I am indebted, I will be adding more to this section. But Joe is the one whose paragraph stands above the rest, separated by a `\bigskip`.

During my early years as a graduate student, the staff members and older students taught me almost everything I know about working in the laboratory. The guys in the Aero Shop, Brad St. John, Joe Haggerty, and Ali Kiani gave me free lessons in machining and let me off with a gentle ribbing whenever I'd break a tool. I was very fortunate to be able to apprentice myself to Chris Krok during his twilight years at GALCIT. Working with him on the laboratory control systems was an incredibly valuable experience, and whenever I put together an experiment I am hoping to achieve a fraction of his professionalism. Dan Lieberman and Scott Jackson mentored me through my earliest experiments in the lab, and provided excellent and much needed encouragement to a fledgling researcher. I had many fruitful discussions with Shannon Browne–Kao, and she always brought an affable air to the group.

I have been very fortunate to be able to work with many students who joined the EDL after I did, and helping them in their early lab days has been one of my greatest joys as a student. I graded Sally P. M. Bane's (always impeccable) papers in Ae101,

and consider myself lucky to have worked with her on a variety of projects and to enjoy her friendship and support. I met Phil Boettcher when he was doing his 104c project in the 6" shock tube, and since then he's been as good a pal and colleague as you could ask for.

When it comes to the work that comprises my thesis, my closest collaborators in the beginning were Florian Pintgen and Rita Liang. Florian's friendship and mentorship as we worked on a variety of experiments were some of the most important and formative elements when I was starting out. Through many late nights of experiment, evening trips to Wahoo's, and surprize visits to campus, Florian has always been a true and valued friend. Rita came on as a postdoc, and we worked together on the second generation of the experiment. She could always make me laugh and proved to be an infectious source of energy, as well as a sounding board on whom to practice my (limited) Mandarin.

During the time that Rita and I were working on the experiment, we started an extremely helpful collaboration with Professor Alexis Rusinek of Paul Verlaine University. Alexis and his student, Cindy Sauvelet provided the material testing data, without which we would've been at a total loss on how to simulate the experiment. They also performed the simulations which made it clear that a third generation of the experiment was needed.

Working with me on that third generation was Jason Damazo. Jason designed the tube coupling flange, rewrote the data acquisition software, and bonded hundreds upon hundreds of strain gauges. It is a strange feeling to see the plans for continued development of the experiment knowing that I won't be working on it, but I can't imagine a better man for the job.

My committee members: Ravi, Dan Meiron, and Guillaume Blanquart gave me useful comments on my work and on the thesis. Paco Lopez Jimenes read my thesis in its entirety and proved himself an excellent proofreader. Olive Stohlman and Nick Parziale also offered helpful corrections.

I couldn't ask for a better lab, a better group, or a better advisor than those found in the Explosion Dynamics Lab.

Abstract

When a detonation wave propagates through a piping system, it acts as a traveling pressure load to the pipe wall. The detonation wave must be followed by an expansion wave in order to bring the combustion products to zero velocity at the ignition end. When it reaches a closed end-wall, a reflected shock is formed which propagates back into the tube with a decaying pressure. The present study aims to develop predictive models for the stresses and strains produced in such a situation. To this end, two series of experiments are discussed. The first series used strain gauges and a laser vibrometer to measure the elastic response of the tube to the incident detonation in thin aluminum tubes. The second series used strain gauges and high speed video to measure the plastic response of steel tubes to incident detonations and reflected shocks. In these experiments a novel mode of plastic deformation was discovered in which the residual plastic deformation in the tube wall had a periodic sinusoidal pattern.

A semi-empirical model of the pressure history was developed for use as a boundary condition in models of the mechanical response of the tube. This model was tested against experiment, and it was found that the pressure and arrival time could not be simultaneously predicted from the simple model. This and the general form of the pressure traces in the experiment seem to suggest an interaction between the reflected shock and the boundary layer behind the detonation resulting in a possible bifurcation in the reflected shock wave.

With these considerations in mind, the model was applied to single degree of freedom and finite element models of the tube wall. The ripples observed in the experiment were present in the 1-D single degree of freedom models, indicating that

they are a result of the interaction of the reflected shock wave with the elastic oscillations set in motion by the detonation wave. Strain-rate hardening was found to be an important consideration under detonation loading conditions. With proper consideration of rate hardening, a single material model may be used to arrive at reasonable predictions the plastic strains resulting from detonations and reflections at initial pressures of 2 and 3 bar initial pressures.

Contents

Acknowledgments iii

Abstract v

Contents vii

List of Figures x

List of Tables xix

1 Introduction 1

1.1 Detonation Waves in Tubes . . . 2

1.1.1 Chapman Jouguet Theory . . . 2

1.1.2 Taylor–Zel'dovich Expansion . . . 5

1.1.3 Reflected Shock Wave . . . 10

1.2 Material Properties . . . 12

1.3 Structural Response . . . 16

1.3.1 Elastic Response . . . 16

1.3.2 Plastic Response . . . 20

2 Elastic Response to Detonation in Aluminum Tubes 23

2.1 Introduction . . . 23

2.2 Experimental Set-Up . . . 24

2.3 Series 1 . . . 27

2.3.1 Baseline Tests With Strain Gages . . . 32

2.3.2 Vibrometer Measurement . . . 34
2.3.3 Nonideal Effects on Strain Measurements . . . 39
2.3.3.1 Wall thickness variation . . . 39
2.3.3.2 Prestress . . . 41
2.3.3.3 Gauge Bonding and Creep . . . 42
2.3.3.4 Initial pressure variation . . . 44
2.3.3.5 Thermal Effects . . . 44
2.3.3.6 Transient Response . . . 47
2.3.3.7 Gauge location and angular misalignment . . . 49
2.4 Series 2 . . . 51
2.4.1 Tests in Original Apparatus . . . 51
2.4.2 Tests in The Modified Facility . . . 53
2.4.3 Modifications . . . 53
2.4.4 Results . . . 58
2.4.4.1 Experimental Uncertainties . . . 59
2.4.5 Detonation Simulation Method . . . 62
2.4.6 Comparison . . . 63
2.5 Solid Mechanics Simulations . . . 64
2.6 Summary . . . 68

3 Plastic Response to Incident and Reflected Detonation 69
3.1 Introduction . . . 69
3.2 Experiments in the Thick Tube . . . 70
3.3 First Experiments in the Thin Tube . . . 74
3.4 Experiments in the Driven Thin Tube . . . 77
3.4.1 Experimental Setup . . . 78
3.4.2 Results . . . 85
3.4.2.1 Tube 1 . . . 85
3.4.2.2 Tube 2 . . . 88
3.4.2.3 Tube 3 . . . 89

3.4.2.4 Tube 4 . . . 90
3.4.2.5 Tubes 5 and 6 . . . 94
3.4.2.6 Tube 7 . . . 94

4 Modeling Plastic Response **99**
4.1 Introduction . . . 99
4.2 Pressure Model . . . 100
4.2.1 Summary of Algorithm to Implement the Approximate Model 103
4.2.2 Testing the Model . . . 105
4.3 Material Testing . . . 112
4.4 Single Degree of Freedom Modeling . . . 114
4.5 Finite Element Analysis . . . 121
4.6 Summary . . . 126

5 Conclusions **130**
5.1 Elastic Response . . . 130
5.2 Plastic Response . . . 131
5.3 Suggestions for Future Work . . . 133

Bibliography **135**

A Thermally Induced Stress **142**

B Reflected Shock Bifurcation **145**

C Material Testing **149**

D Drawings **152**

E Data for aluminum tubes **167**
E.1 Series 1 . . . 167
E.2 Series 2 . . . 218

F Data for Driven Thin Tubes **230**

List of Figures

1.1 Pressure-time traces for an ethylene-oxygen detonation 3
1.2 Rayleigh line and Hugoniots in P–v plane. 4
1.3 Detonation and TZ expansion wave in a tube. 5
1.4 Spatial pressure distributions for several times prior to reflection. . . . 6
1.5 Space-time diagram showing an ideal detonation. 8
1.6 Diagram of situation A) before and B) after reflection with the end wall. 10
1.7 Stress strain curves for various material models. 14
1.8 Computed stress waves 19
1.9 Plastic response of SDoF model 22

2.1 Basic layout and key dimensions of the experimental fixture. 24
2.2 Tube setup for closed tube shots. 25
2.3 Test fixture photographs. 26
2.4 Strain measurement locations 28
2.5 Hoop strains for axial gauge locations in tests 2–5 32
2.6 Hoop strains for azimuthal gauge locations in tests 2–5 33
2.7 Detonation velocities for closed tube tests 1-20. 34
2.8 Comparison of shots 1–5 results. 35
2.9 Raw and processed vibrometer data 36
2.10 Representative hoop strain data from gauges and vibrometer 36
2.11 Comparison of peak strains measured with vibrometer. 37
2.12 Comparison of peak strains measured with strain gauge. 38
2.13 Wall thickness variation 40

2.14 Test of prestress effect. 42
2.15 Test of gauge bonding and calibration using static loading and unloading. 43
2.16 Comparison of peak hoop strain amplitudes. 44
2.17 Gauge alignment example. 49
2.18 Error due to gauge misalignment. 50
2.19 Tube dimensions for the shot 30-34 performed in the unmodified facility. 52
2.20 Experimental detonation velocity. 53
2.21 Superimposed pressure traces for shots 30-34. 54
2.22 Comparison of computations and shot 31. 55
2.23 Modified end plugs. 56
2.24 Modified clamp. 57
2.25 Tube dimensions for shots 1-7. 58
2.26 Detonation arrival time and velocity. 64
2.27 Comparison of simulations and shot 4 at four locations. 65
2.28 Comparison of computations and shot 7 at four locations. 65
2.29 Computed strain response with thickness variation. 66
2.30 Comparison of measured and simulated displacement at V3. 67
2.31 Comparison of measured and simulated displacement at V1. 67

3.1 Experimental setup in the thick tube. 70
3.2 Detailed drawing of tube setup. 71
3.3 Obstacles. 72
3.4 Pyrometer temperature measurements of glow plug. 73
3.5 Results of thick tube testing. 74
3.6 Thin tube experimental set-up. 75
3.7 Strain resulting from DDT in thin tube. 76
3.8 Strain traces for detonation in thin tube 76
3.9 The collet on the thin tube. 79
3.10 Driver tube. 79
3.11 Coupled tubes. 80

3.12 Asymmetrical deformation. 85
3.13 Redesigned reflecting end mount. 86
3.14 Gauge configuration for tube 1, dimensions in inches. 86
3.15 A) Hoop and B) longitudinal strain data for tube 1 shot 5, P_0 = 80 kPa. 87
3.16 A) Hoop and B) longitudinal strain data for tube 1 shot 1, P_0 = 100 kPa. 87
3.17 Gauge configuration for tube 2, dimensions in inches. 88
3.18 A) Hoop and B) longitudinal strain data for tube 2 shot 1, P_0 = 50 kPa. 89
3.19 A) Hoop and B) longitudinal strain data for tube 2 shot 2, P_0 = 200 kPa. 89
3.20 The tube after the three bar shot. 90
3.21 Strain calculated from video. 91
3.22 Gauge layout for tubes 3 and 4. 91
3.23 Hoop strains from repeated 2 bar shots in tube 4. 92
3.24 Rippling in tube 4. 93
3.25 OD and thickness after 2 bar detonations. 93
3.26 Ratio of longitudinal to hoop strain in tube 4. 94
3.27 High-strain strain gauges. 95
3.28 Gauge layout for tubes 5–7, dimensions in inches. 95
3.29 Hoop strains from repeated 3 bar shots in tube 7. 96
3.30 Hoop strain measured 19.05 mm from the end in tube 7 shot 8. 96
3.31 Fully deformed tube after three 3 bar detonations. 97
3.32 OD and thickness after 3 bar detonations. 98
3.33 Breathing mode of the tube as computed by SolidWorks. 98

4.1 Pressure curve-fit at the end-wall 103
4.2 P–x diagrams after reflection 104
4.3 Modeled pressure traces 105
4.4 x–t diagram in thick tube 106
4.5 Closed off driver tube used to test the pressure model 106
4.6 Pressure profiles from Euler simulations. 108
4.7 Schematic of tube for pressure tests. 109

4.8 Pressure transducers near the end wall. Dimensions in inches. 109
4.9 x–t diagram for driven thin tube. 110
4.10 Pressure traces for the 8 locations in the tube wall 111
4.11 Pressure traces computed with the revised fit 113
4.12 Results from dynamic testing of tube material 114
4.13 Measured and computed elastic peak strains 116
4.14 Plastic SDoF results 117
4.15 Pointwise traces from the SDoF model 119
4.16 2 and 3 bar SDoF results 120
4.17 Mesh used for finite element computations 121
4.18 Comparisons of measured and calculated residual strains 122
4.19 Maximum calculated strain-rate 123
4.20 Residual plastic strain with rate-hardening 124
4.21 Rate-hardening model used in computations 124
4.22 Measured and computed strain traces 125
4.23 2 bar strain trace comparison 127
4.24 3 bar strain trace comparison 128
4.25 Half bar strain trace comparison 129

A.1 Strain measurements with and without insulation 142
A.2 Thermal penetration depth into inner tube surface. 143

B.1 Ideal, one-dimensional (a) detonation and (b) reflection in a closed tube. 145
B.2 Assumed velocity profile in the boundary layer for Mark's analysis. . . 146
B.3 Reference frame used in calculations. 146
B.4 Theory predicts bifurcation for $M_R < 1.3$. 148

D.1 End plug. 153
D.2 Collet 154
D.3 Collet 155
D.4 Collet retaining ring. 156

D.5 Driver to specimen connector flange. 157
D.6 End plate with bolt holes for end plug and retaining ring. 158
D.7 Bottom plate for old support. 159
D.8 Angle bracket for old support. 160
D.9 Old end support mount. 161
D.10 Old end support tray. 162
D.11 Hyjet flange with bolt circle for end support plate. 163
D.12 Support plate for end braces. 164
D.13 Center brace for new support. 165
D.14 Side braces for new support. 166

E.1 Pressure traces for shot 10 168
E.2 Axial location hoop strain comparisons for shot 10. 169
E.3 Radial strain comparisons for shot 10 169
E.4 Pressure traces for shot 11 170
E.5 Axial location hoop strain comparisons for shot 11. 171
E.6 Azimuthal location hoop strain comparisons for shot 11 171
E.7 Pressure traces for shot 12 172
E.8 Axial location hoop strain comparisons for shot 12. 173
E.9 Azimuthal location hoop strain comparisons for shot 12 173
E.10 Pressure traces for shot 13 174
E.11 Axial location hoop strain comparisons for shot 13. 175
E.12 Azimuthal location hoop strain comparisons for shot 13 175
E.13 Pressure traces for shot 14 176
E.14 Axial location hoop strain comparisons for shot 14. 177
E.15 Azimuthal location hoop strain comparisons for shot 14 177
E.16 Pressure traces for shot 15 178
E.17 Axial location hoop strain comparisons for shot 15. 179
E.18 Azimuthal location hoop strain comparisons for shot 15 179
E.19 Pressure traces for shot 16 180

E.20 Axial location hoop strain comparisons for shot 16. 181
E.21 Azimuthal location hoop strain comparisons for shot 16 181
E.22 Pressure traces for shot 17 182
E.23 Axial location hoop strain comparisons for shot 17. 183
E.24 Azimuthal location hoop strain comparisons for shot 17 183
E.25 Pressure traces for shot 18 184
E.26 Axial location hoop strain comparisons for shot 18. 185
E.27 Azimuthal location hoop strain comparisons for shot 18 185
E.28 Pressure traces for shot 19 186
E.29 Axial location hoop strain comparisons for shot 19. 187
E.30 Azimuthal location hoop strain comparisons for shot 19 187
E.31 Pressure traces for shot 20 188
E.32 Axial location hoop strain comparisons for shot 20. 189
E.33 Azimuthal location hoop strain comparisons for shot 20 189
E.34 Pressure traces for shot 21 190
E.35 Axial location hoop strain comparisons for shot 21. 191
E.36 Azimuthal location hoop strain comparisons for shot 21 191
E.37 Pressure traces for shot 22 192
E.38 Axial location hoop strain comparisons for shot 22. 193
E.39 Azimuthal location hoop strain comparisons for shot 22 193
E.40 Pressure traces for shot 23 194
E.41 Axial location hoop strain comparisons for shot 23. 195
E.42 Azimuthal location hoop strain comparisons for shot 23 195
E.43 Pressure traces for shot 24 196
E.44 Axial location hoop strain comparisons for shot 24. 197
E.45 Azimuthal location hoop strain comparisons for shot 24 197
E.46 Pressure traces for shot 25 198
E.47 Axial location hoop strain comparisons for shot 25. 199
E.48 Azimuthal location hoop strain comparisons for shot 25 199
E.49 Pressure traces for shot 26 200

E.50 Axial location hoop strain comparisons for shot 26. 201
E.51 Azimuthal location hoop strain comparisons for shot 26 201
E.52 Pressure traces for shot 27 202
E.53 Axial location hoop strain comparisons for shot 27. 203
E.54 Azimuthal location hoop strain comparisons for shot 27 203
E.55 Pressure traces for shot 28 204
E.56 Axial location hoop strain comparisons for shot 28. 205
E.57 Azimuthal location hoop strain comparisons for shot 28 205
E.58 Pressure traces for shot 29 206
E.59 Axial location hoop strain comparisons for shot 29. 207
E.60 Azimuthal location hoop strain comparisons for shot 29 207
E.61 Pressure signals of shot 30 with a short time scale. 208
E.62 Pressure signals of shot 30. 209
E.63 Pressure signals of shot 31 with a short time scale. 210
E.64 Pressure signals of shot 31. 211
E.65 Pressure signals of shot 32 with a short time scale. 212
E.66 Pressure signals of shot 32. 213
E.67 Pressure signals of shot 33 with a short time scale. 214
E.68 Pressure signals of shot 33. 215
E.69 Pressure signals of shot 34 with a short time scale. 216
E.70 Pressure signals of shot 34. 217
E.71 Pressure signals of shot 1 with a short time scale. 219
E.72 Pressure signals of shot 2 with a short time scale. 220
E.73 Pressure signals of shot 3 with a short time scale. 221
E.74 Pressure signals of shot 4 with a short time scale. 222
E.75 Pressure signals of shot 4. 223
E.76 Pressure signals of shot 5 with a short time scale. 224
E.77 Pressure signals of shot 5. 225
E.78 Pressure signals of shot 6 with a short time scale. 226
E.79 Pressure signals of shot 6. 227

E.80 Pressure signals of shot 7. 228
E.81 Pressure signals of shot 7 with a short time scale. 229

F.1 Hoop strain data for elastic shots in tube 1. 231
F.2 Hoop strain data for elastic shots in tube 1. 232
F.3 Longitudinal strain data for elastic shots in tube 1. 233
F.4 Pressure data for elastic shots in tube 1. 234
F.5 Hoop strain data for plastic shots in tube 1. 235
F.6 Hoop strain data for plastic shots in tube 1. 236
F.7 Longitudinal strain data for plastic shots in tube 1. 237
F.8 Pressure data for plastic shots in tube 1. 238
F.9 Hoop strain data for elastic shots in tube 2. 239
F.10 Hoop strain data for elastic shots in tube 2. 240
F.11 Longitudinal strain data for elastic shots in tube 2. 241
F.12 Pressure data for elastic shots in tube 2. 242
F.13 Hoop strain data for plastic shots in tube 2. 243
F.14 Hoop strain data for plastic shots in tube 2. 244
F.15 Longitudinal strain data for plastic shots in tube 2. 245
F.16 Pressure data for plastic shots in tube 2. 246
F.17 Hoop strain data for elastic shots in tube 3. 247
F.18 Hoop strain data for elastic shots in tube 3. 248
F.19 Longitudinal strain data for elastic shots in tube 3. 249
F.20 Pressure data for elastic shots in tube 3. 250
F.21 Hoop strain data for plastic shots in tube 3. 251
F.22 Hoop strain data for plastic shots in tube 3. 252
F.23 Longitudinal strain data for plastic shots in tube 3. 253
F.24 Pressure data for plastic shots in tube 3. 254
F.25 Hoop strain data for elastic shots in tube 4. 255
F.26 Hoop strain data for elastic shots in tube 4. 256
F.27 Longitudinal strain data for elastic shots in tube 4. 257

F.28 Pressure data for elastic shots in tube 4. 258
F.29 Hoop strain data for plastic shots in tube 4. 259
F.30 Hoop strain data for plastic shots in tube 4. 260
F.31 Longitudinal strain data for plastic shots in tube 4. 261
F.32 Pressure data for plastic shots in tube 4. 262
F.33 Hoop strain data for elastic shots in tubes 5 and 6. 263
F.34 Hoop strain data for elastic shots in tubes 5 and 6. 264
F.35 Pressure data for elastic shots in tubes 5 and 6. 265
F.36 Hoop strain data for plastic shots in tubes 5 and 6. 266
F.37 Hoop strain data for plastic shots in tubes 5 and 6. 267
F.38 Pressure data for plastic shots in tubes 5 and 6. 268
F.39 Hoop strain data for elastic shots in tube 7. 269
F.40 Hoop strain data for elastic shots in tube 7. 270
F.41 data for lastic shots in tube 7. 271
F.42 Hoop strain data for plastic shots in tube 7. 272
F.43 Hoop strain data for plastic shots in tube 7. 273
F.44 Pressure data for plastic shots in tube 7. 274

List of Tables

1.1 Critical speeds (in m/s) for tubes used in the experiments. 18

2.1 Test Specimen Properties, 6061-T6 Aluminum. 25
2.2 Closed tube tests 28
2.3 Thickness and peak hoop strain variation with azimuthal location. . . 41
2.4 Location of pressure gauges. 52
2.5 Peak pressures and arrival times 52
2.6 Conversion factors of the re-calibrated pressure transducers. 55
2.7 Notes for shots 1-7. 58
2.8 Arrival time of the incident wave 59
2.9 Location of gauges. 59
2.10 Computed variation of CJ velocity and pressure 61

3.1 Shot List for Driven Thin Tube Experiments 80
3.2 Gauge Locations in Config. 1 84
3.3 Gauge Locations in Config. 2 and 3 84
3.4 Gauge Locations in Config. 4 84

4.1 Pressure transducer locations. 109
4.2 Parameters used in the pressure model 112
4.3 Material properties used in single degree of freedom calculations. . . . 117
4.4 Material properties used in the finite element simulations. 122

Chapter 1

Introduction

The structural response of piping systems to an internal explosion is a problem of continued interest in the nuclear and chemical processing industries (Shepherd, 2009). Even restricting the scope of our focus to pipelines with purely gaseous reactants, the overall scope of the problem is quite large. The combustion front may either be a subsonic deflagration or a supersonic detonation, and it may transition from one to the other in a deflagration to detonation transition (DDT) event (Lee, 2008). Each of these cases imposes unique loading conditions on the walls of the pipeline. If the detonation wave impinges upon a blockage or a closed end, a reflected shock forms which propagates back into the combustion products, and further raises the pressure. Finally, if the detonation diffracts around a corner, the resulting asymmetrical load imparts axial loads and bending stresses in the pipe which may translate into forces at the supports.

The material response of the tube will fall into different regimes, depending on the magnitude of the pressure loading in relation to the tube inner diameter and wall thickness. If the pressure is low enough for a given tube, then the material deformation will be entirely elastic, and no residual deformation will occur. Above a certain threshold, the deformation becomes plastic, and permanent deformation exists after unloading. Finally, if the loading is severe enough or there are sufficient stress concentrations, the material may fracture.

The present work is primarily interested in the elastic and plastic responses induced by gaseous detonations and the shock waves generated by the reflection of

detonations from closed ends. While previous researchers (Beltman and Shepherd, 1998, Beltman et al., 1999, Beltman and Shepherd, 2002, Chao and Shepherd, 2005) have studied the elastic problem in detail, the elastic portion of this study was aimed at acquiring data to use as benchmarks for coupled simulations. No prior study existed in the literature for the plastic case.

1.1 Detonation Waves in Tubes

A detonation is the self-sustaining supersonic propagation of a combustion reaction (Fickett and Davis, 2001, Lee, 2008). It consists of a shock wave coupled with a reaction. The shock wave provides the initiation energy for the reaction, and the release of energy in turn sustains the shock wave. Figure 1.1 contains an example set of pressure-time traces for four locations in a closed detonation tube.

This figure shows the typical behavior for detonations in such circumstances. The detonation is observed as a sharp rise in pressure which travels at a near constant velocity. An expansion wave follows the detonation, reducing the pressure in its trail and bringing the combustion products back to zero velocity. When the detonation reaches the reflecting end wall, a reflected shock wave is formed. This shock wave travels at a non-constant velocity, with a decaying pressure peak. In this section we will develop the theory covering the incident detonation, the expansion wave, and the strength and velocity of the shock wave immediately upon reflection.

1.1.1 Chapman Jouguet Theory

The simplest model of a detonation wave is the so-called Chapman–Jouguet (CJ) model, after Chapman (1899) and Jouguet (1905). This theory considers a control volume containing a shock wave and a reaction zone. The conservation equations of

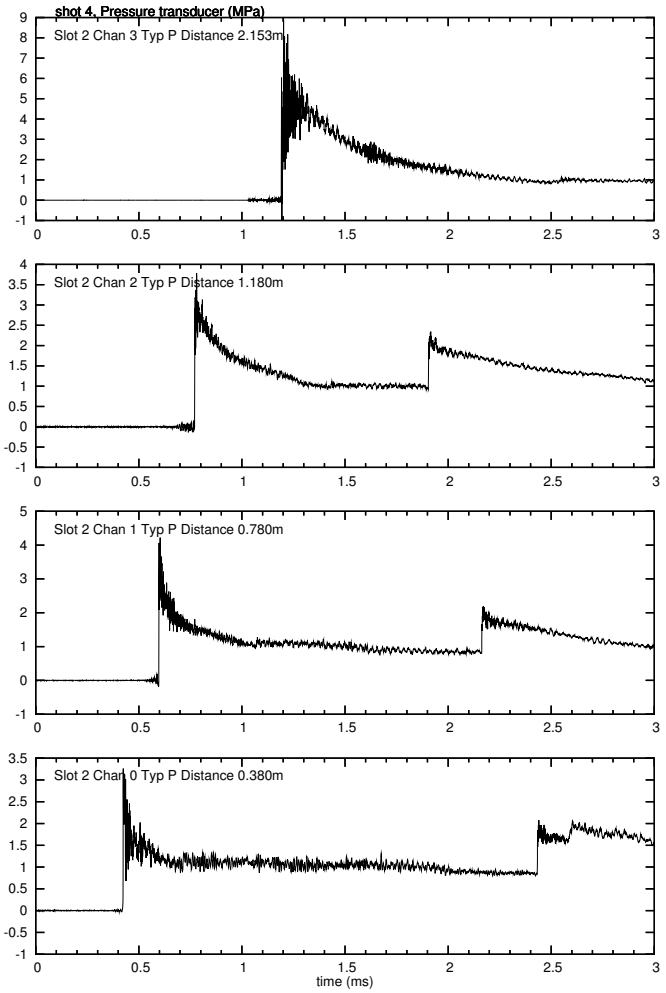

Figure 1.1: Pressure-time traces for an ethylene-oxygen detonation at four locations in a detonation tube (data from experiments in Chapter 2).

mass, momentum, and energy for a control volume in the wave-fixed frame are:

$$\rho_1 w_1 = \rho_2 w_2 \tag{1.1}$$

$$\rho_1 w_1^2 + P_1 = \rho_2 w_2^2 + P_2 \tag{1.2}$$

$$h_1 + \frac{w_1^2}{2} = h_2 + \frac{w_2^2}{2} \tag{1.3}$$

where ρ is the density, w the fluid velocity in the shock-fixed frame, P the pressure, and h is the specific enthalpy. State 1 represents the reactants upstream of the wave, and state 2 the downstream products.

Combining the equations of continuity and momentum, we arrive at the equation

for the Rayleigh line:

$$\frac{P_2 - P_1}{v_2 - v_1} = -\left(\frac{w_1}{v_1}\right)^2 = -\left(\frac{w_2}{v_2}\right)^2. \tag{1.4}$$

Using the three equations (1.1,1.2,1.3) to eliminate velocity results in the shock adiabat or Hugoniot:

$$h_2 - h_1 = \frac{v_2 + v_1}{2}(P_2 - P_1), \tag{1.5}$$

where $v = 1/\rho$. Combining these relations (1.4,1.5) enables a graphical solution to the shock jump conditions in the P–v plane, as seen in Fig. 1.2. The solid line represents the Hugoniot of the frozen reactants, and the dashed line that of the equilibrium products. In the classical picture of a detonation, developed by Zel'dovich (1940), von Neumann (1942), and Döring (1943), a frozen shock-wave takes the reactants to state 2, also known as the von Neumann state. This begins chemical reaction, during which the state travels along segment $\overline{23}$ to the equilibrium state 3, also known as the Chapman–Jouguet or CJ state.

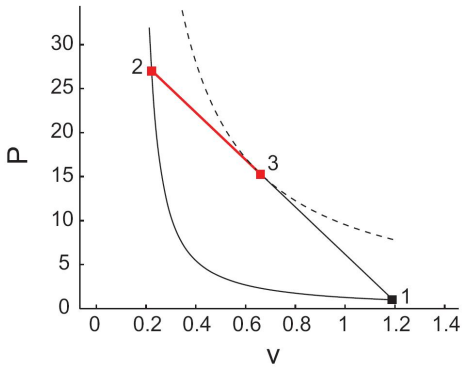

Figure 1.2: Rayleigh line and Hugoniots in P–v plane.

The Chapman–Jouguet criterion is that the Rayleigh line be tangent to the product Hugoniot, which is equivalent to sonic flow velocity at the equilibrium point. This theory allows the computation of the detonation velocity as well as the post detonation state from equilibrium considerations alone. Typical measurements of detonation velocity are within 2% of the calculated CJ value, so long as the detonation is propagating in a confinement which is large relative to the length scale of its cellular

instability (see the data in Chapter 2).

1.1.2 Taylor–Zel'dovich Expansion

In order to bring the detonation products to zero velocity at the boundary, the detonation wave must be followed by an unsteady expansion wave. This flow was first considered and analyzed by Taylor (1950) and Zel'dovich and Kompaneets (1960), and is referred to as a Taylor–Zel'dovich (TZ) expansion wave or simply, the Taylor wave. An analytical solution to this situation may be found through the construction of a piecewise, self-similar solution linking the three regions shown in Fig. 1.3. Region 1 is the unreacted mixture into which the detonation propagates, assumed to be at rest. Region 2 spans from the head to the tail of the TZ expansion wave, and region 3 is comprised of the detonation products at rest behind the expansion wave.

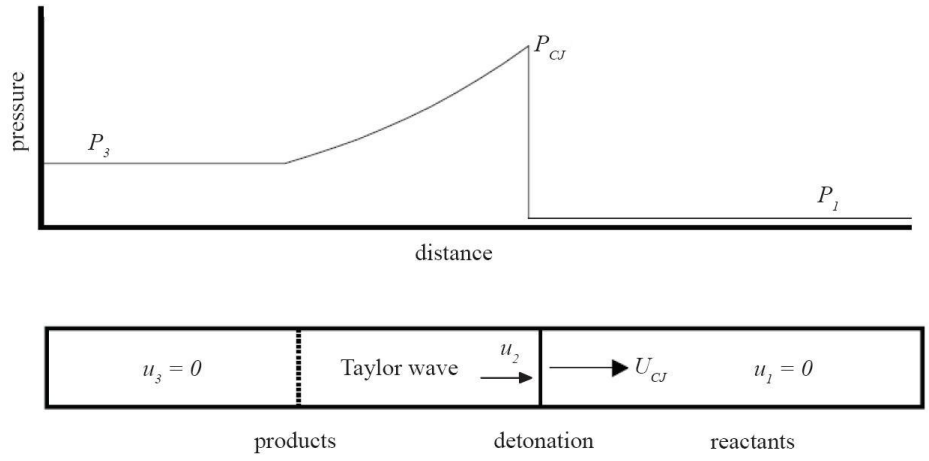

Figure 1.3: Detonation and TZ expansion wave in a tube.

The following analysis assumes that the detonation is ideal, i.e., forming very rapidly within a small distance from the ignition point. Furthermore we assume that the reaction zone length is small compared to the diameter of the tube, so that the interactions of the walls with the transverse instability do not influence the overall propagation of the detonation, resulting in a near-CJ propagation speed (Lee, 2008). Three dimensional effects, heat transfer, and viscosity are neglected, and the deformations of the tube are assumed to be small enough that the effect of tube

motion on the flow within the tube is negligible.

The detonation wave travels from the ignition end ($x = 0$) to the reflecting end ($x = L$) at a constant speed U_{CJ} and has a trailing expansion wave which terminates on the characteristic moving at sound speed c_3. Since $c_3 < U_{CJ}$, the expansion wave broadens as the detonation wave propagates. The corresponding spatial pressure profiles at several points in time are shown in Fig 1.4 and described mathematically below.

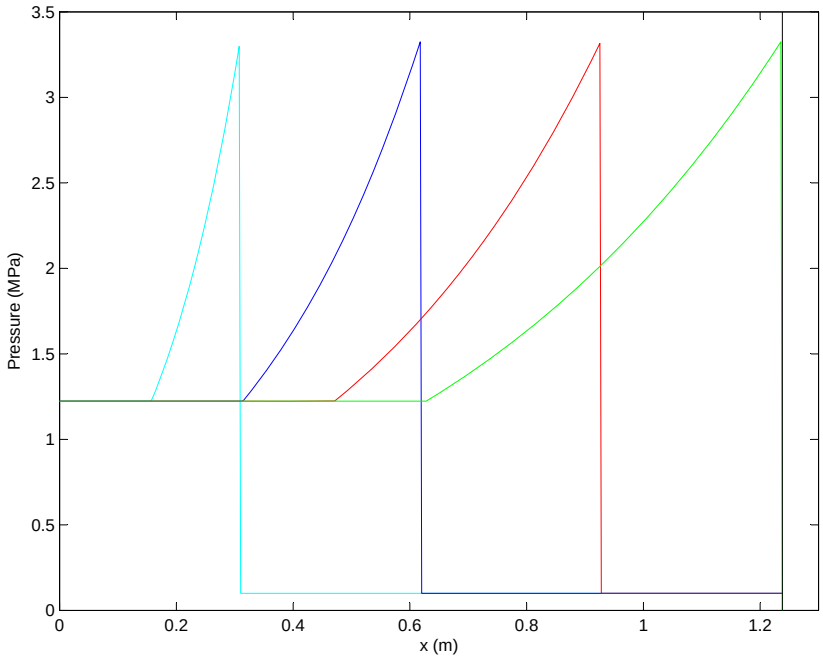

Figure 1.4: Spatial pressure distributions for several times prior to reflection. The detonation wave is the jump in pressure traveling from left to right. The expansion wave is the nonuniform region following the jump. At the left hand side of the wave there is a uniform pressure (no flow) region after the last (leftmost characteristic $x = c_3 t$) of the expansion fan. Results shown are for a stoichiometric C_2H_4–O_2 mixture at 100 kPa initial pressure.

The flow properties in the expansion wave may be found via the method of characteristics. Figure 1.5 contains a space-time diagram of the detonation and expansion wave, with example characteristics drawn in. The C^+ and C^- characteristics are

defined as (Liepmann and Roshko, 2001)

$$C^+ \quad \frac{dx}{dt} = u + c, \tag{1.6}$$

$$C^- \quad \frac{dx}{dt} = u - c, \tag{1.7}$$

and the Riemann invariants are

$$J^+ = u + \int_{P_\circ}^{P} \frac{dP'}{\rho c}, \tag{1.8}$$

$$J^- = u - \int_{P_\circ}^{P} \frac{dP'}{\rho c}, \tag{1.9}$$

on the C^+ and C^- characteristics, respectively. Here c is the the speed of sound, $c = dP/d\rho$, and the integral is carried out along the isentrope containing states 2 and 3. For an ideal gas this simplifies to

$$J^+ = u + \frac{2c}{\gamma - 1} \tag{1.10}$$

$$J^- = u - \frac{2c}{\gamma - 1} \tag{1.11}$$

where γ is the ratio of specific heats. Because the reaction zone length has been assumed to be small, this is taken as the γ for the detonation products in equilibrium (Browne et al., 2008).

As shown in Fig. 1.5, the C^+ characteristics in the expansion waves are simply straight lines beginning at the origin of the x–t plane. The C^- characteristics run from the detonation into region 3. From the Chapman–Jouguet condition, the flow velocity immediately behind the detonation is the detonation velocity U_{CJ} minus the sound-speed at the CJ state, c_{CJ}. Using the Riemann invariant along the C^- characteristics, and recognizing from the boundary condition that $u_3 = 0$, we find that

$$-\frac{2}{\gamma - 1} c_3 = U_{CJ} - c_{CJ} - \frac{2}{\gamma - 1} c_{CJ}, \tag{1.12}$$

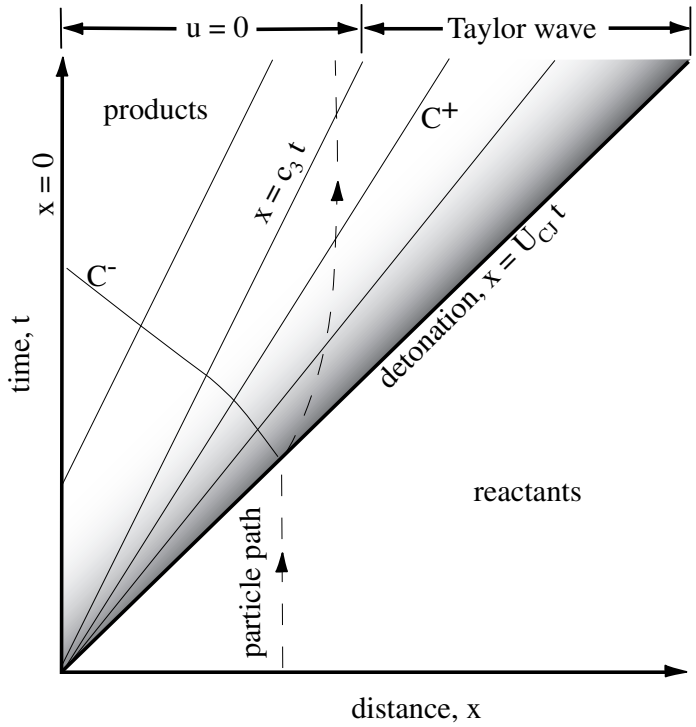

Figure 1.5: Space-time diagram showing an ideal detonation and following Taylor wave originating from x =0 at t= 0 and propagating in the $+x$ direction. Representative characteristics C^+ and C^- are shown as well as a particle path.

or

$$c_3 = \frac{\gamma+1}{2}c_{CJ} - \frac{\gamma-1}{2}U_{CJ}. \tag{1.13}$$

The variation of the sound-speed within the expansion may be found from the similarity properties of the C^+ characteristics and the Riemann invariants along the C^- characteristics as

$$c(x,t) = c_3\left[1 - \frac{\gamma-1}{\gamma+1}\left(1 - \frac{x}{c_3 t}\right)\right], \tag{1.14}$$

and the remaining properties may be found in this region using the isentropic flow

relationships

$$\frac{T}{T_3} = \left(\frac{c}{c_3}\right)^2, \qquad \frac{\rho}{\rho_3} = \left(\frac{T}{T_3}\right)^{\frac{1}{\gamma-1}}, \qquad \frac{P}{P_3} = \left(\frac{\rho}{\rho_3}\right)^{\gamma}. \tag{1.15}$$

The pressure in the post-expansion region is

$$P_3 = P_{CJ}\left(\frac{c_3}{c_{CJ}}\right)^{\frac{2\gamma}{\gamma-1}}. \tag{1.16}$$

From these, the sound-speed throughout the tube for all times up to the reflection is

$$c(x,t) = \begin{cases} c_1 & \text{if } U_{CJ} < x/t < \infty \\ c_3\left[1 - \frac{\gamma-1}{\gamma+1}\left(1 - \frac{x}{c_3 t}\right)\right] & \text{if } c_3 < x/t < U_{CJ} \\ c_3 & \text{if } 0 < x/t < c_3 \end{cases}. \tag{1.17}$$

The flow velocity is

$$u(x,t) = \begin{cases} 0 & \text{if } U_{CJ} < x/t < \infty \\ \dfrac{2c_3}{\gamma+1}\left(\dfrac{x}{c_3 t} - 1\right) & \text{if } c_3 < x/t < U_{CJ} \\ 0 & \text{if } 0 < x/t < c_3 \end{cases}. \tag{1.18}$$

The resulting pressure distribution is

$$P(x,t) = \begin{cases} P_1 & \text{if } U_{CJ} < x/t < \infty \\ P_3\left[1 - \dfrac{\gamma-1}{\gamma+1}\left(1 - \dfrac{x}{c_3 t}\right)\right]^{\frac{2\gamma}{\gamma-1}} & \text{if } c_3 < x/t < U_{CJ} \\ P_3 & \text{if } 0 < x/t < c_3 \end{cases}. \tag{1.19}$$

It is possible to approximate the spatial pressure distribution in the Taylor wave with a simple exponential decay function. This has been used in previous studies (Beltman and Shepherd, 2002) on elastic vibrations of tubes.

1.1.3 Reflected Shock Wave

When the detonation wave reaches the end wall, a reflected shock wave is created in order to bring the moving gas immediately behind the detonation wave back to rest (Shepherd et al., 1991). The first reflected shock wave travels in the opposite direction to the original detonation wave and propagates back to the ignition end. At the ignition end, a second reflected shock wave is created to bring the flow back to rest at the end of the tube and this shock propagates in the same direction as the original detonation wave. This process of shock wave propagation and reflection continues for a number of cycles until the shock wave is attenuated by entropy generation and other dissipative effects in the flow, as discussed in Shepherd et al. (1991). In experiments, this is observed on the pressure transducers as a sequence of pressure pulses with diminishing amplitude. In order to model the sequence of pressure pulses, it is necessary to carry out a computational fluid dynamics simulation of the gas dynamics in the tube, as described in Shepherd et al. (1991). However, a simplified model may be developed to model the pressure due to the first reflected wave, which is the most important in modeling the material response near the reflecting end.

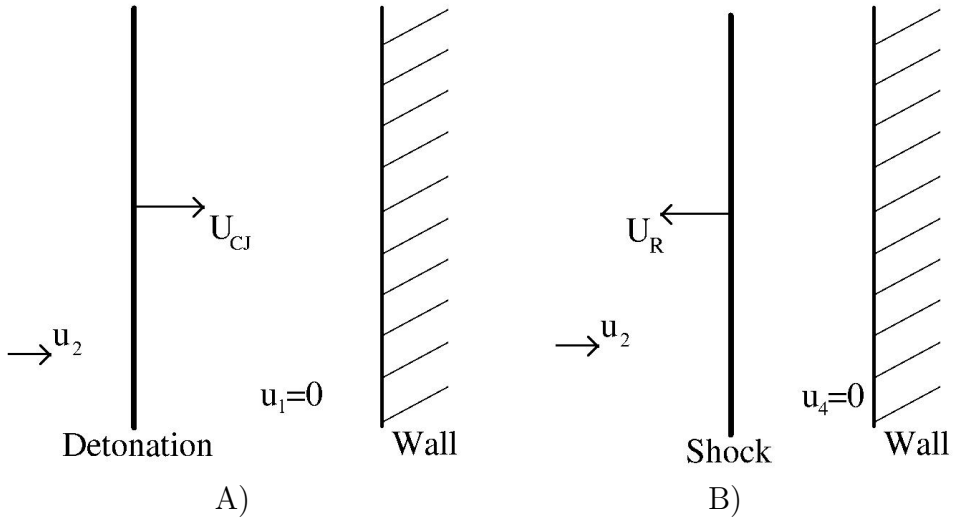

Figure 1.6: Diagram of situation A) before and B) after reflection with the end wall.

First, we derive an approximate solution for the peak pressure at the moment of reflection, as in Stanyukovich (1960). The Rayleigh line relationship for the incident

detonation can be written as

$$u_2^2 = (P_2 - P_1)(v_1 - v_2), \tag{1.20}$$

or in the limit of strong detonations (Stanyukovich, 1960),

$$u_2^2 \approx \frac{P_2 v_1}{\gamma + 1}. \tag{1.21}$$

The Rayleigh line for the reflected shock wave can be written as

$$u_2^2 = (P_4 - P_{CJ})(v_2 - v_4). \tag{1.22}$$

The volumes may be eliminated using the following form of the Hugoniot relation

$$\frac{v_4}{v_{CJ}} = \frac{(\gamma + 1)P_4 + (\gamma - 1)P_{CJ}}{(\gamma - 1)P_4 + (\gamma + 1)P_{CJ}}, \tag{1.23}$$

and the strong detonation approximation

$$v_{CJ} \approx \frac{\gamma v_1}{\gamma + 1}. \tag{1.24}$$

This results in a quadratic for the pressure ratio P_4/P_{CJ},

$$2\gamma P_4^2 - P_{CJ}P_4(5\gamma + 1) + (\gamma + 1)P_{CJ}^2 = 0, \tag{1.25}$$

the solution to which is

$$\frac{P_4}{P_{CJ}} = \frac{5\gamma + 1 + \sqrt{17\gamma^2 + 2\gamma + 1}}{4\gamma}. \tag{1.26}$$

For gases with $1 < \gamma < <5/3$, this formula predicts that the shock wave has a peak pressure of about $2.5P_{CJ}$. Exact solutions (Browne et al., 2008) give values closer to $2.4P_{CJ}$.

Given a value of P_4, we can use the shock jump relations (Thompson, 1972) to

find the initial velocity U_R of the reflected shock. The result is

$$U_{R_0} = c_{CJ}\sqrt{\frac{\gamma+1}{2\gamma}\left[\frac{P_4}{P_{CJ}}-1\right]+1} - u_{CJ} \tag{1.27}$$

where u_{CJ} is the velocity in the lab frame of the combustion products just behind the detonation. For typical hydrocarbon detonations, $U_{R_0} \approx 0.6 U_{CJ}$. Note that P_{R_0} and U_{R_0} are the *initial* pressure and velocity of the reflected shock. In practice the pressure of the reflected shock wave is observed to decay monotonically, and its speed increases until it exits the expansion wave, at which point it decays. A semi-empirical model for this behavior is developed in Chapter 4.

1.2 Material Properties

When a material is subjected to an imposed stress, it undergoes deformation. In metals at low stress levels, the response is elastic—that is it follows Hooke's law, which for a purely one-dimensional situation is

$$\sigma = E\epsilon \tag{1.28}$$

where σ is the applied stress, E is Young's modulus of elasticity, and ϵ is the resulting strain. For steels, typically $E \approx 210$ GPa.

A metal may undergo only a small amount of strain, typically about 0.2%, before yielding occurs. Beyond the yield point, permanent plastic deformation occurs. The strain increment for a given stress increment in the plastic regime is much larger than that in elastic deformation. For this reason, the simplest material model for use in circumstances of plastic deformation is the so-called perfectly plastic model, in which the material is rigid up to a yield stress,

$$\epsilon = 0 \quad \text{for} \quad \sigma < \sigma_y \tag{1.29}$$

and then the stress is constant and the material permanently deforms with a constant stress for forces that produces stresses in excess of the yield value

$$\sigma = \sigma_y \quad \text{for} \quad \epsilon > 0 \; . \tag{1.30}$$

A slightly more complicated model is that of an elastic–perfectly plastic material, which follows Hooke's law until yield is achieved,

$$\sigma = E\epsilon \quad \text{for} \quad \sigma < \sigma_y \tag{1.31}$$

whereupon it deforms freely

$$\sigma = \sigma_y \quad \text{for} \quad \epsilon > \epsilon_y \quad \text{with} \quad \epsilon_y = \sigma_y / E \; . \tag{1.32}$$

Figure 1.7a contains representative stress–strain curves for materials exhibiting these behaviors. Plastic strain is permanent, and in the case of the elastic–perfectly plastic material, unloading is accompanied by elastic strain recovery. Perfectly plastic models are useful in obtaining analytical results that give a qualitative guide to behavior. However, more realistic models that include strain hardening and strain rate effects are required for quantitative studies.

Most metals undergo strain hardening, in which plastic strain is accompanied by an increase in the yield strength of the material. A very simple model of this behavior assumes that the material deforms elastically up to the yield stress

$$\sigma = E\epsilon \quad \text{for} \quad \sigma < \sigma_y \tag{1.33}$$

and an effective modulus E_1 is used for plastic strains

$$\sigma = \sigma_y + E_1(\epsilon - \epsilon_y) \quad \text{for} \quad \sigma > \sigma_y \; . \tag{1.34}$$

We will call this model an elastic–linear hardening model. In general, realistic strain-

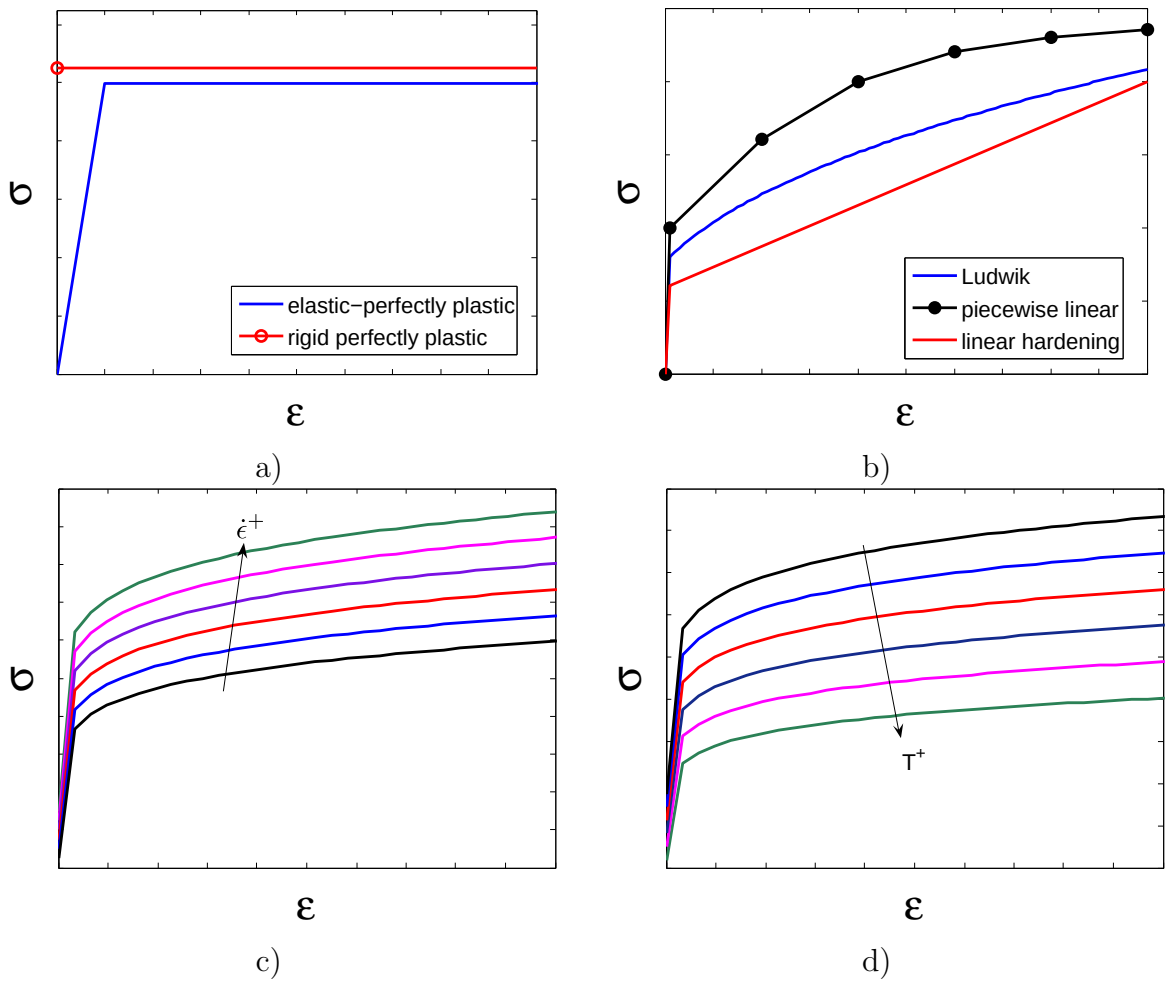

Figure 1.7: Stress strain curves for a) perfectly plastic materials, b) strain hardening materials, c) a strain rate hardening material, and d) a material undergoing thermal softening.

hardening curves exhibit a more complicated relation between plastic strain and yield stress. An extension of this model which is common and useful in numerical simulations is a piecewise-linear stress-strain relationship, which adds a number of segments to interpolate an approximation of the actual stress–strain curve of the material. One empirical model of a stress–strain relation for strain-hardening materials is Ludwik's equation (Ludwik, 1909):

$$\sigma = \sigma_0 + K\epsilon_p^n \tag{1.35}$$

where σ_0 is the stress at the onset of yielding, K is the strength index, ϵ_p is the plastic strain, and n is the strain-hardening exponent. Examples of stress-strain

curves for elastic–linear hardening, piecewise-linear, and Ludwik materials are shown in Figure 1.7b.

For situations involving detonations and other cases in which loadings are rapidly applied, viscoplastic effects become important. In these cases, the flow stress is dependent not only on the plastic strain, but on the rate at which it is applied. One model of strain rate hardening is the Cowper-Symonds model (Cowper and Symonds, 1957), which has:

$$\sigma_y = \left[1 + \left(\frac{\dot{\epsilon}}{C}\right)^{1/p}\right] \cdot \sigma_0 \tag{1.36}$$

where σ_y is the strain-rate hardened yield stress, $\dot{\epsilon}$ is the strain rate, and C and p are the Cowper-Symonds parameters, which are specific to the material. Another strain-rate hardening model is the simplified Johnson-Cook model (Johnson and Cook, 1983)

$$\sigma_y = (A + B \cdot \epsilon^n) \cdot (1 + C \cdot \ln \dot{\epsilon}^*)\,, \tag{1.37}$$

where $\dot{\epsilon}^*$ is the normalized strain rate, n is the strain-hardening exponent, and A, B, C, and m are constants. Figure 1.7c shows an example of stress-strain curves for a strain-rate hardening material.

Finally, most metals also undergo thermal softening. At elevated temperatures, larger deformations occur for given strains. For most single cycle detonation applications, heat transfer rates from the combustion products are slow enough that they can be neglected on the time scale of the pressure rise. For situations in which large plastic strains occur however, softening can be caused by the adiabatic temperature increase due to plastic heating. A model for this behavior is due to Johnson and Cook (1983) and has

$$\sigma_y = \left(A + B\bar{\epsilon}^{p^n}\right)\left(1 + c \ln \dot{\epsilon}^*\right)\left(1 - T^{*^m}\right) \tag{1.38}$$

where A, B, C, n, and m are the Johnson-Cook parameters and $\bar{\epsilon}^p$ is the effective plastic strain,

$$\dot{\epsilon}^* = \frac{\dot{\bar{\epsilon}}^p}{\dot{\epsilon}_0} \tag{1.39}$$

is the normalized effective plastic strain rate, and

$$T^* = \frac{T - T_{room}}{T_{melt} - T_{room}} \tag{1.40}$$

where the temperature T^* is computed by assuming the work done by plastic deformation goes into adiabatic heating of the material (Meyers and Chawla, 2008). Figure 1.7d contains example stress-strain curves for a material undergoing thermal softening.

1.3 Structural Response

1.3.1 Elastic Response

As the detonation wave travels along the tube, the pressure profile discussed above acts as a traveling impulsive load on the wall of the tube. This in turn excites stress waves which propagate in the wall of the tube. The velocity of propagation of the stress waves depends on their mode of oscillation. Typically longitudinal and shear waves will travel at velocities greater than the Chapman–Jouguet velocity, while dispersive flexural waves are carried along by the detonation, having a phase velocity equal to the velocity of the load (Beltman and Shepherd, 2002). Figure 1.8 shows stress profiles for 10 equally spaced elements in a finite element simulation of a specimen tube in the experiments described in Chapter 3. The material is purely elastic, and the mesh parameters and boundary conditions are described in Chapter 4. In this case, the tube was loaded with a step function pressure loading of 1 MPa traveling at 2000 m/s.

Tang (1965) and Reismann (1965) used shell theory to formulate a model (Eq. 1.41) of the elastic response of thin-walled tubes to contained traveling pressure loads. Beltman and Shepherd (2002) used this model to analyze the deformations arising from ideal detonations, and demonstrated the possibility of resonances when the detonation

velocity approaches one of several critical velocities of the tube. The model is:

$$\frac{\partial N_{xx}}{\partial x} = \rho h \frac{\partial^2 u}{\partial t^2}, \qquad \frac{\partial M_{xx}}{\partial x} - Q_x = \rho h^3 \frac{\partial^2 \psi}{\partial t^2},$$
$$\frac{\partial Q_x}{\partial x} - \frac{N_{\theta\theta}}{R} + \Delta P = \rho h \frac{\partial^2 w}{\partial t^2}. \tag{1.41}$$

For elastic motions, the stress resultants are defined as

$$N_{xx} = \frac{Eh}{1-\nu^2}\left[\frac{\partial u}{\partial x} + \nu\frac{w}{R}\right], \qquad M_{xx} = \frac{Eh^3}{12\left(1-\nu^2\right)}\frac{\partial \psi}{\partial x},$$
$$N_{\theta\theta} = \frac{Eh}{1-\nu^2}\left[\nu\frac{\partial u}{\partial x} + \frac{w}{R}\right], \qquad Q_x = \kappa G h\left[\psi + \frac{\partial w}{\partial x}\right], \tag{1.42}$$

where u is the axial displacement, w is the radial displacement, ψ is the rotation about the azimuth, R is the mean radius of the cylinder, and h is the thickness. ΔP is the pressure loading applied to the shell.

Simkins (1987) arrived at a closed form solution for the first critical wave speed, neglecting the effects of shear and rotary inertia:

$$V_{gf} = \left[\frac{E^2 h^2}{3\rho^2 R^2\left(1-\nu^2\right)}\right]^{1/4}. \tag{1.43}$$

This is the group velocity of flexural waves, and the velocity at which resonances were observed by Beltman and Shepherd (2002). The next critical speed is the modified shear wave velocity,

$$V_\gamma = \sqrt{\frac{\kappa G}{\rho}}\,, \tag{1.44}$$

where κ is the shear correction factor and G is the shear modulus. Next we have the bar dilatational wave speed

$$V_b = \sqrt{\frac{E}{\rho}}\,, \tag{1.45}$$

and the plate dilatational wave speed

$$V_p = \sqrt{\frac{E}{\rho\left(1-\nu^2\right)}}\,. \tag{1.46}$$

The fastest material waves travel at the velocity of dilatational waves in an infinite elastic medium:

$$V_\infty = \sqrt{\frac{K + \frac{4}{3}G}{\rho}} \,, \tag{1.47}$$

where K is the bulk modulus. All of these velocities for the two varieties of tubes used in the present study are collected in Tab. 1.1. The modified shear wave velocities are found from finite element simulations of the tube walls.

Table 1.1: Critical speeds (in m/s) for tubes used in the experiments.

Tube	V_{gf}	V_γ	V_b	V_p	V_∞
Aluminum (Ch. 2)	1010	2850	4980	5280	6150
Steel (Ch. 3)	625	3070	5190	5440	6020

From Eq. 1.41, the traveling load will act as a forcing term in both the hoop and shear stresses. The hoop stresses affect stress in the longitudinal direction through Poisson coupling.

For thin-walled tubes, the flexural wave group velocity V_{gf} is smaller than either the Chapman–Jouguet speed or the speed of the reflected shock wave. This means that the only waves which run ahead of the traveling load are the longitudinal wave (Fig. 1.8A), which in the simulation is observed to travel at a velocity between V_b and V_p, and the shear wave (Fig. 1.8B), which travels at V_γ. When these waves reach the boundary they will reflect, and because they lead the detonation the reflected waves will interfere with the incident flexural wave. Our experiments and simulations utilized built-in (i.e., perfectly rigid) boundary conditions, meaning that tensile waves were reflected as tensile waves. From the simulations, the peak stress developed in the reflected longitudinal wave is about 60% greater than the stress generated by Poisson coupling in the flexural wave. Once the flexural wave arrives at a given location, the longitudinal motion is dominitated by the Poisson coupling. The shear wave is a very high frequency (364 kHz in the simulation) wave with a peak shear stress of about one quarter the magnitude of the longitudinal wave. This motion does not couple into the observable stresses in the tube.

The flexural wave is observed in the hoop stress, and has about 18 times the mag-

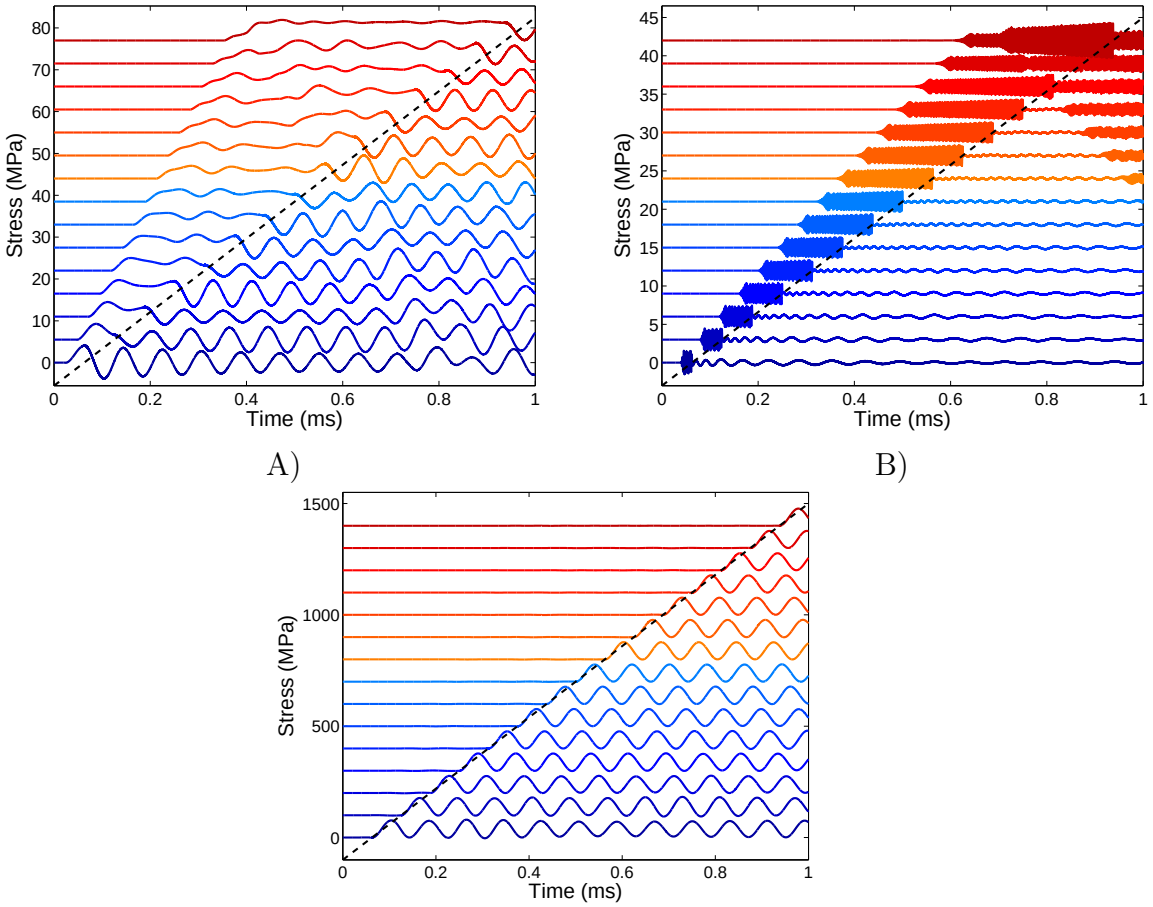

Figure 1.8: Computed examples of A) longitudinal, B) shear, and C) hoop stresses at 15 equally spaced locations in a tube. The dashed black line represents the position of the traveling load.

nitude of the longitudinal wave. The flexural waves have a characteristic frequency of

$$f = \frac{1}{2\pi R}\sqrt{\frac{E}{\rho\,(1-\nu^2)}} \tag{1.48}$$

which is 41.5 kHz for the tubes used in Chapter 2 and 13.6 kHz for the tubes used in Chapters 3 and 4. The peak hoop stress is

$$\sigma_{H,max} = A\Delta P\frac{R}{h}, \tag{1.49}$$

where A is the dynamic amplification factor, and is a function of the time-dependent loading. Beltman and Shepherd (2002) predicts that when the loading velocity is

sufficiently greater than the group velocity of the flexural waves this factor will have a value of between 1.5 and 2, and in fact the observed value in our computation is 1.8. Much larger values (up to ≈ 4) were observed when the traveling load had a velocity close to the critical velocity, but for thin-walled tubes under detonation loading, we do not expect this to be the case.

Chao (2004) found resonant coupling in the computed shear stress when the traveling load is moving at V_γ. This is extremely difficult to observe experimentally due to the difficulties of measuring the shear stress, and we do not expect such coupling in the present studies, as the detonation velocities are typically much slower than the modified shear wave velocities.

1.3.2 Plastic Response

There has been a large amount of prior work done on the containment of explosions in cylindrical pressure vessels. Duffey and Mitchell (1973) performed experiments on the structural response of pipe walls to high explosive charges. Duffey and Mitchell (1973), Benham and Duffey (1974), Hodge (1956), Duffey (1971), Duffey and Krieg (1969), and Fanous and Greiman (1988) performed analysis on the plastic deformation of impulsively loaded cylinders using single degree of freedom modeling. Hodge (1956) considered the solution for a rigid-perfectly plastic ring with arbitrary pressure history, but was unable to find analytical solutions for loads of practical importance. Benham and Duffey (1974) arrived at an analytical solution for a rigid-plastic material with linear hardening, assuming constant dynamic yield stress. Duffey and Krieg (1969) and Duffey (1971) discussed the inclusion of elastic loading and unloading.

There has been significantly less investigation of the plastic response to traveling and reflected loads. Smith (1986) performed experiments in a thin aluminum shock tube and found that the measured strain signals showed a steady-state response (i.e., a signal which propagates with the shock speed). Smith (1990) used the model of Tang (1965) (Eq. 1.41) with the modulus E varying as a function of time. Using a bilinear representation for the modulus with exponential relaxation to represent

strain-hardening, he was able to achieve qualitative similarity with his measured results, and concluded that for a traveling pressure load the short-time response can be attributed to elastic behavior and long-time behavior could be treated modeled as a quasi-static relaxation.

In the preceding section, we discussed how the highest strains are found in the flexural waves, which travel with a phase velocity equal to the velocity of the traveling load. Thus it is in these waves that we can expect the onset of plastic deformation. The waves which typically travel ahead of shock and detonation waves are the longitudinal and shear waves. In the elastic regime these have peak strains of 6% and 2% that found in the flexural wave, respectively. For most metals, we can expect the stress to reach failure levels in the flexural wave before it reaches plastic yield in the faster waves. Furthermore, as discussed in Kolsky (1953), plastic waves are highly dissipative, and if they are not supported by a constant load, then unloading waves cause them to decay to elastic waves. This agrees with the observations of Smith (1986), that no plastic waves propagate at greater velocities than the load.

These observations imply that we may adequately model the plastic response of a tube to a traveling impulsive load using one dimensional computations. Figure 1.9 contains the numerical solution to a single degree of freedom model of a cylinder with an elastic–linear hardening constitutive model being loaded by a step function followed by decay. The arrival of the load causes an initial yielding, after which the material undergoes elastic unloading and oscillation. It will be seen in Chapter 3 that this is generally the case when a traveling load is applied to a pipe or tube that does not deform significantly so that the fluid and structural motions are coupled. It will also be seen that further considerations are required when dealing with situations where the fluid and structural motions are coupled, such as when a reflected shock propagates in a deforming tube.

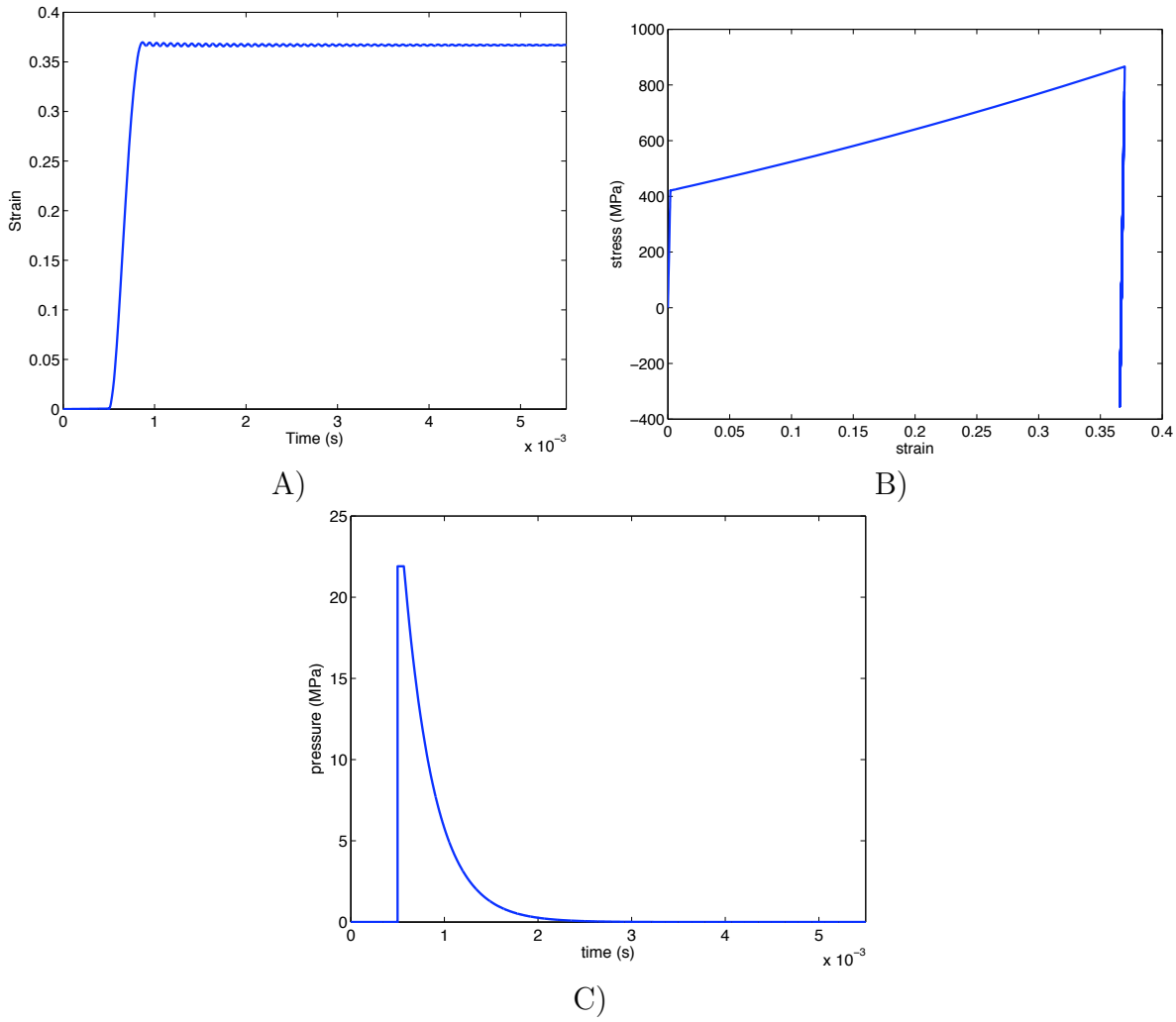

Figure 1.9: Computed A) strain trace and B) stress–strain plot of a single degree of freedom model of the tubes used in Chapter 3 to a pressure loading C).

Chapter 2

Elastic Response to Detonation in Aluminum Tubes[1]

2.1 Introduction

Experiments were carried out in a closed tube to obtain measurements of incident and reflected pressure histories for detonations in stoichiometric ethylene-oxygen mixtures. The data are compared with the Chapman-Jouguet and Taylor-Zeldovich ideal model and also numerical simulations of the Euler equations. Detonation waves are observed to propagation within 1% of the Chapman-Jouguet velocity and the pressure history is slightly lower (8%) than the predicted ideal behavior. Reasonable agreement between experiment and numerical simulation of the Euler equations is found for incident waves and reflected waves close to the reflecting end of the tube. The disagreement is larger for reflected waves far from the reflecting end. Possible reasons for this disagreement are discussed.

Strains were measured in the specimen tubes to investigate the elastic response to detonations. In order to facilitate comparison with simulations, the specimen tube was held firmly in place by a pair of collets, approximating built in boundary conditions. The strain was measured with bonded strain gauges, and many shortcomings of these were addressed. A laser vibrometer was also used, and was found to give more reliable measurements. These were useful in quantifying various uncertainties

[1]This chapter is partially based on and uses material which was first published in the form of an internal report (Shepherd et al., 2008).

arising from the bonded gauge measurements.

2.2 Experimental Set-Up

The test fixture is based on that described in Chao (Chap. 6 and App. B of 2004), and shown schematically in Fig. 2.1. It consists of a driver tube coupled with a test specimen, all attatched to an I-beam. The detonation was initiated in the driver tube, and propagated into the test specimen. The driver tube was 1.6 m in length with an internal diameter of 38 mm and a wall thickness of 6.4 mm. It was affixed to the I-beam by a pair of tube clamp supports, and a third support held in place the slip fit, gland sealed fitting by which the driver tube was coupled to the specimen tubes.

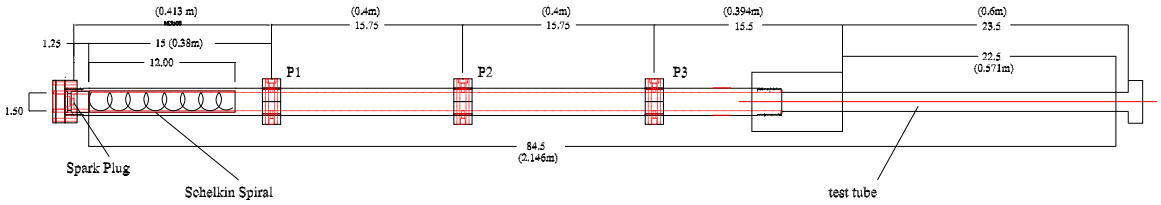

Figure 2.1: Basic layout and key dimensions of the experimental fixture.

The test specimens were thin-walled cylindrical extruded tubes of 6061-T6 aluminum. These seamless tubes had an outer diameter of 41 mm and a nominal wall thickness of 0.9 mm. They were held in place by a pair of collets that were bolted to the I-beam. These collets were 420 mm apart, and were tightened to provide a good approximation of a built-in boundary condition. A final tube clamp fixture attached to the gland sealed slip on flange which served as the reflecting end of the detonation tube. The whole set up, including the clamps and I-beam, is shown schematically in Fig. 2.2, and photographically in Fig. 2.3.

Table 2.1: Test Specimen Properties, 6061-T6 Aluminum.

Thermal expansion coefficient	24.3	μm/mK
Thermal conductivity	155.8	W/mK
Mass density	2780	kg/m^3
Young's modulus	69	GPa
Specific heat capacity	963	J/kgK
Poisson's ratio	0.33	
Average (between inner and outer) radius	22.275	mm
Average wall thickness	0.87	mm

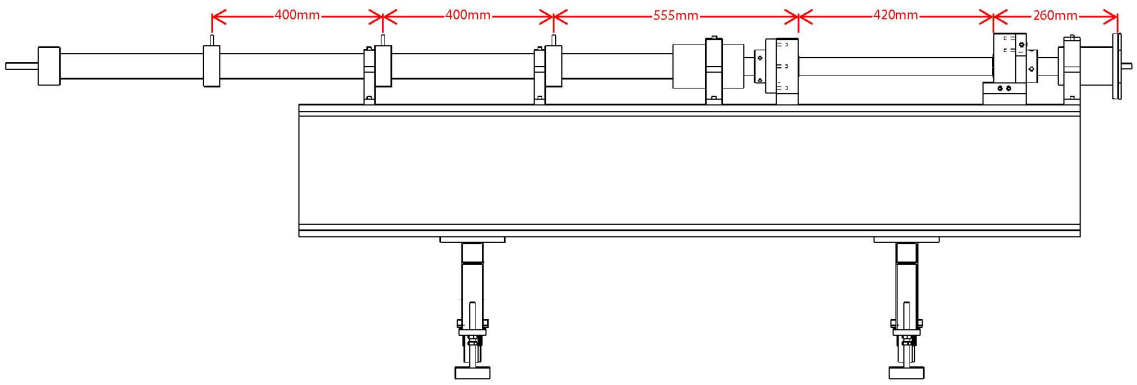

Figure 2.2: Tube setup for closed tube shots.

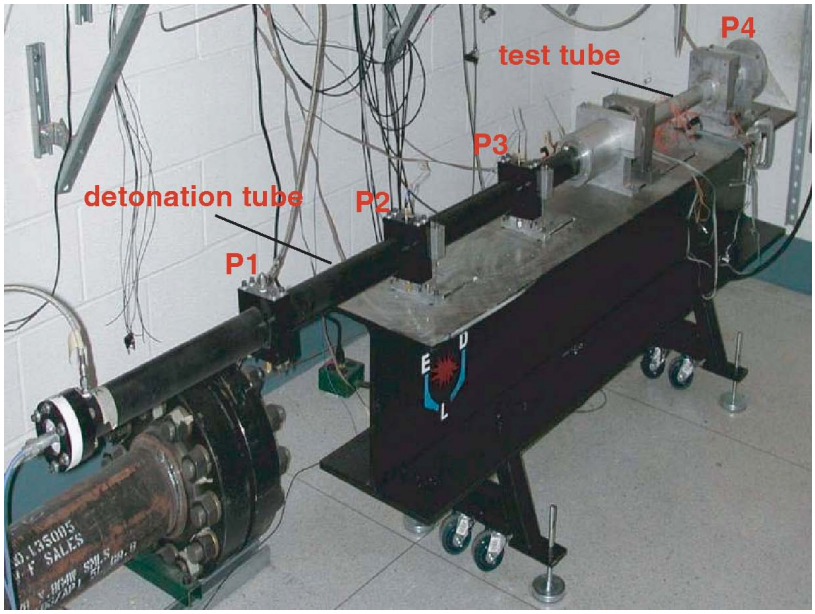

(a)

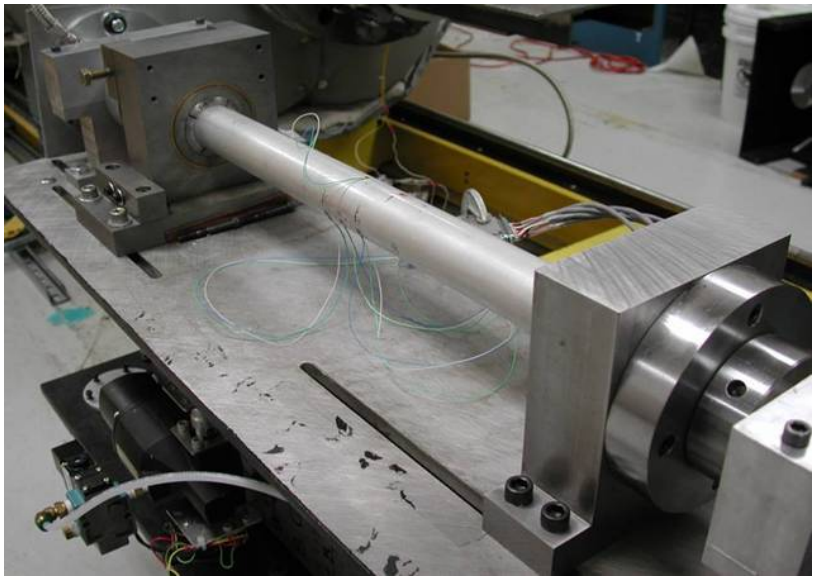

(b)

Figure 2.3: Test fixture photographs showing a) detonation and specimen tubes and b) close-up of collets and strain gauges on specimen

All experiments used a stoichiometric mixture of ethylene and oxygen, initially at room temperature, with the initial pressure varied between tests. The tube was evacuated to below 50 mTorr prior to being filled via the method of partial pressures, and mixed using a circulation pump.

Combustion was initiated using a capacitor discharge system with 0.4 J stored energy, discharging through a spark plug. A 300 mm long Schelkin spiral was welded to the interior of the tube to accelerate transition to detonation in the initiator tube.

The detonation was monitored using three PCB piezoelectric pressure transducers located along the length of the driver tube. A fourth transducer was located in the reflecting end. The measured detonation velocity was usually within 1% of the computed (Reynolds, 1986) Chapman-Jouguet value of 2375.6 m/s. Repeated tests carried out to examine the pressure histories showed that these were highly reproducible.

Two series of experiments were conducted. The first series was aimed at investigating the elastic stress waves in the test specimen. Hoop strains were measured with both bonded strain gauges and an optical displacement instrument.

After discrepancies were found in the predicted and observed pressure traces, a series of modifications were made to the experimental setup, and a second series of tests was conducted.

2.3 Series 1

The tests in Series 1 were concerned with developing repeatable and accurate strain measurements in the specimen tubes under detonation conditions. Repeated tests were carried out using strain gauges and a vibrometer to measure the material deformation. The vibrometer is a non-contact instrument which uses optical interferometry, thereby eliminating many drawbacks associated with strain gauges. Comparisons were made with simulations

Figure 2.4 contains a photograph and a diagram showing the location of measurement for the strain gauges and vibrometer for most of the tests, with the exceptions

being noted in Table 2.2. The center line of the gauge pattern in the axial direction was located at the half-way point between the two collets.

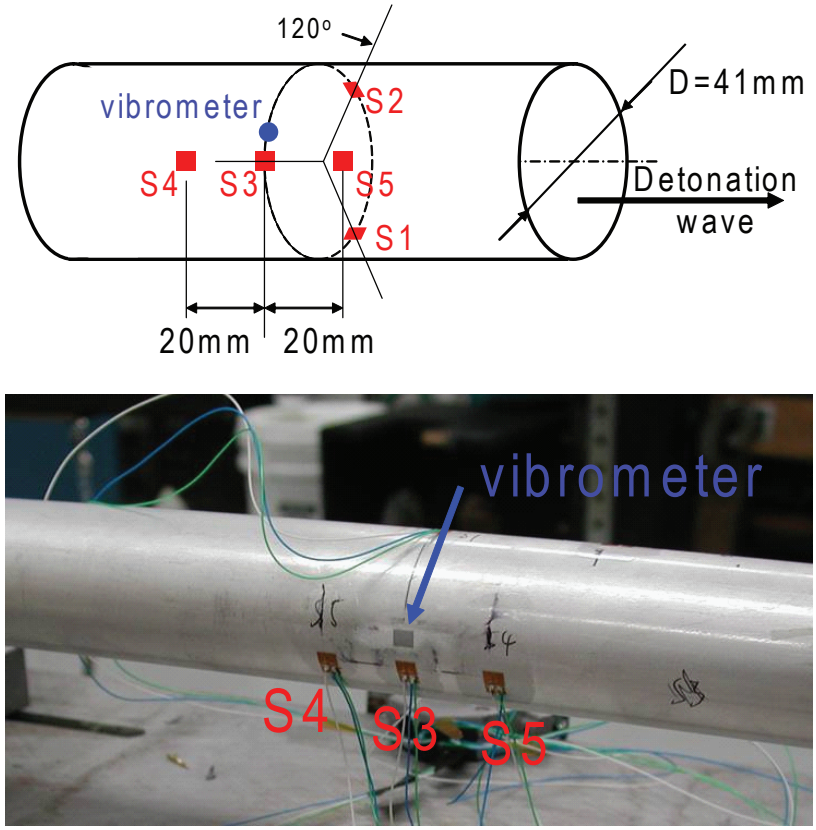

Figure 2.4: Strain measurement locations

Table 2.2: Closed Tube tests with stoichiometric ethylene-oxygen.

Shot	Average V_{det} (m/s)	P_O (kPa)	Notes
1		0.8	no vibrometer. no data
2	2318.9	40	no vibrometer 1.1kPa of air added to tube, this is to get pump going by bleeding up between isolation valves
3	2319.2	40	no vibrometer
Continued on next page			

Table 2.2 – Continued from previous page

Shot	Average V_{det} (m/s)	P_0 (kPa)	Notes
4	2325.8	40	no vibrometer
5	2315.7	40	vibrometer in place
6	2375.4	100	test shot. no pretrigger. DAS triggered by falling edge from scope back panel output
7	2036.7	50	all good
8		100	no vibrometer. no data - wrong edge
9	2378.2	100	no vibrometer
10	2491.6	100	with vibrometer. prestress might introduce difference in strain
11	2275.0	100	with vibrometer
12	1832.2	100	with vibrometer
13	1307.4	100	with vibrometer
14	2378.2	100	with vibrometer
15	2378.2	100	with vibrometer
16	2375.4	100	with vibrometer
17	2347.6	50	with vibrometer
18	2347.6	50	with vibrometer
19	2344.8	50	with vibrometer
20	2378.2	100	tube turned by 120 deg compared to shot 19. collets unaltered. Vibrometer measurement point is now also 120 degrees turned, so now close to S1.
21	2375.4	100	same conditions as shot 20
Continued on next page			

Table 2.2 – Continued from previous page

Shot	Average V_{det} (m/s)	P_0 (kPa)	Notes
22	2378.2	100	measurement setup same as shot 21. tube was prestressed by setting collet on end in a slight angle such that side with vibrometer measurement point is in compression
23	2375.4	100	measurement setup unchanged - no prestress.
24	2372.6	100	setup unchanged, just pressed on reflector to reinforce its attachment
25	2372.6	100	tube turned back into original position (shot 10-19). Vibrometer laser diaode position was not changed from shot 10 till shot 25 (this shot) (position in room)
26	2375.4	100	vibrometer moved to other side of tube. Tube turned such that measurement location on the tube surface is unchanged; the measurement location still S3.
27	2378.2	100	repeat of last shot, nothing altered
28	2372.6	100	measurement position unaltered, but (S4 (in axial directon of spark plug) was removed. tube polished aferwards - no epoxy rests
29	2375.4	100	tube turned back such that vibrometer points on S1. Vibrometer itself has not been moved
30	2379.0	100	no vibrometer, closed tube
31	2377.4	100	no vibrometer, closed tube
32	2376.5	100	no vibrometer, closed tube
33	2374.7	100	no vibrometer, closed tube

Continued on next page

Table 2.2 – Continued from previous page

Shot	Average V_{det} (m/s)	P_0 (kPa)	Notes
34	2373.8	100	no vibrometer, closed tube

The first series of tests examined a number of issues associated with using bonded strain gauges. Strain gauges are well-studied and are known (see Chap. 2 of Kobayashi, 1993) to be subject to a number of effects that need to be considered in making high precision measurements. These include:

1. Bonding of gauges
2. Fatigue of gauges
3. Creep of gauges
4. Bending of tube due to preloading
5. Temperature compensation of gauges
6. Temperature control of tube
7. Differential thermal expansion of gauge and substrate
8. Thermal stress induced by temperature gradient between inner and outer tube surfaces

In order to examine these issues, 28 tests were carried out using the same sample tube at initial pressures of 40, 50 and 100 kPa. The conditions for all tests are given in Table 2.2. Plots of the strain and pressure signals for tests 10–29 are also given in Appendix E. Strain measurements were taken at five locations (Fig. 2.4) with bonded strain gauges (Vishay Micromeasurements CEA-06-125UN-350 or CEA-06-125UN-120) using precision bridges and instrumentation amplifiers (Vishay 2310 Signal Conditioning Amplifier).

2.3.1 Baseline Tests With Strain Gages

These tests used only strain gauges and examined the repeatability of the signals for replica tests at the same initial conditions. Data from the strain gauges in these tests is compared along the axial direction in Fig. 2.5 and along the azimuthal direction in Fig. 2.6 for shots 2–5.

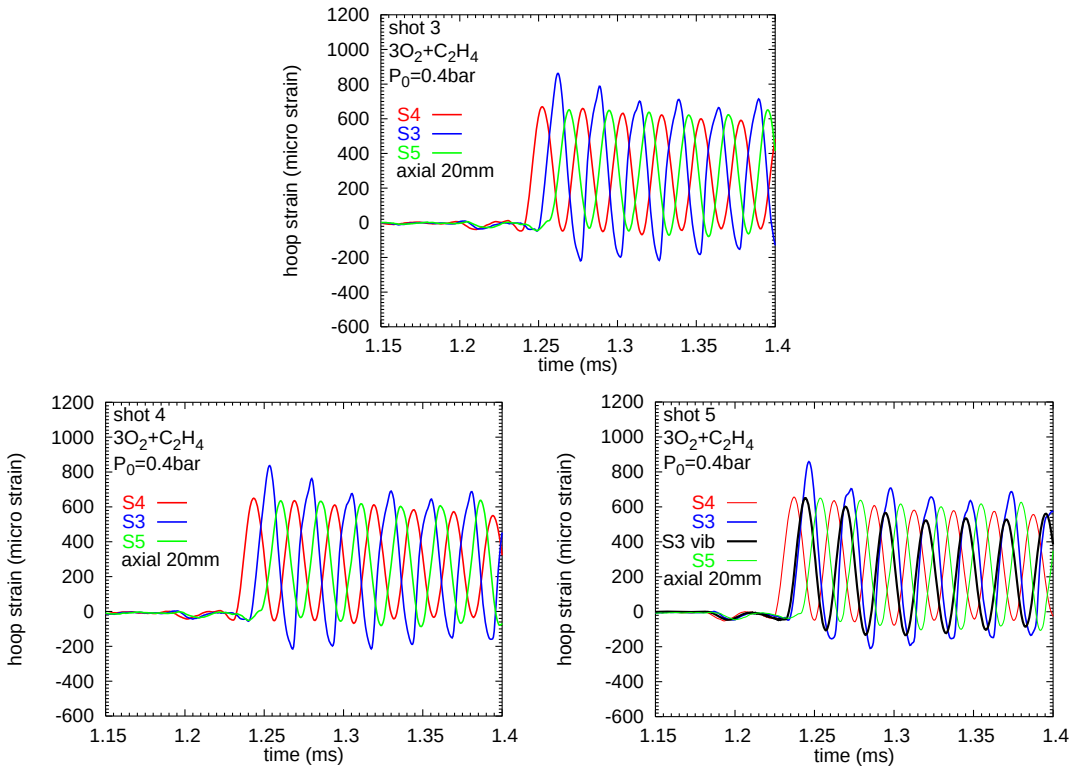

Figure 2.5: Hoop strains for the axial gauge locations in tests 2–5. Initial pressure of 40 kPa.

Velocity measurements in the first 20 tests are shown in Fig. 2.7. With the exception of tests 7-13, in which the gases were not properly mixed, the average detonation velocity is within 1% of the computed CJ value.

Figure 2.10 shows the strain signals observed in shot 5. These data are representative of the results obtained in all of these tests. The signals show the characteristics observed in previous testing with detonation as documented in Beltman and Shepherd (2002). There is a small precursor prior to the arrival of the detonation wave and the main signal is an almost sinusoidal oscillation with a frequency of approximately 38

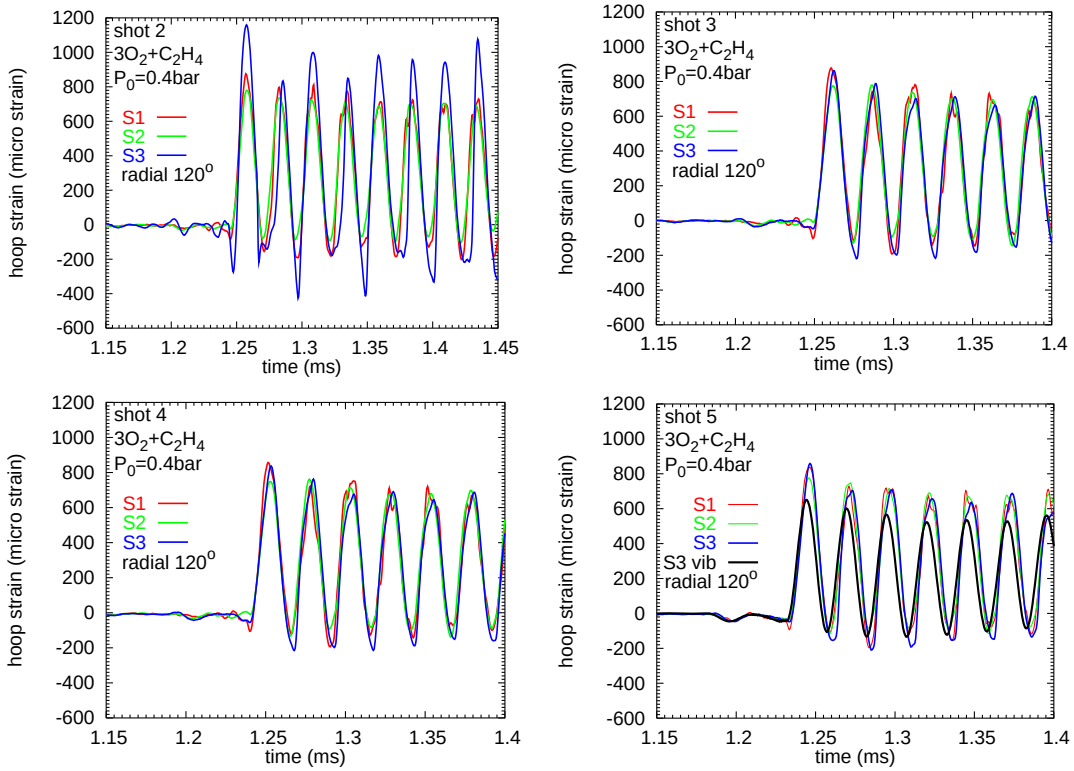

Figure 2.6: Hoop strains for the azimuthal gauge locations in tests 2–5. Initial pressure of 40 kPa.

kHz. This is close to the hoop frequency of 41 kHz for an infinite cylindrical shell (Chap. 12 Blevins, 1979)

$$f = \frac{1}{2\pi R}\sqrt{\frac{E}{\rho(1-\nu^2)}}\,. \tag{2.1}$$

A more exact computation of the frequency requires solution of the dispersion relation as discussed by Beltman and Shepherd (2002).

Figures 2.5 and 2.6 show that peak measured strain amplitudes differ significantly between measurement locations. A shot to shot comparison of the measured peak strains and oscillation periods is shown in Fig. 2.8. There is a 20% variance in the amplitude and a 4% variance in the period of the strain signals. These discrepancies are significantly greater than expected from the repeatability of the detonation wave, as found in the second series of experiments. In fact, there appear to be systematic differences in the strain signals based on particular gauges or locations. Also, the

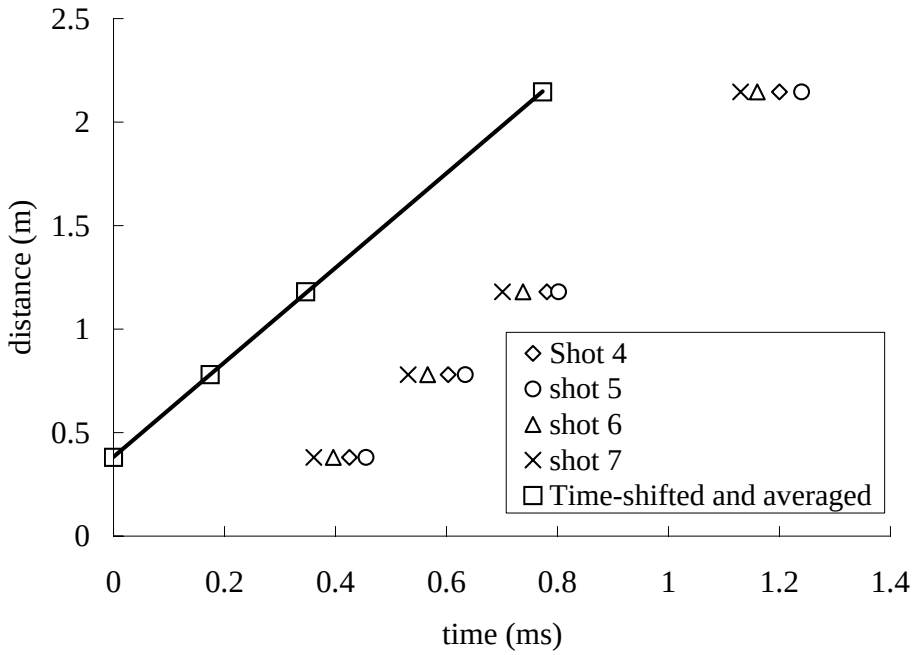

Figure 2.7: Detonation velocities for closed tube tests 1-20. Various initial pressures - see Table 2.2 for details.

strain signals show jumps which depart from the expected smooth oscillatory behavior associated with elastic oscillation with no wave interaction.

2.3.2 Vibrometer Measurement

To investigate the source of variability noticed in the previous section, a laser vibrometer was used to obtain independent measurement of the strain at various locations on the test specimen. The vibrometer used was a Polytec OFV-551 Fiber-Optic Interferometer with an OFV-5000 controller. The vibrometer operates by measuring the Doppler shift in a laser reflected off of the tube surface and giving a very acurate reading of the radial velocity v_r. This can then be integrated to obtain the deflection as

$$\delta_r(t) = \int_0^t v_r(t')\, dt' \,. \tag{2.2}$$

The hoop strain ϵ_{hoop} for a thin-wall tube is computed from the displacement as

$$\epsilon_{hoop} = \frac{\delta_r}{R} \tag{2.3}$$

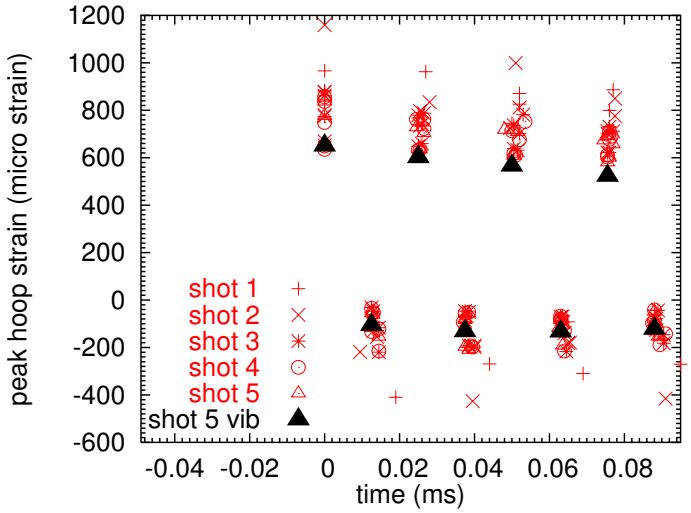

a)

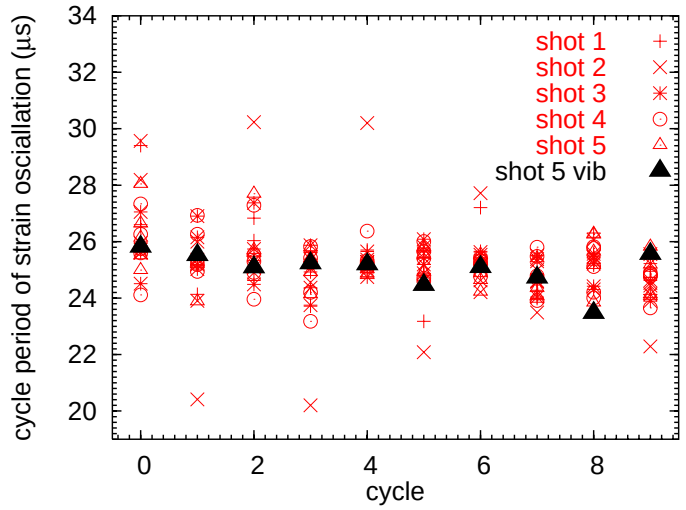

b)

Figure 2.8: Comparison of shots 1–5 results for a) peak hoop strain amplitudes and b) frequencies. Initial pressure of 40 kPa.

Data obtained from the vibrometer is presented in terms of the calculated hoop strain so that it may be directly compared with measurements from strain gauges. The raw and processed vibrometer data and the signal from the adjacent strain gauge S3 are presented in Fig. 2.9

A comparison between the vibrometer and all strain gauges for shot 5 is given in Fig. 2.10. Note the absence of jumps and the smooth appearance of the vibrometer data in comparison to the strain gauges.

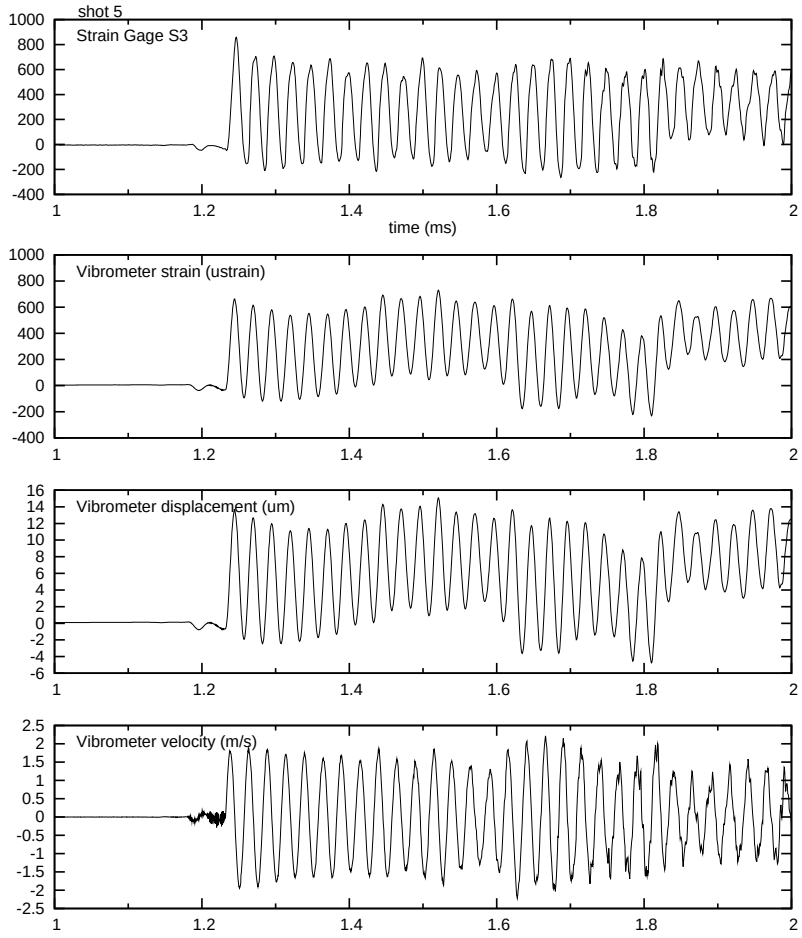

Figure 2.9: Raw and processed vibrometer data and comparison with strain gauge S3 adjacent to the vibrometer measurement location.

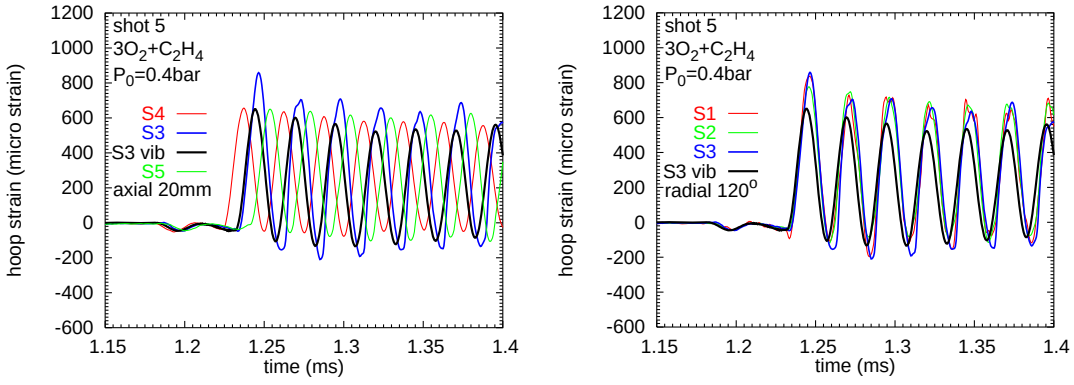

a) b)

Figure 2.10: Hoop strain data from gauges and vibrometer for a) gauges distributed along the tube axis and b) gauges distributed azimuthally at the central axial location. Shot 5 at 40 kPa initial pressure.

A number of tests carried out with the vibrometer showed that it was a much more repeatable and reliable strain measurement technique than the bonded gauges. For example, the shot-to-shot variation in the peak amplitutes for tests 1–5 is shown in Fig. 2.8. Additional data from simultaneous measurements with the vibrometer and strain gauges are given in Appendix E. Comparisons of peak strains from three repeated tests at 100 kPa are shown in Fig. 2.11a and at 50 kPa in Fig. 2.11b. Note that the peak amplitudes are highly repeatable for both sets of tests with shot-to-shot variation less than 2%, consistent with the repeatability of the detonation wave itself.

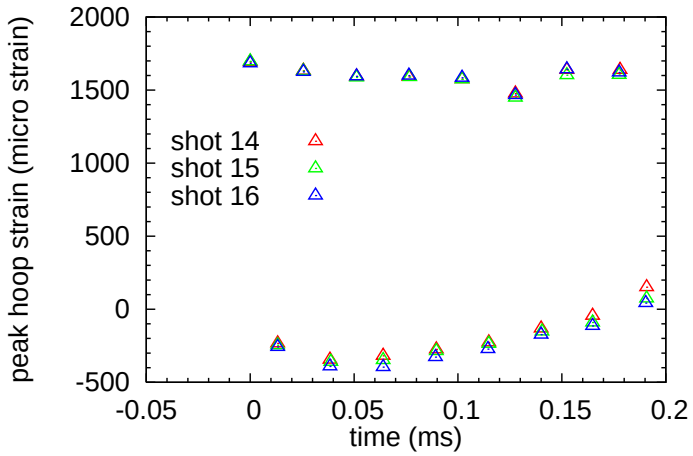

a)

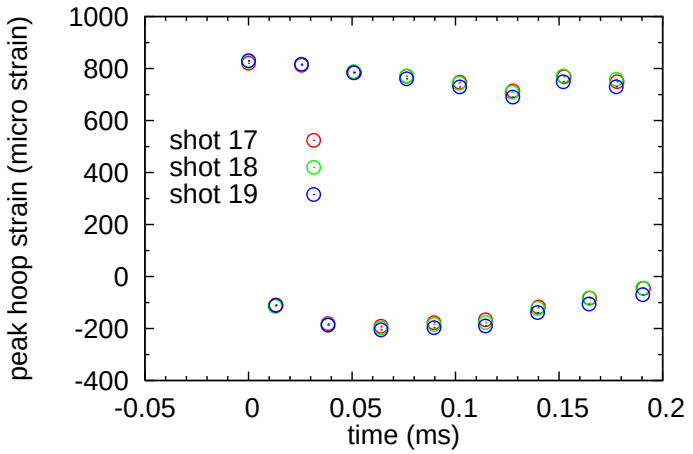

b)

Figure 2.11: Shot to shot comparison of peak hoop strains measured with the vibrometer at a) 100 kPa and b) 50 kPa.

The corresponding comparison for strain gauge S3 is shown in Fig. 2.12. Note that

the scatter is larger than in the vibrometer data, the maximum differences in the peak amplitude are up to 7% with the strain gauge measurement. Also, the damping rate (decrease in peak strain amplitude with successive cycles) appears to be higher for the strain gauge than for the vibrometer data.

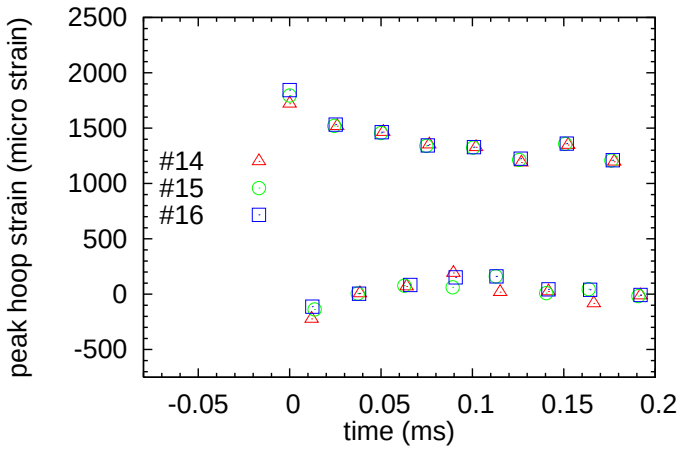

a)

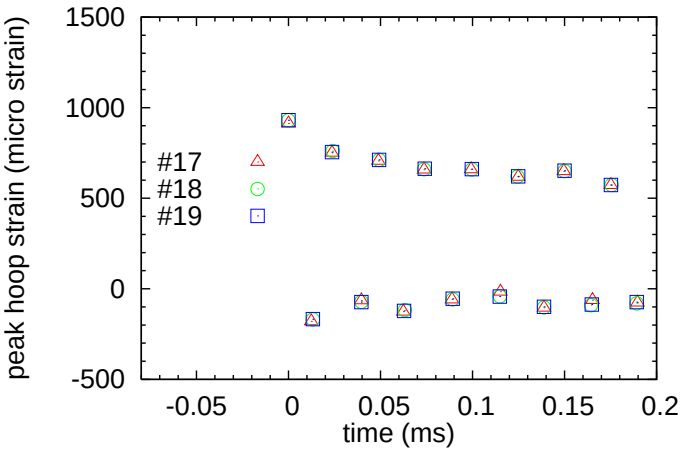

b)

Figure 2.12: Shot to shot comparison of peak hoop strains measured with strain gauge S3 at a) 100 kPa and b) 50 kPa.

It is clear from these comparisons that imperfections in the strain gauges are causing artifacts in the recorded strain signals. Examples of these may be seen in Fig. 2.9. Notice the jagged bumps in the peaks on the strain gauge signals which do not occur in the vibrometer signal. The raw velocity signal from the vibrometer signal shows that at these times there is a variation in velocity with a much higher frequency

component (>100 kHz) than the main hoop oscillation. The most likely explanation for the jagged artifacts in the strain gauge signals is that the high frequency vibration results in fatigue and micro-cracking of the strain gauge elements, as described in Vishay TN508 (2007). The jumps in the signal are caused by sudden changes in resistance of the gauge as the cracks open and close. The gauges were operated close to their maximum strain range, and the high frequency oscillation may result in gauge degradation.

2.3.3 Nonideal Effects on Strain Measurements

A number of issues may contribute to uncertainties in the measurements. The extruded tubing does not have a uniform wall thickness, which may cause variations in the strain over the azimuthal direction of the tube. The collets which provide the built in boundary conditions may not be perfectly aligned, which would introduce a prestress in the test specimen. The strain gauges may have imperfect bonding and exhibit creep. Finally, there is the possibility of nonlinear material response.

In the following sections, efforts are made to isolate and account for each of these imperfections, and to quantify the uncertainties they introduce into the measurement. Repeatability of the detonation initiation was examined in the second test series.

2.3.3.1 Wall thickness variation

In tests 20, 21, and 25–29, it was found that a systematic difference existed in the strains measured at different azumuthal locations. The most probable reason for this is nonuniformity in the wall thickness of the tube. To verify this the tube was sectioned and its wall thickness was measured with a micrometer, showing that indeed the wall thickness was nonuniform. This is most likely due to an asymmetry in the mandrel used in the extrusion process by which the tubes were formed. The measured wall thickness variation is shown in Fig. 2.13.

Two of the gauge locations, numbers one and three, were (except where noted in Table 2.2) located at 0° and 240° respectively, which are close to the extrema

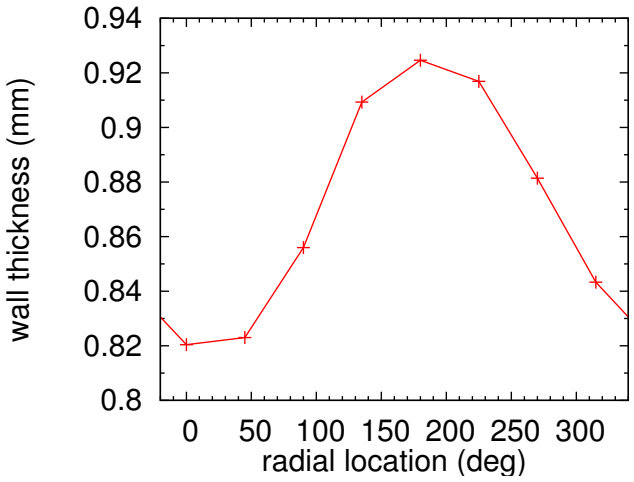

Figure 2.13: Wall thickness variation at the measurement location as a function of azimuthal coordinate.

of thickness. The relationship between thickness and hoop strain for thin-walled cylindrical tube of uniform wall thickness h is

$$\epsilon_{hoop} = \Phi \frac{R}{h} \frac{\Delta P}{E} \tag{2.4}$$

where Φ is the dynamic load factor and ΔP is characteristic pressure difference between the inside and outside of the tube. For a static load, $\Phi = 1$ and the ΔP is just the applied internal pressure. For a detonation ΔP is a reference value characterizing the peak pressure in the detonation wave. The dynamic load factor Φ depends on the wave speed, construction and size of the tube (see the discussion in (Beltman and Shepherd, 2002). For the present case, if we use the CJ pressure as the reference pressure, $\Delta P = 3.261$ MPa and for the nominal tube dimensions, we find that

$$\frac{R}{h} \frac{\Delta P}{E} = 1210 \quad \mu\text{strain} \, . \tag{2.5}$$

However, if we use the local tube thickness at the location of gauge S3 or V3, then the computed reference strain (2.5) will be lower, 1136 μstrain, since the tube is thicker at this location. Using the actual thickness, we find that $\Phi \approx 1.5$ for the first peak in hoop strain of 1700 μstrain. This is consistent with the values and analysis

discussed in Beltman and Shepherd (2002).

Treating the tube as a cylindrical shell (see Chap 13 Ugural and Fenster, 1987), (2.4) will also apply locally to a shell of nonuniform thickness so that for a constant applied pressure difference ΔP and dynamic load factor Φ, the local hoop strains are inversely related to the local shell thickness.

$$\frac{\epsilon_2}{\epsilon_1} = \frac{h_1}{h_2} \, . \tag{2.6}$$

Using the results of the vibrometer measurements at two locations V1 (at 15°) and V3 (at 225°), we have tested the relationship between thickness and peak strain, given in Table 2.3.

Table 2.3: Thickness and peak hoop strain variation with azimuthal location.

Location	h (mm)	ϵ_{max} μstrain
V1	0.815	2050
V3	0.926	1695

The ratio of thicknesses is $h_1/h_3 = 0.87$, and the inverse ratio of strains is $\epsilon_3/\epsilon_1 = 0.83$ as measured by the vibrometer. From these results, it appears that the wall thickness variation appears to be the most significant factor in systematic differences in peak strain amplitudes between measurement locations. In order to make quantitative comparisons and validation of the numerical simulations of the elastic wave propagation, this thickness variation has to be modeled. The effect appears to be primarily azimuthal in orientation and the wall thickness was found to be almost constant in the axial direction.

2.3.3.2 Prestress

The tubing was clamped into collets that were held by rigid blocks and fastened to the I-beam. The collet blocks (shown in Fig. 2.3) were adjusted to approximately align the specimen tube with the detonation tube and minimize any prestress in the

specimen. However, it is difficult to eliminate prestress altogether. The likeliest sort of prestress is a bending moment applied to the tube due to the misalignment of the collet blocks at each end of the specimen. A bending moment is expected to create differences in the response at different azimuthal locations, and may contribute to the noted differences in strain gauge response in the tests. In shot 22, deliberate and substantial misalignment of the collet blocks was introduced to test the sensitivity of the measured strains to the prestress. Vibrometer measurements were made at location S1 in tests 20, 21, 22, 23, 24 and at location S3 in tests 13, 14, 15, 16, 25, 29. All of these tests were done at 100 kPa initial pressure and the peak strain amplitudes for the first 6 cycles of oscillation are shown in Fig. 2.14. Prestress was not deliberately introduced in the other tests but no special efforts were made to minimize it either. There is no distinct effect of prestress observable in these results.

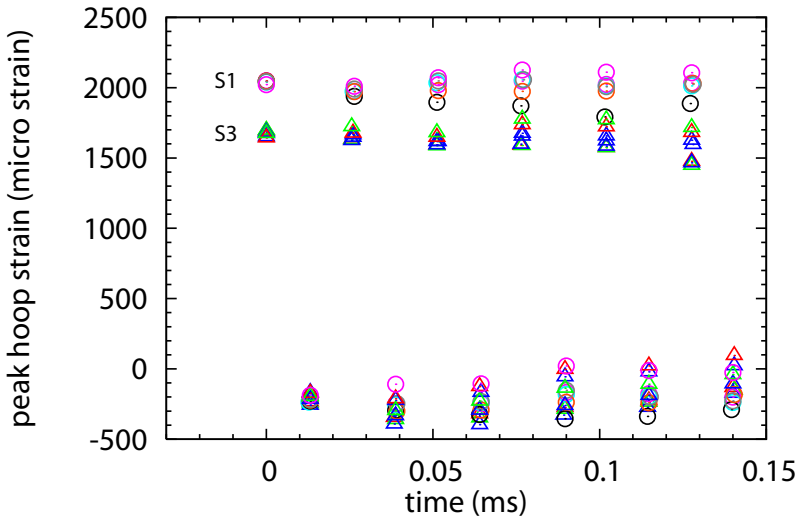

Figure 2.14: Test of prestress effect. The open black circle is data from test 22 with prestress.

2.3.3.3 Gauge Bonding and Creep

If the gauges are not properly bonded or the bond has a creep response, this can be determined by carrying out static testing and determining if there is hysteresis. This is done by recording data while applying stepwise increasing and decreasing pressure.

This can also be used as static calibration on the strain measurement, comparing the measured strains with the values computed using elasticity theory. To this end, the tube was pressurized with nitrogen at room temperature and the strain gauge signals were measured for a static pressure load at pressures of 0,20,40,60,...,140 psi. The tube was clamped by collets mounted solidly to the beam on both sides during this test so that the section with the strain gauges was not able to expand in the axial direction. The tube "caps" with the O-rings were solidly mounted to the I-beam, so that no force (either hoop or longitudinal) could be exerted onto the tube from the caps. The strain gauge excitation voltage was 10 V, the signal conditioner gain was 1000, the gauge factor was 2.09, and 120 Ohm gauges were used. The bridges were initially zeroed (balanced) at atmospheric pressure and no load applied for one hour before the test. The total loading duration was 12 minutes (2 minutes per step of 20 psi). The tube was held at 140 psi for 5 minutes before starting the unloading process. The duration for unloading was also 12 minutes (2 minutes per step of 20 psi). The results are shown in Fig. 2.15, which indicate a modest (12 μstrain) level of hysteresis that can be neglected compared to the peak strains measured in the present tests.

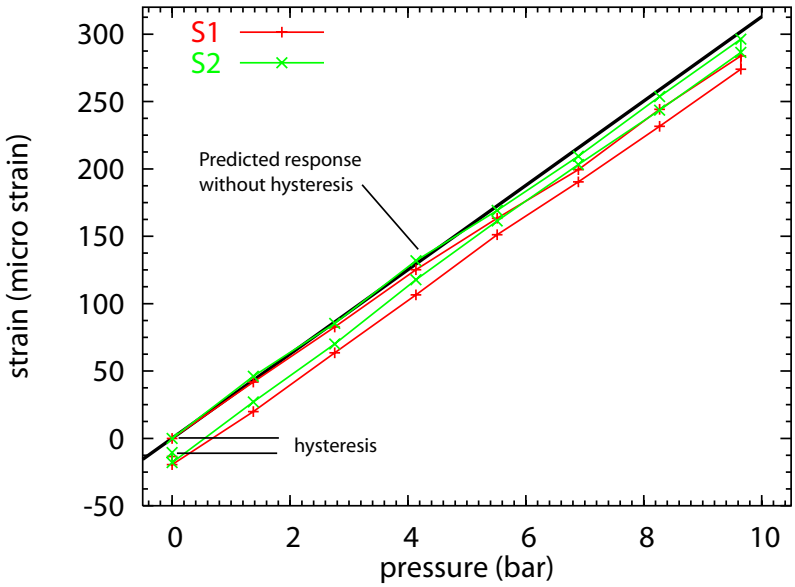

Figure 2.15: Test of gauge bonding and calibration using static loading and unloading.

2.3.3.4 Initial pressure variation

Figure 2.16 shows a comparison of the peak measured strains for initial pressure levels of 50 and 100 kPa. The 50 kPa tests have been scaled by a factor of the ratio of the computed CJ pressures for the two cases, the scaling factor is 33.4/16.2 = 2.06. The coincidence of the scaled data with the data taken at the higher initial pressure clearly indicate that the response is in the linear regime. Also note that the peak strains at the highest pressures tested were below 1700 μstrain, within the 0.2% (2000 μstrain) region that is conventionally taken to be the linear elastic regime.

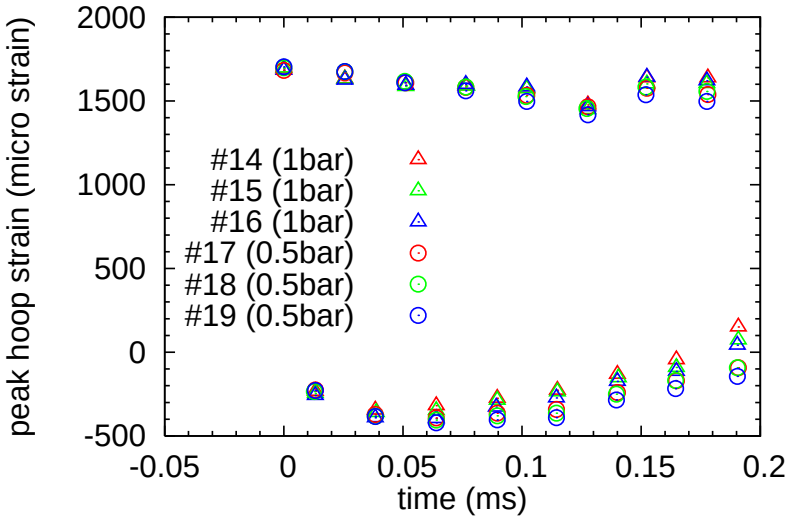

Figure 2.16: Comparison of peak hoop strain amplitudes for two initial pressure levels. The results for the 50 kPa initial pressure tests have been scaled by a factor of two to test the linearity of the tube response.

2.3.3.5 Thermal Effects

There are two types of thermal effects. 1) bulk temperature rise of the tube and gauge, and 2) thermal stress created by temperature difference between the inside and outside of the test specimen. The maximum bulk temperature rise can be estimated by assuming that all of the thermal energy in the combustion products is absorbed into the tube. A thermal energy balance assuming there are no other losses yields a

temperature rise of

$$\Delta T = \frac{\Delta e_{gas} \rho_{gas}}{\rho_s C_{p,s}} \frac{R}{2h} \,, \tag{2.7}$$

where $\Delta e_{gas} = 10.67$ MJ/kg is the energy change of the products in cooling from the constant volume combustion conditions to room temperature, $\rho_{gas} = 1.26$ kg/m^3 is the gas density, $\rho_s = 2780$ kg/m^3 is the specimen metal density, and $C_{p,s} = 963$ J/K kg is the specific heat capacity of the specimen metal. For an initial pressure of 100 kPa, the bulk temperature rise is predicted to be 63°C. The characteristic time over which this temperature rise occurs is on the order of the thermal diffusion time of h^2/κ, where $\kappa = k/\rho C_p = 5.82{\times}10^{-5}$ m^2/s is the thermal diffusivity of the specimen metal. The thermal diffusion time is 14 ms for the present experiment, about 500 times longer than the period of hoop oscillation. Thus on the time scale of the measurements, 0.2-0.5 ms, the strain gauge temperature and substrate temperatures are essentially unchanged. However, there will be a substantial temperature gradient between the inside and outside of the tube and this has to be considered.

Bulk Temperature Effects The gauges used in the present study are made for "self compensation" with a substrate that has a thermal expansion coefficient of 6 ppm/°F ($1.32{\times}10^{-5}$ K^{-1}). This value is matched to the thermal expansion of steel but aluminum alloys have a higher value, closer to 11–13 ppm/°F ($2.43{\times}10^{-5}$ K^{-1} for 6061T6). This mismatch in the gauge self-temperature coefficient (STC) with the substrate coefficient of thermal expansion will result in a thermal artifact in the gauge output if there are significant thermal changes during the measurement period (Vishay TN504, 2007). The resistance change due to thermal response for very small temperature changes is

$$\frac{\Delta R}{R_o} = \left[\beta_G + S_g \left(\frac{1 + K_t}{1 - \nu_o K_t} \right) (\alpha_s - \alpha_g) \right] \Delta T \,, \tag{2.8}$$

where K_t is the gauge transverse sensitivity coefficient Vishay TN509 (2007), β_g is the resistance coefficient of temperature of the gauge, $\alpha_s - \alpha_g$ is the difference between the substrate and gauge coefficient of thermal expansion. For A-alloy gauges, the

factor involving transverse sensitivity is close to unity and resistance coefficient of temperature is actually extremely small over the range of interest in the present experiment. The last term $2(\alpha_s - \alpha_g)\Delta T$ represents the effect of differential thermal expansion and amounts to 22 μstrain K^{-1}. For temperature changes of a few Kelvin during the measurement period, this is negligible compared to the peak strains of 2000 μstrain.

An additional effect is that the gauge constant S_g is a function of temperature and for large temperature variations, this must be accounted for in analyzing the data. For a strain gauge in a quarter-bridge configuration that is used in the present experiments, the conversion of the strain ϵ to voltage output E of the signal conditioner (Kobayashi, 1993) is given by

$$E = \frac{1}{4} E_i G S_g \epsilon \ , \tag{2.9}$$

where S_g is the gauge factor (approximately 2 for the gauges used in the present study), G is the amplifier gain (typically 100 for peak strains of 2×10^{-3}), and E_i is the excitation voltage (10 V in the present study). Variations in the gauge factor will therefore directly translate to variations in the output voltage of the signal conditioner. For the CEA type gauges, the gauge metal is constantan (A-alloy) and the variation of gauge factor with temperature is 1.1% per 100°C or 1.1 $\times 10^{-4}$ K^{-1}. Over the range of interest in the present experiment, the effect of temperature on the gauge constant can be neglected.

Thermal Stress The strain induced by thermal stress associated with the temperature gradient through the tube wall thickness is discussed in Appendix A. The theory of elasticity can be used to show that contribution to the hoop stress at the outer wall due an energy deposition Q' per unit length of the tube, is

$$\sigma_{\theta\theta} = \frac{\alpha E}{2\pi \rho_s C_{p,s}} \frac{2}{r_o^2 - r_i^2} Q' \ . \tag{2.10}$$

This expression is valid for the case of no axial force, i.e., no restraint in the axial

direction. We can evaluate the energy input per unit length by carrying out an energy balance and expressing this in terms of Δe, the energy per unit mass of combustion products that is transferred to the wall. Using the stress-strain relationship for plane stress (Timoshenko and Goodier, 1970), the hoop strain increment due to the thermal effects for a thin-wall tube is approximately

$$\epsilon_{\theta\theta} = \alpha \frac{\rho_g}{\rho_s} \frac{\Delta e}{C_{p,s}} \frac{R}{2h} \, . \tag{2.11}$$

This is valid for both uniform and nonuniform heating. In the case of uniform heating (constant temperature), there will be thermal expansion but no thermal stress. For the present situation, we can evaluate the constants in (2.11) to obtain $\epsilon_{\theta\theta} =$ 145 μstrain per MJ/kg of energy. If all the energy from the gas is absorbed into the tube wall, this results in 1547 μstrain. The fraction of this that is absorbed during the measurement period can be estimated using the results of Radulescu and Hanson (2005), who showed that the heat transfer occurs primarily during the time when the gas is moving inside the tube. Using an estimated peak heat flux of 30 MW/m^2 and a Taylor wave duration of 0.3 ms, the thermal energy per unit length transferred into the tube wall is 1130 J/m. According to (2.10), this will result in 82 μstrain or about 4% of the peak value of 2000 μstrain. We infer from (2.11) that only about 5% of the thermal energy is lost from the gas in this time period, which is consistent with the very slight droop observed in the pressures measured in shots 30-34 by the first transducer inside the detonation tube. The effect on the first few cycles of the strain signal will be negligible since each cycle only takes 26 ms, during which we would expect a maximum thermally-induced strain of 7 μstrain per cycle.

2.3.3.6 Transient Response

Strain gauges are typically calibrated for static (or low speed, i.e., quasi-static) measurements of strain but in the present experiments were used to measure dynamic strain. Capturing and interpreting dynamic strain signals with fidelity requires considering a number of factors. First, the instrumentation must have the proper band-

width so that the high frequency signals are not attenuated and aliasing is avoided during the recording process. The typical hoop frequency is about 38 kHz and the bandwidth of the signal conditioners used in the present experiments is nominally 100 kHz on the "wideband" setting. The actual bandwidth of the amplifiers depend on the gain setting. For the present experiments, a nominal gain of 100 was used to record strain signals with a maximum of 2000 μstrain. For this gain value, the -0.5 dB point for the amplifier is 80 kHz (Vishay 11255, 2006). The signals were digitized with a sampling rate of at least 1 MHz and in some cases 2 MHz was used to check some of the artifacts that were observed in the signals.

We estimate that the maximum error introduced by the frequency response and digitizing error of the measuring system is on the order of 0.5%.

The gauge element area is approximately 2.5 $\times$ 3.0 mm. For gauges of this size, Ueda and Umeda (1998) showed that with the appropriate signal conditioning equipment, these gauges could be used with frequency content up to 300 kHz and strain rates up to 750 s^{-1} with less than 5% attenuation when measuring longitudinal pulses in Hopkinson bars. In the present case, the primary frequency of the signals is 38 kHz so that for peak strains of 2000 μstrain, the strain rate will be about 600 s^{-1} and the conditions of Ueda and Umeda's experiments are satisfied by the present tests.

There is a slight averaging effect due to the propagating wave nature of the disturbance. The hoop oscillations have a period of 26 μs and propagate with the wave front which is moving at the detonation velocity, about 2300 m/s. This means that the wavelength is 60 mm, about 20 times larger than the gauge element width. This means that a small amount of averaging will occur due to the strain variation across the gauge. The magnitude of the averaging will depend on the phase of the wave, with the greatest effect occurring at the maxima and minima of the signals. For the peak of a sinusoidal waveform with wavelength λ centered on a gauge with width w, the strain averaged over the width will be

$$\epsilon = \epsilon_m \left[1 - \frac{(2\pi)^2}{24} \left(\frac{w}{\lambda} \right)^2 + O\left(\frac{w}{\lambda} \right)^4 \right] . \tag{2.12}$$

Using the values appropriate for the present tests, the measured peak strain will be at most reduced by 0.4% from the actual peak value.

2.3.3.7 Gauge location and angular misalignment

The gauges were intended to measure strain in the hoop direction only but due to slight errors in aligning the gauge during the gluing operation the gauge output may be slightly in error, see Fig. 2.17.

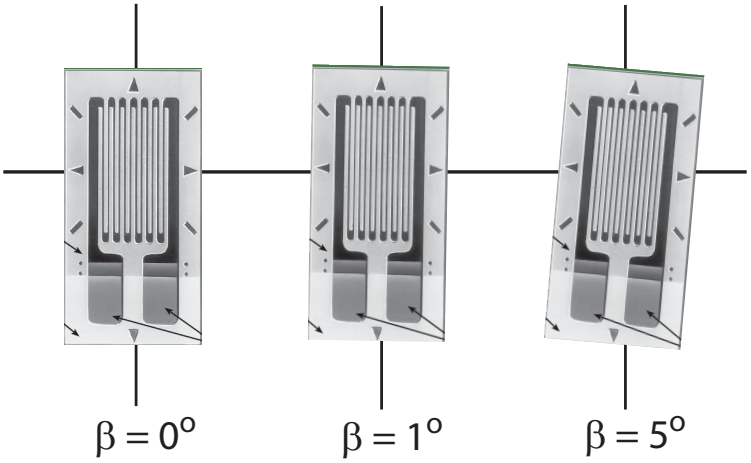

Figure 2.17: Appearance of gauges with perfect, 1°, and 5° angular misalignment showing that detection of misalignment is possible to do visually at these levels.

The axial location error can be eliminated by careful measurement of the final position but the direction that the gauge is pointing (angular alignment) is harder to control or measure. The error due to angular misalignment depends on the strain field and the orientation of the gauge relative to the principal axes of the strain, see the discussion in Vishay TN511 (2007). For a single gauge that is misaligned by an angle $\pm\beta$ relative to the intended angle ϕ relative to the major strain axis, the gauge indication will be in error by

$$\frac{\epsilon_p - \epsilon_q}{2} \left[\cos 2(\phi \pm \beta) - \cos 2\phi\right] \ , \tag{2.13}$$

where ϵ_p is the maximum value of the principal strain and ϵ_q is the minimum value of the principal strain. For the present situation, the hoop strain is the maximum

principal strain for gauges aligned with the hoop direction, and the error is

$$\frac{\epsilon_p - \epsilon_q}{2} \left[\cos 2\beta - 1\right] \ . \tag{2.14}$$

Consider measurements of hoop strain. The hoop direction is the direction of maximum principal strain for axially-symmetric loading on a tube so that $\epsilon_p = \epsilon_{hoop}$. For a thin tube with zero axial prestress (see Appendix B, part I Beltman and Shepherd, 1998), the relationship between the hoop and axial strain is $\epsilon_{axial} = -\nu\epsilon_{hoop}$. The relative error in hoop strain for a gauge that is intended to be aligned with the hoop direction ($\phi = 0$) but is misaligned by an angle β is

$$\text{Error} = \frac{(1+\nu)}{2} \left[\cos 2\beta - 1\right] \ . \tag{2.15}$$

For a gauge that is intended to measure axial strain, the relative errors are a factor of $1/\nu$ higher. A plot of relative error (in terms of percentages) is given in Fig. 2.18 for the hoop strain case.

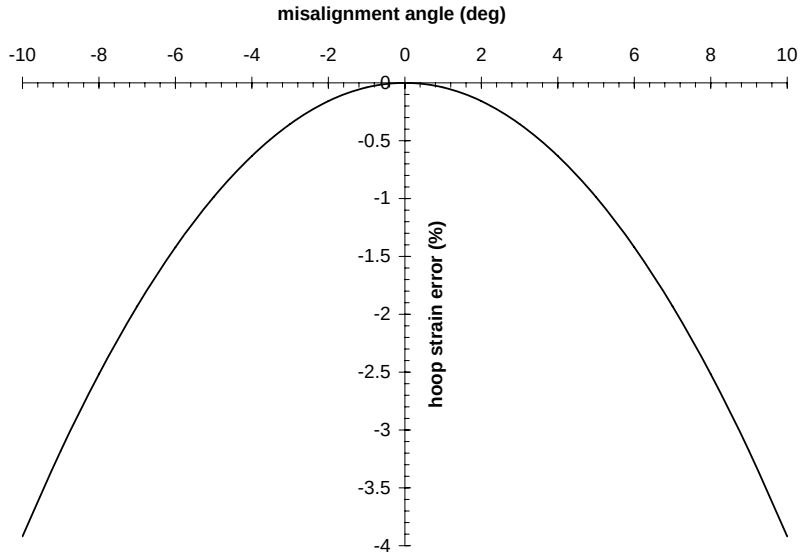

Figure 2.18: Percentage error is hoop strain as a result of angular misalignment, computed with (2.15).

Based on these considerations and our visual estimations of alignment error, we expect that the strain gauge output may systematically be in error by as much as

3%. Note that the effect of the misalignment is to systematically reduce the measured strain relative to the actual value.

2.4 Series 2

Preliminary efforts to simulate the detonation propagation in the experiments of Series 1 were found to exhibit large discrepancies between the predicted and measured pressure signals. In order to investigate these discrepancies and the repeatability of the detonation waves from shot to shot, a series of modifications was made to the experimental setup and several new tests were performed. In the end the modifications were found to greatly improve the fidelity of the pressure signals, and the simulation was able to do a much better, albeit still imperfect, job of predicting the measured traces.

2.4.1 Tests in Original Apparatus

The dimensions of the test specimen tube for shots 30–34 with the original setup are shown in Fig. 2.19. One pressure transducer was mounted in the middle of the test section and one was located at the end. The locations of the pressure transducers relative to the ignition point are shown in Table 2.4. The arrival times and the maximum pressures recorded at each transducer are listed in Table 2.5. The detonation waves propagated within -0.5% to +1% (see Fig. 2.20a) of the computed Chapman-Jouguet (CJ) velocity for these five tests. A comparison of the distance-time relationship for these tests is shown in Fig. 2.20b. The data are very repeatable with a small offset in arrival times for each data set. This offset is due to the intrinsic variability in the process of deflagration-to-detonation transition that is used to initiate the detonation. An average detonation velocity of 2357±12 m/s is computed by finding the average of slope to least squares fits of lines to the data in Fig. 2.20b.

Figure 2.4.1 demonstrates the repeatability of the pressure signals from test to test. Although the incident data were very repeatable and consistent with the CJ values, the measured peak pressures and arrival time for the reflected wave were not

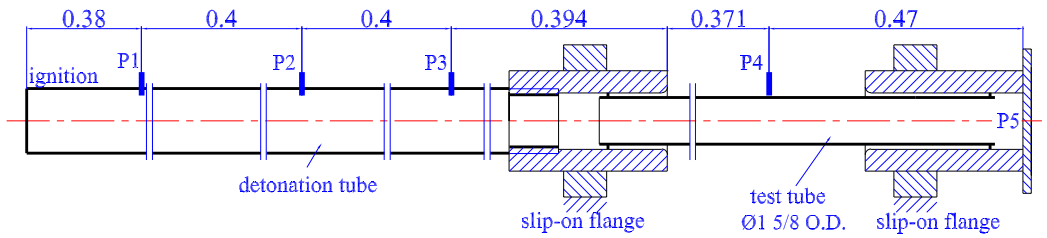

Figure 2.19: Tube dimensions for the shot 30-34 performed in the unmodified facility.

Table 2.4: Location of pressure gauges.

Station	X (in)	X (m)
P_1	15	0.38
P_2	30.75	0.78
P_3	46.5	1.18
P_4	76.6	1.945
P_5	96	2.439

Table 2.5: Peak pressures and pressure wave arrival times for tests 30-34. The initial pressure is nominally 100 kPa for all tests.

shot	T_0 (K)	t_1 (ms)	P_1 (MPa)	t_2 (ms)	P_2 (MPa)	t_3 (ms)	P_3 (MPa)	t_4 (ms)	P_4 (MPa)	t_5 (ms)	P_5 (MPa)
30	296	0.389	5.22	0.556	4.28	0.723	4.43	1.62	3.22	1.25	8.162
31	297.5	0.397	5.27	0.568	4.13	0.734	4.52	1.05	3.30	1.26	7.79
32	297.3	0.426	5.31	0.600	4.03	0.764	4.47	1.08	3.12	1.31	9.07
33	296	0.366	4.33	0.538	4.02	0.709	4.50	1.03	3.42	1.25	10.13
34	296	0.421	4.37	0.593	3.95	0.764	4.42	1.08	3.19	1.27	8.103

in as good agreement with the simulations. After careful analysis of the data, we found four main reasons for these discrepancies.

1. The distance between the ignition and the reflecting end was not properly measured.

2. The detonation speed computed based on the incident wave arrival time was slightly decreasing as the detonation propagated through the tube. This velocity variation was not considered in the simulations.

3. The five pressure transducers used in these tests had never been recalibrated since they were purchased.

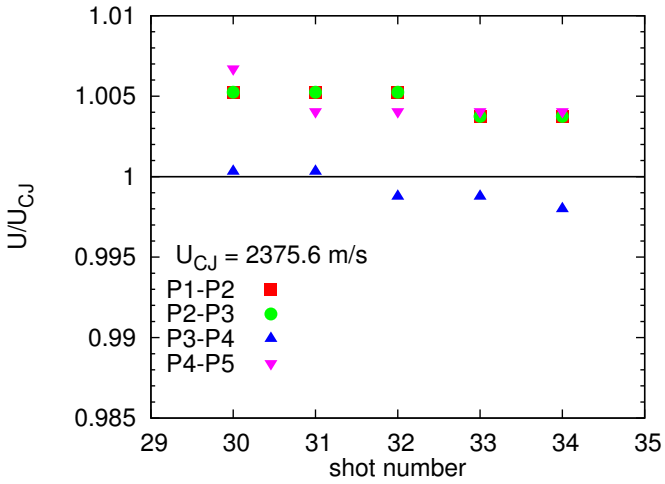

a)

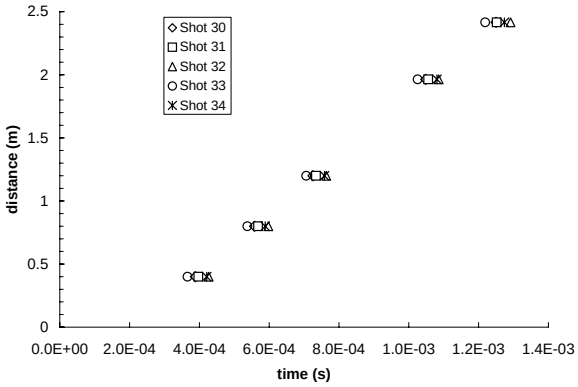

b)

Figure 2.20: a) Detonation velocity computed from the arrival times using pressure data of tests 30-34. b) Corresponding space-time diagram.

4. Some pressure transducers were not thermally protected, and the pressure signals contained artifacts.

After the first three problems were addressed, the comparison shown in Fig. 2.22 was obtained.

2.4.2 Tests in The Modified Facility

2.4.3 Modifications

To address the deficiencies in the earlier tests, a number of changes were made and new tests were carried out. The modifications are discussed below.

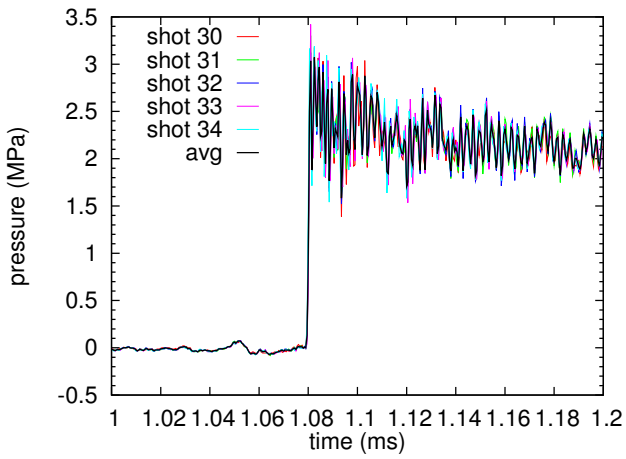

a)

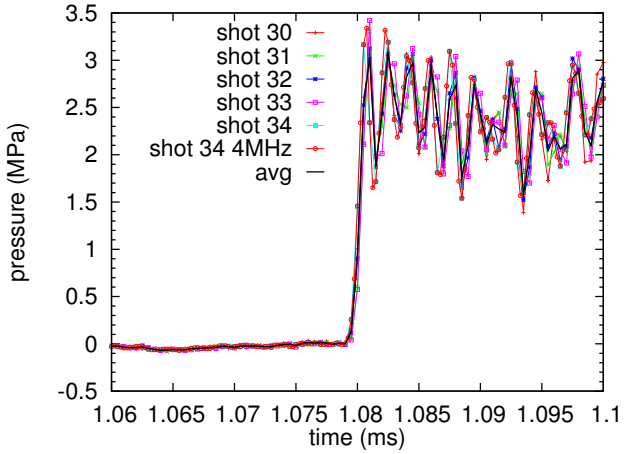

b)

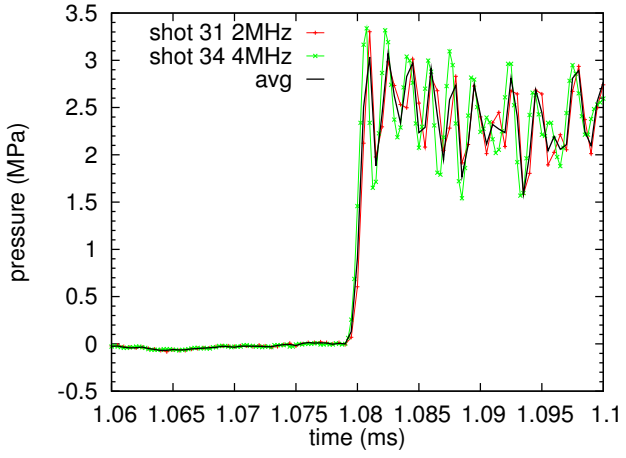

c)

Figure 2.21: Superimposed pressure traces for shots 30-34.

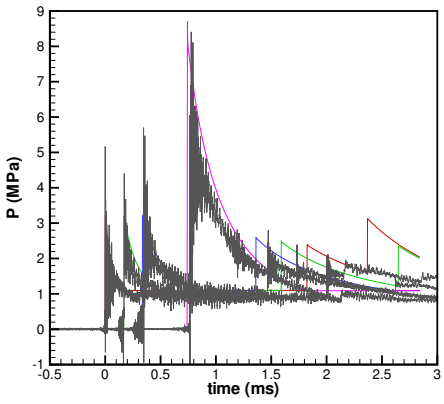

Figure 2.22: Comparison of computations and shot 31 at four stations after addressing problems 1, 2 and 3.

(1) Recalibration of pressure transducers

The pressure transducers were returned to the factory for evaluation and calibration. Table 2.6 lists the new conversion factors for the recalibrated pressure transducers.

Table 2.6: Conversion factors of the re-calibrated pressure transducers.

Station	Type	Conversion factor
P_1	113A24 SN 14835	702.5 mV/MPa
P_2	113A24 SN 13277	700.4 mV/MPa
P_3	113A24 SN 14771	732.4 mV/MPa
P_4	113A24 SN 13909	727.7 mV/MPa

(2) Modification of the reflecting ends.

In order to measure the strain signals close to the reflecting end, the previous slip-on flange was replaced with two plugs; one fits into the test tube end, and the other one mated with the collet, see Fig 2.23.

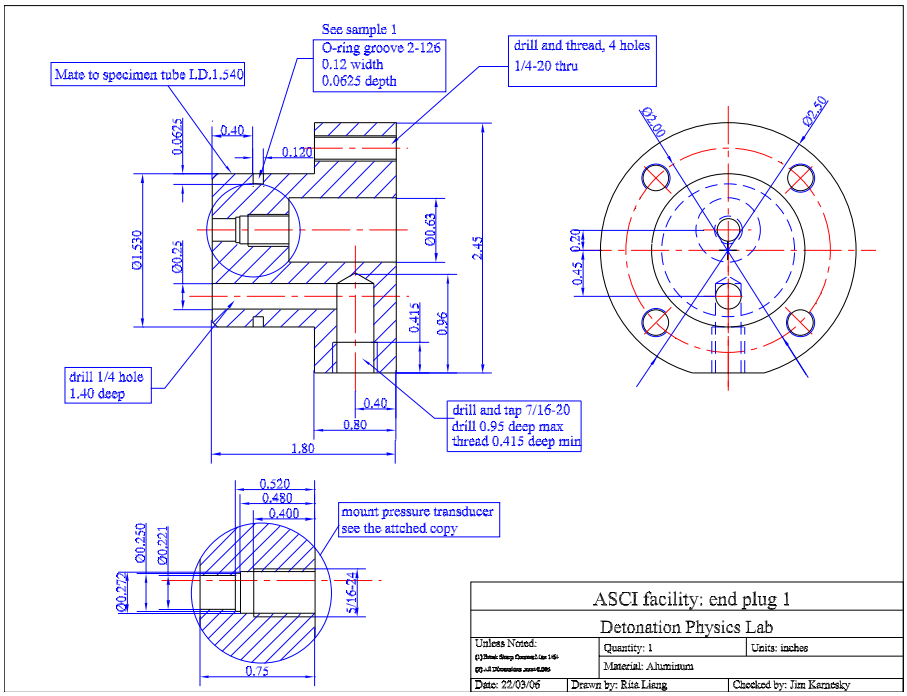

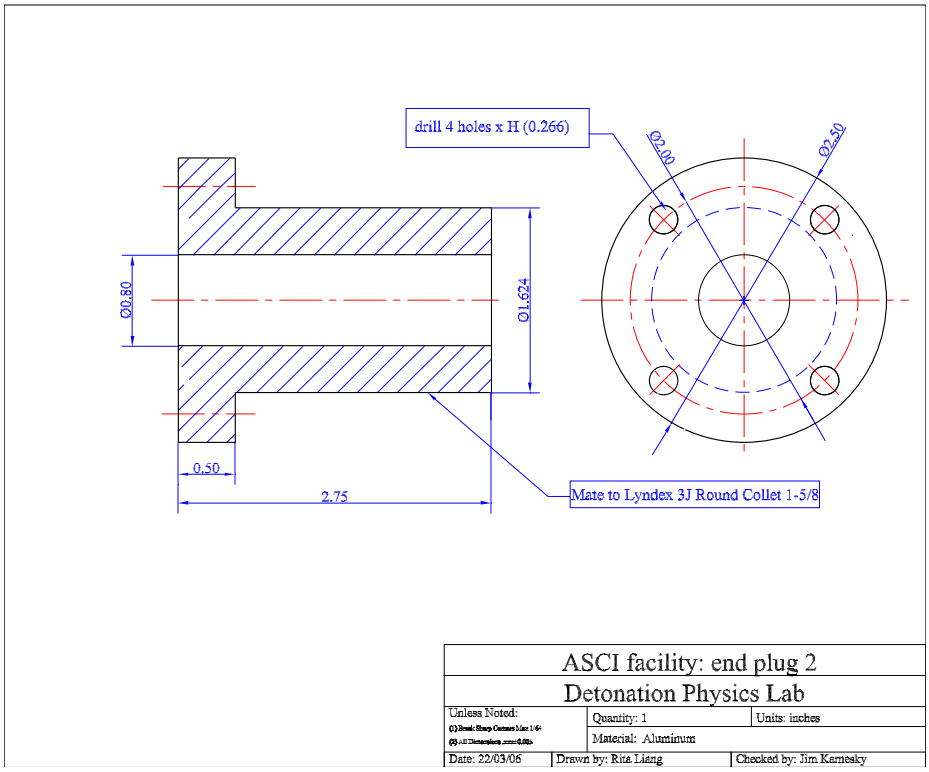

Figure 2.23: Modified end plugs.

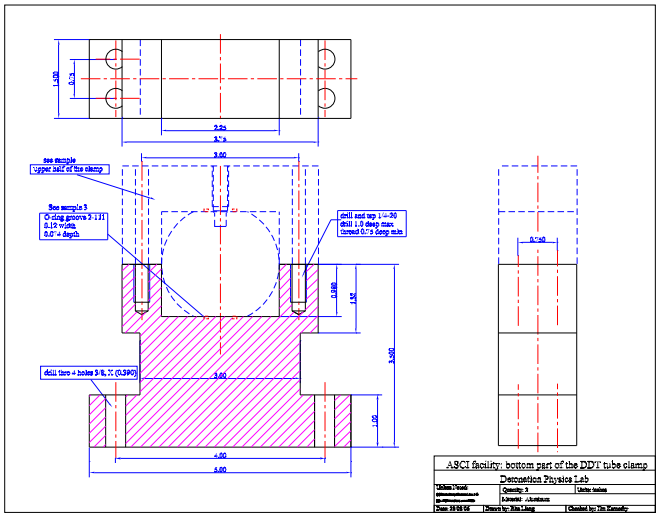

Figure 2.24: Modified clamp.

(3) Modification of clamps for mounting the pressure transducers

The critical wave speed (Beltman and Shepherd, 2002) for the detonation initiation tube (Fig 2.25) is about 2200 m/s, which is within 8% of the CJ detonation speed (2373.6 m/s) for C_2H_4+3O_2 mixtures at an initial pressure of 100 kPa and temperature of 23°C. As discussed in Beltman and Shepherd (2002), this will result in a resonant response of the tube wall that can produce artifacts in the pressure signals due to acceleration sensitivity of the piezoelectric pressure gauges. This is manifested as high-frequency oscillations observed ahead of the detonation front and superposed on the detonation wave pressure in the pressure traces of Fig. 2.22. To decrease the magnitude of the accelerations, we locally increased the tube stiffness with two new clamp assemblies (see Fig. 2.24) to hold the transducers to the tube. Pressure transducers were mounted on the top half of the clamp and the bottom half was mounted to the stiff work table. The improvement for the pressure signals was not as good as expected, so further changes were made, as discussed in Modification 5 below.

(4) Improvement of reflecting pressure transducer signal

We added a piece of rubber between the test tube and the end cap to dampen the effect of tube oscillation on the pressure transducer mounted in the end cap.

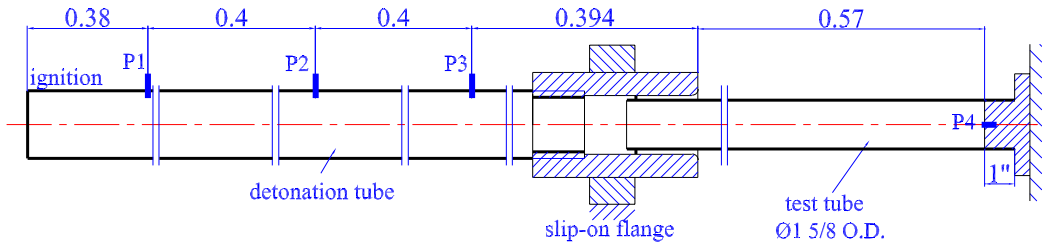

Figure 2.25: Tube dimensions for shots 1-7.

Table 2.7: Notes for shots 1-7.

shot	P_0 (bar)	T_0 (K)	Mixture	Notes
1	0.4	295	$0.3H_2+0.7N_2O$	changes 1-2
2	0.4	296	$0.3H_2+0.7N_2O$	changes 1-2
3	0.4	296	$0.3H_2+0.7N_2O$	changes 1-2
4	0.99	297	$C_2H_4+3O_2$	changes 1-3
5	1.0	295	$C_2H_4+3O_2$	changes 1-4
6	0.9974	296	$C_2H_4+3O_2$	changes 1-2, 4-5
7	0.9995	297	$C_2H_4+3O_2$	changes 1-2, 4-5

(5) Modification of mounting pressure transducers

In the previous tests, pressure transducers were directly mounted on the tube and the seals were copper rings. A Swagelok adaptor was added between the tube and the pressure transducer. The rubber o-ring seal between the tube and the adaptor dampened the tube oscillation significantly.

2.4.4 Results

A total of 7 shots ware carried out with the modified setup, see Tables 2.7 and 2.8. Shots 1-3 were performed only for validation of the initial tube setup. Shots 4-7 were used for comparison with the computations. Signals in shots 6 and 7 have the best quality of all the shots that were performed. The locations of the pressure transducers for these tests are listed in Table 2.9.

Table 2.8: Arrival time of the incident wave as determined by time of peak pressure for shots 4-7.

shot	t_1 (ms)	$P_{1,max}$ (MPa)	t_2 (ms)	$P_{2,max}$ (MPa)	t_3 (ms)	$P_{3,max}$ (MPa)	t_4 (ms)	$P_{4,max}$ (MPa)
4	0.425	3.26	0.603	4.22	0.781	3.78	1.20	8.88
5	0.455	4.41	0.634	5.77	0.802	4.85	1.24	9.02
6	0.396	5.02	0.566	6.44	0.738	5.86	1.16	10.60
7	0.361	4.96	0.531	5.46	0.701	6.00	1.130	9.82

Table 2.9: Location of gauges.

Station	X (in)	X (m)
P_1	15	0.38
P_2	30.75	0.78
P_3	46.5	1.18
P_4	84.5	2.146

2.4.4.1 Experimental Uncertainties

The detonation wave arrival time data shown in Fig. 2.26 indicates that there is some variability in the DDT process that results in some scatter of the wave arrival at the first transducer. Subtracting the arrival time at gauge 1 from all subsequent gauges for a given test enables us to better compare tests. On this basis, the data are extremely consistent from test to test and the results can be represented as the average over all four tests. This is shown in Fig. 2.26 as the points labeled average.

Although the data appear to be adequately fit by the straight line shown in Fig. 2.26, careful analysis shows that the wave speed is slightly decreasing as the wave propagates from gauge 1 to 4. Using a parabolic curve fit, a velocity of 2286.0 m/s is obtained at gauge 1 and 2100.9 m/s at gauge 4. These correspond to a deficit, $(U - U_{CJ})/U_{CJ}$, of -3.7% gauge 1 and -11.5% at gauge 4. The estimated single-sample uncertainty of the computed velocity between stations 1–2 and 2–3 is 28 m/s and between stations 3–4 is 11 m/s. Given these values of the uncertainty in the individual observations, we conclude that the decrease in velocity between stations 1 and 4 is a real effect which is consistent with the data shown in Fig. 2.20. The deceleration of the wave is also consistent with observations on deflagration-to-detonation transition

Ciccarelli and Dorofeev (2008) that show the detonation wave is overdriven, $U > U_{CJ}$, upon emerging from the transition event. The variation in wave velocity with distance is not accounted for in the simulations but instead an average value is used. A linear least-squares fit to the time-shifted data for shots 4–7 yields an average velocity of 2284 m/s with a standard deviation of 12 m/s. Compare this with the value obtained in the previous tests (Section 2.4.1 of 2357 ± 12 m/s. The systematic difference of 73 m/s far exceeds the standard deviation computed for either set of data.

To account for the variation arising due to the uncertainty in the initial conditions, the CJ wave speed was computed for a range of initial conditions. Factors which were varied were the initial compositions, pressures, and temperatures that correspond to the estimated range that results from the uncertainty in the facility operation and instrumentation. The composition is set using the method of partial pressures with an electronic capacitance pressure gauge (MKS Baratron Model 121A) with a full scale range of 1000 Torr and an accuracy of 0.5% of the reading and minimum resolution of 0.5 Torr. From these values we estimate the ethylene mole fraction to be 0.25 ±0.002. The average initial temperature was 23°C with a typical variation of 1°C and an additional instrument uncertainty of 1°C, so that the initial temperature range is 23 ± 2°C. The estimated range in initial pressure is 100 ± 0.5 kPa.

The CJ state and isentrope in the products was computed for variations of each individual parameter using the `demo_CJState-isentrope.m` program of the Shock and Detonation Toolbox (Browne et al., 2008). The effect of the variations on CJ velocity and pressure is shown in Table 2.10. From this sensitivity study, we see that the potential variation in composition will contribute the most to uncertainty in the detonation velocity, $U_{CJ} = 2373.6 \pm 5$ m/s. The effect of initial temperature and initial pressure variations on the computed CJ velocity are an order of magnitude smaller than the composition effects.

Based on these uncertainty estimates, it appears that there is a systematic difference in the velocities between the two sets of data in the modified and unmodified setups that cannot be explained by variations in composition or initial conditions. Other potential significant sources of uncertainty are the gauge locations and arrival

Table 2.10: Computed variation of CJ velocity and pressure as a function of the initial parameters.

P_0 (kPa)	T_0 (K)	$X_{ethylene}$	U_{CJ} (m/s)	P_{CJ} (MPa)
100.0	296.1	0.250	2373.6	3.361
100.0	296.1	0.252	2368.3	3.347
100.0	296.1	0.248	2378.9	3.374
100.5	296.1	0.250	2373.8	3.378
99.5	296.1	0.250	2373.3	3.343
100.0	298.1	0.250	2373.2	3.337
100.0	294.1	0.250	2374.0	3.384

time measurements. Consider computing velocity from two gauges located a distance X apart with the wave arrival time difference of T. From the arrival time velocity computation, we can compute the velocity uncertainty as

$$\frac{\delta U}{U} = \frac{\delta X}{X} - \frac{\delta T}{T} \tag{2.16}$$

where δX is the uncertainty in the gauge position difference and δT is the uncertainty in the pressure arrival time difference.

Consider a typical gauge spacing of $X = 500$ mm and a nominal wave speed of approximately 2300 m/s, which gives a nominal arrival time difference $T = 215$ μs. If the arrival times were measured precisely, then the observed wave speed difference $\delta U/U$ = -0.03 between the two sets of tests corresponds to a gauge spacing difference of $\delta X = -15$ mm. If the gauge spacing was measured precisely, then the observed wave speed difference corresponds to an arrival time difference of +6.45 μs. Based on the measurement capabilities in the lab, the gauge spacing should have been known to ± 1 mm and for a sampling speed of 2 MHz, the wave arrival time should be determined within ± 1 μs. The main source of uncertainty in this measurement is the selection of which peak to assign as the arrival time when the signals are noisy. This is most important for the gauge on the reflecting end. This means that the measurement uncertainty should be at most ± 5 m/s due to spatial location

uncertainty and ± 12 m/s due to arrival time uncertainty. The observed difference is a factor of 4 times larger than the maximum possible combined uncertainty which indicates a systematic error occurred in one of these sets of experiments. Based on post-test visual inspection and the location of witness marks made by the collets on the specimen tubes, the error was in the position measurements for the 2005 tests.

2.4.5 Detonation Simulation Method

The simulations were carried out using AMROC Deiterding et al. (2006b) with a rigid confining tube. The detonation was simulated using a CV-burn model (see (Deiterding et al., 2006a)) which gives product pressure profiles and detonation wave speeds that are very similar to the computationally more complex one-step model of reaction described by Deiterding et al. (2007). The CV-burn model has been extensively used in high-explosive simulations as discussed by Bdzil et al. (2001) and although the details of the reaction process are not resolved, this technique is computationally efficient for a problem where the dynamics of the detonation products are of interest. This is the case in the present problem.

The flow is simulated using the one-dimensional Euler model of a perfect gas with energy addition. The specific energy release used to simulate the detonation was $q =$ 4,704,080 J/kg and the ratio of specific heats was constant $\gamma = 1.24$. The computed CJ detonation velocity using these parameters is 2291.7 m/s, which is selected to approximate the observed average velocity of 2285 m/s shown in Fig. 2.26. The parameters are not completely consistent with the thermodynamics of the products but give the best results for the comparison of the data and simulation. As discussed by Radulescu and Hanson (2005) and Wintenberger et al. (2004) and also used in previous computations (Shepherd et al., 1991) of wave motion in detonation products, the appropriate values of the specific heat ratio is closer to the equilibrium value of 1.14 rather than the post-shock frozen value of 1.24.

2.4.6 Comparison

Data from Shots 4 and 7 are compared with simulation results in Fig 2.27 and Fig 2.28. The measured arrival times of the incident waves at four stations, as well as the pressure history, now show excellent agreement with simulations for incident waves. The experiment peak pressures are substantially higher than the simulated values but this is typical of unfiltered experimental data which shows large amplitude pressure fluctuations superposed on the general trend of a shock followed by an expansion wave. The high frequency signals are not noise but a combination of secondary shock waves (transverse waves and transients from the initiation) and artifacts due to the acceleration sensitivity of the gauges and vibration of the tube wall. The experimentally measured pressure behind the reflected wave is systematically lower than the simulated values. The agreement between experiment and simulation is now reasonable for the reflected waves but there remain systematic differences between simulations and data for the arrival time and amplitudes.

There are several possible explanations for the remaining systematic differences between simulation and experiment that we have considered:

1. The fluid dynamics model is highly idealized and does not account for heat loss to the tube walls. Radulescu and Hanson (2005) show that this effect is significant in tubes of this length and can result in up to a 10% difference in the thermodynamic state of the products that the reflected waves are propagating through.

2. The thermodynamic model of the detonation products does not account for the correct relationship between enthalpy (or internal energy) and temperature. A two-gamma or detailed model of the thermochemistry would be needed to resolve this.

3. The simulation does not account for the turbulent motion and nonuniform state that must exist sufficiently far behind the detonation front. The turbulent flow will be associated with a spatially nonuniform thermodynamic state and will

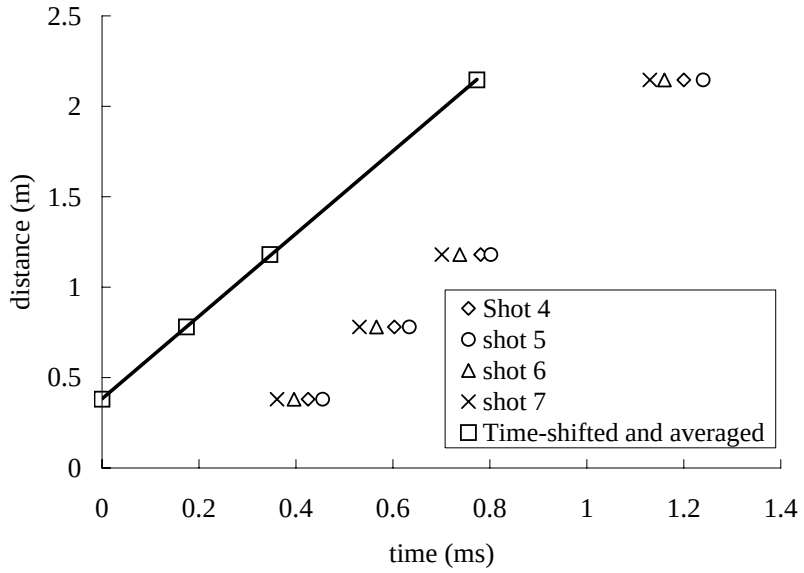

Figure 2.26: Arrival time of the incident wave (peak pressure time) vs. location of the pressure gauges. $X = 0$ is the ignition location. Prior to averaging, the time values were shifted by subtracting the arrival time at gauge 1 for each shot. The trend line is a linear least-squares fit to the average values of arrival time.

cause more rapid attenuation of the reflected shock waves than predicted by the idealized simulation.

4. There are heat transfer and gauge response effects on the measured peak pressures. Heat transfer becomes increasingly important at longer time scales.

5. The pressure transducer signals still show significant contamination due to acceleration sensitivity and vibration in the tube walls.

2.5 Solid Mechanics Simulations

The response of a thin-wall shell was simulated by F. Cirak using the methods described in Cirak et al. (2006) and Deiterding et al. (2007). In doing the simulations, it was necessary to take careful account of the azimuthal variation of tube wall properties and calibration of the detonation model to the data. Instead of actually computing the hydrodynamics of unsteady detonation, the detonation was treated as a traveling internal pressure load. The wave speed was given by the ideal detonation (CJ) model

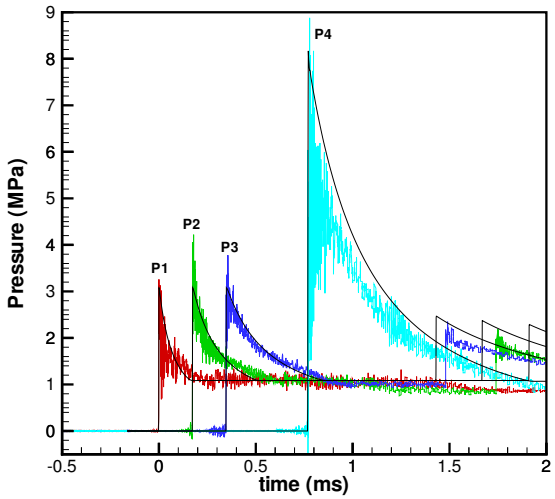

Figure 2.27: Comparison of simulations and shot 4 at four locations.

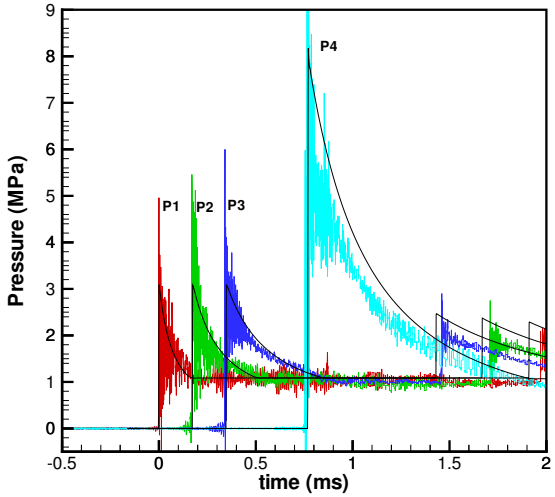

Figure 2.28: Comparison of computations and shot 7 at four locations.

and the spatial distribution of pressure behind the front was computing using an approximation to the analytical solution to the perfect gas Taylor-Zeldovich expansion wave. The approximate model of a traveling pressure load is described in the Appendix to Beltman and Shepherd (2002). The calibration of the decay time used the pressure transducer data from tests 30-34 at the location corresponding to the axial measurement station.

The effect of using a nonuniform wall thickness is shown in the results of Fig. 2.29 in which the strain history is given corresponding to locations S1, S2 and S3 in our experiments. The simulated radial displacements are compared with vibrometer measurements for two locations (V1 and V3) in Figs. 2.30 and 2.31 using the same detonation case.

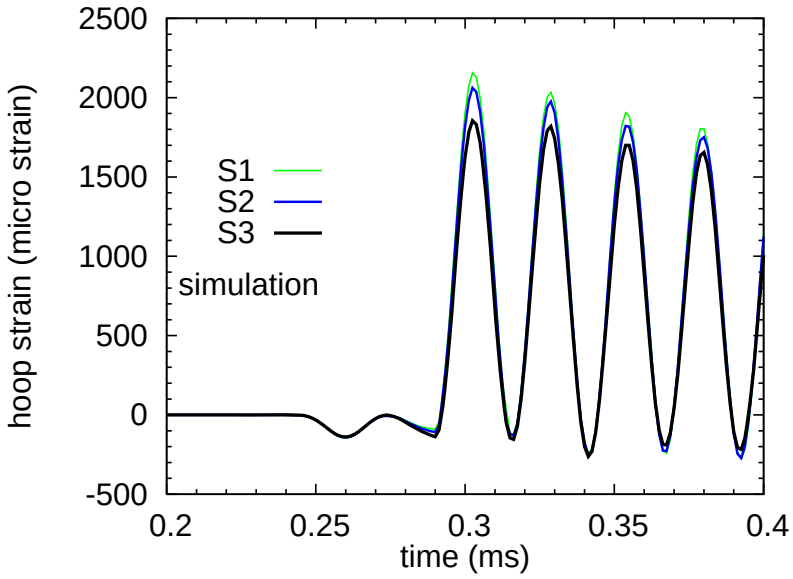

Figure 2.29: Computed strain response to stoichiometric ethylene-oxygen detonation (100 kPa initial pressure) in an aluminum tube with wall thickness variation shown in Fig. 2.13.

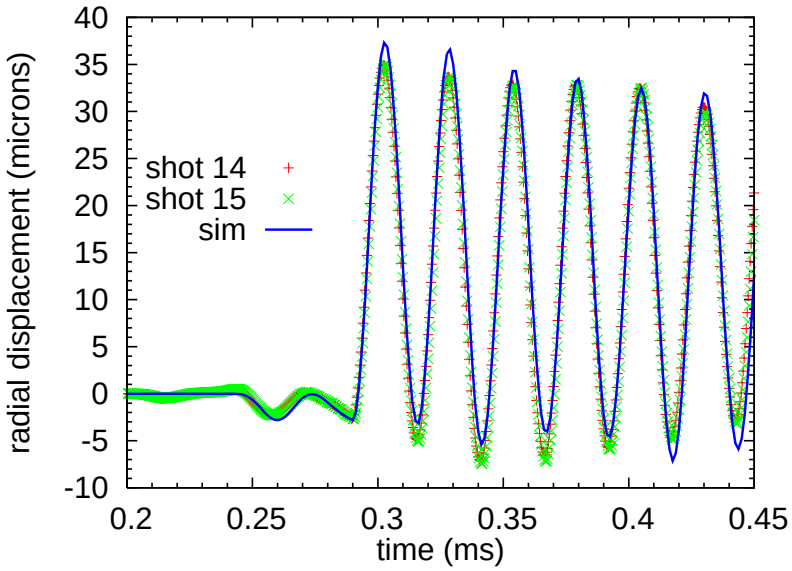

Figure 2.30: Comparison of measured and simulated displacement response at location V3 (225°). Stoichiometric ethylene-oxygen detonation (100 kPa initial pressure) in an aluminum tube with wall thickness variation shown in Fig. 2.13.

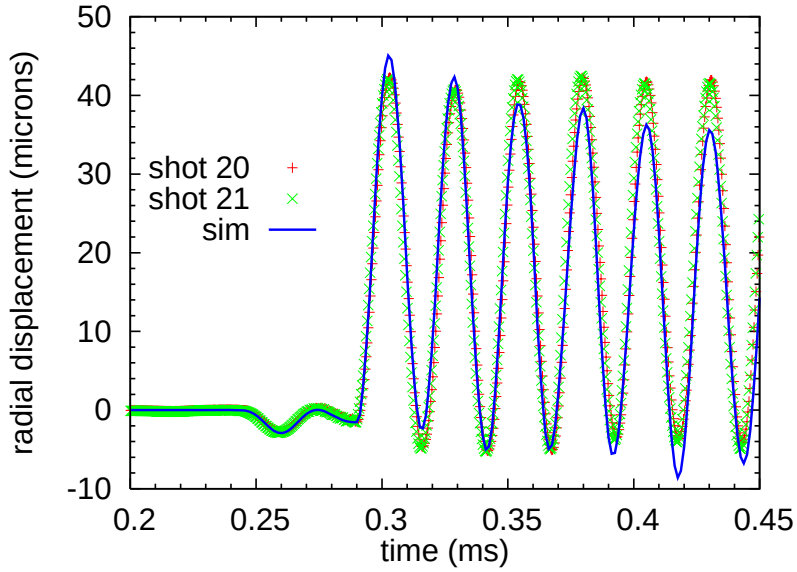

Figure 2.31: Comparison of measured and simulated displacement response at location V1 (15°). Stoichiometric ethylene-oxygen detonation (100 kPa initial pressure) in an aluminum tube with wall thickness variation shown in Fig. 2.13.

2.6 Summary

A series of tests involving detonation propagation and elastic tube response were carried out. Measured signals from bonded strain gauges were compared with those from a laser vibrometer, addressing the limitations of strain gauges under these conditions.

Preliminary experiments identified a number of issues with measurement of the pressure signal, so modifications were made to the apparatus which resulted in significant improvement of the fidelity of the measured pressure traces, as well as the comparison between computed and experimental results. Some systematic differences in simulations and measured quantities remain, particularly in the long-time reflected waves. Several simulation and experimental shortfalls are posited to explain the remaining differences.

The detonation loading process is repeatable. The vibrometer measurements of displacement were very repeatable and much more useful for comparison to simulation than the strain gauge signals. The vibrometer data had a $\pm$ 2% shot to shot variation in peak amplitude with systematic differences between gauge locations and no noticeable effect of prestress. The strain gauges had 7% shot-to-shot variation in peak amplitude and showed artifacts characteristic of micro-cracking in the gauge element.

Tube wall thickness variation is significant for making accurate comparisons with simulations. These variations are apparently due to eccentric mandrel locations used in manufacturing. The wall thickness variations was measured by destructive testing and the circumferential variation was found to be much more significant than the longitudinal variation. Tests at two different initial pressures demonstrated linear scaling of the strains with the applied load and a static loading test demonstrated a small amount of hysteresis in the strain gauge response.

Chapter 3

Plastic Response to Incident and Reflected Detonation

3.1 Introduction

After the experiments described in Chapter 2, several series of experiments were performed with the goal of investigating plastic deformation. These experiments were all conducted in steel tubes with a 127 mm inner-diameter. The first set of experiments was conducted in a 316L stainless steel with a 12.7 mm wall thickness. This 'thick tube' was used to investigate the elastic response to deflagration to detonation transition (DDT) and detonation reflection. We measured the DDT run-up distance and spatial pressure histories for a variety of mixtures in preparation for experiments in thinner-walled tubes.

Subsequent experiments took place in 'thin tubes' which had the same inner-diameter as the thick tube, but were constructed of flush-controlled welded, cold rolled C1010 mild steel, with a 1.65 mm wall thickness. This enabled the study of plastic response to DDT and detonation. The first series of experiments had a number of issues which resulted in difficulties in interpreting the data. In particular, the end conditions of these tubes were not clearly defined, and the occurrence of DDT and the presence of obstacles inside the tube made it difficult to model the internal pressure loading.

In order to address these issues, the experiment was redesigned. The same speci-

men tubes were used, but a specially designed collet attached to a large mass was used to impose a nearly-ideal fixed end condition. The collet imparted a high clamping force to the tube at the reflecting end wall, where the bulk of the plastic deformation takes place. A flange with an internal gland seal was designed to couple the thin tubes to the thick tube from the first set of experiments. The thin tube was inserted into this flange, and the detonation was started in the thick tube. Thus not only was the thin tube free of internal components, but the pressure of the detonation wave could be monitored in the thick tube as it approached the test specimen. The new geometry also allowed the use of a high speed camera to record the deformation of the tube in the vicinity of the reflecting end. This final set of experiments resulted in plastic deformation data of very high quality. After a brief discussion of the earlier experiments, the 'driven thin tube' experiment is described in detail in this chapter.

3.2 Experiments in the Thick Tube

The experiments in the thick tube are described in detail in Liang et al. (2006) and Pintgen and Shepherd (2006b). The tube in question was comprised of 316L stainless steel with a 12.7 mm wall thickness and an inner diameter of 127 mm. On each end of the 1.25 m tube, a 50.8 mm thick flange was welded, to which circular plates were bolted to close the tube. Mounts for 8 pressure transducer ports were welded to the tube as shown in Fig. 3.1. Figure 3.2 contains a dimensional drawing of the tube.

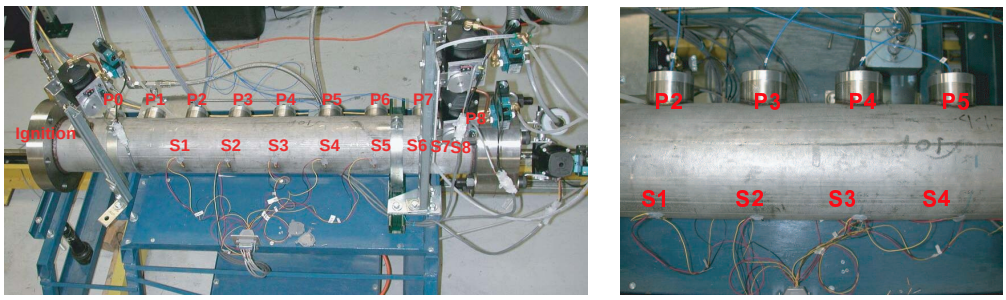

a) b)

Figure 3.1: Experimental setup in the thick tube. a) 9 Pressure transducer ports (P_0-P_8), and 8 strain gauges (S_1-S_8). b) Top view: Pressure transducers P_2-P_6 and strain gauges S_1-S_5 are mounted opposite each other (Pintgen and Shepherd, 2006b).

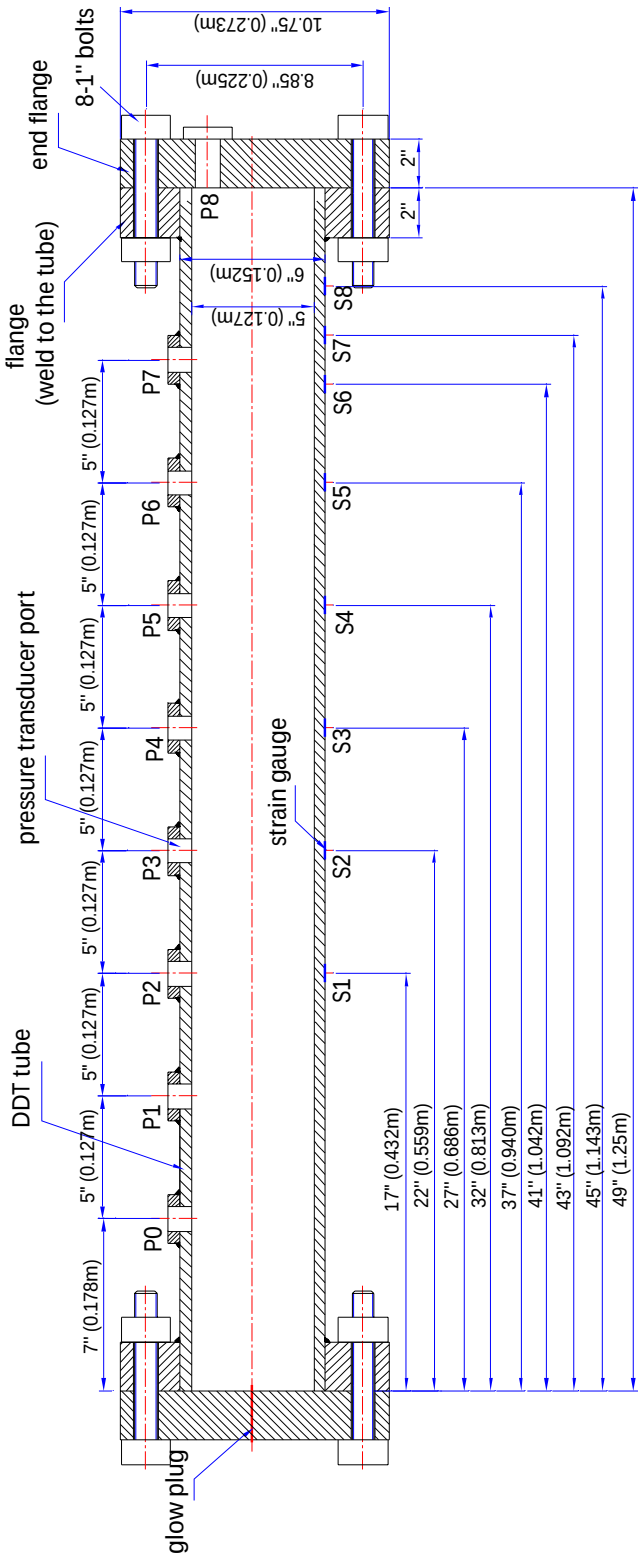

Figure 3.2: Detailed drawing of tube setup (Liang et al., 2006).

Flame accelerating obstacles were added to some of the tests to promote transition to detonation. The obstacles consisted of rectangular 'paddles' in a 90° alternating pattern with a 37% blockage ratio, as shown in Fig. 3.3.

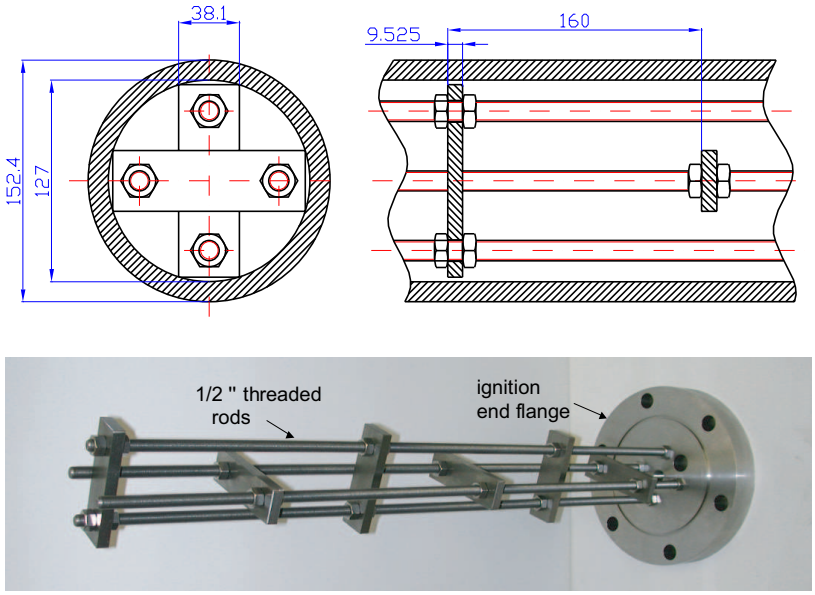

Figure 3.3: Obstacles. Top: Drawing of an obstacle pair mounted in the tube, units are given in mm. The blockage ratio is 0.37 and the obstacle spacing is 1.25 D. Bottom: Photograph of obstacle assembly outside the tube.

Ignition was accomplished by applying a voltage of 10 V at a current of 9.5 A to a Bosch 0-250-202-051 glow plug. The glow plug was mounted in the center of one of the tube end flanges, and ignition typically took place within 17 seconds of applying the voltage. Pyrometer temperature measurements of the glow plug surface as a function of time and applied voltage can be seen in Fig 3.4. In the combustion testing, a voltage of 10 V was applied, and ignition typically took place within 15 seconds, when the approximate temperature was 900°C.

Eight ports for pressure transducers were welded onto the cylindrical face of the tube spaced at 127 mm apart, and a single pressure transducer was mounted on the flange opposite the igniter. The port nearest the ignition flange was closed with a blank plug, and pressure transducers were mounted in plugs that fit snugly within the remaining ports. The diaphragm of each transducer was flush with the interior surface of the tube. The peak pressure was observed to vary over several orders of

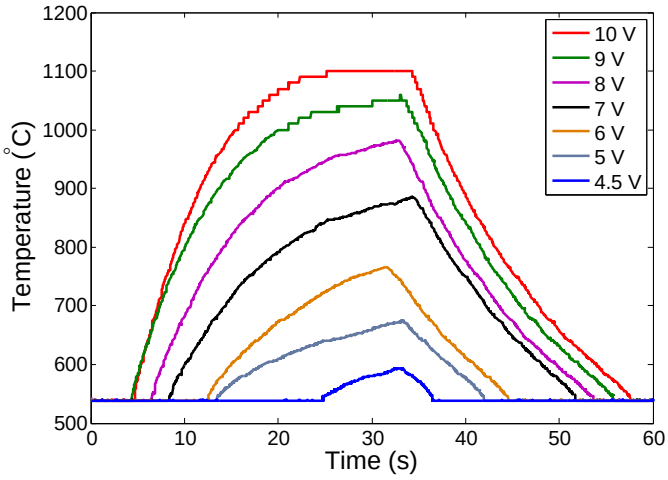

Figure 3.4: Pyrometer temperature measurements of glow plug surface temperature for various fixed voltages applied. The voltage was applied from time $t = 0$ for approximately 30 seconds.

magnitude, so piezoelectric pressure transducer (PCB) models 113A24 and 113A23 were used; these have a dynamic range of 69 bar and 1034 bar, respectively. The PCB gauges were connected to a PCB Model 482A22 Signal Conditioner.

The tests were conducted over a wide range of methane–oxygen mixtures, with the DDT locations varying from the ignition flange to the reflecting end wall, and some tests did not exhibit DDT. Some of the results are shown in Fig. 3.5. Here the dynamic load factor is defined as the ratio of the peak measured strain to the expected strain resulting from a static load. Perhaps the most interesting results obtained from these experiments involved the insulation of the tube with neoprene rubber to eliminate the effects of thermal stress. This showed that thermal stress could be responsible for as much as two thirds of the measured strain in the case of a subsonic deflagration, but that it is not important in the detonation case, where the relative size of the stresses due to thermal effects is much smaller than those due to the pressure loading. Additionally, the time-scale of the pressure loading is smaller than the thermal energy transfer time.

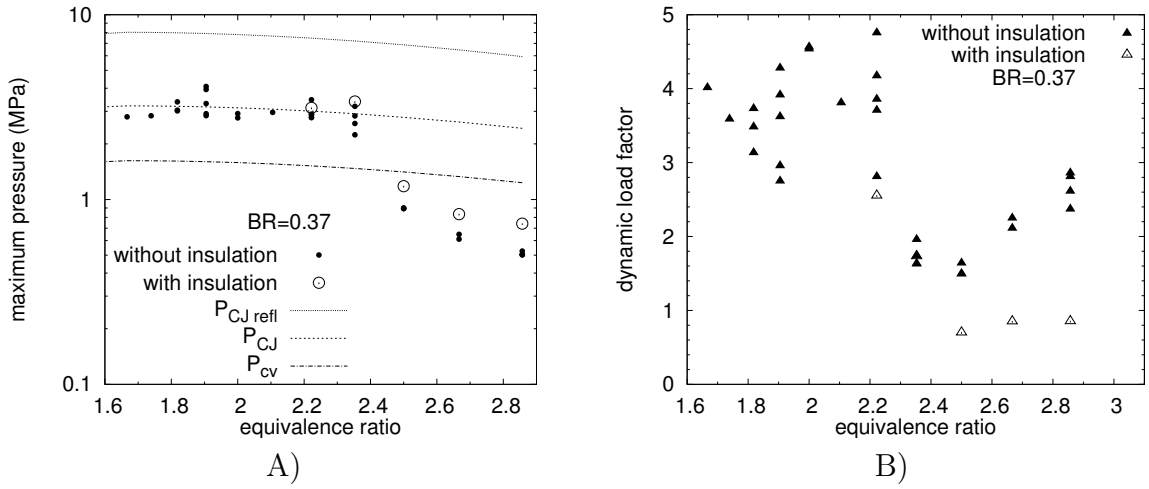

Figure 3.5: Results of thick tube testing with CH_4–O_2 mixtures at 1 bar initial pressure. A) Peak pressure of averaged pressure signals. Pressure signals were averaged with a 100 μs wide box-car average in order to eliminate the von Neumann spike present in several of the pressure traces. B) Dynamic load factor based on the peak pressure of the averaged pressure signals (Pintgen and Shepherd, 2006b).

3.3 First Experiments in the Thin Tube

The experimental setup in the closed off thin tube is described in detail in Pintgen and Shepherd (2006a). The specimens used in these experiments were made out of flush-controlled welded, cold-rolled steel tube constructed to ASTM specification A513, type 2, material type C1010 with a minimum yield stress of 220 MPa (32 ksi), and a tensile stress of 310 MPa (45 ksi). The tubes were cut to a length of 1.24 m, had an inner diameter of 127 mm and a specified nominal wall thickness of 1.65 mm. The wall thickness was measured at a number of locations both by micrometer and by ultrasound, and was found to be 1.50 mm (0.059 in) with a variation of less than .025 mm (.001 in) around the circumference of the tube at several axial locations. The tube specimen was mounted between a flange and an end plug using o-ring seals. Drawings of these and other components are given in Appendix D.

In order to confine possible blast waves in the event of a rupture or venting, the tube specimen was placed inside a 1.2 m^3 pressure vessel (Krok, 1997), Fig. 3.6b. The tank was evacuated to a pressure below 1 kPa. Quick clamps were used to attach the ignition flange assembly (Appendix D) to the tank and a pressure/vacuum seal was

formed by an o-ring face seal. The reflecting end flange of the tube was held on with four threaded rods which ran the entire length of the tube. The gas was mixed by using a bellows pump for circulation through a piece of half-inch tubing with holes drilled at various locations along the length. This tube was inserted in the thin tube, and ran 3/4 of the overall length. The installation of the tube is illustrated in Fig. 3.6 and described in detail in Pintgen and Shepherd (2006a).

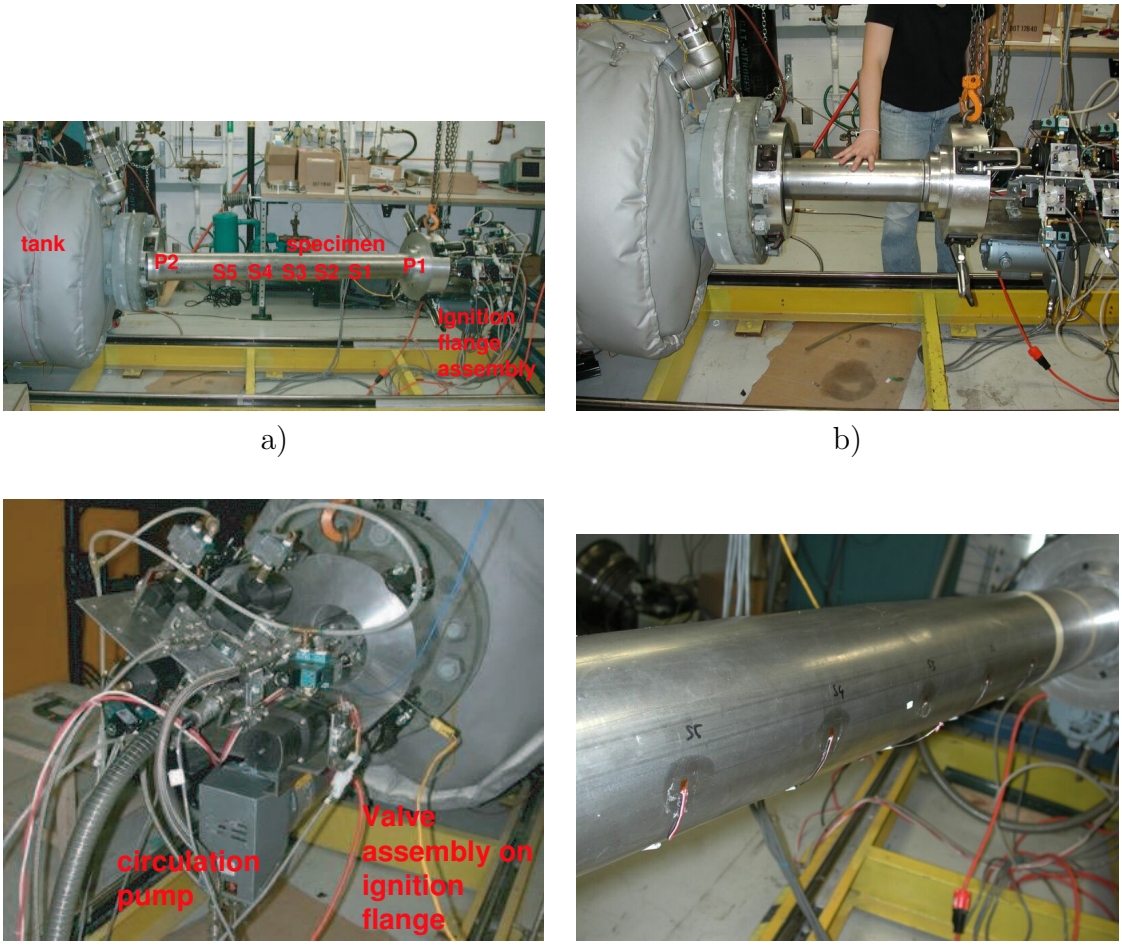

Figure 3.6: Experimental set-up. a) Tube specimen outside the tank. b) Tube assembly being inserted into tank. c) Valve assembly at the ignition flange. d) Strain gauges glued on tube.

With sufficiently high initial pressures, we were able to observe plastic response to DDT, as shown in Fig. 3.7, as well as a plastic flexural wave induced by a propagating detonation, as shown in Fig. 3.8. Attempts to analyze these experiments in detail

(Sauvelet et al., 2007) identified a number of shortcomings of this experimental design. In particular, the detonation loading (internal pressure as a function of distance and time) was poorly characterized and the tube boundary condition at the reflecting end was very difficult to model.

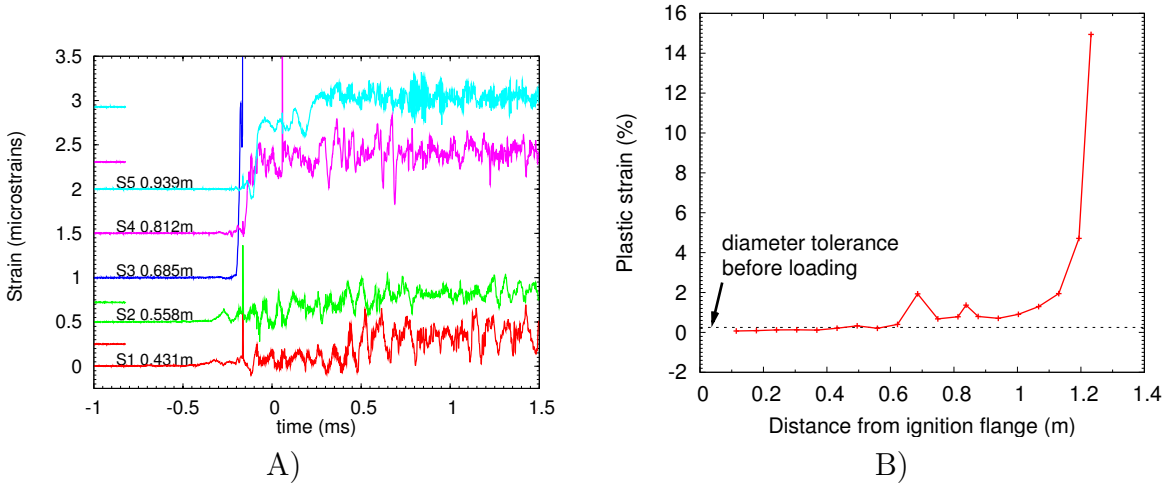

Figure 3.7: A) Strain traces and B) residual strain calculated from post-shot radial measurement for a thin-tube experiment using methane–oxygen mixture with equivalence ratio $\Phi = 2$ at an initial pressure of 3.5 bar. DDT occured very near the third strain-gauge, which broke during the experiment.

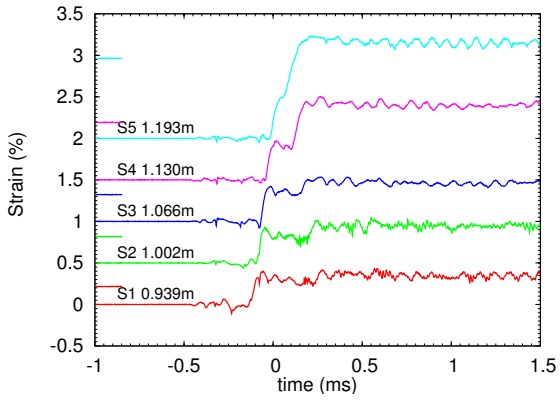

Figure 3.8: Strain traces using a stoichiometric methane–oxygen mixture at 3.5 bar initial pressure. The DDT run-up distance for this case is very short, and the resulting detonation is very near CJ.

3.4 Experiments in the Driven Thin Tube

The shortcomings of the thin tube experiment discussed in the preceding section were addressed with a complete redesign of the experiment. Several conditions were imposed on this redesign:

1. The same tube specimens should be used as in the previous experiment. While it is certainly an interesting question as to how materials with different dynamic stress–strain relationships will behave under the conditions of detonation loading, we had already characterized the material in these tubes, and had experience with how they would behave in the experiment.

2. Obstacles, threaded rods and recirculation lines should be eliminated from the interior of the test specimens. These structures cause complex wave interactions, and have the potential to result in a non-ideal loading of the tube wall.

3. DDT should not be allowed to occur in the specimen tubes. While the subject of tube response to DDT is of interest, the chaotic and non-axisymmetric nature of DDT introduces difficulties in both predicting the pressure history at the tube wall and in modeling the asymmetrically loaded tube. Instead, it was decided that we would focus on the plastic deformation resulting from detonation reflection.

4. The boundary constraints in the new experiment, at least at the reflecting end, should be constructed in such a way that they translate into clearly defined boundary conditions for a mathematical model and numerical simulations of the experiments.

To these ends, components were designed to couple the thick tube described in Section 3.2 with the thin tube specimens, with the thick tube acting as a driver, essentially creating a larger diameter version of the experiment described in Chapter 2. For the reflecting end of the tube, a plug and collet were designed to provide the large clamping force necessary to achieve a built-boundary condition at this end. This

closure was attached to the outside of the vessel which had been used to confine the thin tubes in the experiments descriped in Section 3.3, using its ≈2000 kg mass as an inertial restraint on the motion of the reflecting end. As a result of these changes, the thin tube was no longer inside of the pressure vessel, enabling the use of high speed video to observe the plastic deformation.

Experiments were performed with stoichiometric mixtures of ethylene-oxygen at initial pressures of 0.5, 0.8, 1, 2, and 3 bar. The 0.5 and 0.8 bar cases were found to result in elastic strains. With 1 bar initial pressure, the strain was just within the plastic regime, at a peak 0.228%. The 2 and 3 bar cases were well within the plastic regime. A total of 7 specimen tubes were tested, with repeated experiments at the initial pressures of 2 and 3 bar to investigate plastic strain ratcheting.

Further computational modeling was done using LS-DYNA (Liv, 2005). The tube was modeled using 2-D axisymmetric shell elements, and various constitutive relations were examined. These included relations accounting for strain and strain-rate hardening, but not thermal softening effects. This series of computations included loading by a realistic pressure model described in Chapter 4 as well as a square-wave loading loading discussed in Chapter 1, which was intended to investigate the wave propagation within the tube wall.

3.4.1 Experimental Setup

In order to achieve a well-defined boundary condition, a collet fixture was designed to clamp on the reflecting end of the specimen tube. The collet was cut by wire-EDM out of tool steel and hardened. At 101.6 mm in length, the collet was designed such that the end point of the collet when tightened down matched the end-point of a newly designed aluminum end-plug which went inside the tube. A tapered ring squeezed the collet and was bolted to a plate using 8 9/16-18 bolts with minimum preloads of 67.790 N–m, resulting in a clamping force of at least 66,723.3 N. Drawings for these and other parts are found in Appendix D, and photographs are shown in Fig. 3.9.

The thick tube described in Sec. 3.2 was used as a driver tube to start the det-

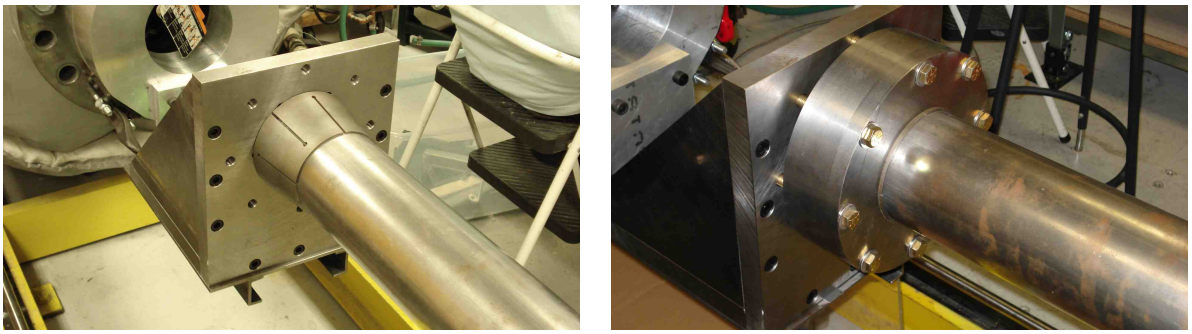

A) B)

Figure 3.9: A) The collet around the tube prior to installation of the outer ring. B) The final configurarion with the tapered retaining ring installed.

onation which propagated into the specimen tube. The pressure of the propagating detonation was monitored using PCB pressure transducers in the ports, as described in that chapter. The driver tube is shown in Fig. 3.10.

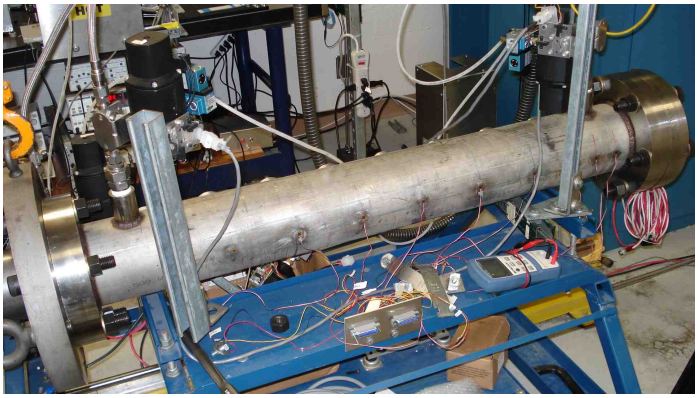

Figure 3.10: Driver tube. The strain gauges were left over from the experiments discussed in Chapter 3.2.

The specimen tubes were coupled with the driver tube through a new flange designed with two internal gland seals. This flange sealed onto the open end of the thick driver tube, and the thin tube was slipped into these gland seals. This arrangement allowed the thin tube to slide relative to the thick tube and prevented the coupling of vibration and motion between the two tubes. The two tubes were held together with chains to prevent the force of the detonation from pulling apart the assembly. The coupled tubes are shown in Fig. 3.11.

A total of seven specimen tubes were tested, using stoichiometric ethylene-oxygen

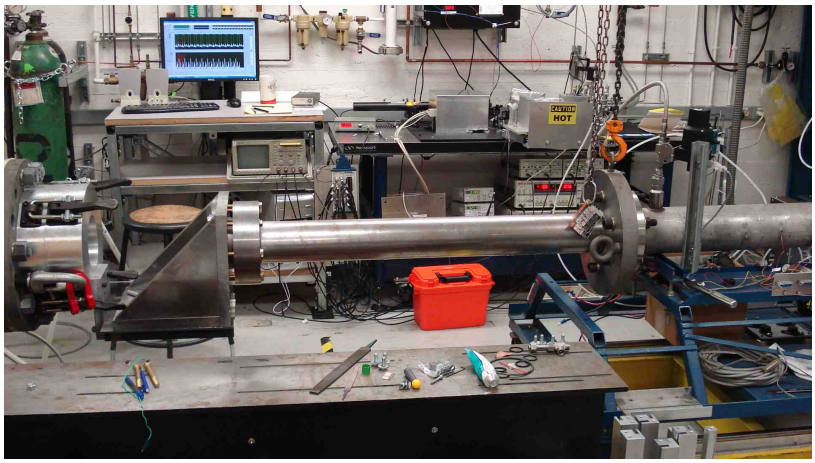

Figure 3.11: Coupled tubes. The chains ran from the I-bolt visible on the coupling flange to the (red) shackle visible at the downstream end.

at initial pressures ranging from 0.5–3.0 bar. The ignition was via glow plug, and the 'paddle' obstacle assembly (Sec. 3.2) was installed in the driver tube. There were no obstructions in the interior of the specimen tube. PCB pressure transducers were located in several ports on the driver tube and in the end plug to monitor the detonation pressure. The wall of the thin tube was instrumented with strain gauges, the number and layout of which varied from tube to tube, but in general about 20 gauges were used. Most of these gauges were placed in a periodic pattern clustered near the reflecting end. The remaining gauges had larger inter-gauge spacing and were mounted at more central locations along the tube. The gauges were always mounted diametrically opposite the tube weld. The plastic deformation at the end wall and the post-shot vibration were monitored using a Phantom model V7.3 or V7.10 high-speed video camera. Post shot diameter and thickness measurements were taken using an outside micrometer and a Checkline TI-007 ultrasonic wall-thickness gauge.

Table 3.1: Shot List for Driven Thin Tube Experiments

Tube	**Shot**	**P_0 (kPa)**	**Gauge Setup**	**Comment**
1	1	80	1	5 pressure gauges, both hoop and long strain
1	2	80	1	

Continued on next page

Table 3.1 – continued from previous page

Tube	Shot	P_0 (kPa)	Gauge Setup	Comment
1	3	80	1	
1	4	80	1	
1	5	80	1	
1	6	100	1	
1	7	200	1	Gauges 14–19 delaminated and were replaced after this test
1	8	80	1	
1	9	80	1	
1	10	200	1	Gauge 1 malfunctioned, gauge 14 broke, gauges 13, 15, 18, and 19 delaminated, causing replacement of gauges these gauges and gauge 12 after this test
1	11	200	1	Gauges 1 and 14 malfunctioned, 18 and 19 delaminated
2	1	50	2	4 pressure gauges, both hoop and long strain, old support
2	2	200	2	Gauge 1 malfunctioned, replaced after shot
2	3	50	2	
2	4	200	2	Gauge 1 malfunctioned, gauges 14–16 delaminated. Replaced after shot.
2	5	50	2	
2	6	200	2	Gauge 12 delaminated and was replaced after the shot
2	7	50	2	
2	8	200	2	No strain data, premature trigger
2	9	50	2	

Continued on next page

Table 3.1 – continued from previous page

Tube	Shot	P_0 (kPa)	Gauge Setup	Comment
2	10	50	2	
2	11	200	2	Gauge 1 malfunctioned
3	1	50	2	
3	2	300	2	Gauge 1 malfunctioned, Gauges 4 and 7 were the only survivors. Asymmetric deformation cause redesign of end support.
4	1	50	3	4 pressure gauges, both hoop and longitudinal strain measurement, new support
4	2	200	3	
4	3	50	3	
4	4	200	3	Gauges 12, 15, 17 delaminated
4	5	50	3	
4	6	200	3	
4	7	50	3	
4	8	200	3	Gauge 1 malfunctioned, 15 and 16 debonded, 17 broke, replaced after shot
4	9	50	3	
4	10	50	3	
4	11	200	3	Gauge 12 debonded
5	1	50	4	4 pressure gauges, only hoop strain, switched to high strain gauges
5	2	50	4	
5	3	300	4	Gauges 1 and 20 malfunctioned, Gauges 2, 6, 13–19 broke
6	1	50	4	

Continued on next page

Table 3.1 – continued from previous page

Tube	Shot	P_0 (kPa)	Gauge Setup	Comment
6	2	50	4	
6	3	300	4	Gauges 1, 2, 4, 6, 8, 13–19 broke
7	1	50	4	Cross-hatched roughening of the tube aided in gauge adhesion
7	2	300	4	Gauge 1 malfunctioned, Gauges 4, 15, 18 broke, all gauges replaced after shot
7	3	50	4	
7	4	300	4	Gauge 19 malfunctioned, Gauge 13 broke, all gauges replaced after shot
7	5	50	4	
7	6	50	4	
7	7	50	4	
7	8	300	4	Gauge 1 malfunctioned, Gauges 2 and 20 broke
8	1	50	5	13 pressure gauges, no strain
8	2	50	5	
8	3	50	5	
8	4	50	5	

The first three tubes that were tested vibrated excessively and deformed asymetrically. This was due to an asymmetry in the support at the reflecting end, as shown in Fig. 3.12. The brackets to which the collet ring and reflecting end plug were attached was originally designed to be mounted on an I-beam with the other end of the thin tube. When it was decided to use the thick tube as a driver, the assembly was adapted to mount on what had been the valve and circulation pump mount for the Section 3.3 experiments. This consisted of a plate bolted to the 2000 kg vessel in a downward-hanging cantilever, with another plate bolted to it in another cantilever. The support bracket was bolted onto this second plate. This setup allowed significant

Table 3.2: Gauge Locations in Config. 1

Pressure	P_1	P_2	P_3	P_4	P_5
mm from end	1700	1568	1441	1314	0
Hoop Strain	S_1	S_2	S_3	S_4	S_5
mm from end	991	864	737	610	483
Hoop Strain	S_6	S_7	S_8	S_{10}	S_{12}
mm from end	356	229	107	88	69
Hoop Strain	S_{14}	S_{16}	S_{18}		
mm from end	50	31	12		
Longitudinal Strain	S_9	S_{11}	S_{13}	S_{15}	S_{17}
mm from end	103	80	65	46	26
Longitudinal Strain	S_{19}				
mm from end	8				

Table 3.3: Gauge Locations in Config. 2 and 3

Pressure	P_1	P_2	P_3	P_4	
mm from end	1568	1441	1314	0	
Hoop Strain	S_1	S_2	S_3	S_4	S_5
mm from end	845	540	235	197	178
Hoop Strain	S_6	S_8	S_9	S_{11}	S_{12}
mm from end	159	140	121	102	83
Hoop Strain	S_{14}	S_{15}	S_{17}	S_{18}	
mm from end	64	44	25	6	
Longitudinal Strain	S_7	S_{10}	S_{13}	S_{16}	S_{19}
mm from end	178	140	102	64	25

Table 3.4: Gauge Locations in Config. 4

Pressure	P_1	P_2	P_3	P_4	
mm from end	1568	1441	1314	0	
Hoop Strain	S_1	S_2	S_3	S_4	S_5
mm from end	845	540	222	110	197
Hoop Strain	S_6	S_7	S_8	S_9	S_{10}
mm from end	184	171	159	146	133
Hoop Strain	S_{11}	S_{12}	S_{13}	S_{14}	S_{15}
mm from end	121	108	95	83	70
Hoop Strain	S_{16}	S_{17}	S_{18}	S_{19}	S_{20}
mm from end	57	44	32	19	6

vibration following the reflection of the detonation wave. From inspection of the high speed video, the boundary begins to move vertically 5 ms after the detonation reflects. Noticable large scale vibration of the reflecting end is observed starting at approx-

imately 25 ms. This time-scale is long compared to the decay time of the reflected shock and the rise time of the strains measured at the strain gauges, so the first plastic shot in each tube which used this geometry still resulted in valuable strain data, since the strain occurs in the first few milliseconds after reflection. Unfortunately the final plastic strain, as well any strain-ratcheting data, were corrupted by the vibration in the first three specimen tubes.

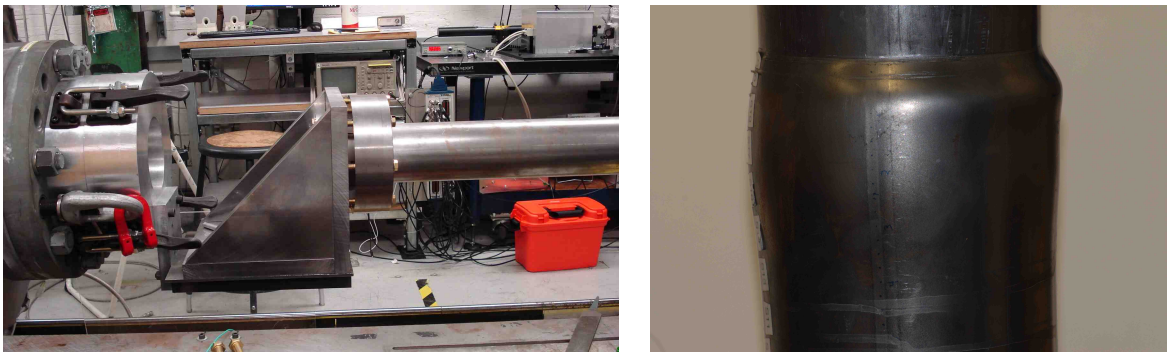

A) B)

Figure 3.12: A) Initial boundary condition of the tube. B) Resulting asymmetrical deformation in tube 3.

To eliminate this vibration, the reflecting end fixture mount was redesigned. A plate was mounted directly to the aluminum flange of the 2000 kg vessel. Two supports of 127 mm length connected this plate with the original plate which held the end plug and retaining ring. A central support was bolted to only the plate on the 2000 kg vessel, with a length allowing it to press on the aluminum plug and further stiffen this connection. The new setup is shown in Fig. 3.13, and was found to eliminate the vibration and asymmetric deformation. Drawings of these and other components are included in Appendix D.

3.4.2 Results

3.4.2.1 Tube 1

The first tube tested in the new experiment utilized 4 pressure transducers in the thick tube plus the one at the reflecting end, leaving 19 channels for strain gauges. This series utilized rosettes for the strain gauges near the reflecting end. Each of

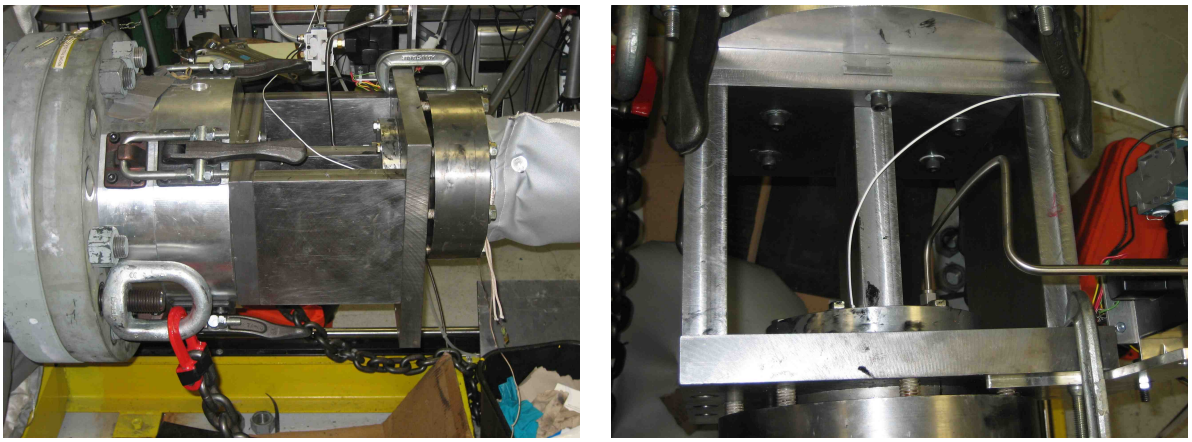

Figure 3.13: Redesigned reflecting end mount.

the six rosettes (Vishay C2A-06-125LT-350) had two strain gauge elements oriented at 90° angles to one another. The gauges were oriented such that the directions of measurement were the hoop and longitudinal direction, with an axial spacing between the elements of 0.125 in. The hoop element of the farthest downstream rosette was located 0.5 in from the reflecting end, with a spacing of 0.75 in between rosettes. In addition to the rosettes, there were seven single-element strain gauges (Vishay C2A-06-125LW-350), one of which was 3 in away from the first rosette, with the rest of the unidirectional gauges having a spacing of 5 in from one another (Fig. 3.14). All unidirectional gauges were oriented in the hoop direction.

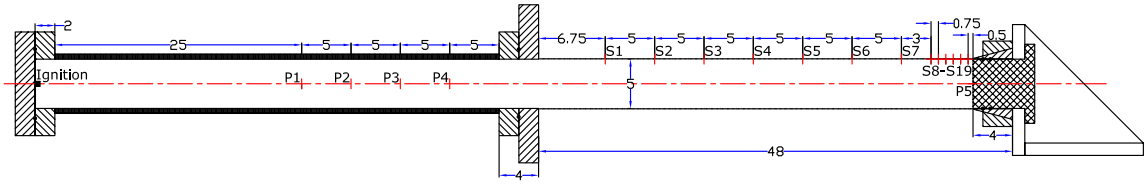

Figure 3.14: Gauge configuration for tube 1, dimensions in inches.

The tube was subject to a total of 11 detonations, with test conditions as summarized in Tab. 3.1. This set of experiments was primarily concerned with ensuring that the facility and all equipment were functioning properly, as well as establishing a baseline for expected deformations resulting from detonations with the new geometry. Close inspection of the data revealed that even in the initial 80 kPa test cases, peak strains were 0.15%, below the 0.2% that is typically associated with plastic de-

formation. The peak strains measured in the 100 kPa case were in slight excess of 0.2%. This meant that all shots had some effect of plastic deformation and strain hardening, however minute. Additionally, the shots at 200 kPa initial pressure were later found to have significant asymmetry introduced from the structural vibration of the support.

The data for the first 80 kPa test for which data was successfully recorded is shown in Fig. 3.15. The data for the 1 bar test are shown in Fig. 3.16, and the rest of the data, as well as the data for all shots in this series, are included in Appendix F.

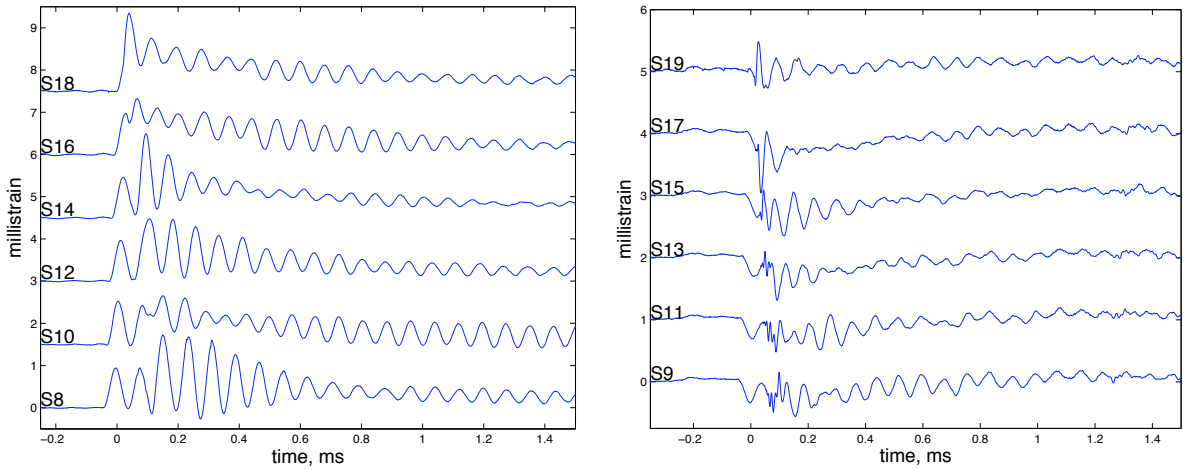

A) B)

Figure 3.15: A) Hoop and B) longitudinal strain data for tube 1 shot 5, $P_0 = 80$ kPa.

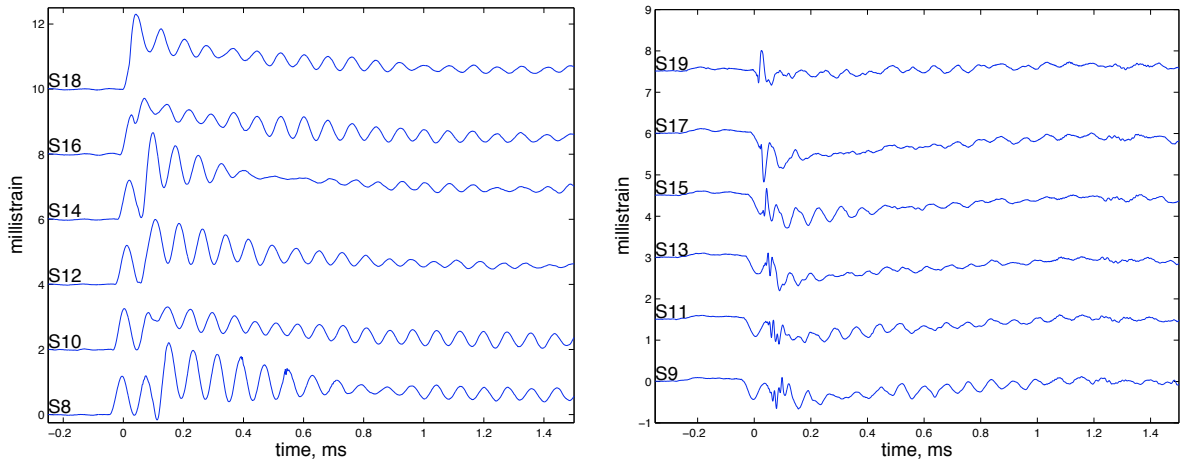

A) B)

Figure 3.16: A) Hoop and B) longitudinal strain data for tube 1 shot 1, $P_0 = 100$ kPa.

3.4.2.2 Tube 2

The goal of the second tube was to investigate the plastic strain resulting from detonations with an initial pressure of 2 bar. Before each 2 bar shot, a 50 kPa shot was performed to ensure that the gauges and data acquisition system were functioning properly. The shots performed in tube 2 are summarized in Tab. 3.1

The strain gauge configuration in tube 2 differed from that in the first specimen. More gauges were clustered closer together at the reflecting end in order to better resolve the large plastic deformation, which we learned from the first tube to be concentrated within 229 mm of the reflecting end. The rosettes were rotated 90° so that the longitudinal and hoop measurements occurred at the same axial location. The last gauge was 6.35 mm from the clamped end, and the alternating single element gauges and rosettes were spaced 19.05 mm apart. Only two gauges were located at more central locations in the tube. In order to accommodate 20 strain gauge circuits in the 24 channels of data acquisition that were available, only three pressure transducers were used to monitor the detonation in the driver tube. The layout of the measurement locations is diagrammed in Fig. 3.17. This was also the first time a high speed camera was used to monitor the plastic deformation in the tube.

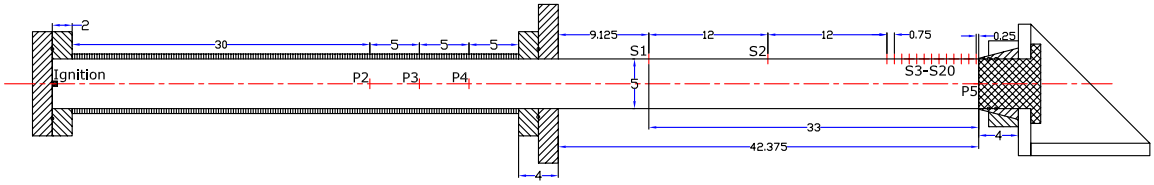

Figure 3.17: Gauge configuration for tube 2, dimensions in inches.

The strain data for the first 50 kPa shot is shown in Fig. 3.18, and that for the first 2 bar shot is shown in Fig. 3.19. The peak strain observed in the 50 kPa experiment was 0.09%, well below the 0.2% limit for yield strain. Subsequent shots in tube 3 were tainted by the asymmetry introduced by structural vibration.

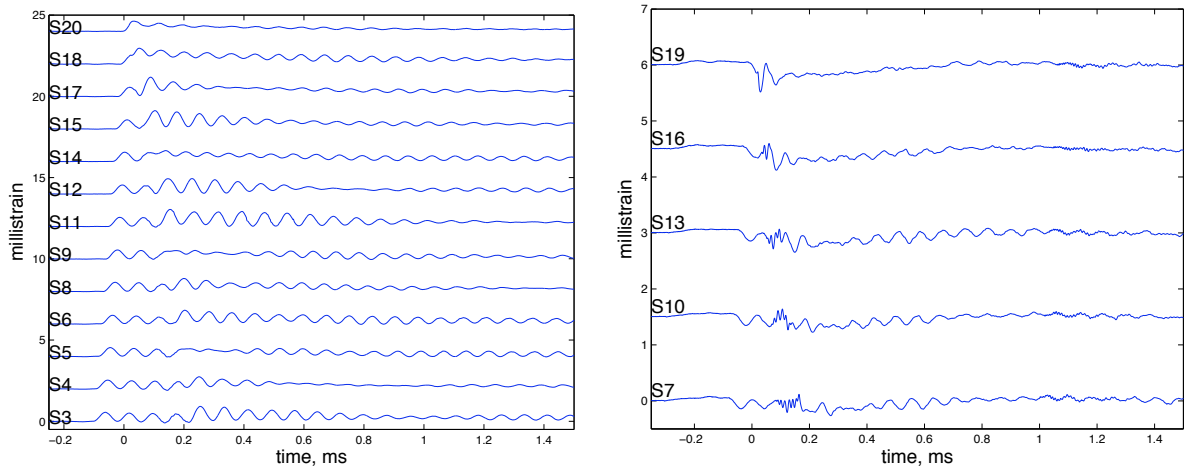

A) B)

Figure 3.18: A) Hoop and B) longitudinal strain data for tube 2 shot 1, $P_0 = 50$ kPa.

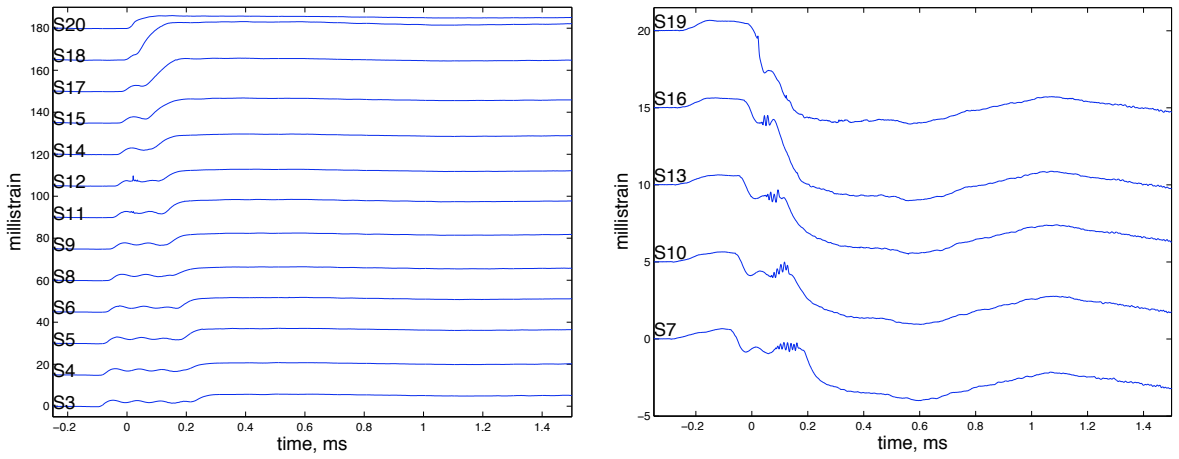

A) B)

Figure 3.19: A) Hoop and B) longitudinal strain data for tube 2 shot 2, $P_0 = 200$ kPa.

3.4.2.3 Tube 3

Tube 3 was the first time in the newly-designed facility that an initial pressure of 3 bar was used. After an initial shot at 50 kPa to ensure that all gauges were functioning properly, the 3 bar test was carried out. The asymmetry of deformation was immediately apparent after the shot, and it was from inspection of the high speed video at long times after reflection that the structural vibration was discovered. Because the vibration sets in 5 ms after the detonation reflects, the measured strain data from the gauges as well as the high speed video are still valid for the time scale

of interest. Unfortunately, the gauges and glue being used in this experiment were incapable of withstanding the strain levels achieved at the reflecting end, and all of the gauges either broke and/or delaminated both over the course of the experiment, as seen in Fig. 3.20.

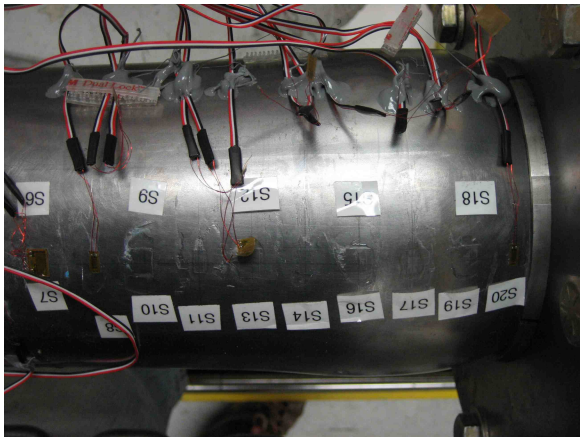

Figure 3.20: The tube after the three bar shot.

Fortunately, the high speed video allowed the measurement of displacement as a function of time and distance along the tube, albeit an imprecise one. The camera was focused on one side of the tube, with the last several inches prior to the reflecting end wall being visible. Just before the experiment, a still image was taken of a ruler located at the tube wall, to arrive at a length-scale calibration for the video. The tube was then back-lit by shining work lights onto a diffusive reflecting surface behind the tube. The resulting high speed video was edge-detected using Matlab to track the displacement of the outer surface of the wall, which provided a measurement for Δr, with the strain being Δr/r. The estimated strain for the location 25.4 mm from the reflecting end is plotted in Fig. 3.21.

3.4.2.4 Tube 4

After the structural vibration was brought to light during the testing of tube 3, the support at the reflecting end was redesigned with added stiffness. The testing sequence on tube 4 was a replica of the testing on tube 2 (see Tab. 3.1), and utilized the same layout of strain gauges (Fig. 3.22) but with the stiffer reflecting end fixture

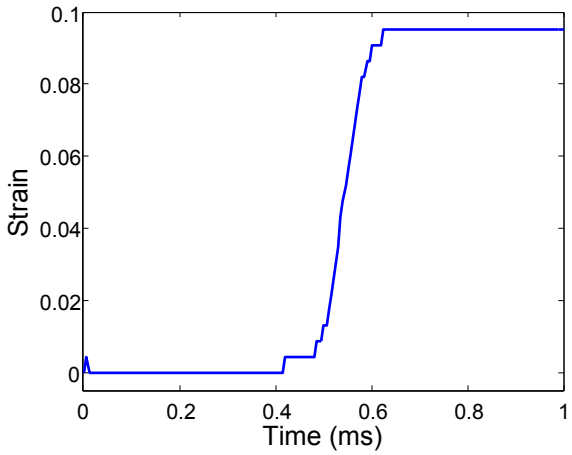

Figure 3.21: Strain history for the 3 bar initial pressure test in Tube 3, calculated from edge-detected video of the tube wall.

to eliminate the asymmetric vibration. This was the first series of tests in which strain ratcheting due strictly to the detonation could be investigated.

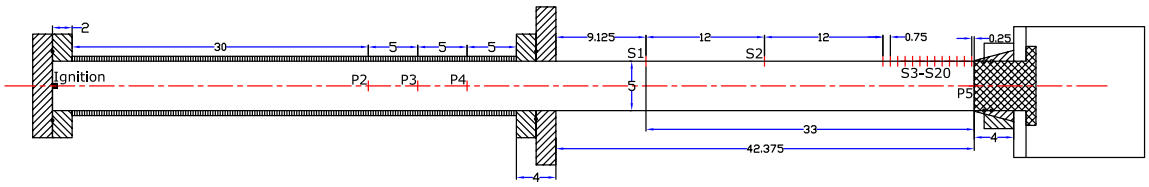

Figure 3.22: Gauge layout for tubes 3 and 4.

The strain gauge readings at 2 bar initial pressure were similar to those from the prior tests, even for the repeated shots with significant strain-hardening. This is because the amplitude of the asymmetric vibration at 2 bar was relatively small and the resulting plastic deformation was of smaller magnitude than that due to the reflected shock. Figure 3.23 compares the strain traces from the five tests at 2 bar initial pressure. The traces show a common trend, in which the measured strain for the first plastic shot has a much larger amplitude than the second one, due to a large amount of strain-hardening. Subsequent shots also resulted in lower strain increments than each previous shot.

One interesting feature of the deformation resulting from repeated shots was the formation of periodic ripples in the tube, shown in Fig. 3.24. The ripples had an average peak to peak spacing of 63 mm. The distance between successive peaks was

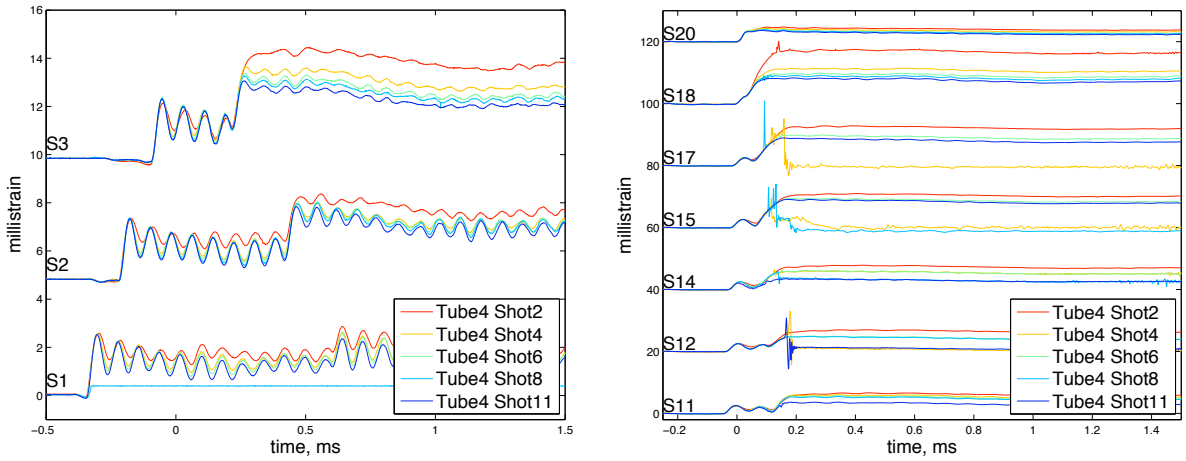

Figure 3.23: Hoop strains from repeated 2 bar shots in tube 4.

monotonically increasing away from the reflected end, with incremental gains of about 1.27 mm per cycle. These ripples were noticed in tubes 1–3, but it was uncertain until tube 4 that they were not an artifact due to the asymmetric vibration of the reflecting end fixture. Figure 3.25 shows measurements taken after each plastic shot of the outer diameter and the thickness of the tube in the vicinity of the reflecting end. The ripples are clearly visible in the last two tests of Fig. 3.25.

Since each longitudinal gauge was accompanied by a hoop gauge, we were able to examine the ratio between longitudinal and hoop strains. Typically for steels this ratio is expected to be around 0.3 during elastic deformation. During plastic deformation it increases to 0.5, which is the expected result for a perfectly incompressible fluid-like material. This is because when the deformation becomes plastic the ability of the material to support shear stresses is reduced, and the deformation is close to isochoric. Figure 3.26 shows the ratio $\epsilon_{long}/\epsilon_{hoop}$ averaged for times of 1 to 50 ms for each rosette and each plastic shot. The value for this ratio fluctuates from shot to shot and gauge to gauge, but there is a discernible trend. For all rosettes except that closest to the reflecting end, we observe that the strain ratio is noticeably higher for the first experiment than for subsequent experiments. This is due to the fact that we see much more plastic strain for this particular shot. For the strain gauge rosette nearest the reflecting end, the ratio is approximately constant for all experiments.

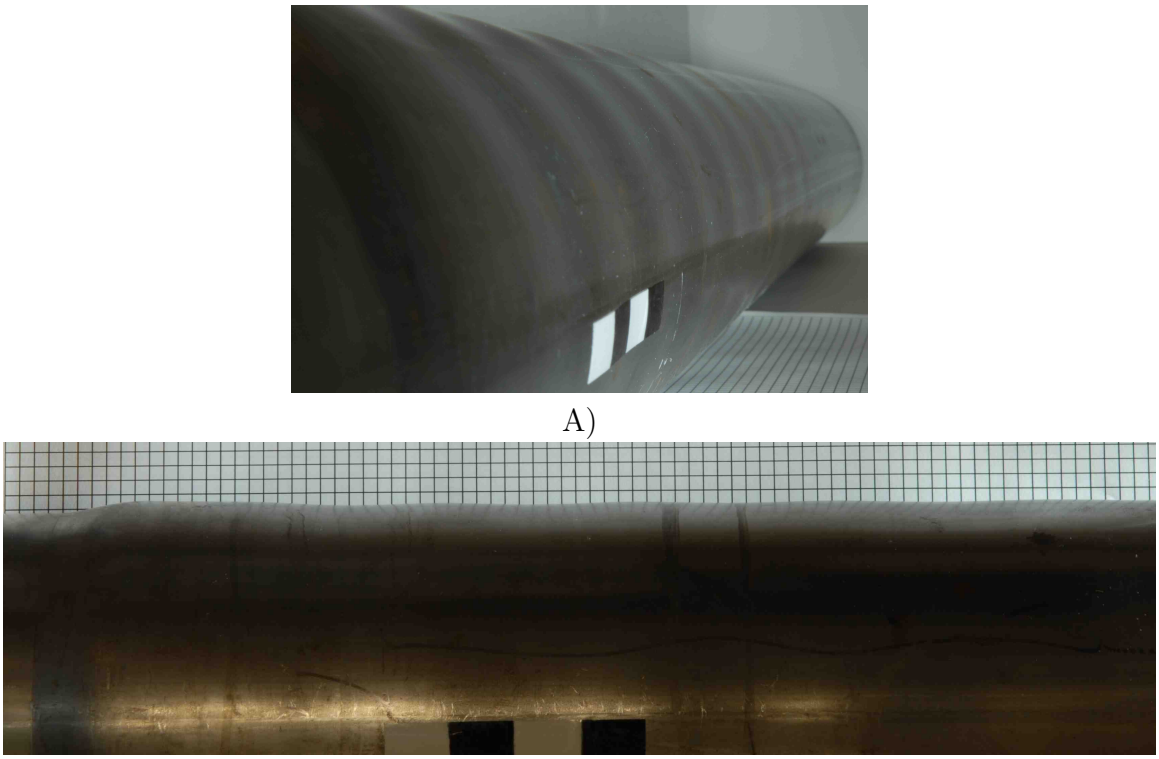

A)

B)

Figure 3.24: A) Rippling in tube 4. B) Side-view of the fully deformed tube. Grid spacing is 5 mm.

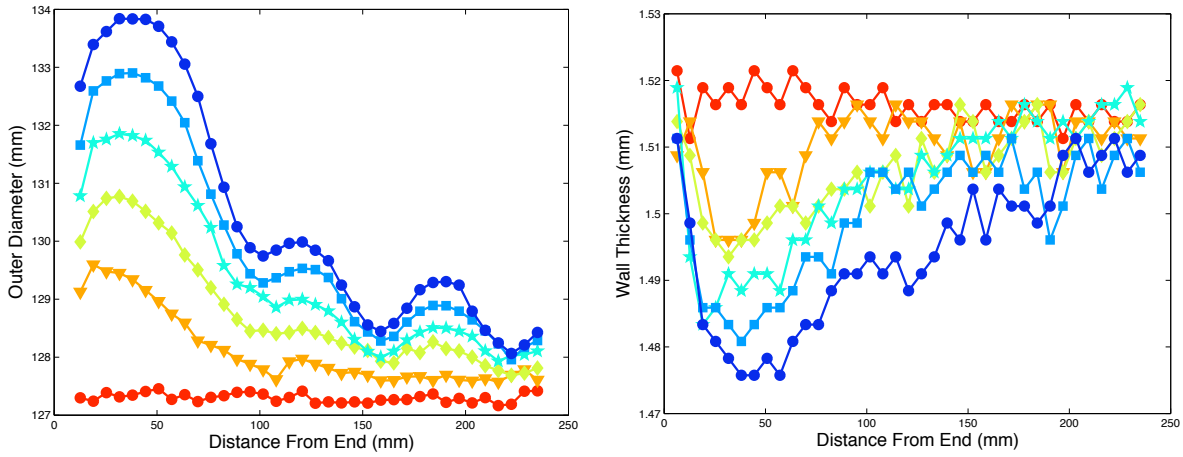

A) B)

Figure 3.25: A) Outer diameter and B) wall thickness measured along the tube after successive detonations at $P_0 = 2$ bar.

This is likely caused by the non-negligible effects from the boundary where there is a sharp change in tube diameter as seen in Fig. 3.25 and a noticeable change in wall

thickness.

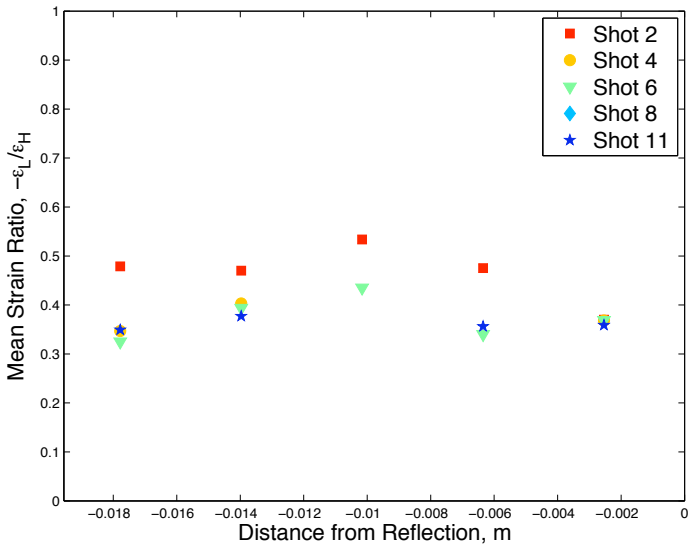

Figure 3.26: Ratio of longitudinal to hoop strain for each rosette for each plastic test in tube 4.

3.4.2.5 Tubes 5 and 6

For the series of repeated tests at 3 bar initial pressure, the change from the Vishay C2A-06-125LW-350 gauges to EP-08-125AC-350 gauges were made. Utilizing an epoxy instead of the typical cyanoacrylate adhesive, these gauges were specified to be able to measure up to 20% strain. The epoxy (M-Bond A-12) was mixed in a 2:3 ratio of resin to hardener and cured for 2 hours at 80°C, as shown in Fig. 3.27. Tubes 5 and 6 were each subjected to two 50 kPa elastic test shots and a single detonation at 3 bar initial pressure. In both of these cases, the majority of the strain gauges debonded during the deformation, due to insufficient roughening of the bonding surface. Because of this, strain ratcheting investigations of these tubes were not pursued, and instead were left to tube 7.

3.4.2.6 Tube 7

The gauge layout for tubes 5, 6, and 7 eschewed longitudinal strain measurement in favor of superior coverage of the axial span of the plastic deformation at the end

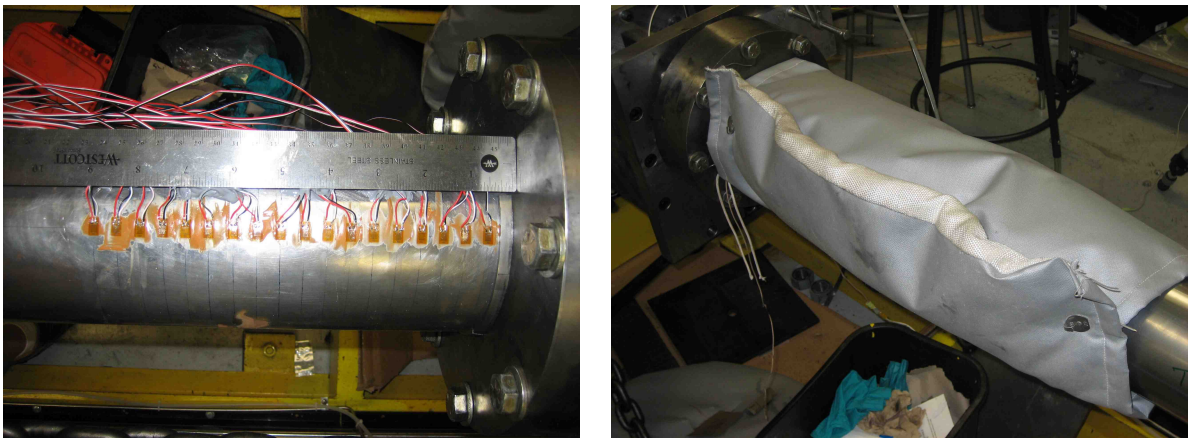

A) B)

Figure 3.27: A) The new gauges with epoxy. B) The bonding was cured for 2 hours at 80°C under fiberglass insulation with a temporary rope heater wrapped around the tube.

wall. The new gauge configuration is shown schematically in Fig. 3.28. A total of 8 experiments were performed in tube 7; three at 3 bar initial pressure and 5 at 50 kPa to test the apparatus.

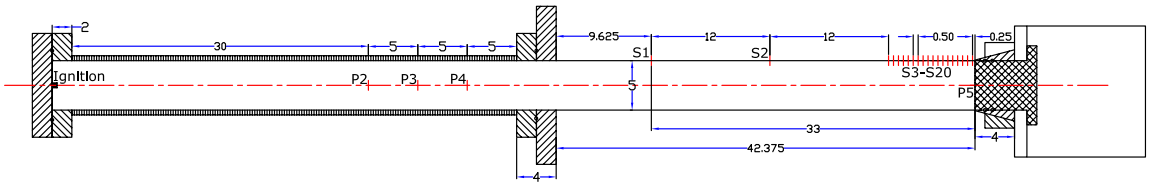

Figure 3.28: Gauge layout for tubes 5–7, dimensions in inches.

The three plastic tests showed the same sort of hardening behavior as the 2 bar series. After a large reduction in incremental strain due to hardening between the first two shots, the third shot showed a reduced effect of hardening. This is shown in Fig. 3.29.

The third plastic shot in the tube demonstrated a very interesting behavior in the vicinity of the reflecting boundary, as shown in Fig. 3.30. The first thing to notice is that the precursor is an order of magnitude larger than in the previous tests, peaking at 0.5% strain. After this the initial deformation of the tube due to the detonation and reflected shock wave follow the familiar pattern, occuring over 0.1 ms. Over the first millisecond period following reflection, the strain continues to rise at a slower

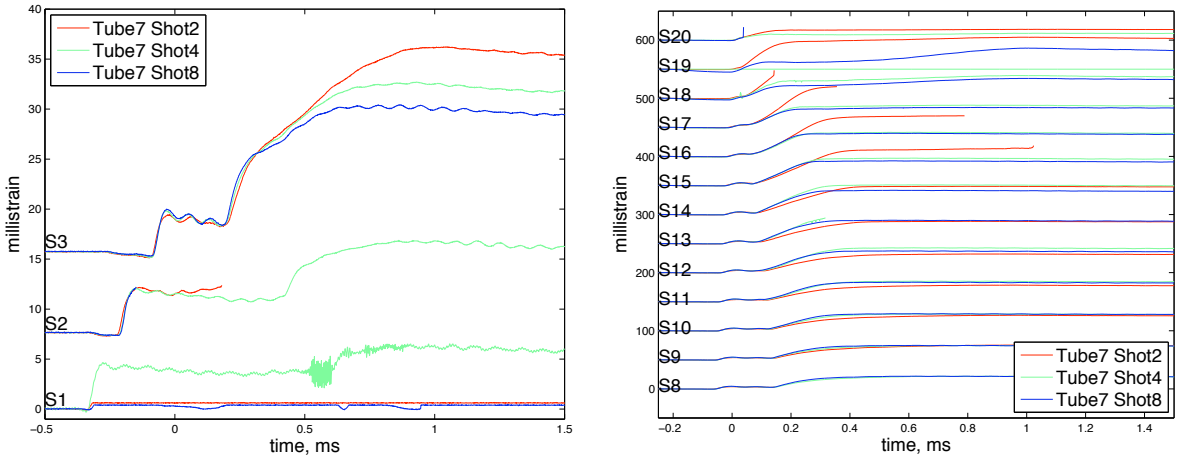

A) B)

Figure 3.29: Hoop strains from repeated 3 bar shots in tube 7.

rate, but to a peak strain of three times that caused by the loading of the reflected shock. The total load on the wall behind the reflected shock is still increasing during this time. A long-period vibration localized to the boundary then sets in.

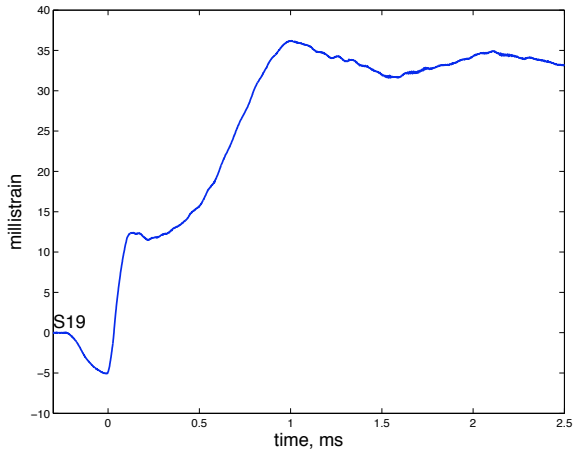

Figure 3.30: Hoop strain measured 19.05 mm from the end in tube 7 shot 8.

The long period vibration has a frequency of 1550 Hz, which corresponds with the natural frequency of the breathing mode of the entire tube, which was calculated from a SolidWorks model (Fig. 3.33) as 1520 Hz. This strain oscillation is observed on other gauges, but is strongest at the location 19.05 mm from the reflecting end. This is partially due to geometric effects, as the gauge in question is at a location where there was already a steep change in slope. Part of this behavior may also be explained

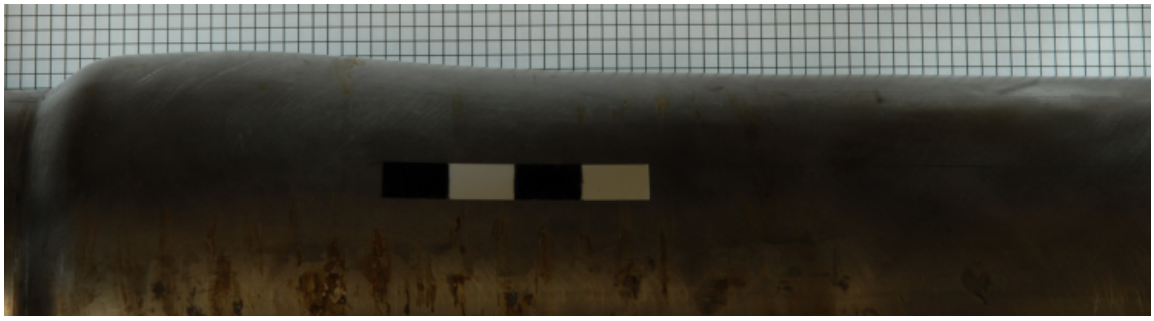

Figure 3.31: Fully deformed tube after 3 detonations at 3 bar initial pressure. Grid spacing is 5 mm.

by the thickness measurements of the tube in Fig. 3.32. The thickness measurement after shot 2 showed largely the same qualitative behavior as the measurements made in tube 4. The already imprecise measurement from the thickness gauge was made even more so by the high degree of curvature in the locations very near the reflecting boundary, but the general trend is clear, and is qualitatively similar to the data in Fig. 3.25B. The measurements taken after the second 3 bar test are very different, however. There is a 38.1 mm wide region of near-constant thickness which shows a sharp decrease in thickness from the surrounding material, unseen in previous tests. This indicates that necking occurred in the material during the test, accounting for the presence of the long rise time strain behavior, and suggests that the necked region may have acted as a plastic hinge responding to the breathing mode. This necking also explains why the change in peak outer diameter increased between the two tests; strain hardening would tend to decrease this change (as was observed for the 2 bar tests), but the plastic instability causes large strains.

Because the point of plastic instability was reached in this test, and the experimental facility was not set up to contain blast waves resulting from tube rupture, no further plastic experiments were performed in tube 7.

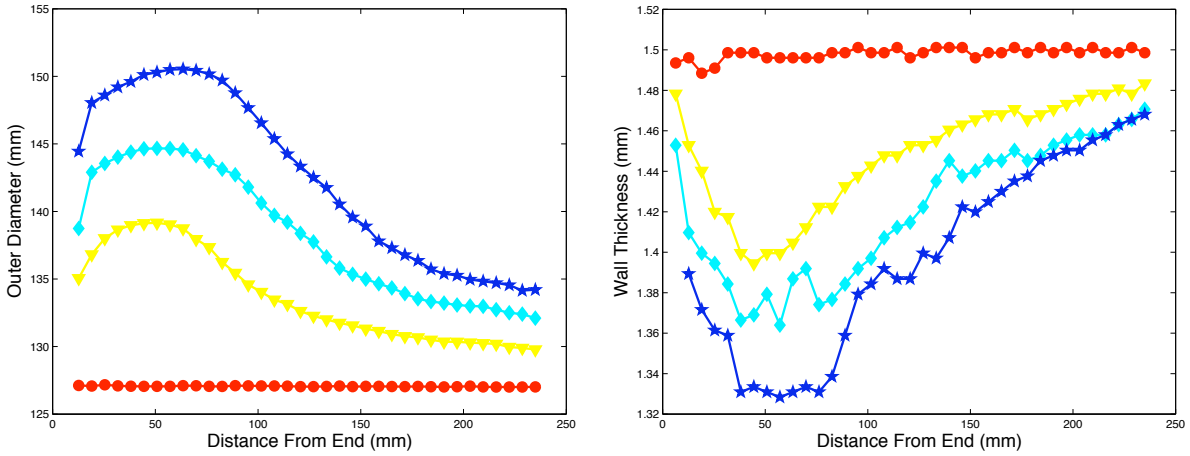

Figure 3.32: A) Outer diameter and B) wall thickness measured along the tube after successive detonations at $P_0 = 3$ bar.

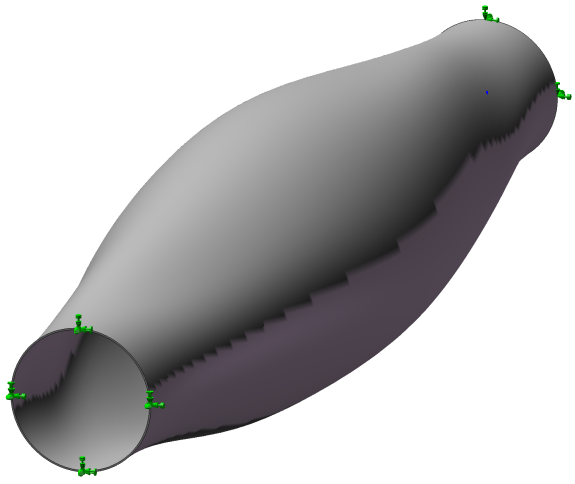

Figure 3.33: Breathing mode of the tube, as computed by SolidWorks. The frequency associated with this mode is 1520 Hz.

Chapter 4

Modeling Plastic Response

4.1 Introduction

A series of computations was performed using various material and structural models to compute the material response of the tube in the experiments of Chapter 3. These computations provided both quantitative and qualitative insights into the mechanical behavior and the constitutive modeling requirements needed for prediction of plastic deformations driven by detonation.

For simplicity we decided to perform completely decoupled simulations rather than coupled fluid-structure simulations as described by Deiterding et al. (2006a). The pressure history on the tube wall was precomputed based on a one-dimensional model of ideal gasdynamics and used as a boundary condition for the structural mechanics computations. Desiring a simple scheme which would allow the rapid calculation of the pressure history for a variety of detonations, we developed a semi-empirical model for detonation reflection and tested it against data from a modified version of the apparatus described in Chapter 3.

This idealized pressure history was then used as the input for models of the structural response of the tube. A single-degree of freedom (SDoF) model predicted the rippled pattern in the plastic deformation which was noticed in the experiment, providing clear evidence that the ripples are the result of the interference of the structural oscillations due to the reflected shock wave with the elastic oscillations set in motion by the incident detonation. The SDoF results also predicted the qualitative trends

with repeated loading and the importance of strain hardening and strain-rate effects.

In order to use more realistic constitutive models and compute the deformation of the tube in the vicinity of the reflecting end, a two-dimensional axisymmetric finite element simulation of the tube wall was carried out in LS-DYNA (Liv, 2005). This model was subjected to repeated loading corresponding to the 2 bar and 3 bar experimental tests. Strain-rate hardening was found to play an important role in the process, as was nonlinear strain hardening. Although good agreement was obtained for residual plastic deformation, some shortcomings were identified.

4.2 Pressure Model

The model of the pressure time history is based on a solution for the shock wave propagating from the reflecting surface back into the classical Taylor–Zel'dovich profile for the incoming detonation.

The analytical solution for the Taylor–Zel'dovich expansion wave was presented in Chapter 1. The results needed for our model are the sound-speed, flow velocity, and pressure everywhere in the tube prior to the arrival of the reflected wave, which were:

$$c(x,t) = \begin{cases} c_1 & \text{if } U_{CJ} < x/t < \infty \\ c_3 \left[1 - \frac{\gamma-1}{\gamma+1}\left(1 - \frac{x}{c_3 t}\right)\right] & \text{if } c_3 < x/t < U_{CJ} \\ c_3 & \text{if } 0 < x/t < c_3 \end{cases} \tag{4.1}$$

for the sound speed,

$$u(x,t) = \begin{cases} 0 & \text{if } U_{CJ} < x/t < \infty \\ \frac{2c_3}{\gamma+1}\left(\frac{x}{c_3 t} - 1\right) & \text{if } c_3 < x/t < U_{CJ} \\ 0 & \text{if } 0 < x/t < c_3 \end{cases} \tag{4.2}$$

for the flow velocity, and

$$P(x,t) = \begin{cases} P_1 & \text{if } U_{CJ} < x/t < \infty \\ P_3 \left[1 - \frac{\gamma-1}{\gamma+1}\left(1 - \frac{x}{c_3 t}\right)\right]^{\frac{2\gamma}{\gamma-1}} & \text{if } c_3 < x/t < U_{CJ} \\ P_3 & \text{if } 0 < x/t < c_3 \end{cases} \tag{4.3}$$

for the pressure. Here γ is the specific heat ratio of the detonation products at equilibrium and the subscripts 1 and 3 represent the pre-detonation and post-expansion properties, respectively, and the post expansion sound-speed and pressure are

$$c_3 = \frac{\gamma+1}{2} c_{CJ} - \frac{\gamma-1}{2} U_{CJ} \tag{4.4}$$

$$P_3 = P_{CJ}\left(\frac{c_3}{c_{CJ}}\right)^{\frac{2\gamma}{\gamma-1}} . \tag{4.5}$$

In order to utilize these relations in the model, the Chapman–Jouguet velocity, pressure and sound-speed (indicated by the subscript CJ) must be found from chemical equilibrium computations, such in Reynolds (1986) or Browne et al. (2008). The peak reflected pressure must also be known, and may either be found through the constant γ model of Stanyukovich (1960), as discussed in Chapter 1, or by the use of detailed calculations using realistic thermo-chemistry, as in Browne et al. (2008) or Shepherd et al. (1991).

The pressure at the reflecting end wall is observed (Fig. 4.1) to decay from the peak pressure to the post expansion pressure P_3 as the shock wave propagates away. To predict the form of this decay requires numerical solution of the Euler equations, which we wish to avoid in creating a simple method to calculate the pressure profiles. Thus it is here that empiricism enters in, and we base the pressure model on two simple ideas:

1. Pressure between the end wall and the reflected shock wave is spatially uniform but time dependent.

2. A simple expression for the reflected shock pressure, $P_R(t)$ is available.

Given these two assumptions, we can find the velocity of the reflected shock wave using the shock jump conditions. The justification of assumption 1 is that the velocity in the region between the shock and the wall must be small to match the boundary condition at the wall. Euler simulations by Shepherd et al. (1991) and Ziegler (2010) have shown that this is a reasonable assumption up to the time when the shock wave reaches the tail of the Taylor–Zel'dovich expansion (see also the discussion and Fig. 4.6 below). From these assumptions, the reflected shock velocity is

$$U_R(t) = c(x,t)\sqrt{\frac{\gamma+1}{2\gamma}\left[\frac{P_R(t)}{P(x,t)} - 1\right] + 1} - u(x,t) \ , \tag{4.6}$$

where $u(x,t)$ and $P(x,t)$ are the velocity and pressure just upstream of the reflected shock, as determined by the Taylor wave solution given previously. The trajectory $X_R(t)$ of the reflected shock can be determined by integrating the equation

$$\frac{dX_R}{dt} = -U_R(t) \qquad \text{where} \qquad X_R(t = t_0) = L \ . \tag{4.7}$$

where $t_o = L/U_{CJ}$ is the time of wave reflection.

We use the computed reflection ($P_{CJ,ref}$) and the post expansion (P_3) pressures, and fit an exponential of the form

$$P_R(t) = (P_{CJ,refl} - P_3)\exp\left[-\frac{t-t_0}{\tau}\right] + P_3 \tag{4.8}$$

to the end-wall pressure trace, where t_0 is the time of detonation reflection. The sole parameter of the fit is τ, the decay constant of the end-wall pressure trace. Combining this solution for the reflected wave with the analytical solution for the Taylor wave, the pressure $P(x,t)$ within the tube following detonation reflection is now completely specified. The spatial distributions for selected times are shown in Fig. 4.2 and the time histories at selected locations are shown in Fig. 4.3.

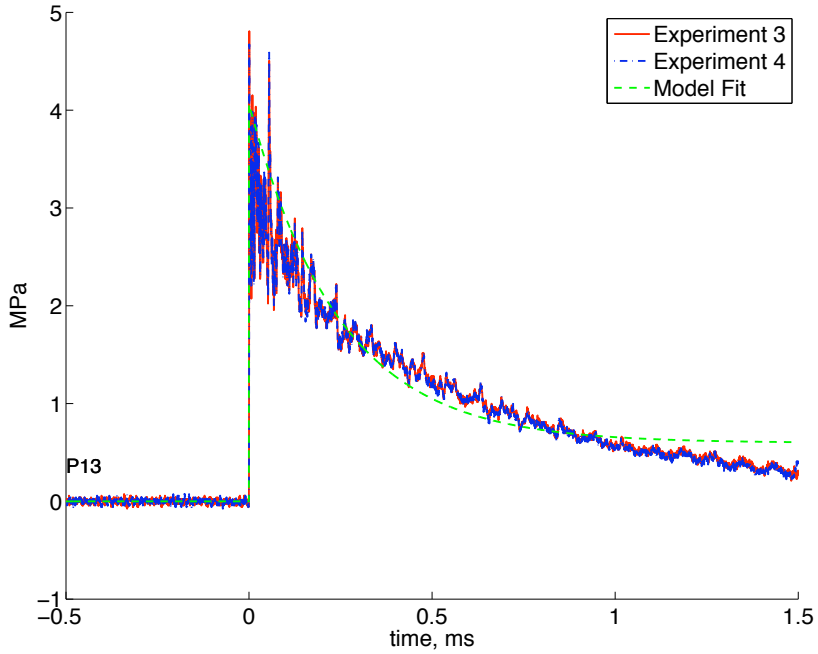

Figure 4.1: Experimental data ($P_0 = 0.5$ bar, tests described in Section 4.2.2) and fit to Eq. 4.8 using the computed values of P_{CJref} and P_3. Two experimental traces shown to demonstrate repeatability.

4.2.1 Summary of Algorithm to Implement the Approximate Model

We now summarize the scheme for the approximate solution of $P(x,t)$. The inputs are the Chapman–Jouguet pressure, velocity, and sound speed, the effective value of specific heat ratio in the products, reflected shock pressure, and the pressure-time history at the end wall.

For each spatial location x, carry out the following steps. The detonation wave is assumed to start at $x = 0$ and $t = 0$.

1. Compute arrival time of detonation wave t_d at location x

$$t_d = \frac{x}{U_{CJ}} \tag{4.9}$$

   where U_{CJ} is the detonation velocity.

2. Compute arrival time of reflected wave t_r at location x. As shown in Eq. 4.7,

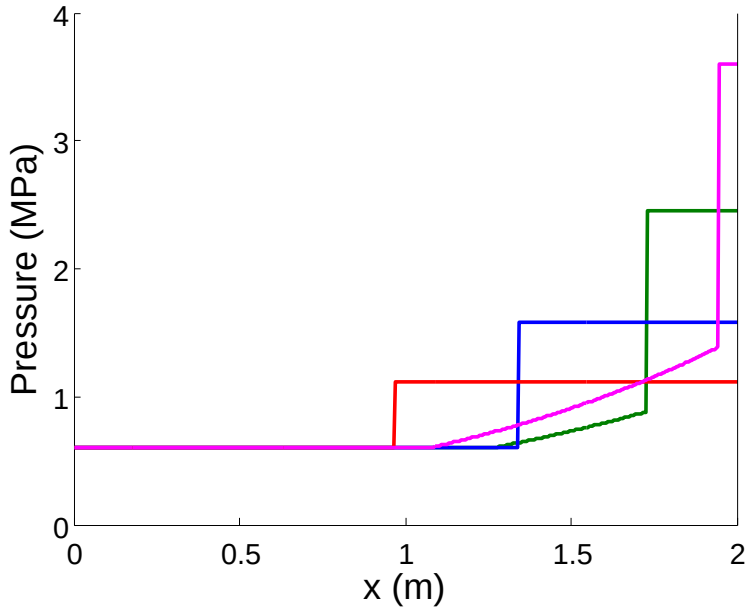

Figure 4.2: Spatial distribution of pressure in the tube according to the idealized model for several times after the reflection and an initial pressure $P_1 = 0.5$ bar. The reflected shock is moving from right to left with a uniform pressure region between the shock and end wall. The pressure gradient upstream (to the left) of the shock is due to the remains of the Taylor wave following the incident detonation.

the trajectory of the reflected wave $X_R(t)$ is

$$\frac{dX_R}{dt} = -U_R(t) \qquad \text{where} \qquad X_R(t = t_0) = L \ , \tag{4.10}$$

therefore

$$x = X_R(t_r) \qquad \text{or} \qquad t_r(x) = X_R^{-1}(x) \tag{4.11}$$

where $t_R(x)$ is the time coordinate when the reflected wave is located at $x = X_R$. The function $X_R(t)$ is found from integrating Eq. 4.7.

3. For $t < t_d$, P is simply the constant initial (pre-detonation) pressure P_1.

4. For $t_d < t < t_r$, P is the pressure-time trace of the Taylor wave from Eq. 4.3.

5. For $t > t_r$, P is the pressure of the reflected wave $P_R(t)$ from Eq. 4.8.

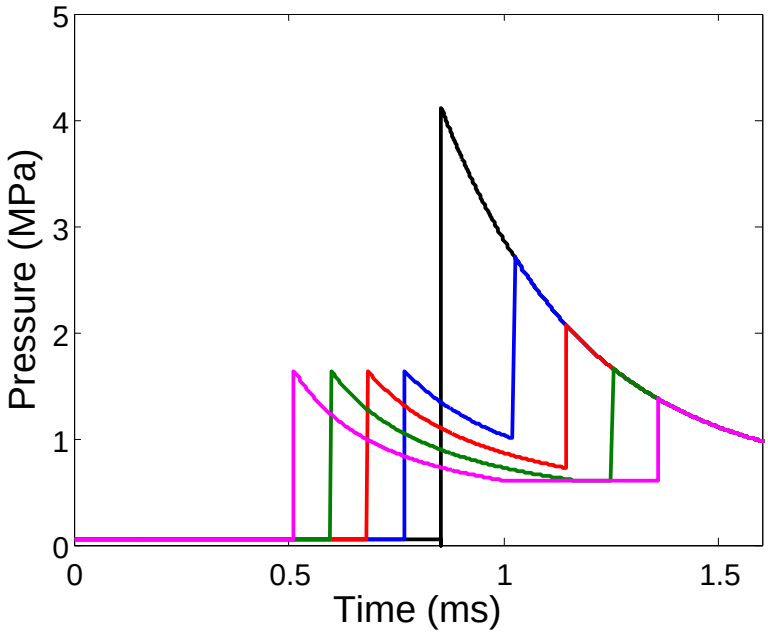

Figure 4.3: Pressure-time traces according to the ideal model for 5 evenly spaced locations and an initial pressure $P_1 = 0.5$ bar.

4.2.2 Testing the Model

Two sets of tests were conducted in order to validate this model against the observed behavior of the reflected shock. The first set utilized only the driver tube from the experimental apparatus described in Chapter 3. The flange with the gland seal was removed and the tube was closed off, as shown in Fig. 4.5. Seven pressure transducers were installed in the ports spaced 127 mm apart in the wall of the tube and one was installed in the reflecting end wall. A space-time diagram with data from two of these tests (Fig. 4.4) compares the computed and observed arrival times for an ethylene–oxygen detonation and the corresponding reflected shock. It is clear that the assumptions used in the model break down after the reflected shock wave reaches the tail of the expansion wave at 0.8 ms. Agreement between the model and experimental arrival data is good for three data points within the tail (0.8 m $< x <$ 1.25 m) but for subsequent times (t $>$ 0.8 ms), the model under-predicts the wave speed. The experimental arrival time data give an approximately constant reflected shock speed of 1640 m/s or $M_s = 1.4$ (based on the sound speed in the plateau region for t $>$ 0.8 ms).

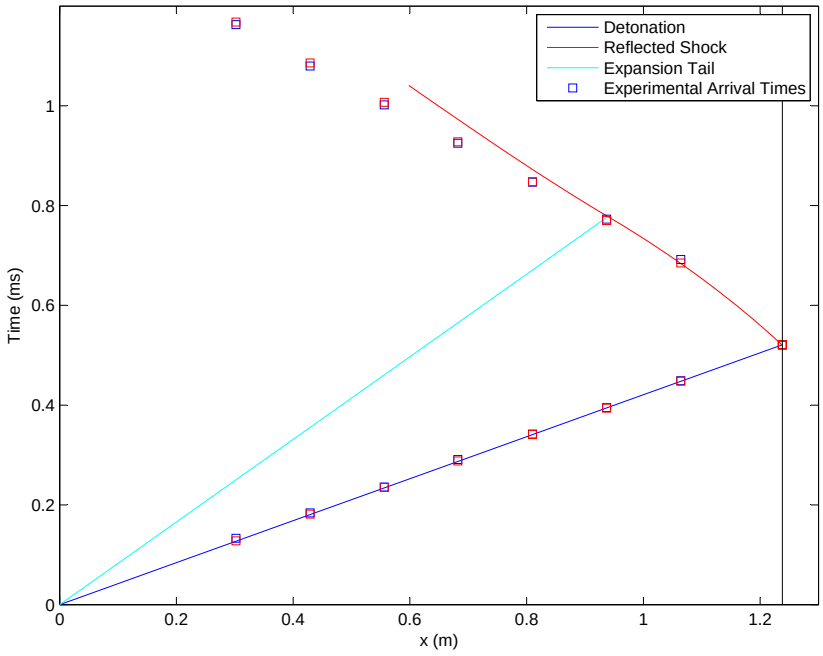

Figure 4.4: Space-time (x-t) diagram for ideal detonation and reflected shock for stoichiometric ethylene-oxygen an an initial pressure $P_1 = 1.0$ bar. Driver tube only as shown in Fig. 4.5.

Our model predicts a wave speed of 1210 m/s, which is the sound speed in the burned gas within the plateau region.

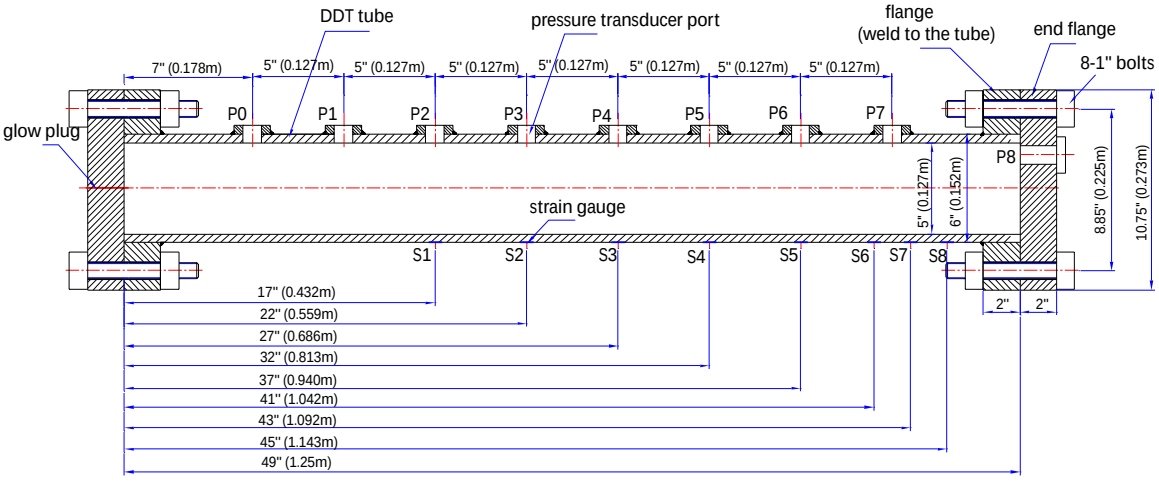

Figure 4.5: Closed off driver tube used to test the pressure model

The source of this problem is the assumption of zero gradient behind the reflected

shock. Numerical simulations that account for the correct fluid dynamics (Shepherd et al., 1991, Ziegler, 2010) show that a pressure gradient will develop behind the reflected shock front once the end of the TZ wave is reached. An example of one of these simulations is shown in Fig. 4.6. These calculations were done with the reacting Euler equations and one-step chemistry and a second order accurate min-mod slope-limited MUSCL scheme. The conditions were a detonation with nodimensional heat release of 50, γ of 1.2,overdrive 1.01, and a reduced activation energy of 3.71. The initial condition included the TZ expansion, and the domain is 10,000 half reaction zone widths with a base grid of 4000 cells and 3 levels of refinement with factors of 2, 4, and 4 (Ziegler, 2010). There is a minimal gradient immediately after reflection, when the pressure is highest. As the reflected shock propagates back up the tube and out of the TZ expansion, there is an inflection in this gradient, and it develops into a triangular pulse shape at later times. By this time, however, the post-shock pressure has decayed to below the CJ pressure of the incident detonation.

Clearly, at late times, the assumption that the pressure is uniform behind the reflected shock is completely incorrect. This is a simple consequence of fluid dynamics since a pressure gradient must be created once the shock is propagating with finite amplitude into a uniform region that is at rest. The velocity behind the shock must be nonzero and a pressure gradient must be created to bring the fluid back to rest (zero velocity) at the fixed end on the right-hand-side. From a purely mathematical point of view, Eq. (4.6) predicts that when the pressure $P_R = P_3$, the reflected shock speed must be equal to the sound speed and the amplitude of the shock should be zero. Therefore, it is clear that the observed discrepancy is a simple consequence of how we have formulated the model. In order to improve the model, we need to predict the shock front pressure once the reflected shock front reaches the tail of the expansion. An empirical solution is to take the reflected shock Mach number to be a fixed value once it has decayed to the minimum value of about 1.4 that is observed in the experiments. However, this does not give a correct representation of the spatial pressure profile.

Although this is a simple correction, we have not pursued this since by the time

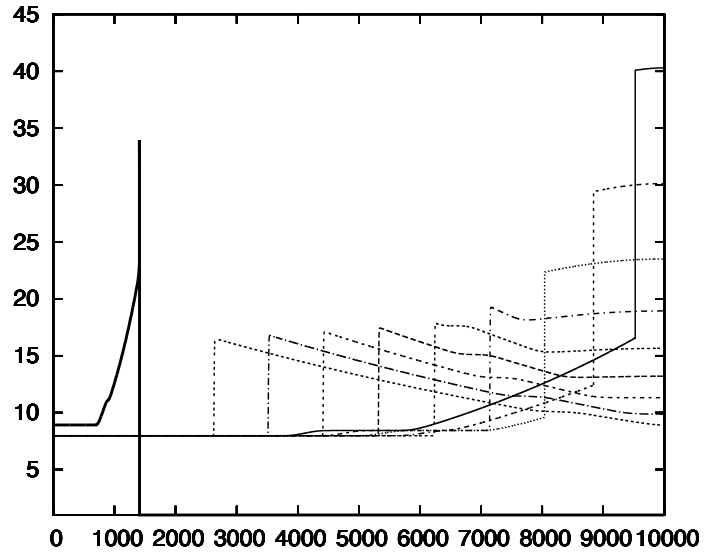

Figure 4.6: Spatial pressure (P/P_0) profiles from reacting Euler simulations of incident ZND detonation with TZ expansion wave. An early pre-reflection detonation is included for scale. X-scale is in half reaction zone widths.

the model fails, the reflected shock amplitude has decayed to less than 20% of the peak value obtained at the instant of reflection. In the present study, we are only interested in computing the deformation close to the reflecting end and we do not make a significant error for predicting the wave speed and arrival time for the locations located in the region between $x/L = 0.7$ and 1.0 (the reflecting end of the tube). If better predictions are needed for the rest of the tube, then a computational solution of the dynamics of the detonation wave and reflected shock motion like the one in Fig. 4.6 will be required. An early such study was described by Shepherd et al. (1991), and more sophisticated simulations followed, such as those described in Deiterding (2003).

The second set of tests was aimed at improving the spatial resolution of experimental pressure measurement in the vicinity of the reflecting end wall, where the bulk of the plastic deformation takes place. The driven tube setup of Chapter 3 was used with 8 pressure transducers installed in the last 125 mm of the tube, as shown in Figs. 4.2.2 and 4.8. Due to the difficulties of installing PCB transducers in a tube with a wall thickness of 1.5 mm, holes were drilled into the tube corresponding to the locations of the gauges, which were mounted to a block of aluminum and

Table 4.1: Pressure transducer locations.

Gauge	P_1	P_2	P_3	P_4	P_5	P_6	P_7
Distance from reflection, m	1.686	1.559	1.432	1.305	0.133	0.121	0.108
	P_8	P_9	P_{10}	P_{11}	P_{12}	P_{13}	
	0.095	0.070	0.057	0.044	0.032	0	

strapped onto the tube with hose clamps, as shown in Fig. 4.8. Table 4.1 contains the locations of the pressure transducers during this set of experiments. In all, six experiments were performed in this setup, all with stoichiometric ethylene–oxygen at 0.5 bar initial pressure to avoid plastically deforming the thin tube. Shot-to-shot repeatability of the detonations and shock waves was excellent, as shown in Fig. 4.10.

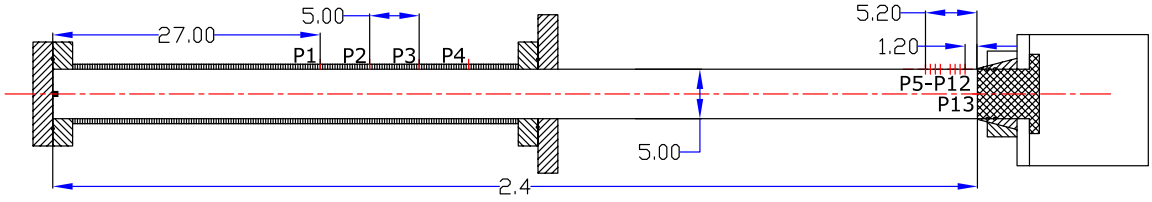

Figure 4.7: Setup for testing the model with the driven tube, and a concentration of pressure gauges at the reflecting end. Dimensions in inches.

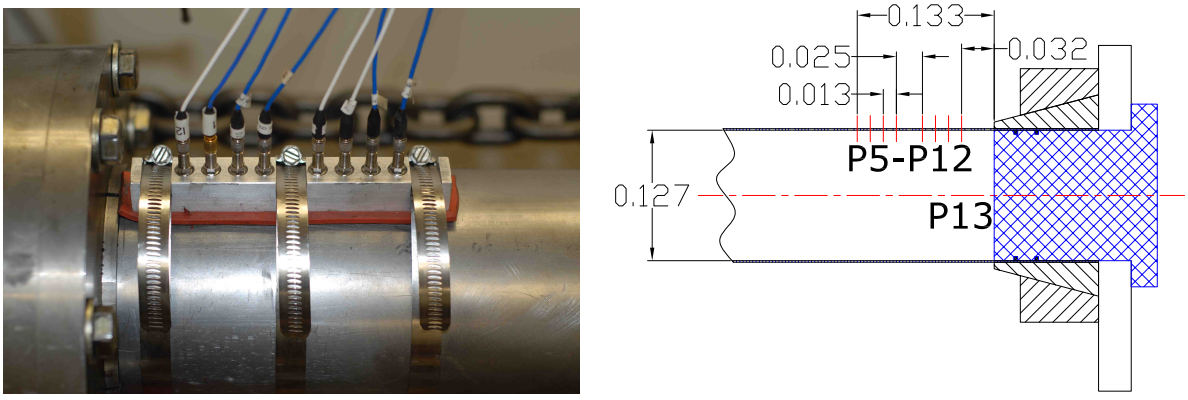

Figure 4.8: Pressure transducers near the end wall. Dimensions in inches.

Figures 4.9 and 4.10 contain the results from the second set of experiments. The experimental traces display a behavior which the model is incapable of capturing: the

pressure rise associated with the arrival of the reflected shock wave is more gradual than would be expected in a plane normal shock. We speculate that this is due to the interaction of the shock wave with the boundary layer following the detonation, resulting in shock-bifurcation as discussed in Mark (1958). This hypothesis is examined in Appendix B.

We hypothesize this effect to be of negligible importance to the solid mechanics, as the rise time of the pressure is still an order of magnitude less than the 73 μs response time (period of hoop oscillation) of the tube wall.

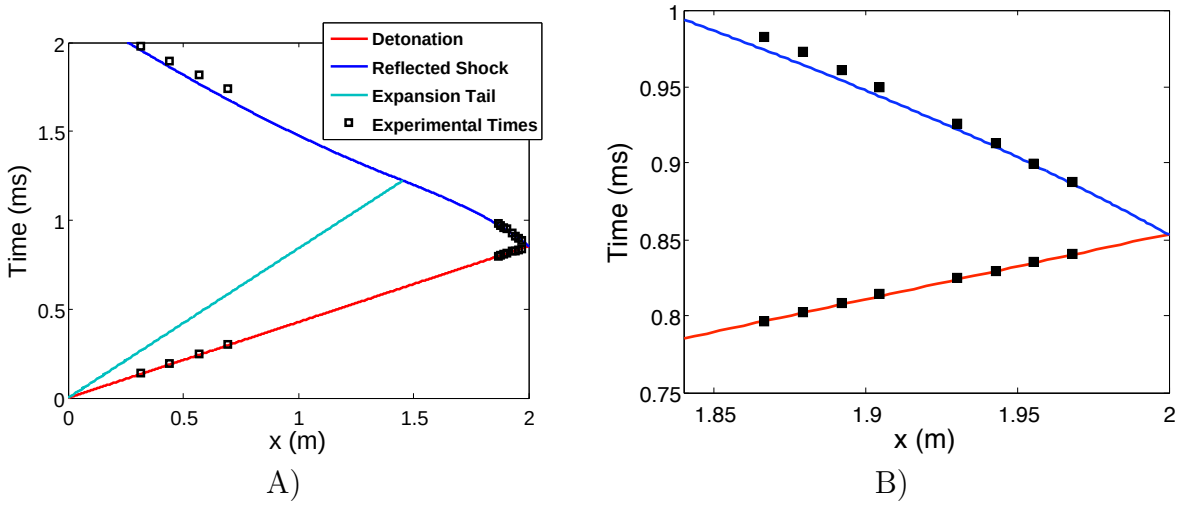

Figure 4.9: A) Experimental arrival times in the driven tube setup compared with space-time diagram computed from the model. B) Detail near the reflecting end.

Close inspection of Fig. 4.10 shows that the predicted peak pressures are consistently 20–30% in excess of the measured peak pressure values. This is due to the fact that the pressure trace at the reflecting end wall is fit using the computed $P_{CJ,ref}$ rather than using the measured result as a fit parameter. We therefore performed a fit of the data using both the peak reflected pressure and the exponential decay rate as fitted parameters, with the goal of achieving a result which more accurately reflected the measured data. Figure 4.11 shows the results of such a fit. The peak pressures are indeed closer to their measured values, with the maximum error in peak pressures reduced to between 10 and 20%. However, while the first fit predicts the arrival times of the reflected wave to within the rise time of the pressure measure-

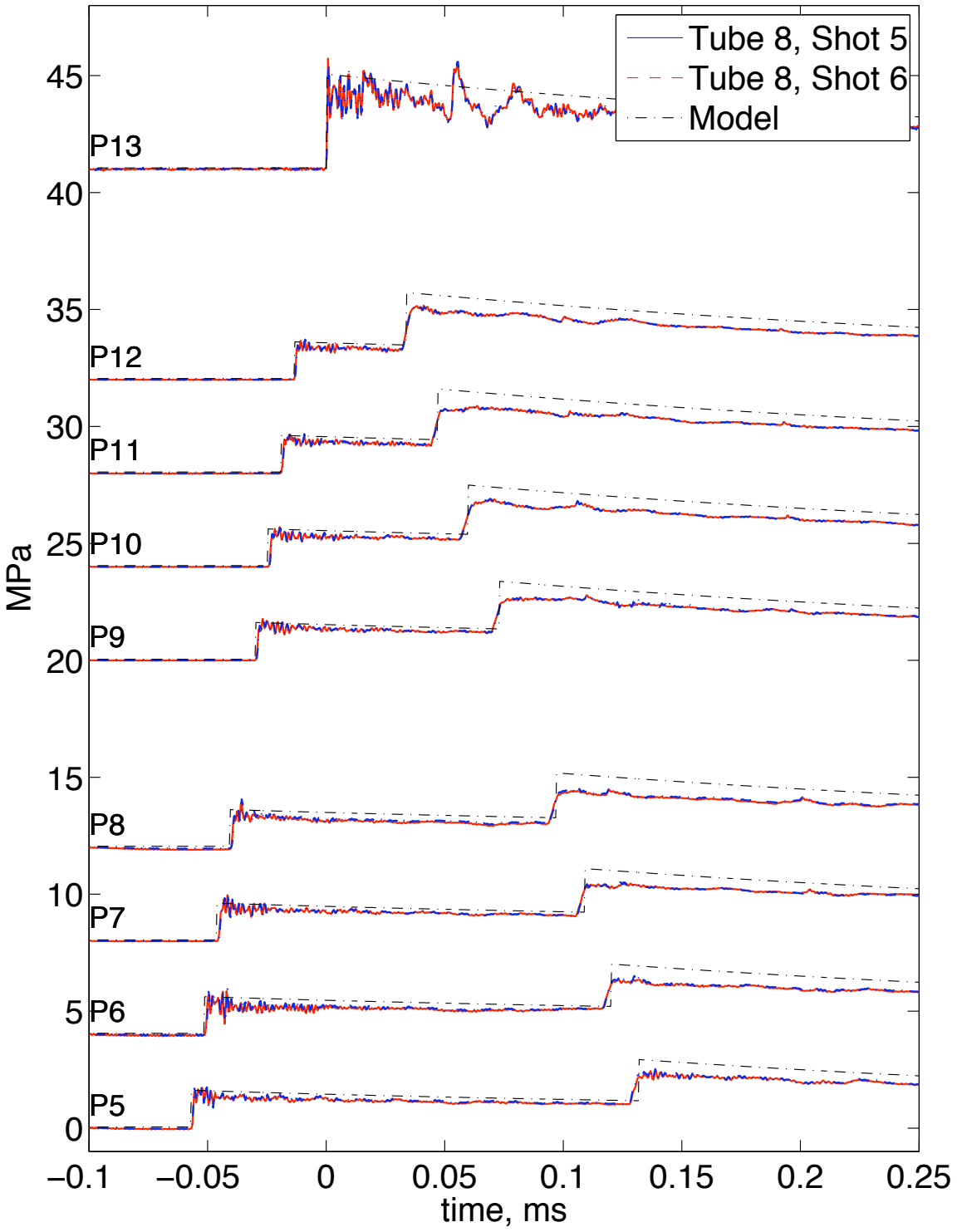

Figure 4.10: Pressure traces for the 8 locations in the tube wall and the reflecting end compared with those computed from the model with parameters based on the ideal pressure $P_{CJ,ref}$ and P_3.

Table 4.2: Parameters used in the pressure model for stoichiometric ethylene–oxygen mixtures

$\mathbf{P}_1$ **(bar)**	$\mathbf{U}_{CJ}$ **(m/s)**	$\mathbf{P}_{CJ}$ **(MPa)**	$\mathbf{c}_{CJ}$ **(m/s)**	γ	$\mathbf{P}_{ref}$ **(MPa)**	τ **(μs)**
0.5	2343	1.643	1264	1.138	4.120	330
2.0	2410	6.831	1303	1.143	17.15	300
3.0	2430	10.54	1316	1.146	26.46	2.96

.

ment, the results from the alternative fit predict a velocity for the reflected shock which is about 30% too slow. The importance of reflected shock arrival time will be shown in Section 4.4, and for this reason the original fit was used for the mechanical response computations. Because the arrival times of the reflected shock wave are well predicted by the original fit, we hypothesize that the pressure defect at the wall is due to 2-dimensional effects, such as the shock–boundary layer interaction and shock bifurcation. The hypothetical flow is driven by the centerline velocity of the shock wave, which has a higher peak pressure than at the wall due to the oblique shocks in the boundary layer (Mark, 1956).

4.3 Material Testing

Regardless of the method used to simulate the structural dynamics, a material model is needed to represent the constitutive relation of the tube wall material. In order to formulate such a model for use in computational testing, specimens of the tube wall were cut and subjected to testing in a double shear test by Professor Alexis Rusinek at the University of Metz. The test is described in Rusinek and Klepaczko (2000), and the results were presented in Sauvelet et al. (2007). The material was tested at strain rates of 10^{-3} to 10^{2} s^{-1}. Results from these tests are shown in Fig. 4.12. Significant strain rate hardening was measured for strain rates on the order of those observed under detonation conditions.

The modulus was not measured but was assumed to be 210 GPa (30.5×10^6 psi), the Poisson ratio was assumed to be 0.3, and the density was assumed to be 7.85×10^3 kg·m^{-3}.

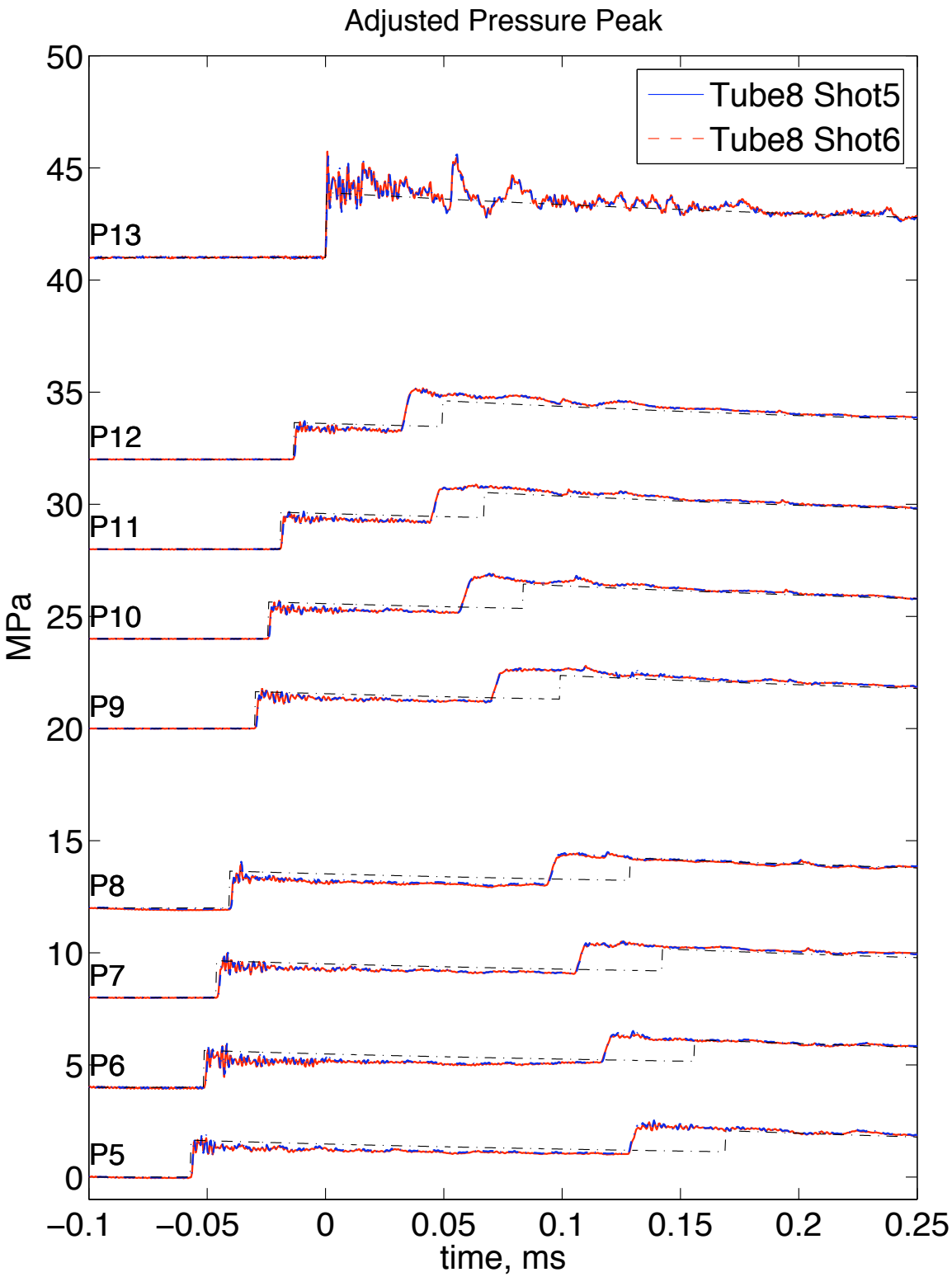

Figure 4.11: Pressure traces computed with the revised fit based on adjusting the peak pressure to better match the measured values.

Efforts to measure the stress-strain relationship in the elastic regime were unsuccessful, but tension testing at an independent laboratory (see Appendix C) found that specimens cut from the tube wall met the standards for the quoted material, with a yield strength (0.2% offset method) of 334 MPa (49.2 ksi), a tensile strength of 432 MPa (63.5 ksi), and an elongation of 33% at failure.

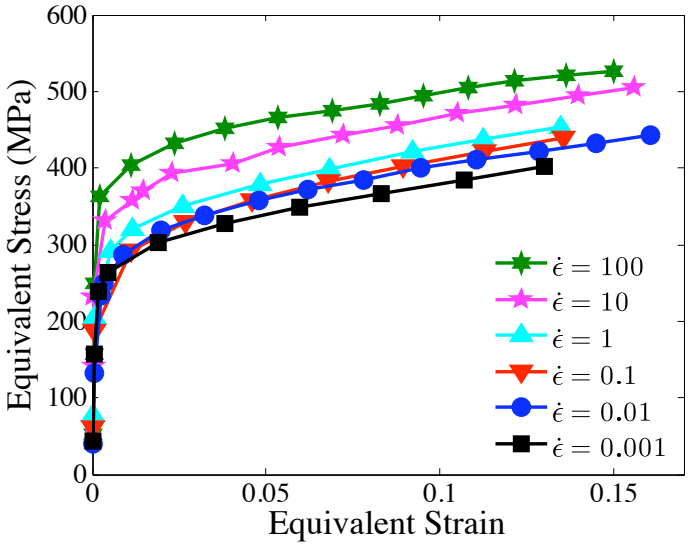

Figure 4.12: Results from dynamic testing of tube material (Sauvelet et al., 2007). Strain rates ($\dot{\epsilon}$) are in s^{-1}.

4.4 Single Degree of Freedom Modeling

The simplest theoretical model of the dynamics of a tube wall considers an infinite tube subjected to a spatially uniform, time-dependent loading. If the stresses in the tube wall are assumed to be uniform, and displacements are small compared to the tube radius R, then the equation of motion for such a system is

$$\rho h \frac{d^2x}{dt^2} + \frac{h}{R}\sigma = \Delta P(t). \tag{4.12}$$

The membrane stress in the tube wall is related to the strain by

$$\sigma = \frac{E}{1-\nu^2}\epsilon_\theta, \tag{4.13}$$

and the hoop strain ϵ_θ is

$$\epsilon_\theta = \ln\left(\frac{R+x}{R}\right) \approx \frac{x}{R} \text{ for } x \ll 1 \tag{4.14}$$

The equation of motion becomes

$$\rho h \frac{d^2x}{dt^2} + \frac{Eh}{R^2\left(1-\nu^2\right)}x = \Delta P(t). \tag{4.15}$$

This is the equation for a forced harmonic oscillator with natural frequency

$$\omega = \frac{1}{R}\sqrt{\frac{E}{\rho\left(1-\nu^2\right)}}. \tag{4.16}$$

The period of the hoop oscillation of the cross section is $T = 2\pi/\omega$, which for the tubes used in the Chapter 3 comes out to 73 μs. This is also four times the characteristic response time for the cross section to a differential pressure loading.

The single degree of freedom model may also be extended to the plastic regime by introducing an inelastic stress-strain relationship into Eq. 4.12. For our purposes, an elasto-plastic model with linear strain hardening was chosen. In such a system,

$$\sigma = E_1\epsilon \quad \text{for} \quad \sigma < \sigma_y \tag{4.17}$$

$$\sigma = \sigma_y + E_2(\epsilon - \epsilon_y) \quad \text{for} \quad \sigma > \sigma_y\ . \tag{4.18}$$

In order to apply this material model with hardening, the yield strain must be monitored as it increases in the plastic regime. This is done through the additional equation

$$\frac{d\sigma_y}{dt} = \frac{\partial\sigma_y}{\partial\sigma}\frac{\partial\sigma}{\partial\epsilon}\frac{\partial\epsilon}{\partial t} \tag{4.19}$$

where

$$\frac{d\sigma_y}{d\sigma} = \begin{cases} 1 & \sigma \geq \sigma_y \\ 0 & \sigma < \sigma_y \end{cases}\ . \tag{4.20}$$

This model has been implemented in Matlab using the Runge–Kutta solver ode45. The most relevant results to the present study are obtained when run in a loop over

spatial locations in the tube, using $P(x,t)$ as that found from the pressure model. Figure 4.13 contains a comparison of the peak elastic strains as computed from the single degree of freedom model with the measured peaks in the experiment. The magnitude of the strains is more accurate for the pressure model which used the reflected pressure as a fit parameter, with the result using the computed pressure overpredicting the strain by 20–25%. The results from the plastic case, discussed below, reveal why we chose to use the calculated $P_{CJ,ref}$ for the rest of the computations.

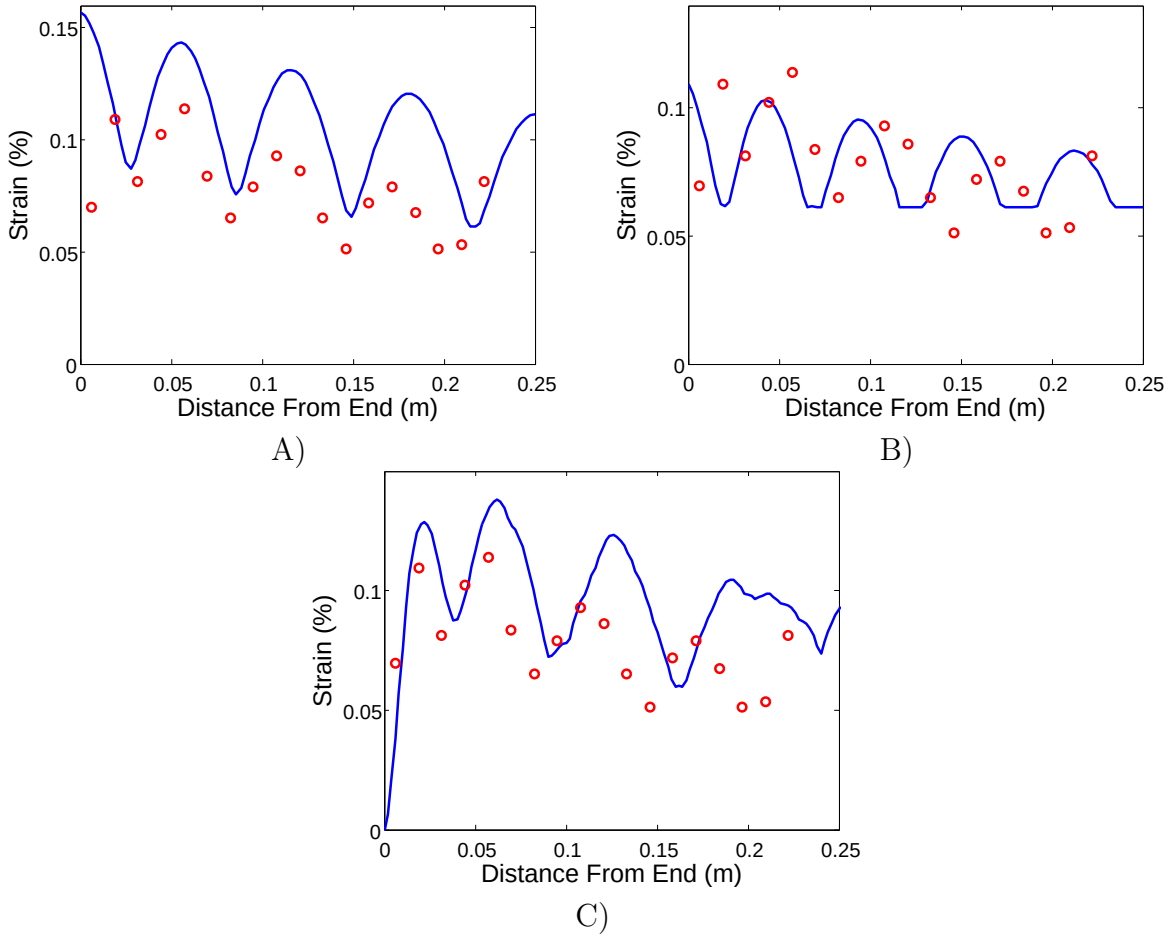

Figure 4.13: Comparison of measured peak elastic strains and A) SDoF model using the first pressure fit, B) SDoF model using the revised fit, and C) finite element model using the original fit.

The results from a plastic case, using the pressure loading for an initial pressure of 2 bar, are shown in Fig. 4.14. The most striking thing about these results is the presence of the ripples that were noted in the experiment. The rippling is present

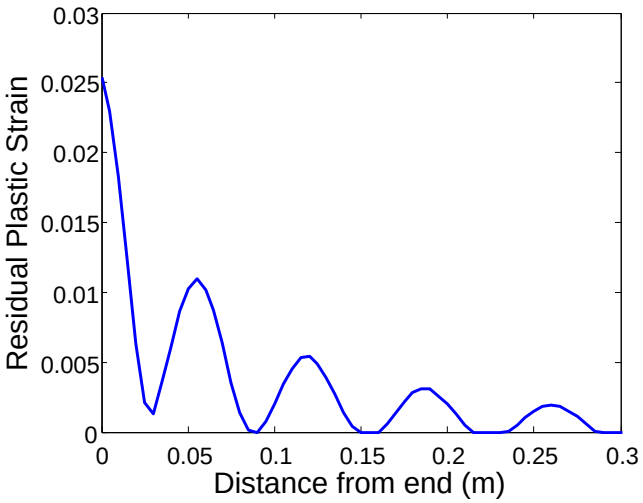

Figure 4.14: Single degree of freedom model results for residual plastic strain with 2 bar initial pressure, first detonation loading cycle.

Table 4.3: Material properties used in single degree of freedom calculations.

E_1 **(GPa)**	E_2 **(GPa)**	ρ **(kg/m^3)**	h **(mm)**	R **(mm)**	ν	ϵ_y
210	1	7800	1.5	63.5	0.3	0.003

in one-dimensional (SDoF) calculations, which are free of any effect of boundary conditions or bending stresses, demonstrating that the underlying cause of the phenomenon is the loading history. The incident detonation sets the wall of the tube in elastic vibration at the natural frequency of the cross section. The subsequent arrival of the reflected shock then imposes a second impulsive pressure loading on the already vibrating wall. Depending on the phase of the oscillation at the time when the shock wave arrives, the reflected shock loading may either augment or diminish the tube deformation. In the range of deformation produced by the tests at 2 bar initial pressure, the plastic deformation is of just the right magnitude so that the elastic oscillations and plastic deformation combine to yield periodic ripples. This is illustrated in Fig. 4.15, which shows the local strain traces for both a local minimum and a local maximum in the ripple pattern.

Knowing the mechanism behind the formation of the rippled pattern allows the calculation of the ripple wavelength. This is dependent on the reflected shock velocity, which increases in the TZ wave and decreases beyond the expansion tail, so we will

analyze this in terms of the average shock velocity $\bar{U}_R$. The total time between the arrival of the detonation wave and the reflected shock at a given location x_0 is

$$\Delta t = \frac{x_0}{U_{CJ}} + \frac{x_0}{\bar{U}_R} \tag{4.21}$$

$$= \frac{\bar{U}_R + U_{CJ}}{\bar{U}_R U_{CJ}} \cdot x_0 \tag{4.22}$$

and the total time difference required for the reflected wave to arrive at locations 360° out of phase of the elastic oscillations of a given point is

$$\Delta t_2 - \Delta t_1 = \frac{1}{f_{xs}} \tag{4.23}$$

where f_{xs} is the natural frequency of the cross section. The wavelength of the ripples, λ_r is estimated to be

$$\lambda_r = x_2 - x_1 = \frac{1}{f_{xs}} \left(\frac{\bar{U}_R U_{CJ}}{\bar{U}_R + U_{CJ}} \right). \tag{4.24}$$

Evaluating this expression with the numbers for the 2 bar condition used in the experiment, $U_{CJ} = 2400$ m/s, $f = 12.8$ kHz, and the average velocity of the reflected shock computed from its arrival time at the second peak in the ripples, $\bar{U}_R = 1380$ m/s, the resulting wavelength is 68.6 mm. The peak-to-peak spacing for this location in the experiment was 70 mm, within 2% of our simple estimate.

Figure 4.16 contains the residual plastic strains computed from the single degree of freedom model plotted with those measured from experiment. The most obvious failing of the model at hand is in the vicinity of the boundary. With a one-dimensional simulation, no modeling of the boundary condition is possible, causing high strains to occur at the reflecting end. The characteristic bending length in the axial direction for a cylindrical shell is (Young and Budynas, 2002):

$$\lambda_b = \left[\frac{R^2 h^2}{3\left(1 - \nu^2\right)} \right]^{1/4}. \tag{4.25}$$

For the tubes used in this study, this comes out to 7.6 mm. Thus from Fig. 4.16, the

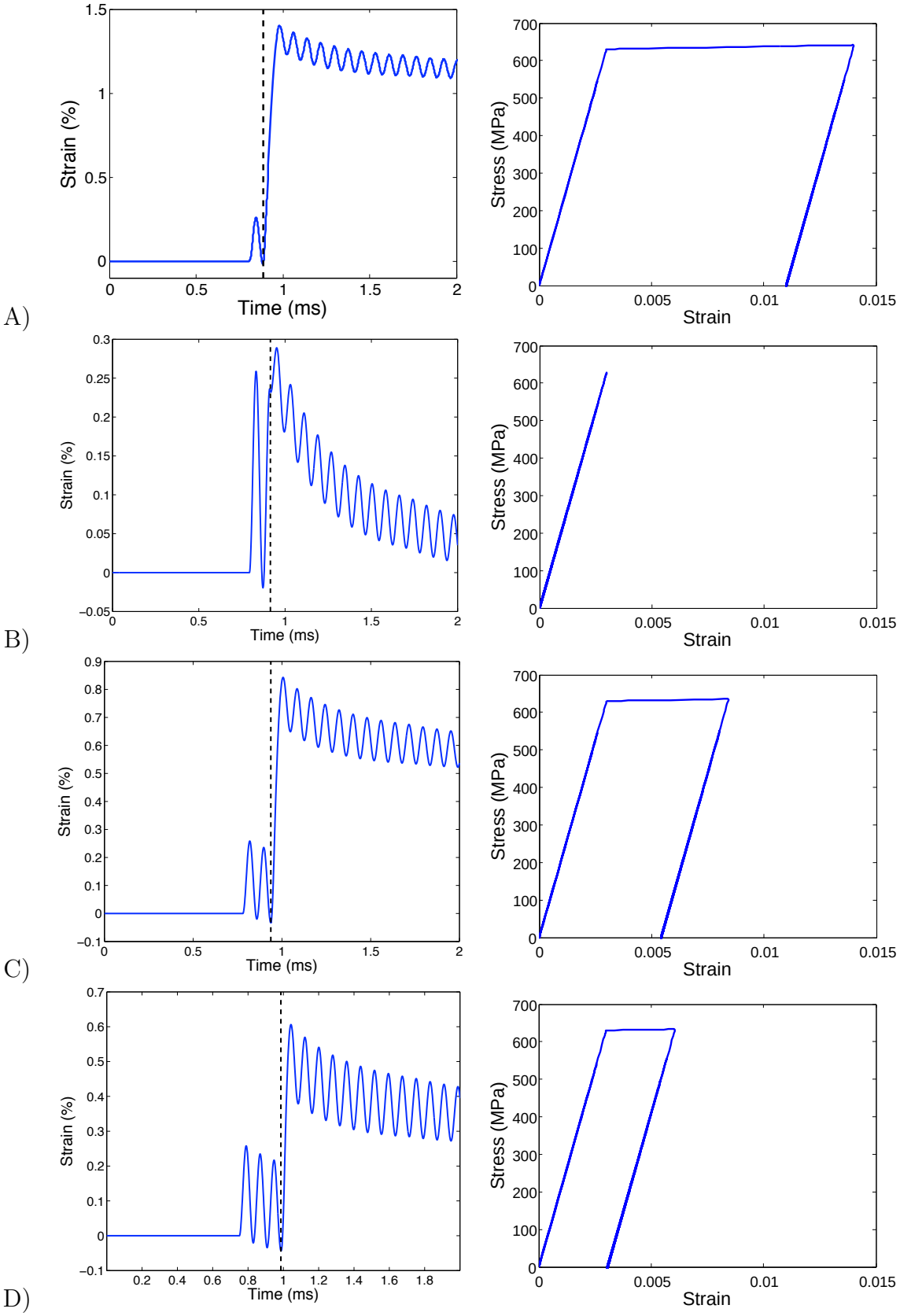

Figure 4.15: Pointwise strain traces and stress–strain diagrams computed from SDoF model. The dashed line indicates the arrival time of the reflected shock. This computation was for the 2 bar initial pressure case, corresponding to Fig.4.16A. A) the peak at $x = 0.055$, B) the trough at $x = 0.09$, C) the peak at $x = 0.12$, and D) the peak at $x = 0.19$.

single degree of freedom model would appear to be reasonable for use with locations greater than about 3–5 bending lengths away from the wall.

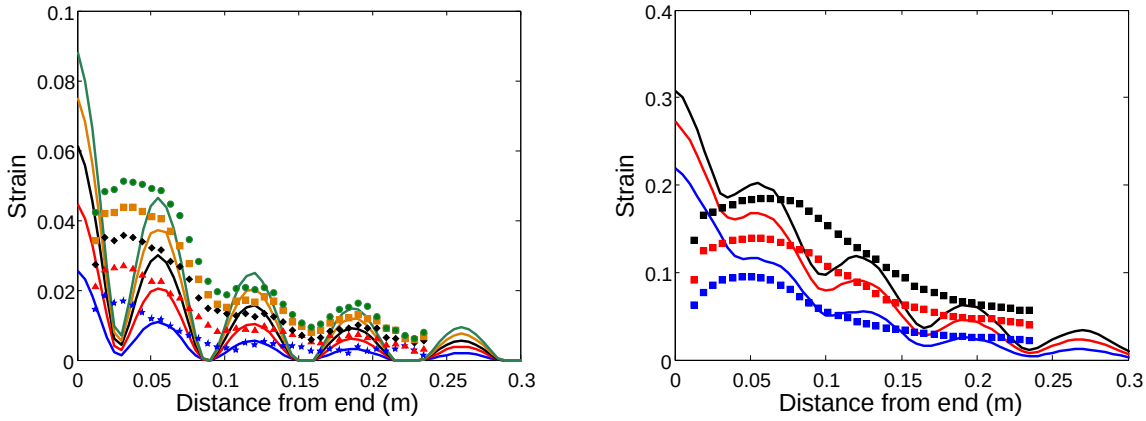

Figure 4.16: Residual plastic strains as computed with the SDoF model compared with the experimentally measured results for repeated tests at A) 2 bar and B) 3 bar initial pressures.

For locations that are several bending lengths away from the wall, the single degree of freedom model with the simple elastic–linear hardening constitutive relation does a remarkably good job of capturing both the locations and magnitudes of the local maxima for the series of tests at 2 bar initial pressure. The errors in the axial locations of the peaks are always within 10% of the wavelength, and the errors in residual plastic strains are within 30%. The troughs of the ripple pattern are consistently underestimated by the single degree of freedom model, to the extent that residual plastic strain goes to zero for most of them. In this case the model is incapable of capturing the bending stresses and flexural waves produced which cause each cross-section of the tube to influence neighboring cross sections.

The single degree of freedom model also seems to do a miraculously good job of estimating the peak deflections in the 3 bar case, but this is the result of a fortuitous combination of assumptions and inaccuracies rather than fidelity to the physical problem. In particular, rate-hardening effects become important at the more extreme loading conditions, as we will show in the next section. Rate-hardening will tend to decrease the incremental strains, which competes with 2-dimensional effects such as

flexural waves and boundary conditions, which will serve to increase strains.

4.5 Finite Element Analysis

A more sophisticated computational investigation of the problem involves the use of the method of finite elements. For the results reported herein, the finite element solver LS-DYNA V970 was used. Figure 4.17 shows the typical numerical mesh for the tube. The tube was modeled using axisymmetric shell elements. Typically 5 elements were used through the thickness and 4000 through the tube length, which was taken to be 2 m. This was in an effort to mimic the overall length of the tube assembly used in the experiment. The driver tube was not modeled separately, as we are most concerned with the deflection in the vicinity of the reflecting end.

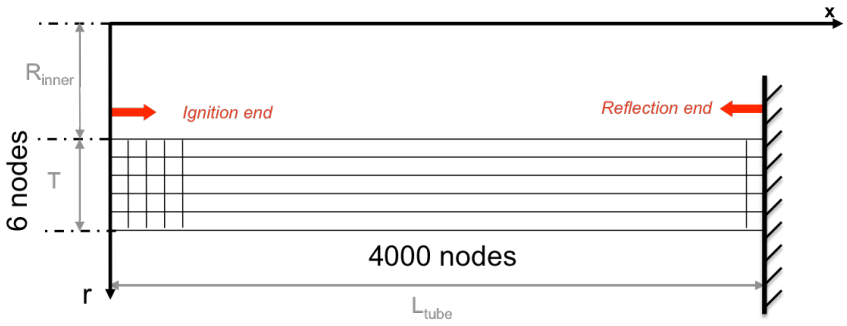

Figure 4.17: Mesh used for finite element computations in LS-DYNA. The detonation propagates from left to right, with the right boundary fixed and the left boundary confined in the radial direction alone.

A variety of material models were used in the calculations, including linear and piecewise linear strain hardening models, both with and without Cowper-Symonds strain-rate hardening. Various attempts to fit the Johnson Cook parameters to the measured stress–strain–strain-rate data (both full and simplified) proved fruitless in generating a material model yielding reasonable results.

The simplest tests performed with the finite element model did not include the effects of strain-rate hardening, instead an average value of the yield strain was chosen and considered constant. For both cases the tangent modulus was taken to be 1 GPa. The location of the yield point ($\epsilon_{y0} = \sigma_{y0}/E_1$) was iterated until reasonable

Table 4.4: Material properties used in the finite element simulations.

Model	E_1 **(GPa)**	E_2 **(GPa)** ($\epsilon_y < \epsilon < 2.5\%$)	E_3 **(GPa)** ($\epsilon > 2.5\%$)	ϵ_{y0} (%)	C	P
Bilinear for 2 bar	210	1	N/A	0.125	N/A	N/A
Bilinear for 3 bar	210	1	N/A	0.28	N/A	N/A
Cowper–Symonds	210	3	1	0.13	2000	6.6

agreement was found with the residual plastic strains from the computation and those from the diameter measurements taken after each experiment. The final values were $\epsilon_{y0} = 0.125\%$ ($\sigma_{y0} = 262$ MPa) for the 2 bar case, and $\epsilon_{y0} = 0.28\%$ ($\sigma_{y0} = 588$ MPa) for the 3 bar case. The difference in the yield points which reproduce the measured results underscores the necessity to include rate-hardening as a component of the material model. Figure 4.18 contains plots showing the residual plastic strain calculated

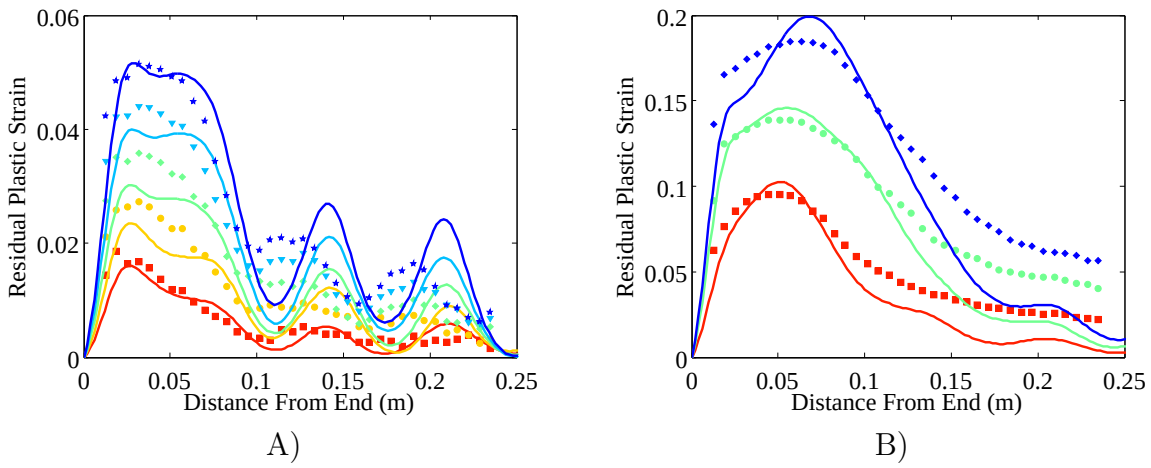

Figure 4.18: Comparisons of measured and calculated residual plastic strains for A) 2 bar and B) 3 bar initial pressure using the elastic–linear hardening model with no rate-hardening.

from these models in DYNA and the corresponding experimental measurements. In general, reasonable agreement is achieved between the peak strains, but this is of questionable value as the yield points were chosen such that this would be the case. Note that the local maxima in the rippled pattern are consistently too high in the 2 bar case. This is most likely due to the simplifications involved in choosing a linear strain-hardening curve, as the real material is stiffer at low strains than it is at high

strains. Also note that the strains in the 3 bar case are lower than the measured values by a factor of 2 or more upstream of the primary bulge. This indicates that rate-hardening plays an important role in the 3 bar case even over the course of a single experiment, a fact which is further illustrated by the record of maximum strain-rate as calculated in DYNA, shown in Fig. 4.19. The peak strain-rate in the 3 bar case is more than a factor of two higher than in the 2 bar case, consistent with the observed variation in the yield point.

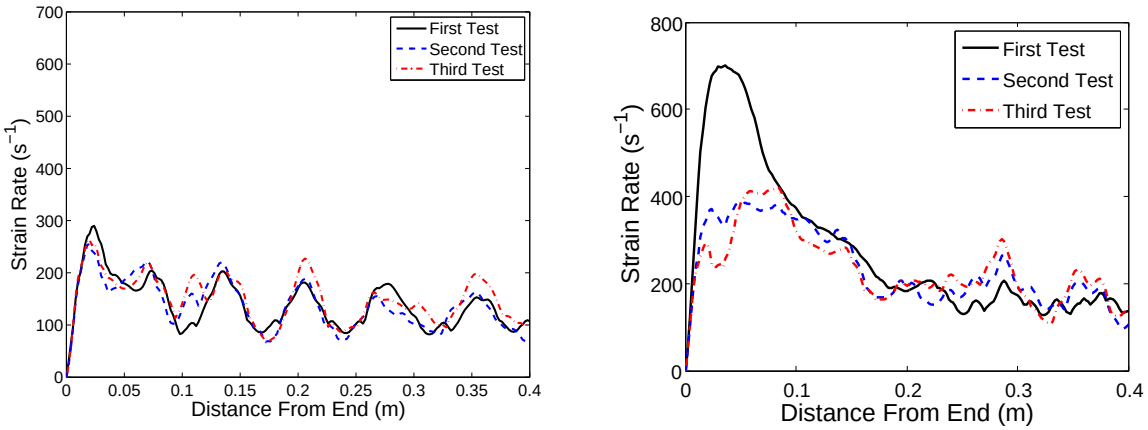

Figure 4.19: Maximum strain rate calculated in the LS-DYNA model for repeated A) 2 bar and B) 3 bar experiments.

Figure 4.20 contains the residual plastic strains calculated using a model with a piecewise linear hardening curve and Cowper-Symonds rate-hardening. The model uses a a multilinear strain-hardening curve with a tangent modulus of 3 GPa between yield and 2.5% strain and 1 GPa above that. The Cowper-Symonds parameters and the yield strain at zero strain-rate were fit to the data of Sauvelet et al. (2007) using least squares error minimization, and the values used in the final computations were $\epsilon_{y0} = 0.13\%$ ($\sigma_{y0} = 273$ MPa), $C = 2000$, and $P = 6.6$. The results of the fit are shown in Fig. 4.21.

The key thing to note in the comparison shown in Fig. 4.20 is that the the two computations were performed using the same material model. Only the loading conditions were changed. The greatest disparity in peak strains between the model and the experiment occurs in the 2 bar case, where the maximum difference is 15% of

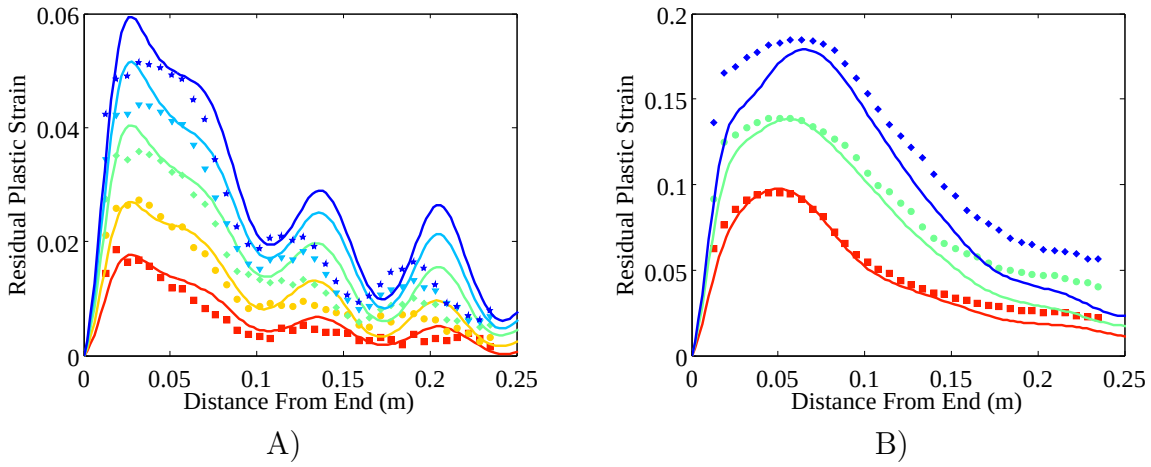

Figure 4.20: Residual plastic strain for A) 2 bar and B) 3 bar with Cowper-Symonds rate-hardening.

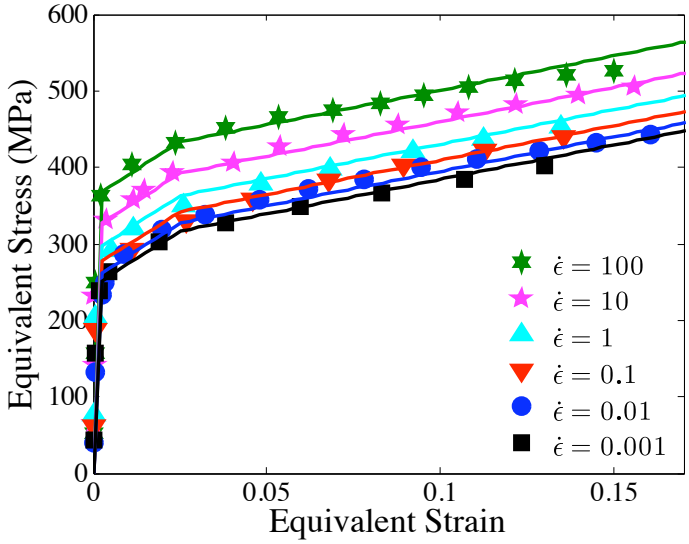

Figure 4.21: Rate-hardening model used in computations, compared with measured data from Sauvelet et al. (2007).

the experimentally measured value. Between 0.02 and 0.05 m from the reflecting end the maximum computed strain is greater than the experimental data, which indicates that the transition from 3 GPa to 1 GPa in the tangent modulus is either too sharp or occurs at too low a strain. The greatest deviation from experiment in the peak strains aside from the last three 2 bar tests occurs in the third 3 bar case, where it is 3%. The error at this condition is substantially in excess of that found in the first two loading cycles of either tube. We speculate that this is due to the fact that this

strain level is beyond the conditions for which we have measured and fit the material response.

The model appears to be too hard for locations away from the peak strain in the 3 bar case; this may be the result of too early or steep a transition in tangent modulus. Computations performed with both material models exhibit large discrepancies in both the locations and amplitudes of the local maxima in the ripple patterns. The amplitudes in the computation are as much as 30% higher than the experimental measurements, and the peaks are displaced by as much as 35% of a wavelength. Figure 4.22 contains comparisons of the measured and calculated strain traces for two different locations along the tube, which illustrates the underlying cause of these discrepancies. In Fig. 4.22A), 44 mm away from the end wall, the two traces show very good agreement with one another, both in arrival time of the reflected wave and in the resulting strain. In Fig. 4.22B), however, 330 mm away from the end wall, the reflected shock in the model arrives nearly half of a natural period before the experimental case, resulting in a completely different excitation of the cross-sectional vibration.

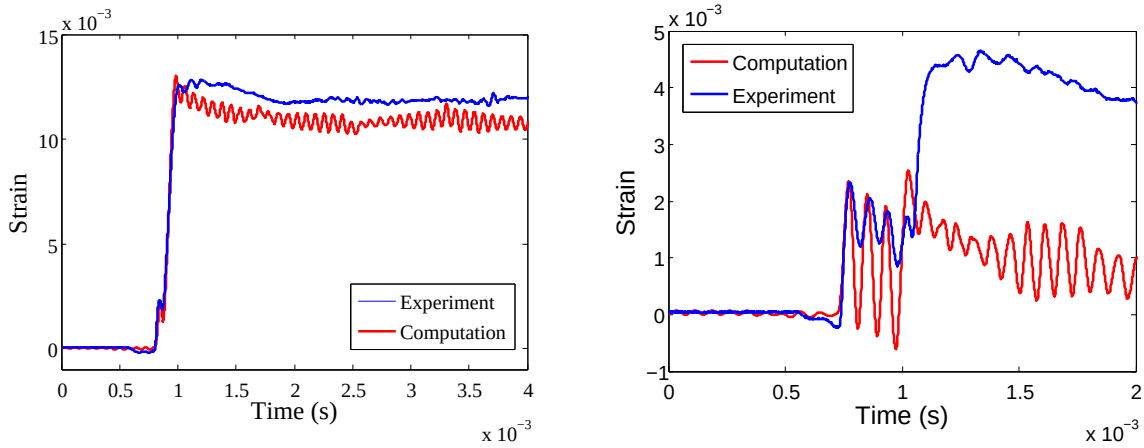

Figure 4.22: Comparisons of strain-time traces for the first 2 bar detonation at A) 44 mm and B) 330 mm away from the reflecting end.

A comparison of the time difference between the moment of reflection and the arrival times of the reflected waves reveals that on average the reflected wave in the model is traveling 3% faster than its laboratory counterpart. There are two factors

which contribute to the velocity differences. First, the manner in which the loading has been applied to the finite element mesh does not take into account the deformation of the tube. The boundary condition at the upstream end allows axial translation, which means that the tube shortens over the course of the calculation, just as it does in the experiment. This shifts the relative axial locations of the elements toward the reflecting end, while the reflected shock velocity was calculated as if no such displacement occurred. The net effect is to increase the apparent shock velocity. The second factor which may have an effect on the velocity is the complete decoupling of the shock pressure from the material deformation. This would seem to be less important than the first effect, since this would also be an issue in the single degree of freedom model, which shows much greater fidelity with the experiments in the peak locations.

Figure 4.23 through 4.25 contain comparison plots of the time histories of the strain gauges and the corresponding node locations in the finite element model. The high-pressure cases use the rate-hardening model described earlier; the 0.5 bar case uses a purely elastic material model. In general, deformation of the modeled tube shows a greater magnitude and a faster rise than that of the experimental result. This is primarily due to the deficiencies of the pressure model, which were discussed in Section 4.2.2. The elastic model shows moderate discrepancies with experiment after the arrival of the reflected wave, illustrating the incredibly sensitive nature of the elastic calculations to minor differences in the reflected shock pressures and arrival times.

4.6 Summary

A simple, semi-empirical, one-dimensional model was developed for the traveling pressure load resulting from a reflecting Chapman–Jouguet detonation. This model was tested at low pressure and found to be in reasonable agreement with experimental data. Using this model, repeated loadings were applied to both a single degree of freedom and a finite element model of the tube used in the experiments, using various

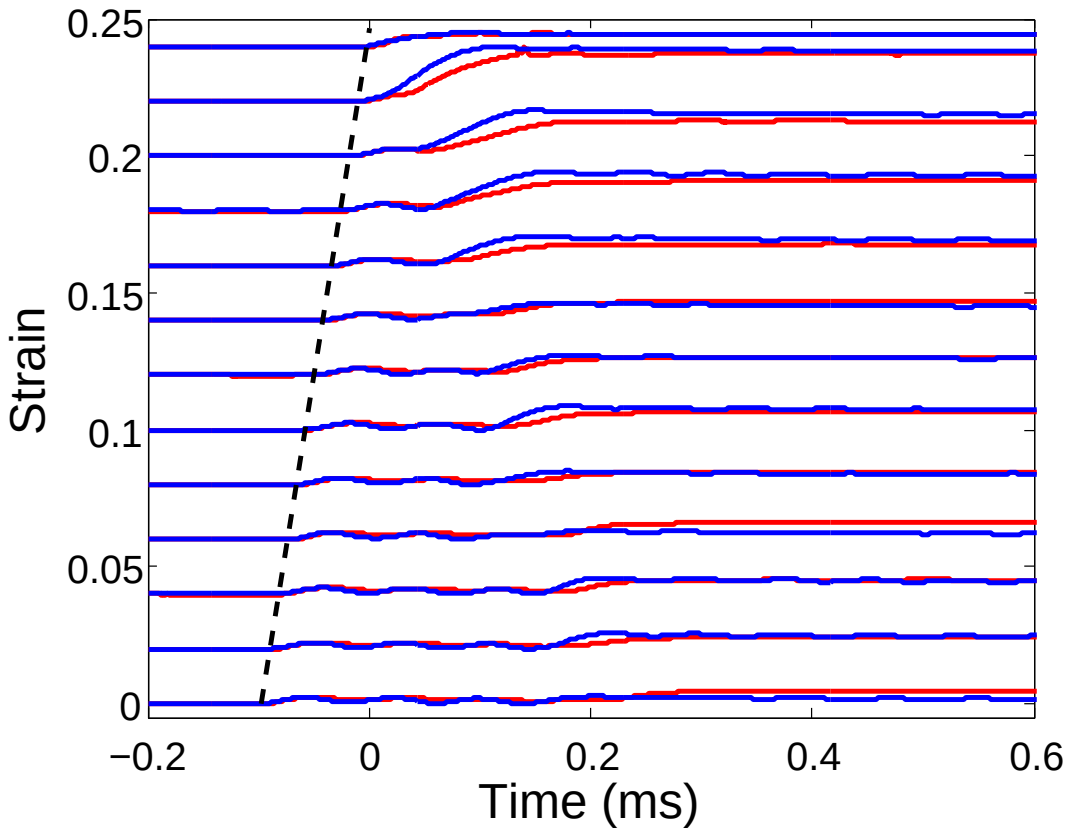

Figure 4.23: Strain history comparison for the first 2 bar detonation. The experimental data is in red, and the results from the finite element model in blue. Dashed line represents position of incident detonation.

constitutive relations for the tube wall material.

Only elastic–linear hardening models were tested in the single degree of freedom case. If the measurement location is sufficiently far (≈5 bending lengths) from the boundary condition, the calculated peak strains agree remarkably well with experiment. The ripples observed in the experiment are reproduced in the single degree of freedom model, providing an explanation for their appearance. The incident detonation wave excites elastic oscillations at the cross section natural frequency. The reflected shock wave imparts a load on the vibrating wall, and depending on the phase of oscillation at the time the shock arrives, the oscillations are either damped out or excited further as the deformation proceeds into the plastic regime. The single degree of freedom model severely underpredicts the magnitude of deformation of the troughs in the ripple pattern, illustrating that bending stresses and wave propagation

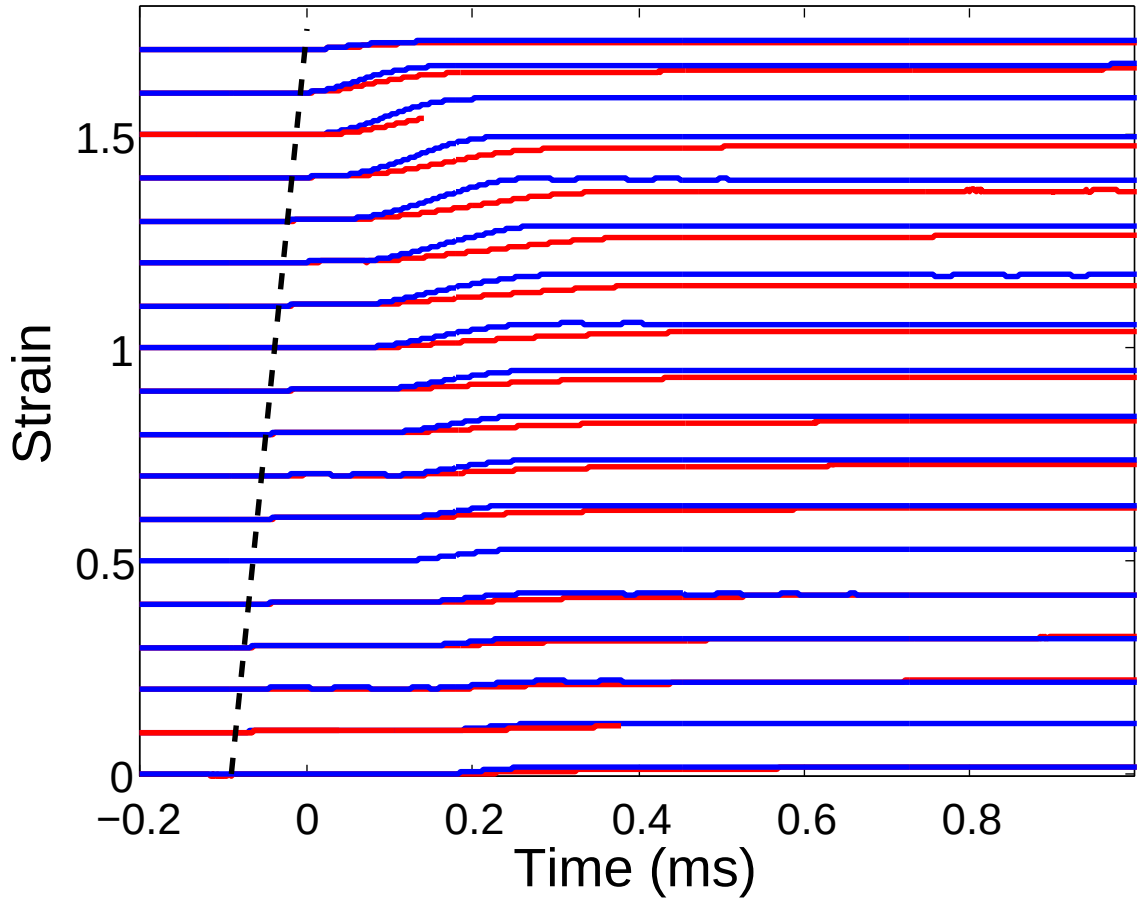

Figure 4.24: Strain history comparison for the first 3 bar detonation. The experimental data is in red, and the results from the finite element model in blue. Dashed line represents position of incident detonation.

are significant for quantitative predictions.

The two-dimensional finite element model used both elastic–linear hardening models and piecewise linear models with Cowper-Symonds rate hardening. Rate hardening was found to be extremely important when attempting to model both high and low pressure experiments with the same constitutive relation, and moderately important within a single set of tests. The manner in which the pressure loading was applied is one possible source of discrepancies between the experiments and computations.

Further refinement of the material model could yield better fidelity with experiment, particularly in the case of the peak strains arising in the 2 bar tests. Still, it is clear that the pressure loading model we are using will never capture the correct result upstream of the initial reflection. The next logical step in modeling would be

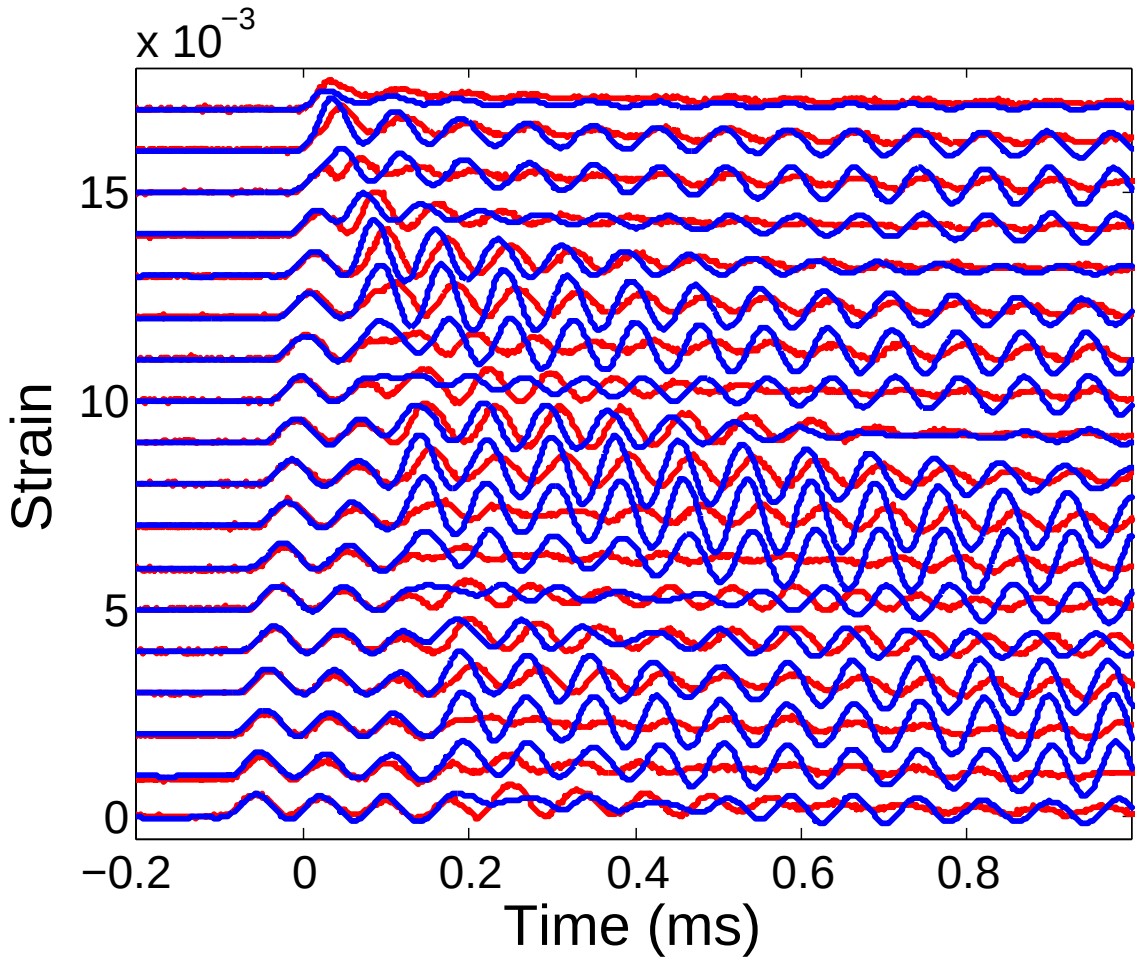

Figure 4.25: Strain history comparison for the first 0.5 bar detonation. The experimental data is in red, and the results from the finite element model in blue.

to conduct coupled simulations of the fluid and solid mechanics.

Chapter 5

Conclusions

This study contributed to our understanding of the structural response of metal tubes to incident and reflected detonations propagating in their interiors. Experimental investigations and numerical computations were performed to investigate the elastic and plastic deformation arising from these loads.

5.1 Elastic Response

The elastic portion of the study extended the work of Beltman and Shepherd (2002) with the aim of achieving greater fidelity between results from the experiment and those of computational models of the tube using idealized loading histories. Strain measurements were carried out through both strain gauge and laser-vibrometry measurements. The resulting data illustrated both the usefulness and the limitations of the measurement of strain using bonded gauges. Several non-ideal effects in these experiments were discussed and quantified, including nonuniform wall thickness, strain-gauge hysteresis, thermally induced strains, and prestress on the tube. Non-uniform wall thickness was found to account for a significant amount of discrepancy between the experiments and simulations.

The experiments were compared with simulations of both the gasdynamics of the detonation process and the mechanical response of the tube wall. The gasdynamics simulations were found to match the incident detonation pressures and velocities extremely well. The reflected shock proved more difficult to predict using this tech-

nique, with errors in pressures and arrival times of up to 20%, which was attributed to heat transfer effects and nonideal flow conditions behind the detonation, effects which were not accounted for in the model.

Mechanical response models of the tubes used in the elastic experiments were loaded using idealized pressure histories for the incident detonations. When the nonuniform wall thickness was taken into account in the simulations, the resulting peak strains could be predicted to within the shot-to-shot repeatability ($\approx 8\%$) of the measurements. Response to reflected shock waves in these tubes was not modeled.

5.2 Plastic Response

Several sets of experiments were conducted to investigate the plastic response of thin-walled tubes to loading by detonation waves and shock waves produced by reflecting detonations. After a series of preliminary experiments which suffered from a number of difficulties, a robust test facility was constructed. Thin-walled steel tubes of highly uniform wall thickness and rigid end-support were subjected to loading by stoichiometric ethylene–oxygen detonations at various internal pressures. These experiments provide the first measurements of traveling flexural waves in the plastic regime generated and sustained by propagating detonations. Dynamic strain measurement was accomplished using bonded gauges, a high speed video camera recorded the deflection of the tube end, and post-shot measurements were made of the residual plastic deformation. The highest strains were measured in the vicinity of the reflecting end wall, with residual strains as high as 10% after a single reflection.

The tubes were subjected to repeated detonations to investigate strain-ratcheting under these conditions, and cumulative deformations of 20% as well as the onset of plastic instability were observed.

A significant discovery was the formation of a novel periodic rippling pattern in the residual deformation of the tubes. Previous studies on explosively loaded tubes have only shown bulges without any oscillations. This pattern was determined to be the result of the interaction of the structural load created by the reflected shock wave

with the elastic vibrations set in motion by the incident detonation. This interaction can be visualized as interference between the oscillations created by the incident and reflected waves. Depending on the vibrational phase at the time of arrival of the reflected shock, the interference will vary from constructive to destructive, resulting in differences in the plastic strain by as high as 40%.

A simple semi-empirical model of detonation reflection was formulated to model the internal pressure history on the tube wall. This model was applied as a boundary condition for a simulation of the mechanical response of the tube. The model used thermochemical computations of the Chapman–Jouguet conditions and the similarity solution for the Taylor–Zel'dovich expansion wave to treat the incoming detonation. The measured end-wall pressure was fit to a simple model to analytically represent the reflected pressure–time history. Assuming zero pressure gradient behind the reflected shock wave, the shock-jump conditions were then integrated to calculate the pressure and position of the reflected shock as a function of time. A modification to the experimental facility with a concentration of pressure gauges at the reflecting end was used to test this model. These measurements found that the measured arrival times agreed with experiments to within 1%, but that the computed pressures were as much as 20% in excess of the measured peaks. These results suggest that a bifurcation in the reflected shock occurred due to the shock-boundary layer interaction.

This model pressure history was applied to a single degree of freedom model of the tube cross section and a finite element model of the entire tube. The constitutive relation of the tube wall material was modeled using both an elastic-linear strain hardening model and a piecewise-linear strain hardening model with Cowper–Symonds rate hardening. Strain rate hardening was found to be extremely important in accurately predicting the peak deformation. A model of the 3 bar tests which did not include the effects of rate hardening required a yield stress more than twice as great as that in the 2 bar case to accurately predict the peaks.

The single degree of freedom model of the tube wall showed qualitative agreement with the experiment, and did a particularly good job of predicting the locations of the local maxima in the ripple patterns. It also illustrated the importance of flexu-

ral waves, as unrealistically high yield stresses were required to achieve quantitative agreements with the peak strains, and the amplitudes of the local minima in the ripple pattern were dramatically underpredicted.

The finite element simulation with a rate-hardening material model resulted in reasonable predictions for the plastic strain in the vicinity of the reflection for both the two 2 and 3 bar initial pressure cases. It is clear that the present material model is insufficient to fully describe the steel used in the test specimens, as deformations between 5% and 10% tend to be overpredicted in the 2 bar case and underpredicted in the 3 bar case.

5.3 Suggestions for Future Work

One area in which the experiment could be improved and extended is in the material used to make the specimen tubes. The limited characterization of the 1010 steel was one of the greatest difficulties encountered in the simulations, and tests with better characterized materials are needed to separate effects of structural and gasdynamic motion.

The computations have wider room for improvement. It is clear from experiment that the pressure model is oversimplified, and the predicted pressure is significantly greater and has a sharper rise time than the pressure measured at the inner wall of the tube. This may be the result of bifurcation and shock–boundary layer interaction, but there are no direct observations to support this. To resolve this will require an experimental investigation of the reflected shock using flow visualization and the modeling of the shock-boundary layer interaction in detonation tests to quantify the effect it has on the pressure at the wall.

Finally, it is clear that the method by which the pressure model is applied to the structural model of the tube could also be improved. The tube shortens during plastic deformation, and the distance between a given element and the boundary is decreased. The pressure model was applied to the tube as if this change did not occur, so the reflected shock appears to be faster in the computational model than it

is in the laboratory. Further difficulties arise after large plastic deformations result in steep angles and a breakdown of the assumptions of 1-dimensional flow. The way to address these difficulties is through coupled computations of the solid and fluid mechanics.

Bibliography

J.B. Bdzil, D. S. Stewart, and T. L. Jackson. Program burn algorithms based on detonation shock dynamics: Discrete approximations of detonation flows with discontinuous front models. *Journal of Computational Physics*, 174:870–902, 2001. 62

W. M. Beltman and J. E. Shepherd. Structural response of shells to detonation and shock loading. Technical Report FM98-3, Graduate Aeronautical Laboratories, California Insititute of Technology, 1998. 2, 50

W. M. Beltman and J. E. Shepherd. Linear elastic response of tubes to internal detonation loading. *Journal of Sound and Vibration*, 252:617–655, 2002. 2, 9, 16, 17, 19, 32, 33, 40, 41, 57, 66, 130

W.M. Beltman, E.N. Burcsu, J.E. Shepherd, and L. Zuhal. The structural response of cylindrical shells to internal shock loading. *Journal of Pressure Vessel Technology*, 121:315–322, 1999. 2

R. A. Benham and T.A. Duffey. Experimental-theoretical correlation on the containment of explosions in cylindrical vessels. *Int. J. Mech. Sci.*, 16:549–558, 1974. 20

R. D. Blevins. *Formulas for natural frequency and mode shape*. van Nostrand Reinhold Company, 1979. 33

S. Browne, J. Zeigler, and J.E. Shepherd. Numerical solution methods for shock and detonation jump conditions. Technical Report FM2006-006, Graduate Aeronautical Laboratories California Institute of Technology, February 2008. 7, 11, 60, 101, 147

T. Chao and J.E. Shepherd. Detonation loading of tubes in the modified shear wave regime. In Z. Jiang, editor, *Proceedings of the 24th International Symposium on Shock Waves*, volume 2, pages 865–870. Springer, 2005. 2

T. W. Chao. *Gaseous detonation-driven fracture of tubes.* PhD thesis, California Institute of Technology, 2004. 20, 24

D. L. Chapman. On the rate of explosion in gases. *Philos. Mag.*, 47:90–104, 1899. 2

G. Ciccarelli and S. Dorofeev. Flame acceleration and transition to detonation in ducts. *Progress in Energy and Combustion Science*, 2008. 60

F. Cirak, R. Deiterding, and S. P. Mauch. Large-scale fluid-structure interaction simulation of viscoplastic and fracturing thin shells subjected to shocks and detonations. *Computers & Structures*, 85((11-14)):1049–1065, 2006. 64

G.R. Cowper and P.S. Symonds. Strain hardening and strain rate effcts in the impact loading of cantilever beams. Technical Report 28, Brown University, Division of Applied Mechanics, 1957. 15

R. Deiterding. *Parallel Adaptive Simulation of Multi-Dimensional Detonation Structures.* PhD thesis, Brandenburgische Technische Universitat, Cottbus, Germany, September 2003. 108

R. Deiterding, F. Cirak, S. Mauch, and D. Meiron. A virtual test facility for simulating detonation-induced fracture of thin flexible shells. In V. N. Alexandrov et al., editor, *Proc. Int. Conf. on Comp. Science, May 28-31, 2006, University of Reading*, number 3992 in Lecture Notes in Computer Science, pages 122–130. Springer, Berlin, 2006a. 62, 99

R. Deiterding, F.Cirak, S. Mauch, and D. Meiron. A virtual test facility for simulating detonation-induced fracture of thin flexible shells. *Int. J. Multiscale Computational Engineering*, 5(1):47–63, 2007. 62, 64

R. Deiterding, R. Radovitzky, S. Mauch, Ludovic Noels, Julian C. Cummings, and Daniel I. Meiron. A virtual test facility for the efficient simulation of solid material response under strong shock and detonation wave loading. *Engineering with Computers*, 22(3-4):325–347, 2006b. 62

W. Döring. On detonation processes in gases. *Ann. Phys.*, 43:421–436, 1943. 4

T.A. Duffey. Approximate solutions of an impulsively loaded long cylinder governed by an elastic-plastic material law. *Acta Mechanica.*, 11:45–57, 1971. 20

T.A. Duffey and R. Krieg. Effects of strain hardening and strain rate sensitivity on the transient response of elastic-plastic rings and cylinders. *Int. J. Mech. Sci.*, 11: 825–844, 1969. 20

T.A. Duffey and D. Mitchell. Containment of explosions in cylindrical shells. *Int. J. Mech. Sci.*, 15:237–249, 1973. 20

F. Fanous and L. Greiman. Simplified analysis for impulsively loaded shells. *Journal of Structural Engineering*, 114:885–899, April 1988. 20

W. Fickett and W. C. Davis. *Detonation: Theory and Experiment*. Dover, 2001. 2

P. G. Hodge. The influence of blast characteristics on final deformation of circular cylindrical shells. *Journal of Applied Mechanics*, 284:617–624, December 1956. 20

G. R. Johnson and W. H. Cook. A constitutive model and data for metals subjected to large strains, high strain rates and high temperatures. In *Proceedings of the 7th International Symposium on Ballistics*, pages 541–547, 1983. 15

E. Jouguet. On the propagation of chemical reactions in gases. *J. de Mathematiques Pures et Appliquees*, 1:347–425, 1905. 2

A. S. Kobayashi, editor. *Handbook on Experimental Mechanics*. Society of Experimental Mechanics, second revised edition, 1993. 31, 46

H. Kolsky. *Stress Waves in Solids*. Clarendon Press, Oxford, 1953. 21

J. Christopher Krok. *Jet Initiation of Deflagration and Detonation*. PhD thesis, California Institute of Technology, Pasadena, California, May 1997. 74

J. H. S. Lee. *The Detonation Phenomenon*. Cambridge University Press, 2008. ISBN 978-0-521-89723-5. 1, 2, 5

Z. Liang, J. Karnesky, and J. E. Shepherd. Structural response to reflected detonations and deflagration-to-detonation transition in H_2-N_2O mixtures. Technical Report FM2006-003, Graduate Aeronautical Laboratories California Institute of Technology, August 2006. 70, 71

H. W. Liepmann and A. Roshko. *Elements of Gasdynamics*. Dover Publications Inc, 2001. 7

LS–DYNA User's Manual, version 971. Livermore Software Technology Corporation, Livermore, CA, 2005. 78, 100

P. Ludwik. *Elemente der Technologischen Mechanik*. Springer-Verlag OHG, 1909. 14

H. Mark. The interaction of a reflected shock wave with the boundary layer in a shock tube. *Journal of the Aeronautical Sciences*, 24:304–306, 1956. 112

H. Mark. *The Interaction of a Reflected Shock Wave with the Boundary Layer in a Shock Tube*. NACA TM 1418, 1958. 110, 145, 146

M. A. Meyers and K. K. Chawla. *Mechanical Behavior of Materials*. Cambridge University Press, 2008. ISBN 0521866758. 16

N. Noda, R.B. Hetnarski, and Y. Tanigawa. *Thermal Stresses*. Taylor and Francis, 2002. ISBN 1-56032-971-8. 143

F. Pintgen and J. E. Shepherd. Elastic and plastic structural response of thin tubes to deflagration-to-detonation transition events. Technical Report FM2005-008, Graduate Aeronautical Laboratories California Institute of Technology, April 2006a. 74, 75

F. Pintgen and J. E. Shepherd. Structural response to deflagration-to-detonation transition events in a tube. Technical Report FM2005-005, Graduate Aeronautical Laboratories California Institute of Technology, May 2006b. 70, 74, 142

M. Radulescu and R. K. Hanson. Effect of heat loss on pulse detonation flow fields and performance. *Journal of Propulsion and Power*, 21(2):275–285, 2005. 47, 62, 63

H. Reismann. Response of a pre-stressed cylindrical shell to moving pressure load. In S. Ostrach and R.H. Scanlon, editors, *Eighth Midwest Mechanics Conference*, pages 349–363. Pergamon Press, 1965. 16

W.C. Reynolds. The element potential method for chemical equilibrium analysis: implementation in the interactive program STANJAN. Technical report, Mechanical Engineering Department, Stanford University, 1986. 27, 101

A. Rusinek and J. R. Klepaczko. A numerical study on the wave propagation in tensile and perforation test. *J. Phys. IV France*, 10:653–658, 2000. 112

C. Sauvelet, A. Rusinek, J. E. Shepherd, Z. Liang, and J. Karnesky. Elastic and plastic deformation waves in tubes with internal gas explosion. In *ASME Applied Mechanics and Materials Conference.* ASME, 2007. MCMAT2007-30024, presented June 3-7 2007 University of Texas at Austin. 76, 112, 114, 123, 124

J. E. Shepherd. Structural response of piping to internal gas detonation. *Journal of Pressure Vessel Technology*, 131(3), 2009. 1

J. E. Shepherd, J. Karnesky, F. Pintgen, and J. C. Krok. Experimental measurements of strains and blast waves resulting from detonations in tubes. Technical Report FM2006.010, Graduate Aeronautical Laboratories, California Insititute of Technology, 2008. 23

J.E. Shepherd, A. Teodorcyzk, R. Knystautas, and J.H. Lee. Shock waves produced by reflected detonations. *Progress in Astronautics and Aeronautics*, 134:244–264, 1991. 10, 62, 101, 102, 107, 108

T.E. Simkins. Resonance of flexural waves in gun tubes. Technical Report ARCCB–TR–87008, US Army Armament Research, Development and Engineering Center, Watervliet, N.Y. 12189–4050, July 1987. 17

W. R. Smith. Fast loading of metals with a shock tube: Application to aluminum. In *Proceedings of the 15th International Symposium on Shock Waves*. Stanford University Press, 1986. 20, 21

W. R. Smith. Modeling inelastic wall response of a thin-walled cylindrical tube to shock waves. In *Proceedings of the 17th International Symposium on Shock Waves*. American Institute of Physics, 1990. 20

K. I. Stanyukovich. *Unsteady Motion of Continuous Media*. Pergamon Press, 1960. 10, 11, 101

S. Tang. Dynamic response of a tube under moving pressure. In *Proceedings of the American Society of Civil Engineers*, volume 5, pages 97–122. Engineering Mechanics Division, October 1965. 16, 20

G. I. Taylor. The dynamics of the combustion products behind plane and spherical detonation fronts in explosives. *Proc. Roy. Soc.*, A200:235–247, 1950. 5

P. A. Thompson. *Compressible Fluid Dynamics*. McGraw-Hill, New York, 1972. Out of print from McGraw-Hill, but reprinted privately and available from the Rensselaer Union Bookstore, RPI, Troy, NY. TEL 518 276 6555. 11

S.P. Timoshenko and J. N. Goodier. *Theory of Elasticity*. McGraw-HIll Publishing Company, third edition, 1970. 47

K. Ueda and A. Umeda. Dynamic response of strain gages up to 300 mhz. *Experimental Mechanics*, 38(2):93–98, 1998. 48

A.C. Ugural and S.K. Fenster. *Advanced Strength and Applied Elasticity*. Elsevier, 2nd si edition, 1987. 41

Vishay 11255. 2300 system. Technical Report 11255, Vishay Micro-Measurements, October 2006. URL http://www.vishay.com/doc?11255. 48

Vishay TN504. Strain gage thermal output and gage factor variation with temperature. Technical Report TN-504-1, Vishay Micro-Measurements, August 2007. URL http://www.vishay.com/doc?11054. 45

Vishay TN508. Fatigue characteristics of micro-measurements strain gages. Technical Report TN-508-1, Vishay Micro-Measurements, August 2007. URL http://www.vishay.com/doc?11058. 39

Vishay TN509. Transverse sensitivity errors. Technical Report TN-509, Vishay Micro-Measurements, August 2007. URL http://www.vishay.com/doc?11059. 45

Vishay TN511. Strain gage misalignment errors. Technical Report TN-511, Vishay Micro-Measurements, August 2007. URL http://www.vishay.com/doc?11061. 49

J. von Neumann. *John von Neumann, collected works. Vol. 6., ed. A. J. Taub. New York: Macmillan*, 1942. 4

E. Wintenberger, J. M. Austin, M. Cooper, S. Jackson, and J. E. Shepherd. Reply to 'Comment on analytical model for the impulse of single-cycle pulse detonation tube'. *Journal of Propulsion and Power*, 20(5):957–959, 2004. 62

W. Young and R. Budynas. *Roark's formulas for stress and strain*. McGraw-Hill, 2002. ISBN 0-07-072542-X. Seventh Edition. 118

Ya. B. Zel'dovich. On the theory of the propagation of detonations in gaseous systems. *JETP*, 10:542–568, 1940. Available in translation as NACA TM 1261 (1950). 4

Ya. B. Zel'dovich and A. S. Kompaneets. *Theory of Detonation*. Academic Press, NY, 1960. English translation of original Russian. 5

J. Ziegler. private communication, 2010. 102, 107

Appendix A

Thermally Induced Stress

In situations of loading due to combustion processes, there is always the question as to whether the thermal loading due to heat transfer from the hot combustion products is important. Depending on the time scale and degree of heat transfer, we have already discussed that the material may undergo thermal softening, but the presence of a temperature gradient in the material itself may also result in additional stress, as the hotter layer of the material undergoes thermal expansion, driving a strain in the cooler part of the wall. Pintgen and Shepherd (2006b) describes a series of experiments investigating the thermal strain arising due to deflagrations. It was found that the thermal strain was insignificant in the detonation regime, but very important under deflagration loading conditions (Fig. A.1).

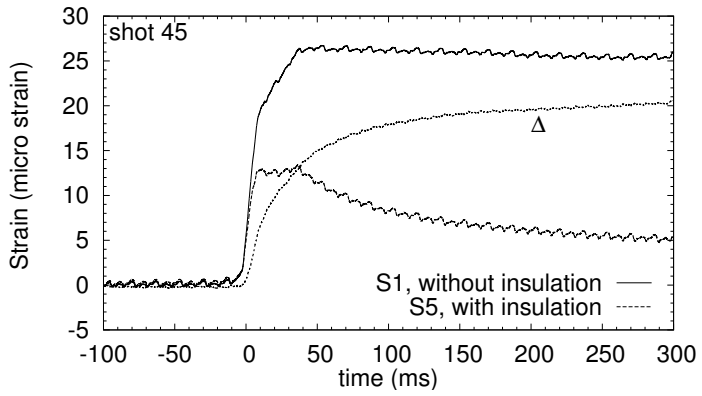

Figure A.1: Strain measurements in section without ($S0$) and with ($S4$) thermal insulation. The difference is the thermally induced strain Δ on outer tube surface.

Figure A.2 contains a sketch of the temperature profile resulting from heat transfer

between the combustion products and the wall. The profile takes the form of an error function with a penetration depth dependent on the time, temperature of the products, heat transfer coefficient between the products and wall, and the thermal diffusivities of the materials.

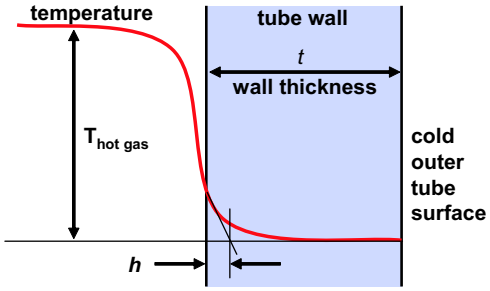

Figure A.2: Thermal penetration depth into inner tube surface.

The thermal hoop stress $\sigma_{\theta\theta}(r)$ induced by an arbitrary temperature profile $T(r)$ is given by Noda et al. (2002) as:

$$\sigma_{\theta\theta}(r) = \alpha E \left(\frac{1}{r^2} \int_{r_i}^{r_o} T(r) r \, dr + \frac{r^2 + r_i^2}{r^2 (r_o^2 - r_i^2)} \int_{r_i}^{r_o} T(r) r \, dr - T(r) \right), \tag{A.1}$$

where α is the thermal expansion coefficient for the wall material ($\approx 10^{-5}$ K^{-1} for most metals). Setting $r = r_o$ and taking $T(r_o)$ as the baseline for $T(r)$, the thermal stress on the outer surface simplifies to

$$\sigma_{\theta\theta}(r = r_o) = \alpha E \frac{2}{r_o^2 - r_i^2} \int_{r_o}^{r_o} T(r) r \, dr. \tag{A.2}$$

The thermal stress on the outer surface is directly proportional to $\int_{r_i}^{r_o} T(r)\, r \, dr$. This integral, in turn, is directly proportional to the thermal energy content Q per unit tube length

$$2\pi c\rho \int_{r_a}^{r_b} T(r)\, r \, dr = Q, \tag{A.3}$$

where c is the specific heat capacity of the tube and ρ is the density of the tube. Therefore, regardless of the specific temperature profile, the thermal stress on the

outer tube surface is governed by only the total thermal energy content of the tube

$$\sigma_{\theta\theta}(r = r_o) = \frac{\alpha E}{2\pi c\rho} \frac{2}{r_o^2 - r_i^2} Q, \tag{A.4}$$

The fact that the thermal stress does not depend on the specific temperature profile within the tube simplifies the problem, as the thermal stress at a given time depends only on the total energy transferred from the hot gas to the tube wall up to that time.

In the fast detonation regime, the time scale of the peak pressure loading is much shorter ($\approx$ 100 μs) than the characteristic time scale of the thermal loading ($\approx$ 100 ms). Only in the slow combustion regime are the time scale of the pressure rise and the thermal loading comparable. Furthermore, the thermal loading is negligible in the fast combustion regime because the peak strain caused by the pressure loading is up to 40 times higher than that caused by thermal stresses. The strain caused by the thermal loading is too small and occurs too late to influence the peak strain measurements in the fast combustion regime.

In general, the strain measured on the outer surface is also a function of the overall tube temperature. When the tube temperature is increased uniformly throughout the wall thickness, the entire tube expands uniformly and no thermal stresses are induced. Nevertheless, the strain resulting from the thermal expansion is detected by the strain gauges. In this case, there is thermally induced strain without thermally induced stress. For the analysis shown above, the outer surface temperature was taken as the reference temperature for the assumed temperature profile within the tube ($\tau(r = r_o) = 0$). The temperature on the outer surface of the tube increases in the experimental setup during a series of ten shots approximately up to 32°C, 10°C above room temperature. This effect does not influence the strain gauge measurements over a series of experiments for two reasons. The strain gauge circuits are balanced prior to each experiment and the gas temperature of the hot combustion products is large compared to the slight increase of the tube temperature, causing a negligible effect on the heat transfer rate from the gas to the tube.

Appendix B

Reflected Shock Bifurcation

Let us examine the case of a one-dimensional detonation propagating through a closed conduit as shown in Fig. B.1. The detonation induces a flow velocity in the gas. For

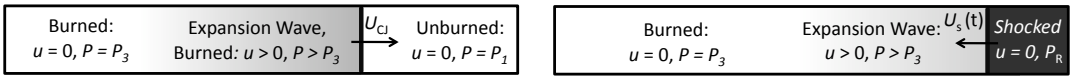

(a) (b)

Figure B.1: Ideal, one-dimensional (a) detonation and (b) reflection in a closed tube.

an ideal, one-dimensional detonation starting at $x = 0$, the velocity is given by

$$u(x,t) = \begin{cases} 0 & \text{if } v_{CJ} < x/t < \infty \\ \dfrac{2c_3}{\gamma+1}\left(\dfrac{x}{c_3 t} - 1\right) & \text{if } c_3 < x/t < U_{CJ} \\ 0 & \text{if } 0 < x/t < c_3 \end{cases} . \tag{B.1}$$

In a real flow, there will be some boundary layer of thickness $\delta(x)$ at the wall wherein the velocity is less than that given by Eqn. (B.1). Following the theory developed by Mark (1958), let us assume the profile shown in Fig. B.2 where the flow is completely stationary in the boundary layer, $y < \delta(x)$, and unaffected outside, $y > \delta(x)$. That is, we take

$$u(x,y,t) = \begin{cases} \dfrac{2c_3}{\gamma+1}\left(\dfrac{x}{c_3 t} - 1\right) & \text{if } c_3 < x/t < U_{CJ} \text{ and } y > \delta(x) \\ 0 & \text{else.} \end{cases} \tag{B.2}$$

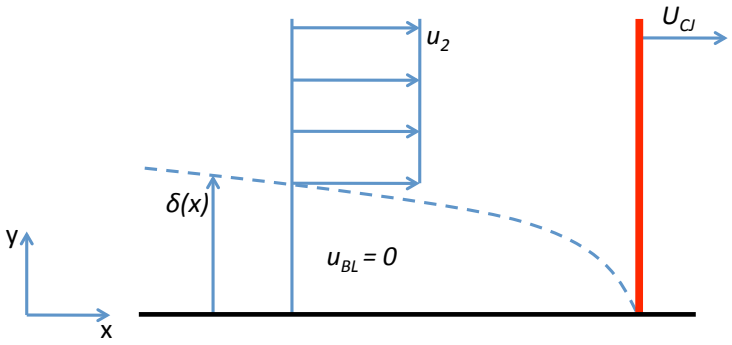

Figure B.2: Assumed velocity profile in the boundary layer for Mark's analysis.

We could clearly choose a more complicated and more accurate form for the flow in the boundary layer, but by considering this simplistic situation we will be able to develop and apply an elementary criterion for bifurcation of the reflecting shock.

Once the detonation reaches the end wall of the conduit, a reflected shock is created to bring the flow to rest. This shock will propagate into the region described in Fig. B.2 where it may result in shock bifurcation. Mark (1958) argues that the reflected shock will bifurcate if $P'_{0,BL} < P_4$ (see Fig. B.3). That is, bifurcation will

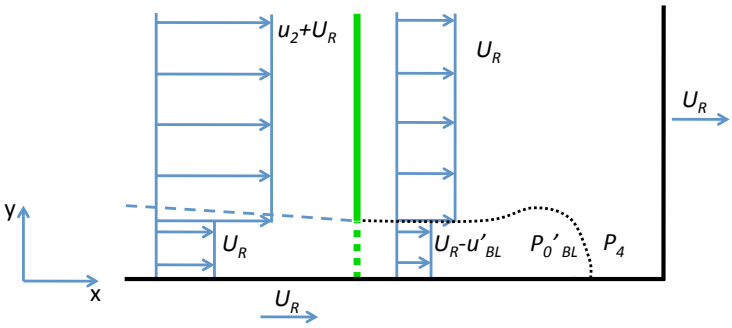

Figure B.3: Reference frame used in calculations.

occur if the stagnation pressure in the boundary layer behind the reflecting shock is less than the pressure in the main flow behind the shock. If this were the case, then even in stagnation this fluid will not reach the pressure of the fluid outside the boundary layer behind the shock and will thus be swept along with the reflecting shock.

Immediately after a detonation reflects, the pressure at the reflecting end wall is

$P_4 = 2.4P_{CJ}$ (Browne et al., 2008). Thus, in order to apply our bifurcation criterion, it remains to determine $P'_{0,BL}/P_{CJ}$. Let us now turn to the shock fixed reference frame shown in Fig. B.3. Here, U_R is the speed of the reflected shock and u_2 is the speed of the fluid induced by the detonation; immediately after detonation reflection, we have $u_2 = u_{CJ}$, the maximum induced velocity.

The shock velocity may be numerically determined if we ignore the boundary layer as done in Chapter 4. If we presume that this solution still applies outside the boundary layer, then the shock speed U_R is known. However, the mach number of the fluid in the boundary layer is still unknown because the temperature of the boundary layer is unknown and the sound speed depends on the temperature through

$$a = \sqrt{\gamma RT} \tag{B.3}$$

where

$$R = \frac{\widetilde{R}}{M} = \frac{8.314 \text{ J/mol K}}{44.0095 \text{ g/mol} + 18.0152 \text{ g/mol}} = 134 \text{ J/kg K} \tag{B.4}$$

for completely combusted ethylene-oxygen. We also know

$$M_R = \frac{U_R}{a_{BL}}. \tag{B.5}$$

Hence we have two cases depending on the temperature:

1. $U_R < a_{BL}$. The flow in the boundary layer is subsonic and may be assumed to undergo an isentropic deceleration process. The pressure ratio through the region underneath the shock is hence given by

$$\frac{P'_{0,BL}}{P_{CJ}} = \left(1 + \frac{\gamma - 1}{2} M_R^2\right)^{\gamma/(\gamma-1)} \tag{B.6}$$

   where we've taken the pressure in front of the shock to be the CJ pressure.

2. $U_R > a_{BL}$. The flow in the boundary layer is supersonic and is processed by a

shock. This yields

$$\frac{P'_{0,BL}}{P_{CJ}} = \left(\frac{\gamma+1}{2}M_R^2\right)^{\gamma/(\gamma-1)} \left(\frac{2\gamma}{\gamma+1}M_R^2 - \frac{\gamma-1}{\gamma+1}\right)^{1/(1-\gamma)}. \tag{B.7}$$

These equations are plotted in Fig. B.4 for varying values of M_R with $\gamma = 1.15$—

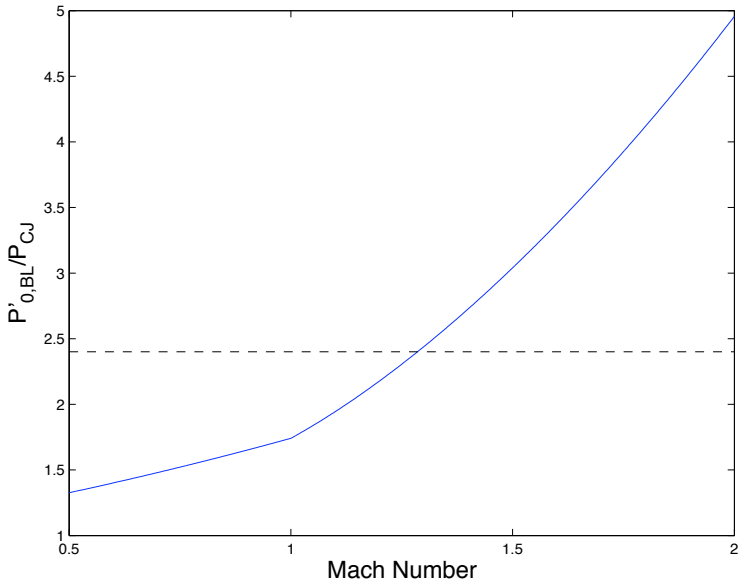

Figure B.4: Theory predicts bifurcation for $M_R < 1.3$.

the ratio of specific heats behind the detonation wave computed for a half-bar initial pressure detonation of stoichiometric ethylene-oxygen. We see that the critical value is $M_R = 1.3$. Following the model described in Chapter 4, we predict an initial reflecting shock speed of $U_R = 886$ m/s. Using this value for U_R and the critical value for M_R, we may therefore determine a critical sound speed and a critical temperature in the boundary layer for which bifurcation will occur:

$$a_{BL,crit} = \frac{U_R}{M_R} = 687 \text{ m/s}$$
$$T_{BL,crit} = \frac{a_{BL,crit}^2}{\gamma R} = 3063 \text{ K}.$$

Appendix C

Material Testing

Tension tests of a specimen cut out of a spare tube were carried out by Stork Materials Testing & Inspection - Huntington Beach, CA. The test results are reproduced below.

STORK®
Materials Technology

Stork Materials Testing & Inspection

Material Testing and Non-Destructive Testing

Contact: Chris Krok
Caltech
138-78 CALTECH

PASADENA, CA 91106

15062 Bolsa Chica
Huntington Beach, CA 92649
USA

Telephone :(714) 892-1961
Telefax :(714) 892-8159
Website :www.storksmti.com

Date: 12/19/2005 **P.O. No.:** Verbal/Chris Krok **W/O No.:** CAL043-12-08-87049-1

TEST CERTIFICATE

Desc.:	Steel Tubing, 5" Dia. x 0.062 Wall Thickness x 5" Length

FULL TENSILE

Specification:	ASTM A513-00 TY.2, COLD ROLLED C1010
Test Method:	ASTM E 8-04

Sample No.	Dimension	Area	Yield Strength At 0.2% Offset (psi)	Ultimate Tensile Strength (psi)	% Elongation in " (4D)
1	.055x.500	.0275	49,200	63,500	33.0
	Requirements:		32,000 MIN	45,000 MIN	15% MIN

MATERIAL CONFORMS TO SPECIFICATION

Respectfully submitted

Lynn Ho
Senior Quality Administrator

The information contained in this certification represents only the material submitted and is certified only for the quantities tested. Reproduction except in full is reserved pending written approval. The recording of false, fictitious, or fraudulent statements or entries on the certificate may be punishable as a felony under federal law. All testing was performed in a mercury free environment. A2LA accreditation No. 0093-01 and 0093-02
Stork Materials Testing and Inspection is an operating unit of Stork materials Technology B.V., Amsterdam, The Netherlands, which is a member of the Stork group

Test Number 6233

Flat, 2 In. Full Tensile and 5K, AS 7101

Specimen ID Sample #1

Work Order # CAL043.87049

Report Number 3844

Test Date 12/16/2005 7:10:09 AM

ACCEPTED

	Test Results	
Yield (lbs)	1,354	49.200
Yield (psi)	49,224.16	
Tensile (lbs)	1,745	63,500
Tensile (psi)	63,446.05	
Total Elong (%)	32.65	33%
Modulus (msi)	21	
Yld @.5%		
Yld .5% (psi)		
Thick (In)	0.0550	
Width (In)	0.5000	
Area (In²)	0.0275	

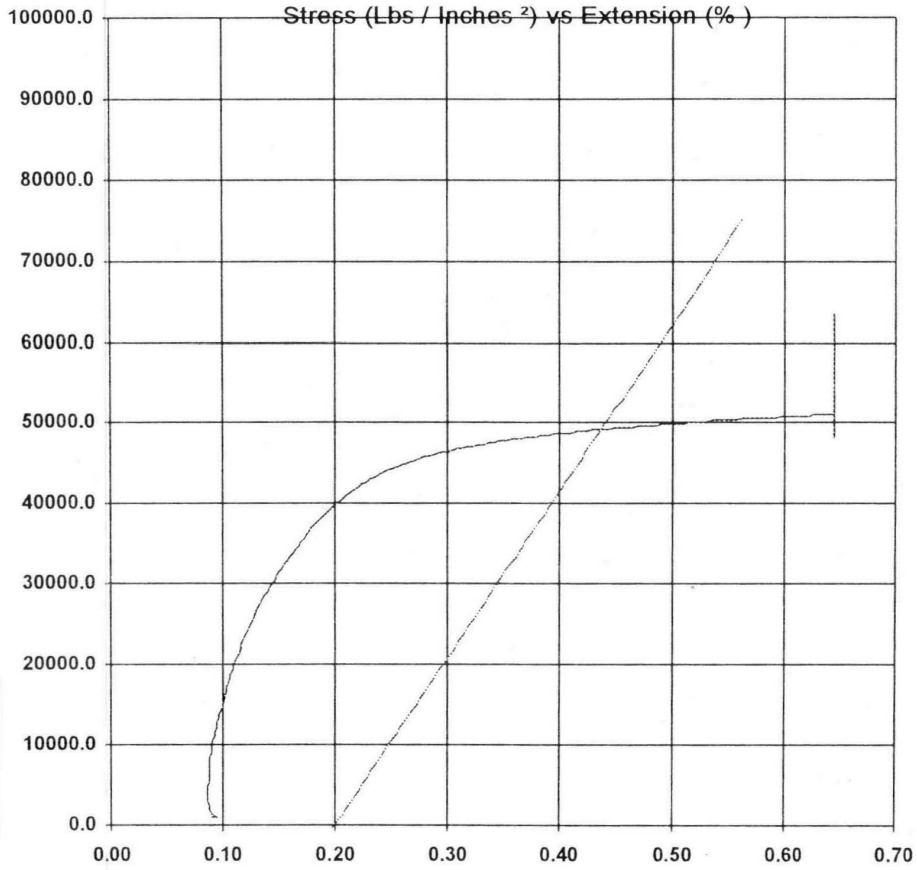

Testing Machine	SFM-120
Load Cell S/N (SB4885), Units (Lbs)	5000
Preload Value (Lbs)	20
Crosshead Speed (Inches / min) or Rate	0.5
Extension or Position Measured by	EZ.1-2 (3204)

By : _____ Date : _____

Customer Name	Cal-Tech	Purchase Order		Operator	Jorge Bocanegra
Heat No.		Test Method	ASTM E 8-04		
Work Order #	CAL043.87049				
				Spec #	

Template No 153	16-Dec-05	Gage Length	2
Stork M.T.			

Appendix D

Drawings

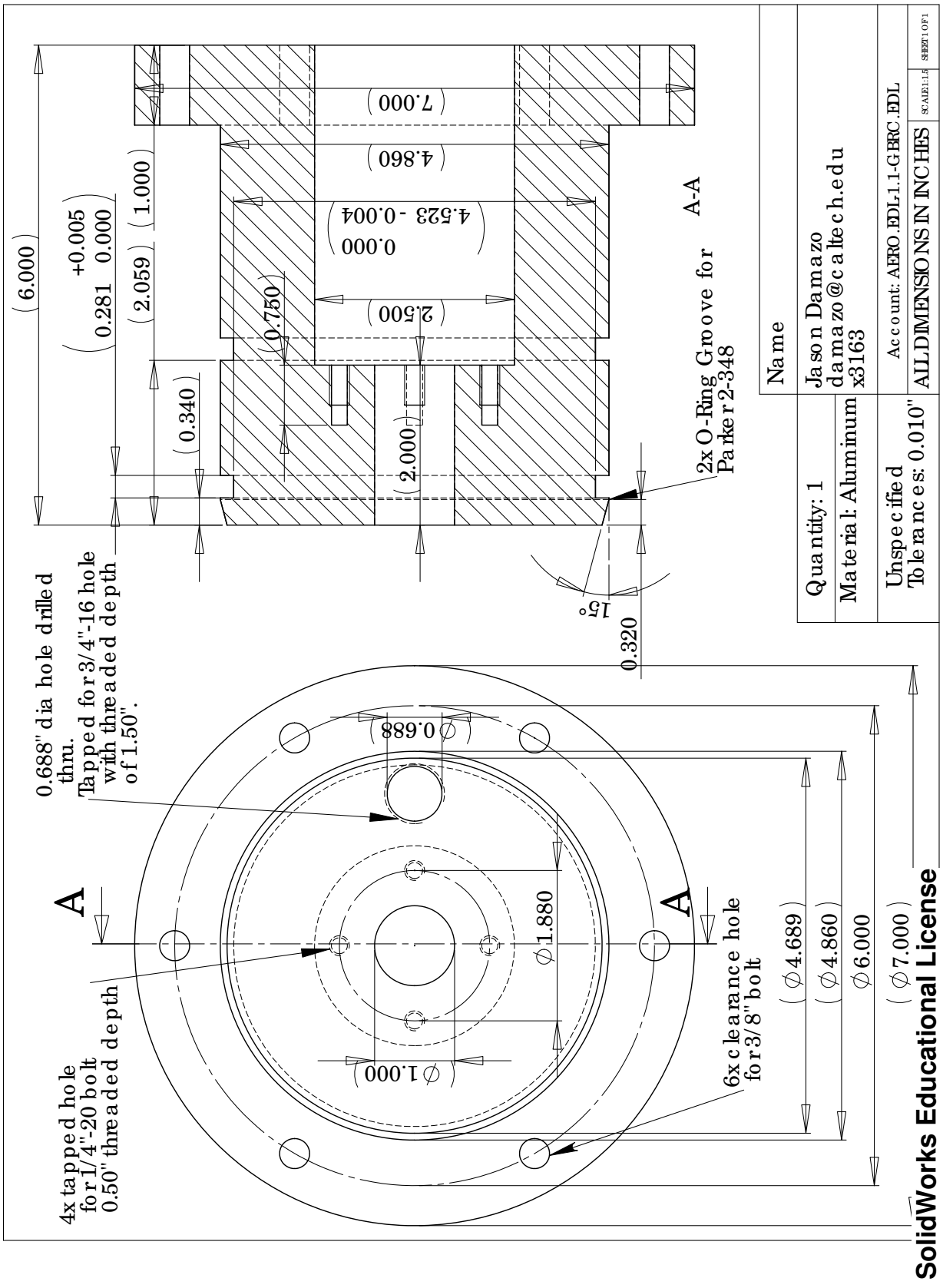

Figure D.1: End plug.

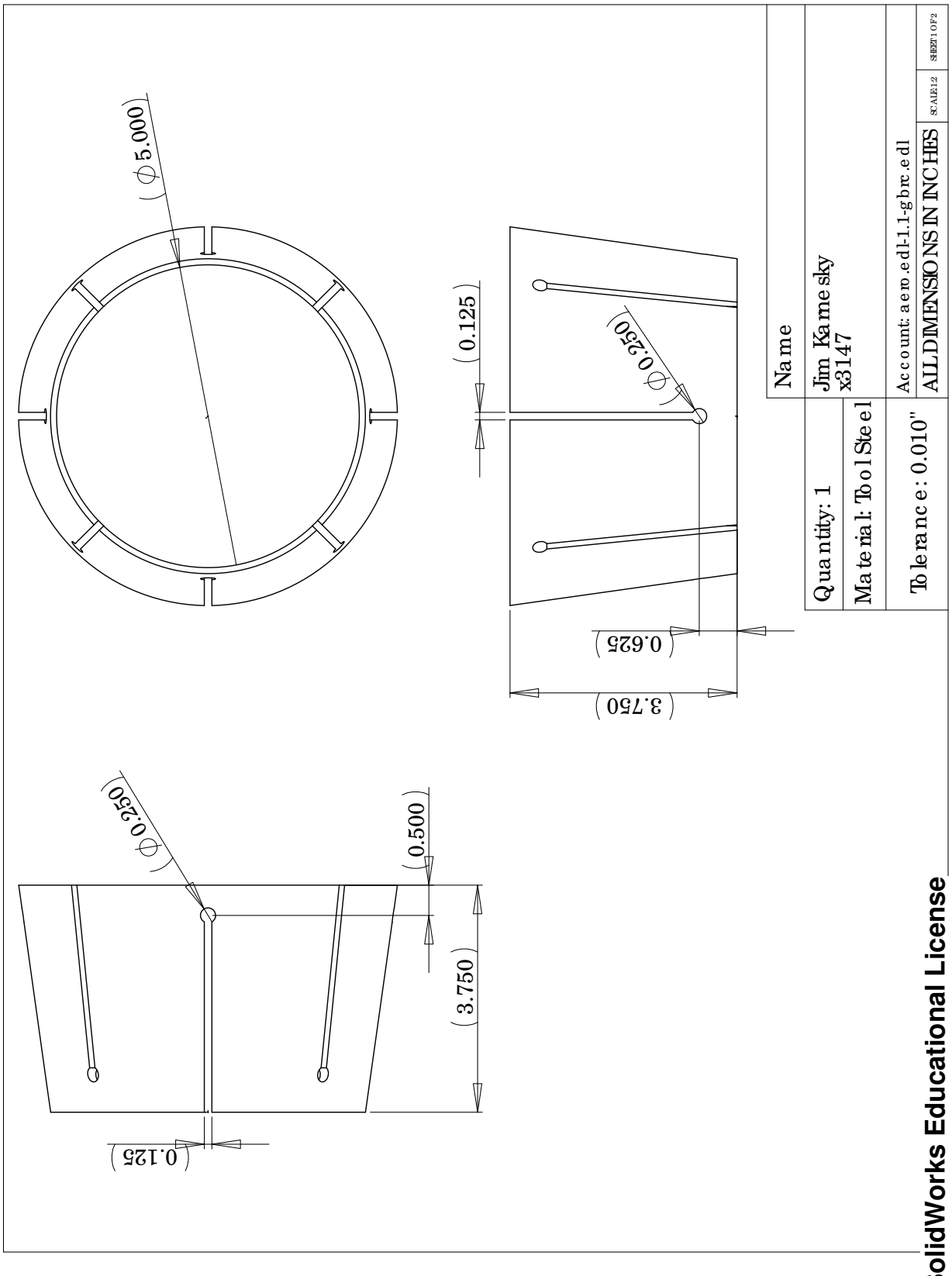

Figure D.2: Collet

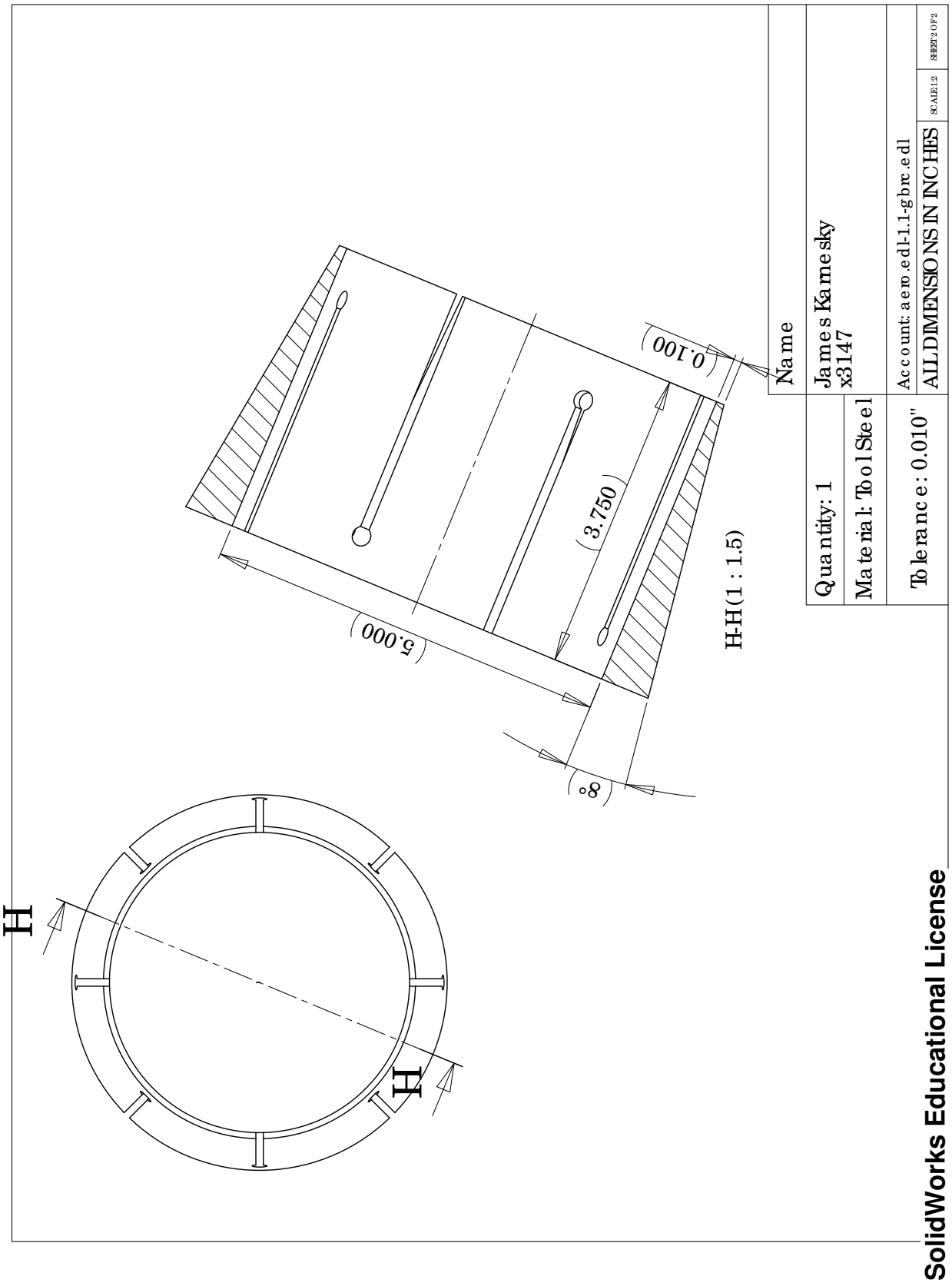

Figure D.3: Collet

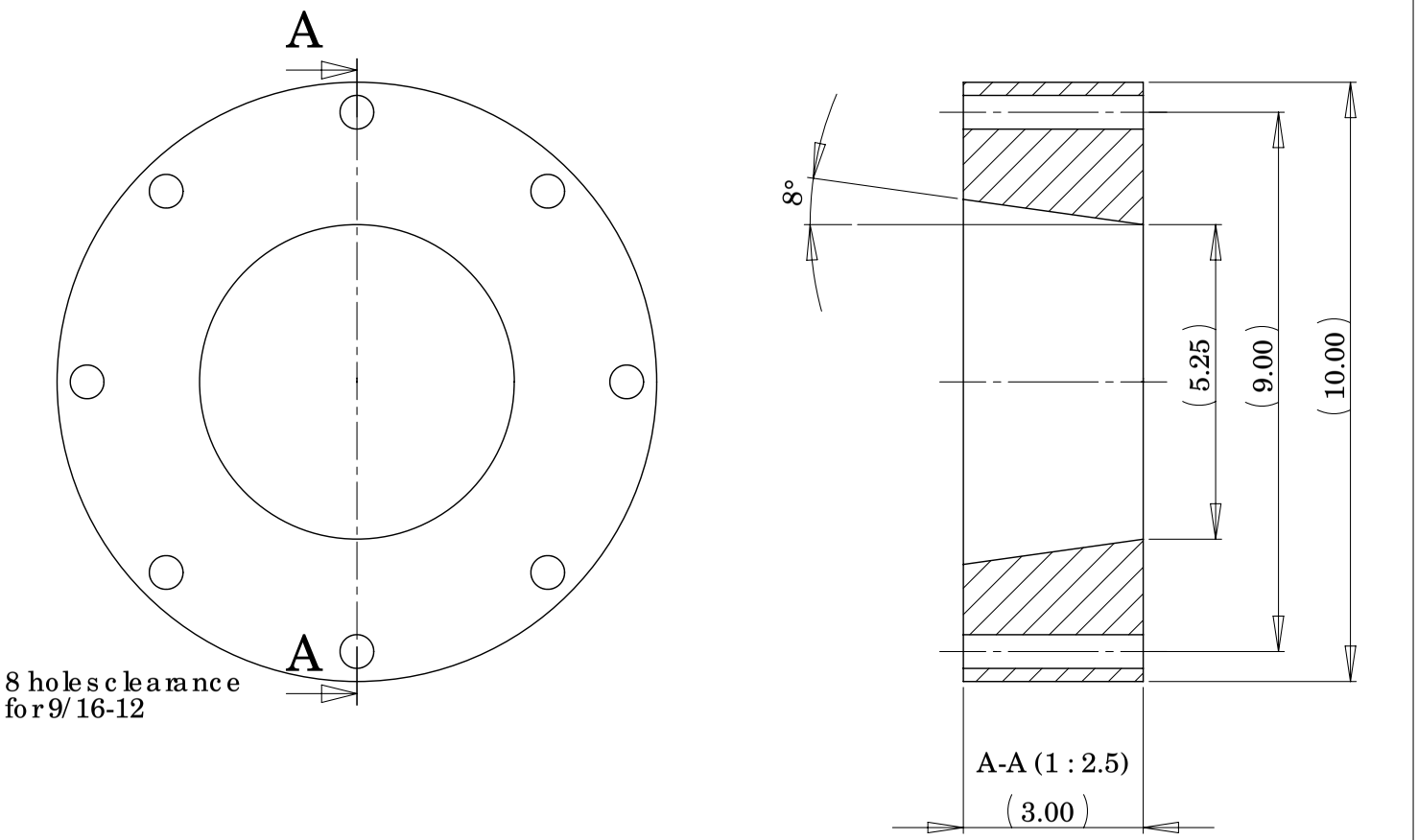

SolidWorks Educational License
Instructional Use Only

Figure D.4: Collet retaining ring.

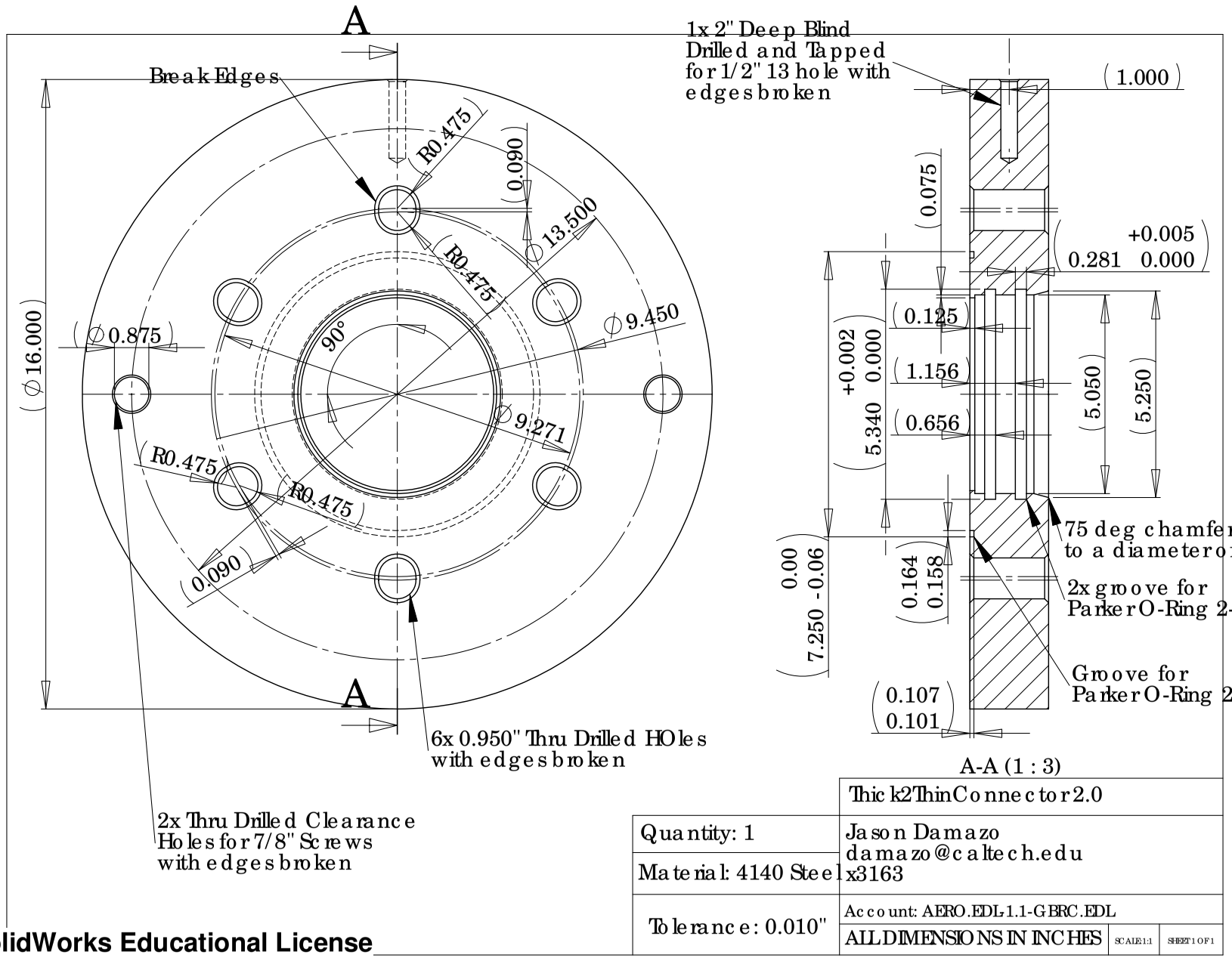

SolidWorks Educational License
Instructional Use Only

Figure D.5: Driver to specimen connector flange.

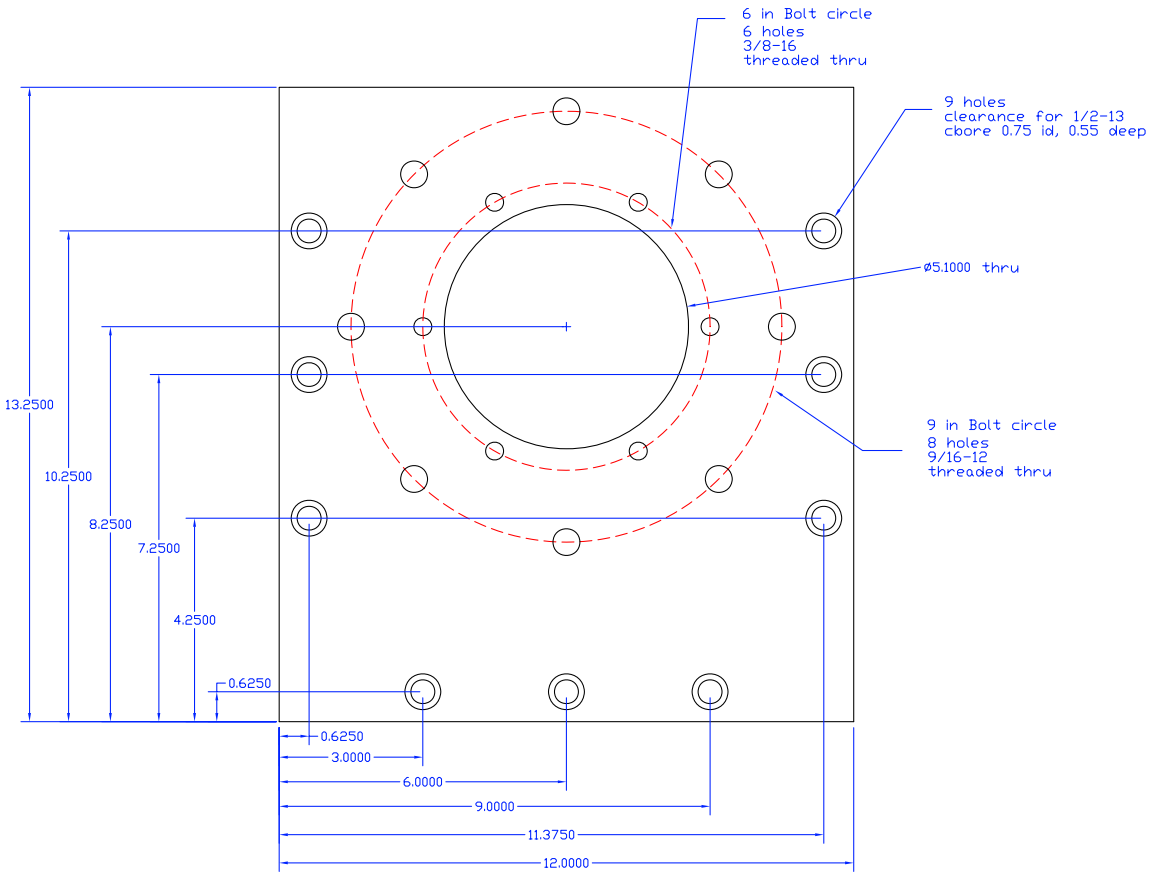

Figure D.6: End plate with bolt holes for end plug and retaining ring.

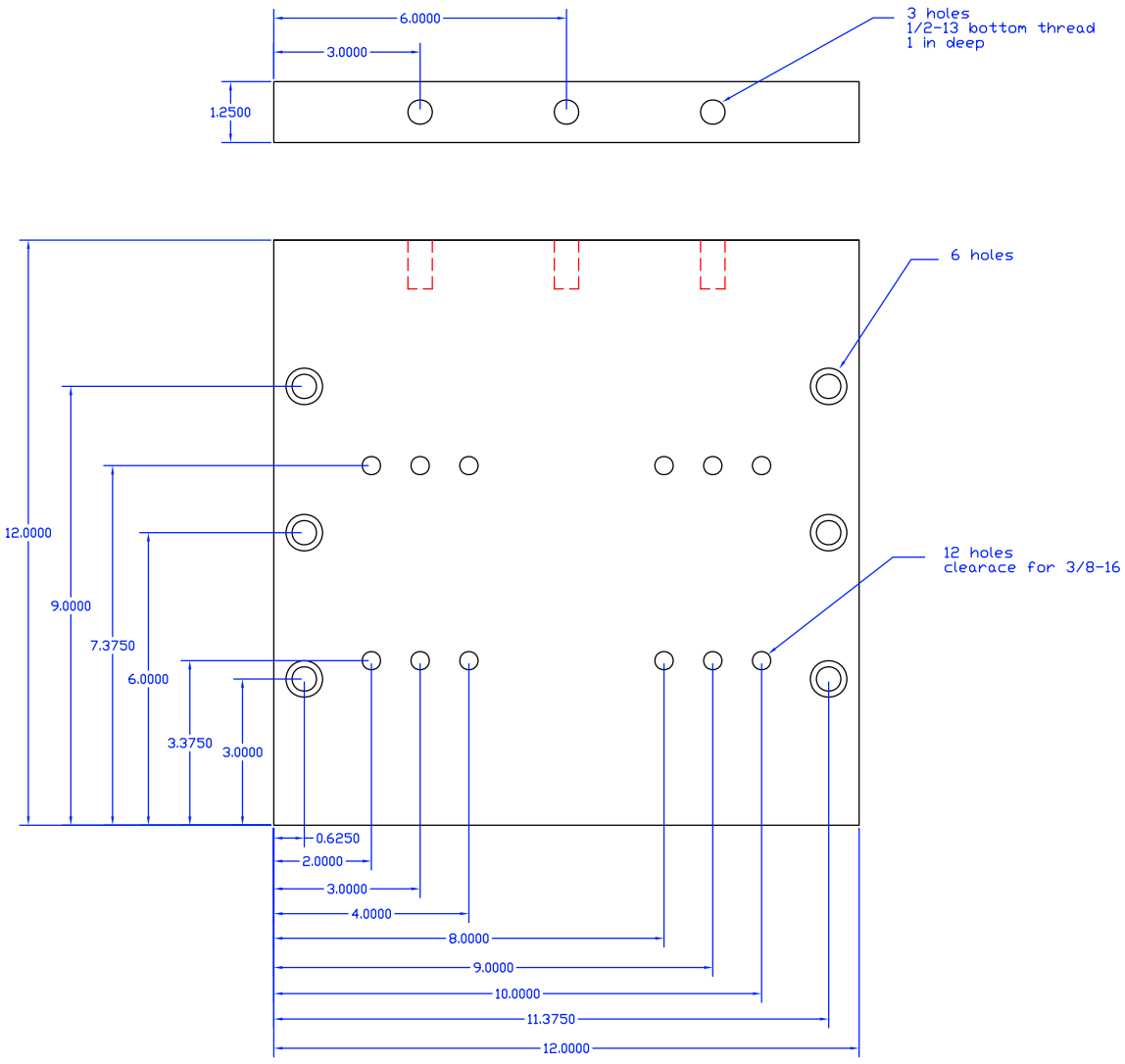

Figure D.7: Bottom plate for old support.

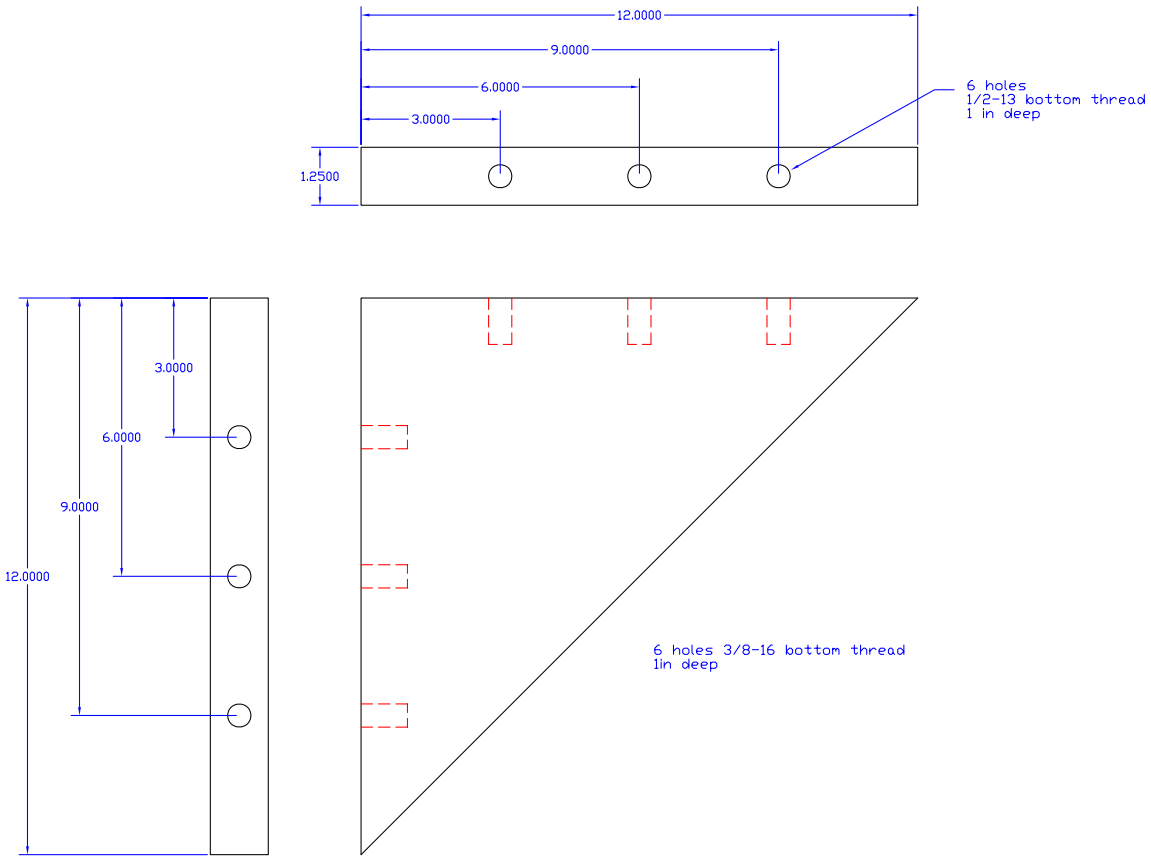

Figure D.8: Angle bracket for old support.

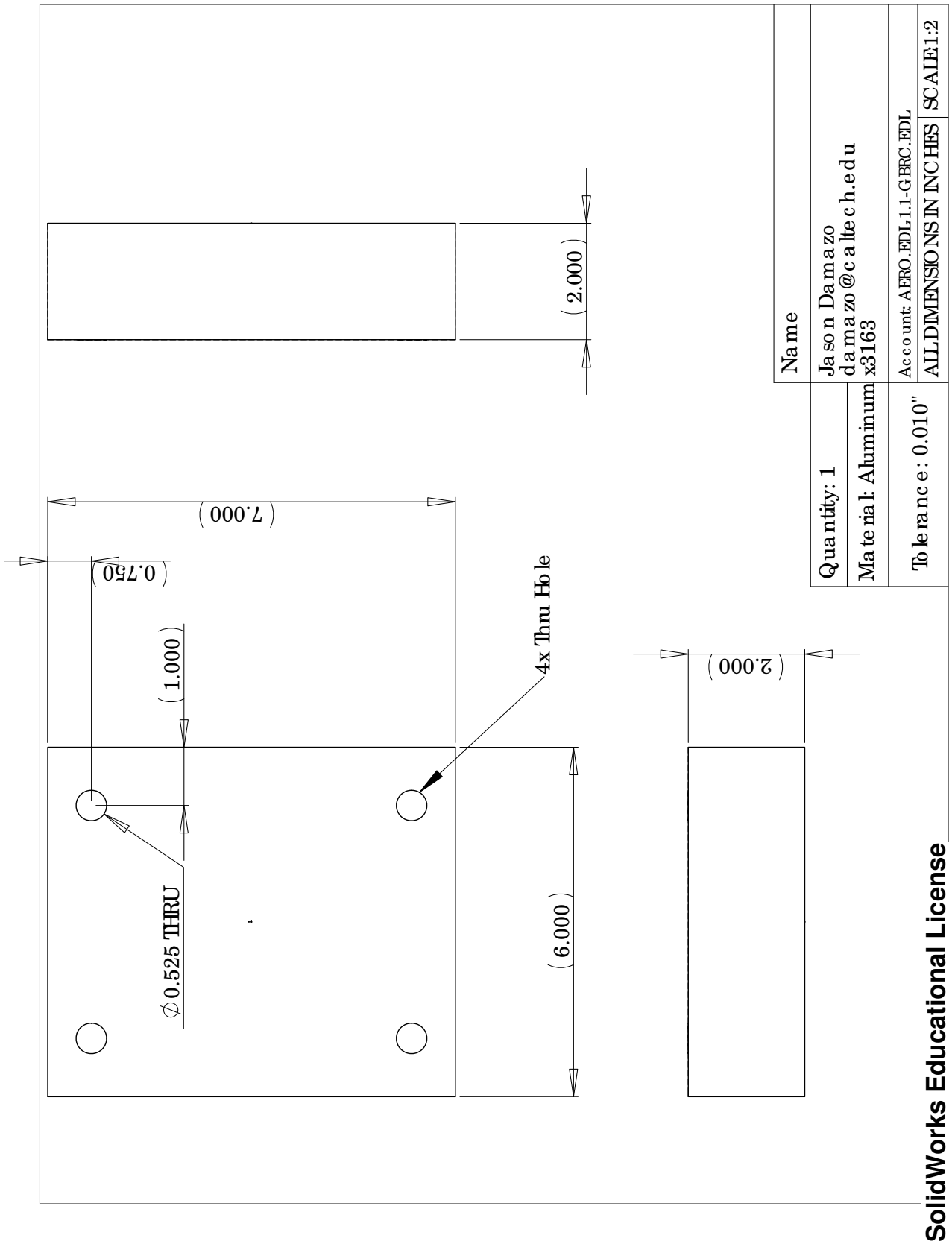

Figure D.9: Old end support mount.

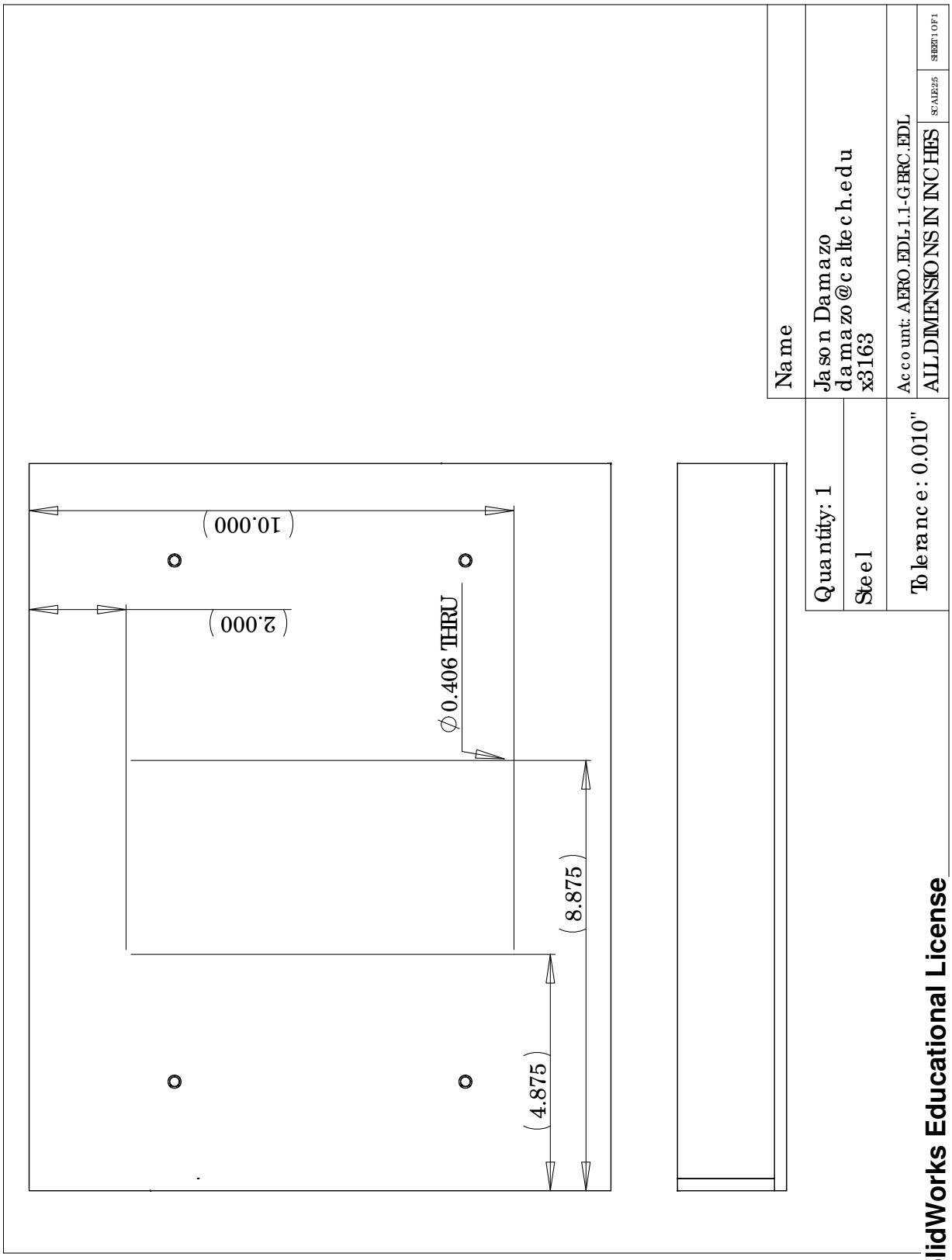

Figure D.10: Old end support tray.

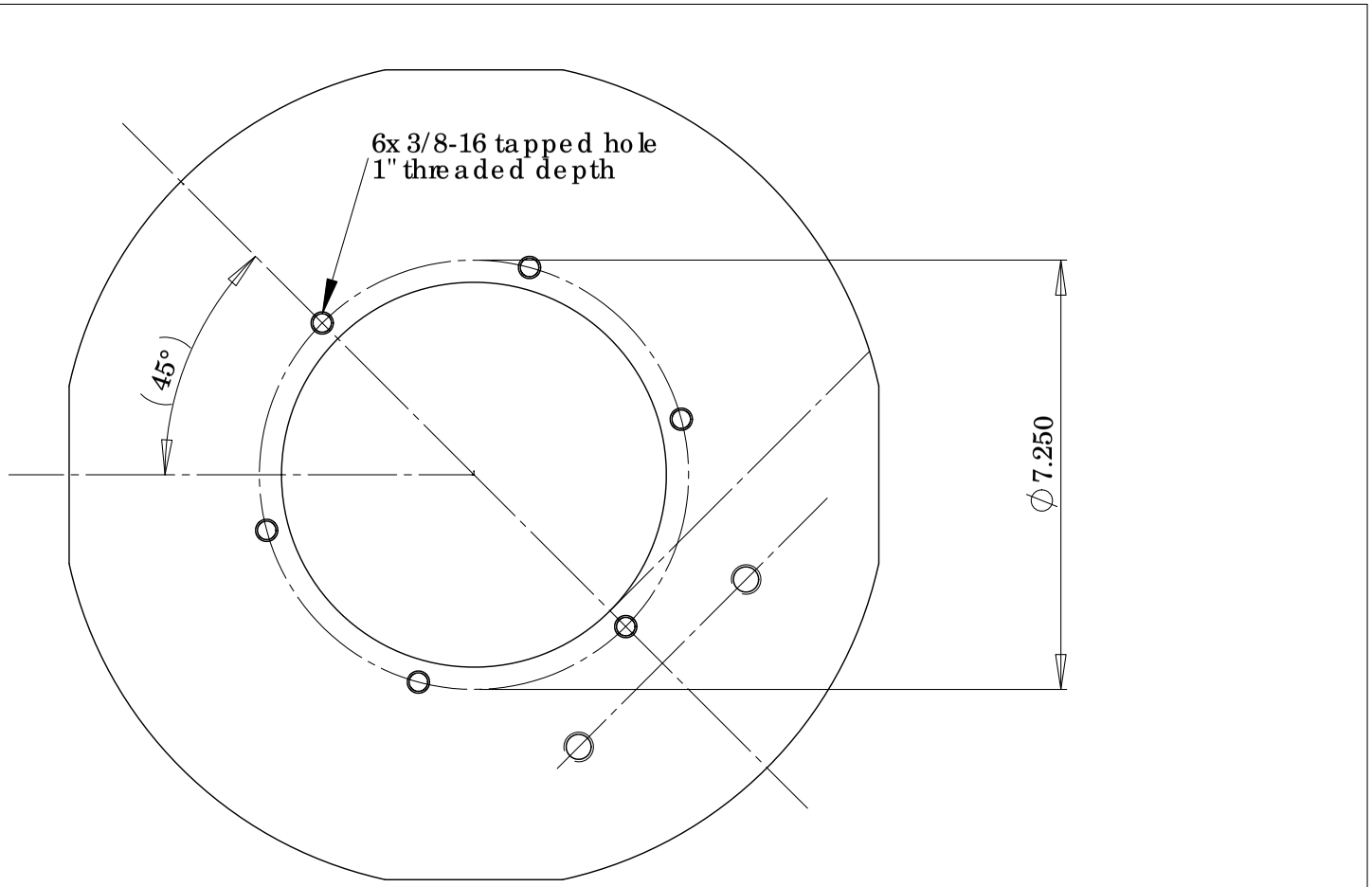

	Name
Quantity: 1	Jason Damazo damazo@caltech.edu x3163
Material: Aluminum	
Tolerance: 0.010"	Account: AERO.EDL.1.1-GBRC.EDL
	ALL DIMENSIONS IN INCHES — SCALE:1:1 — SHEET 1 OF 1

SolidWorks Educational License
Instructional Use Only

Figure D.11: Hyjet flange with bolt circle for end support plate.

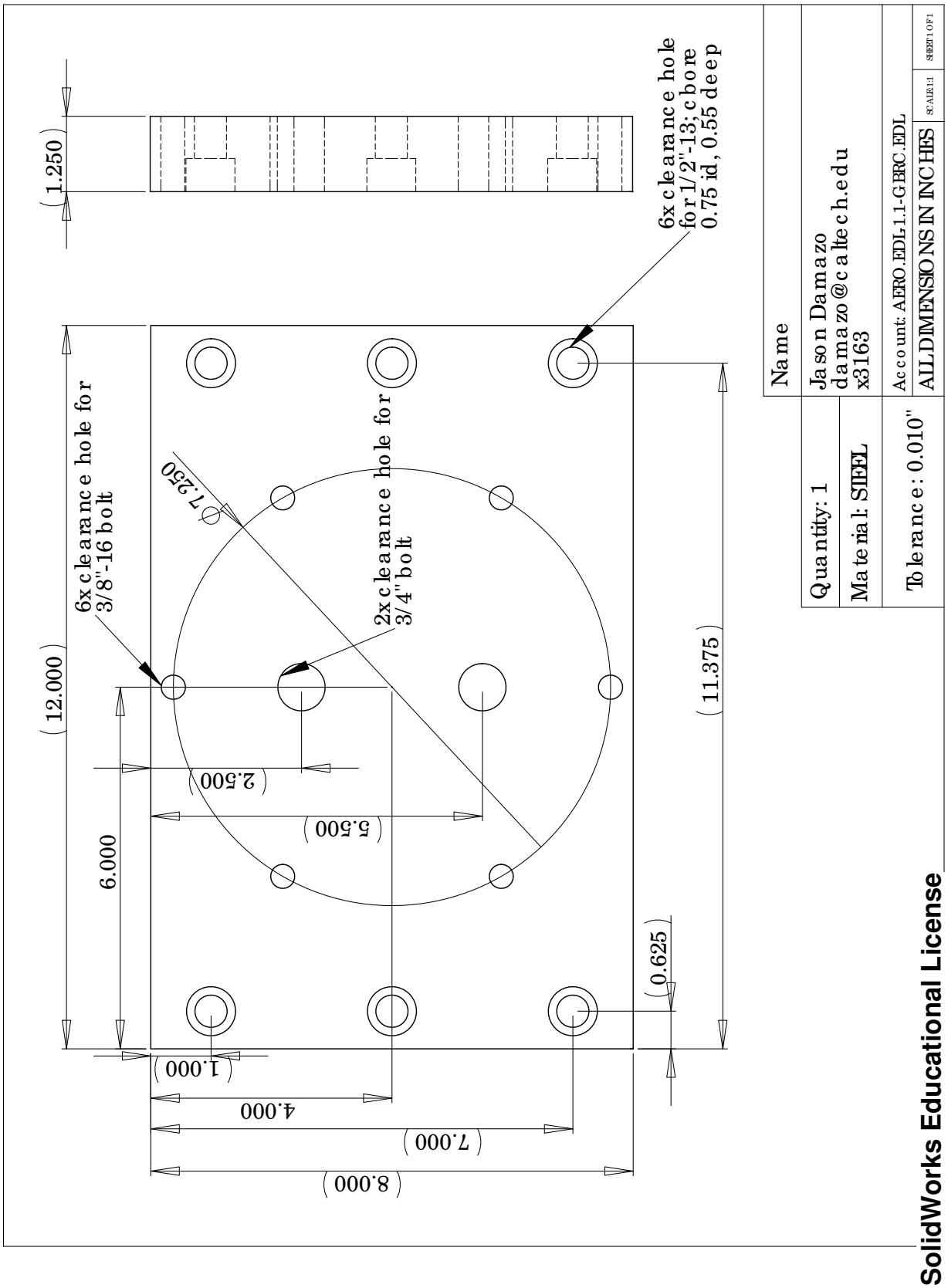

Figure D.12: Support plate for end braces.

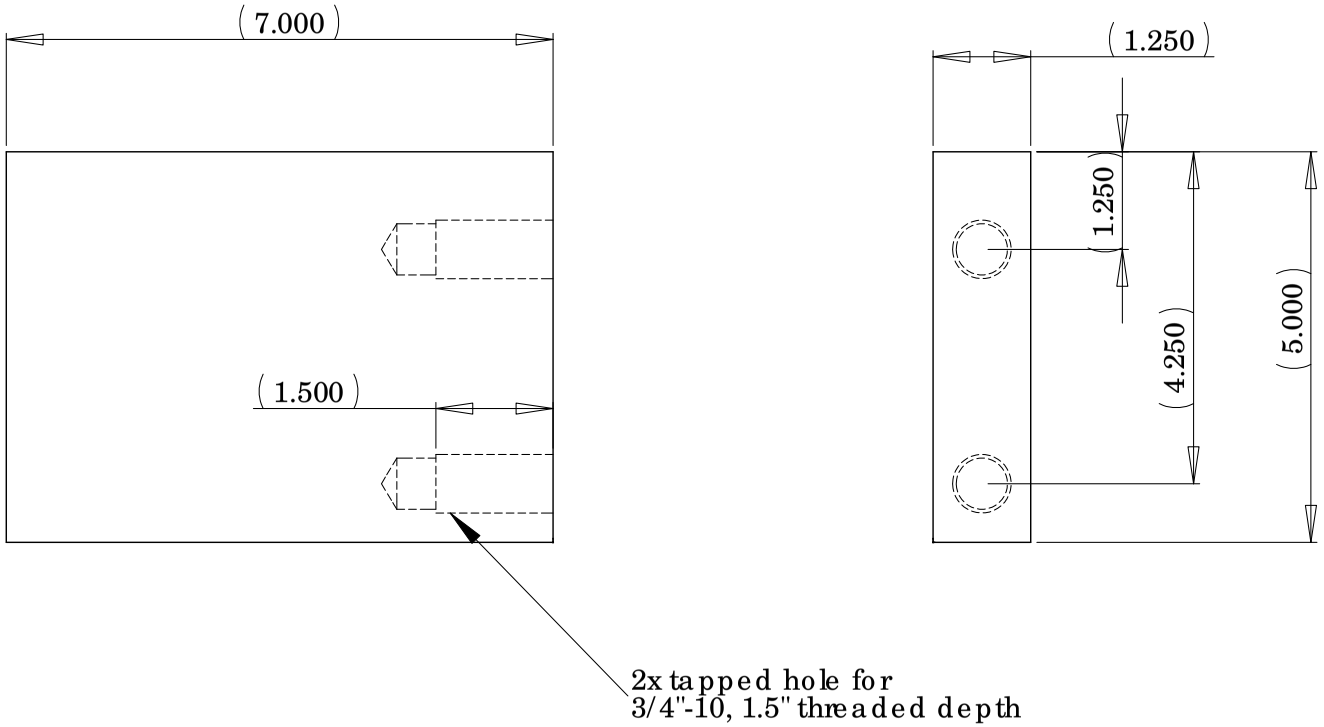

	Name
Quantity: 1	Jason Damazo damazo@caltech.edu x3163
Material: STEEL	
Tolerance: 0.010"	Account: AERO.EDL.1.1-GBRC.EDL
	ALL DIMENSIONS IN INCHES — SCALE:1:1 — SHEET 1 OF 1

SolidWorks Educational License
Instructional Use Only

Figure D.13: Center brace for new support.

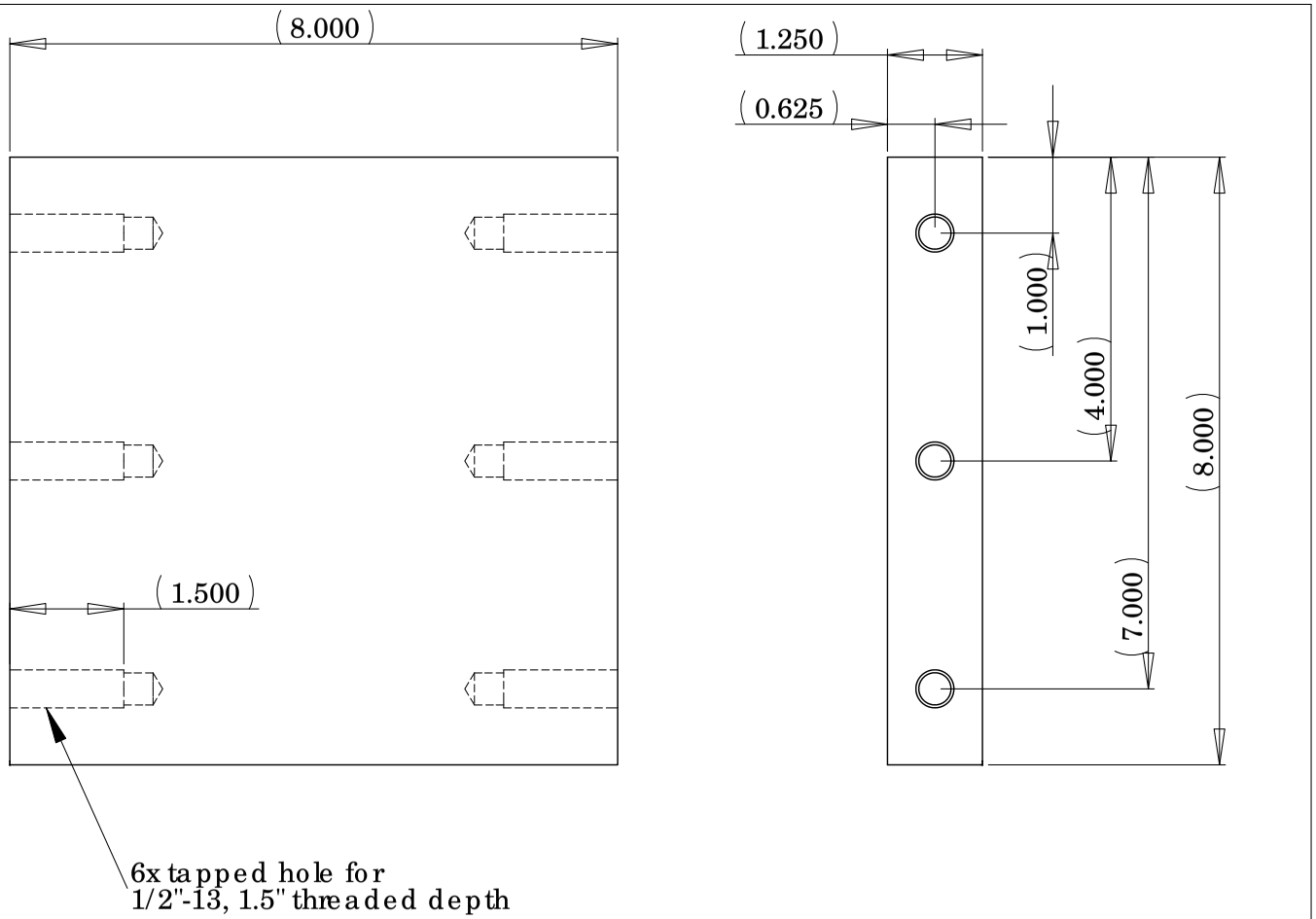

SolidWorks Educational License
Instructional Use Only

Figure D.14: Side braces for new support.

Appendix E

Data for aluminum tubes

E.1 Series 1

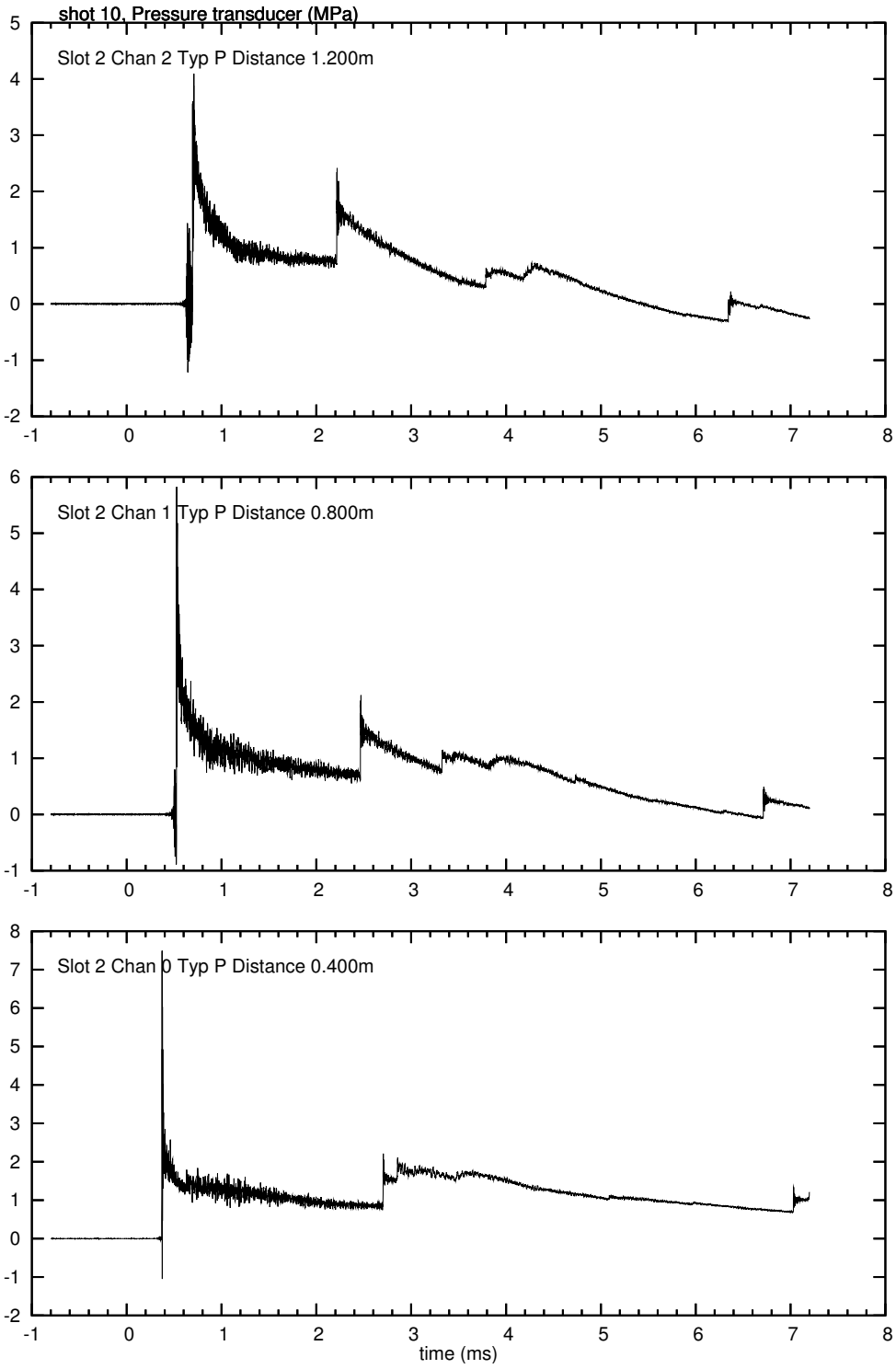

Figure E.1: Pressure traces for shot 10

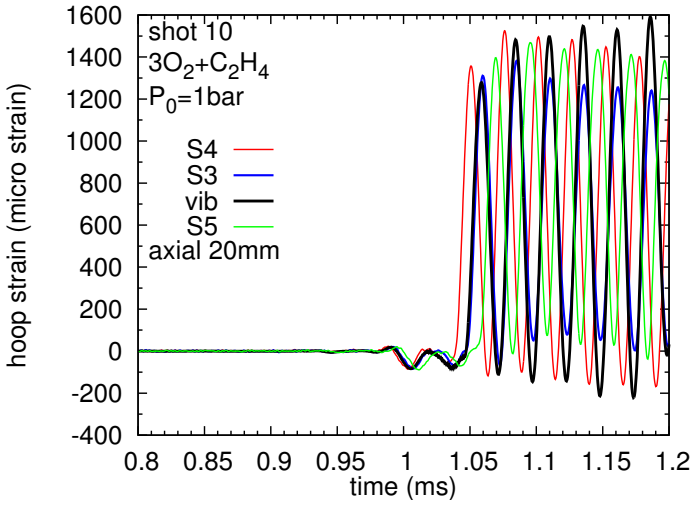

Figure E.2: Axial location hoop strain comparisons for shot 10.

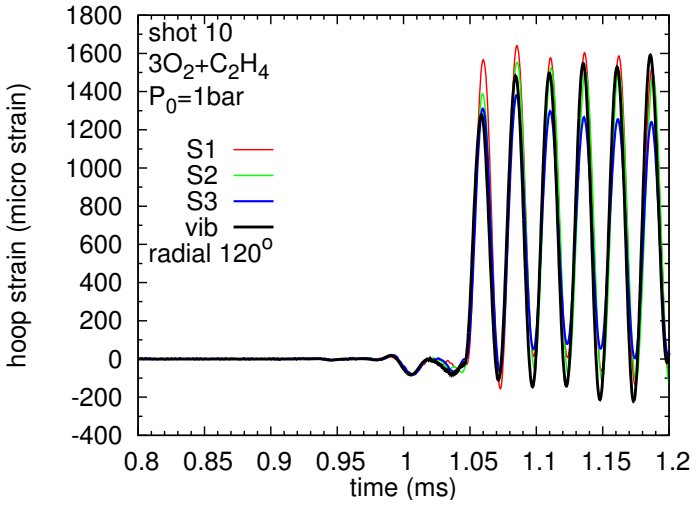

Figure E.3: Radial strain comparisons for shot 10

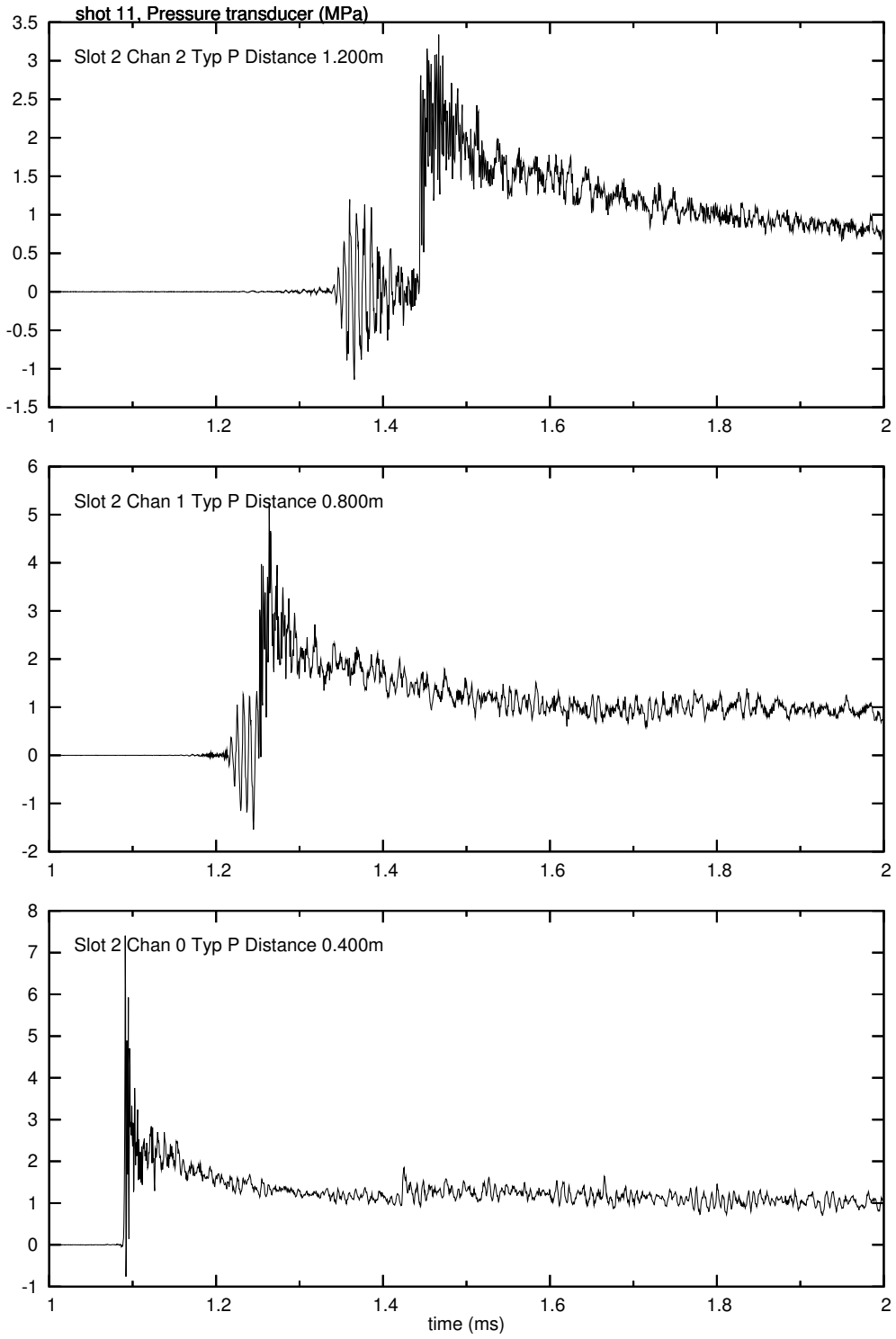

Figure E.4: Pressure traces for shot 11

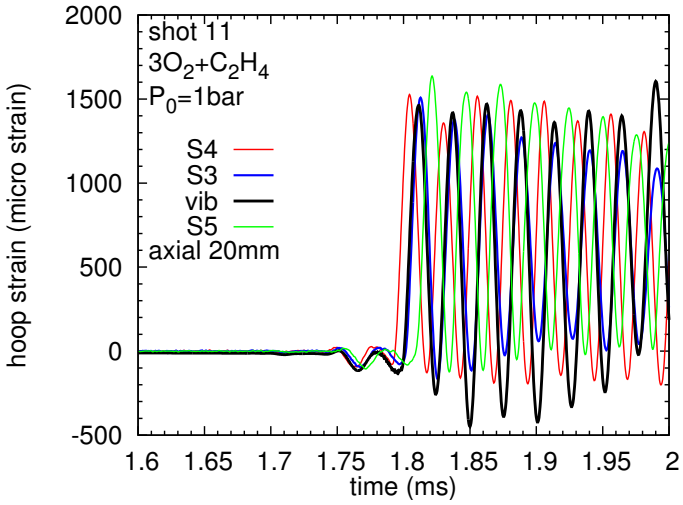

Figure E.5: Axial location hoop strain comparisons for shot 11.

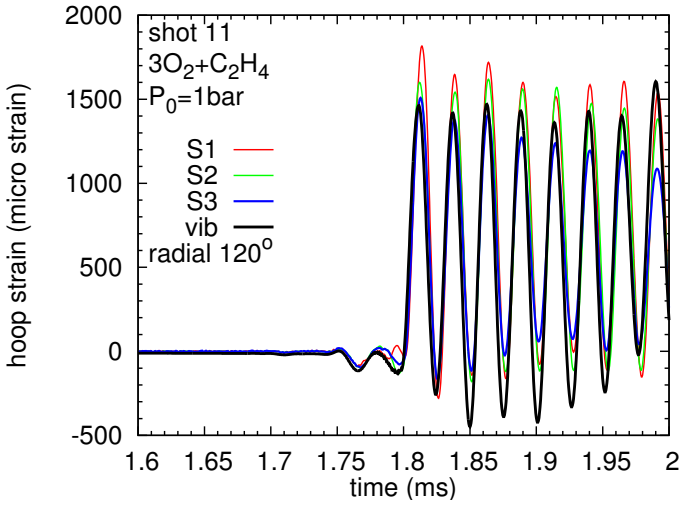

Figure E.6: Azimuthal location hoop strain comparisons for shot 11

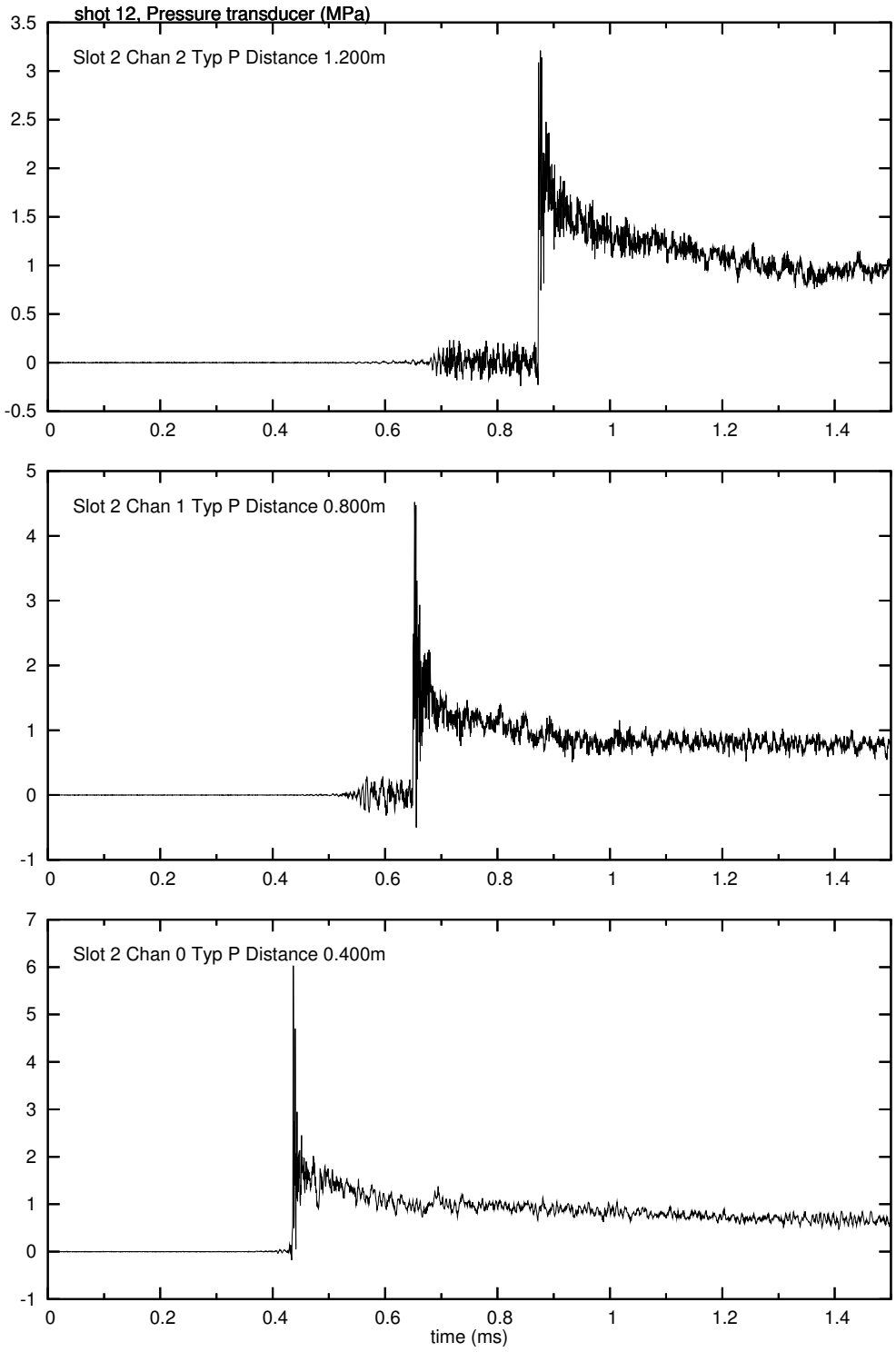

Figure E.7: Pressure traces for shot 12

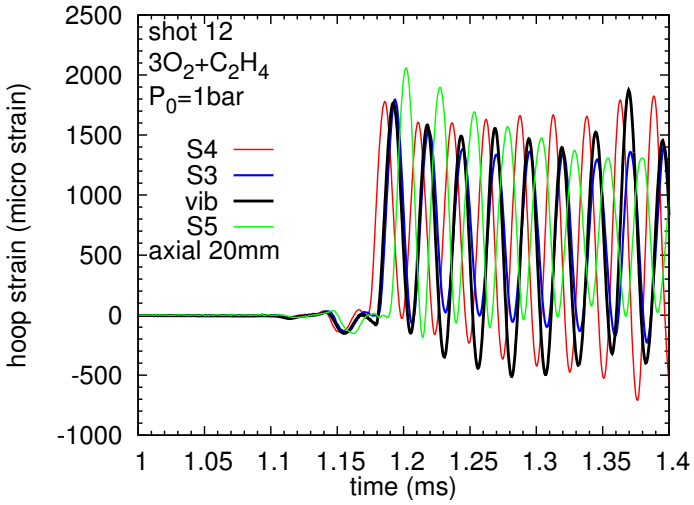

Figure E.8: Axial location hoop strain comparisons for shot 12.

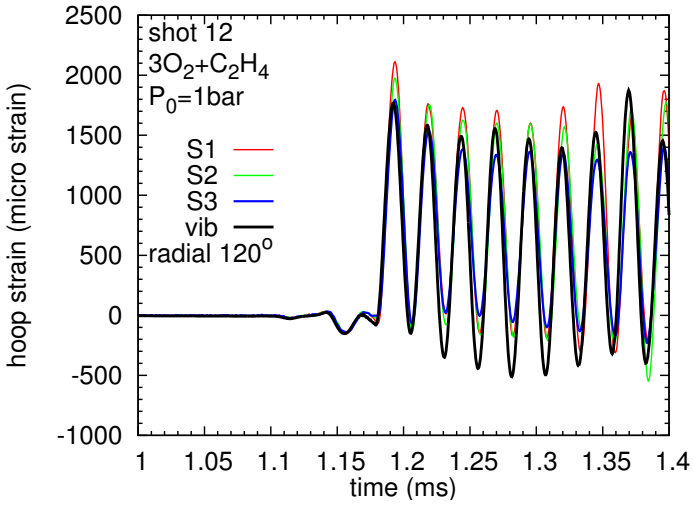

Figure E.9: Azimuthal location hoop strain comparisons for shot 12

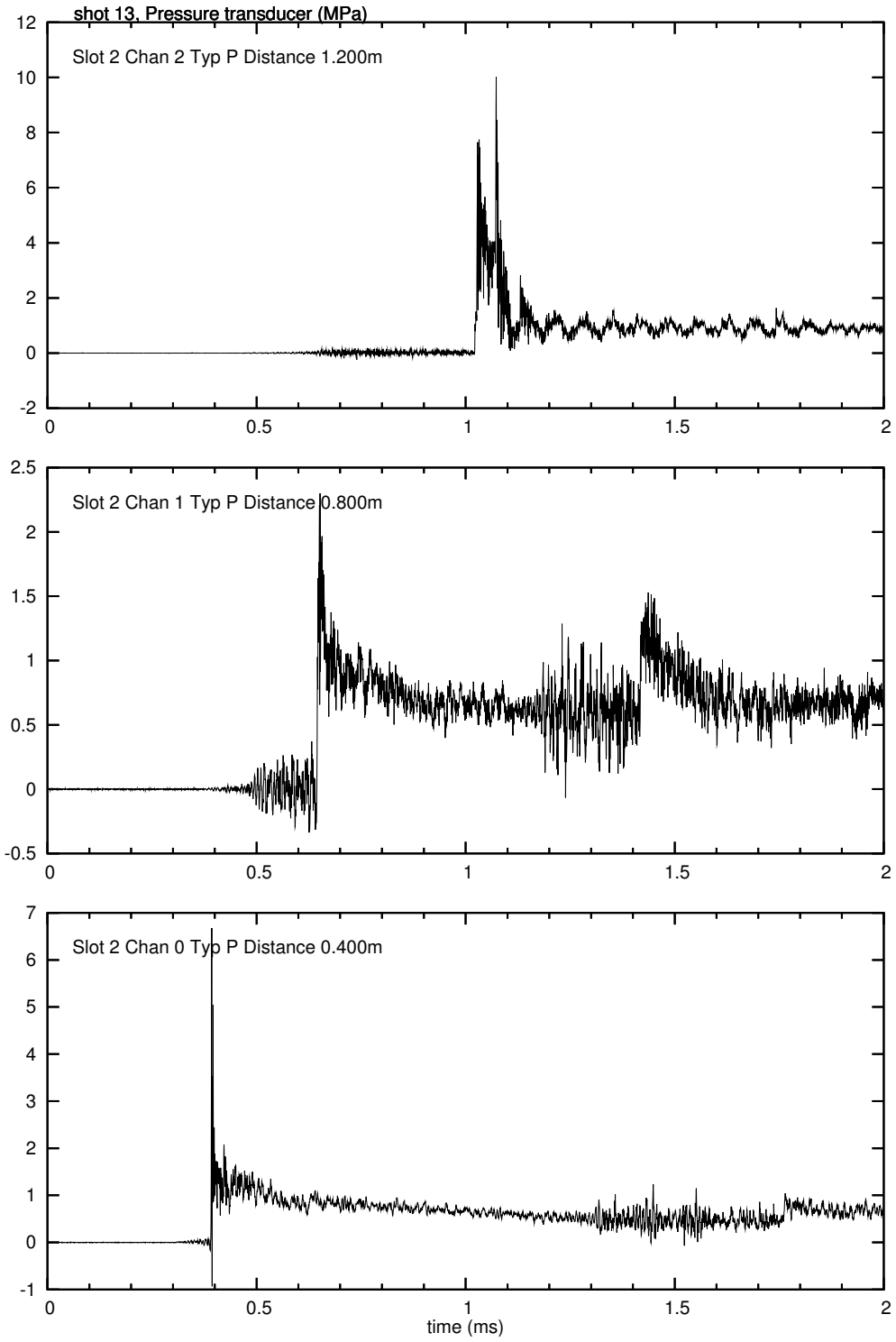

Figure E.10: Pressure traces for shot 13

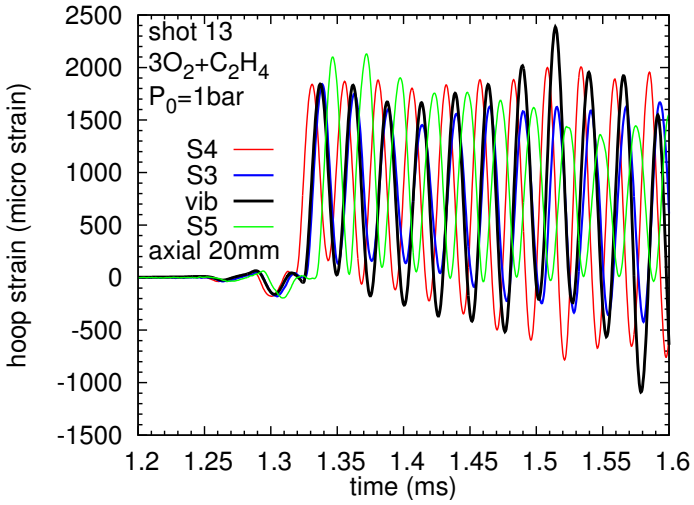

Figure E.11: Axial location hoop strain comparisons for shot 13.

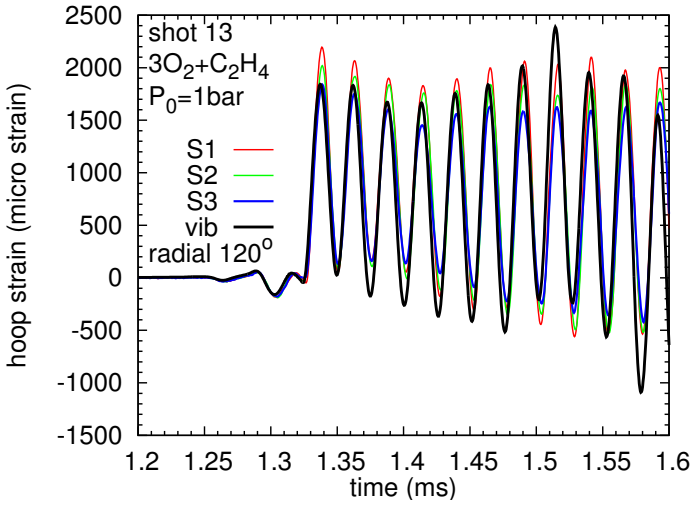

Figure E.12: Azimuthal location hoop strain comparisons for shot 13

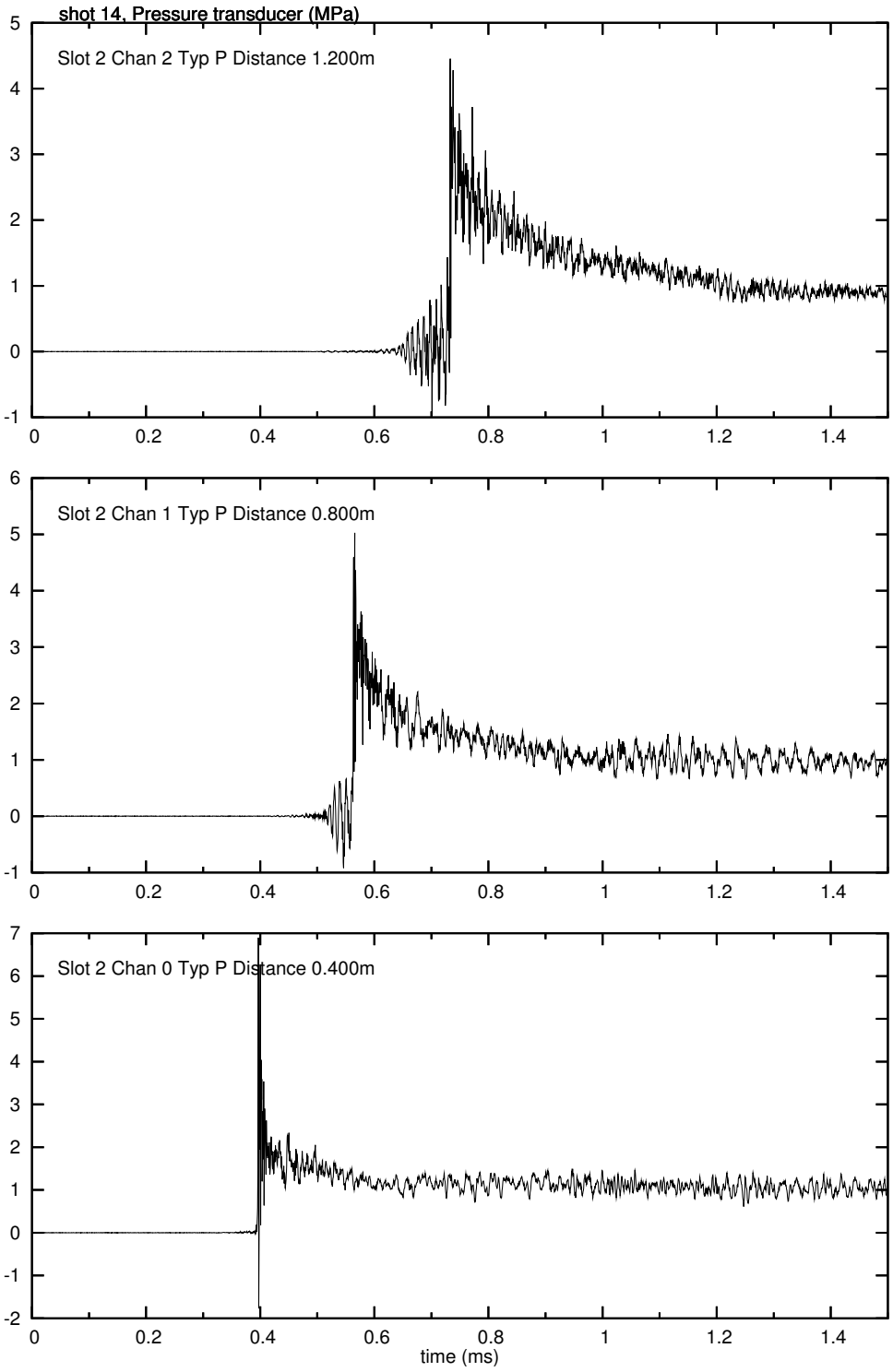

Figure E.13: Pressure traces for shot 14

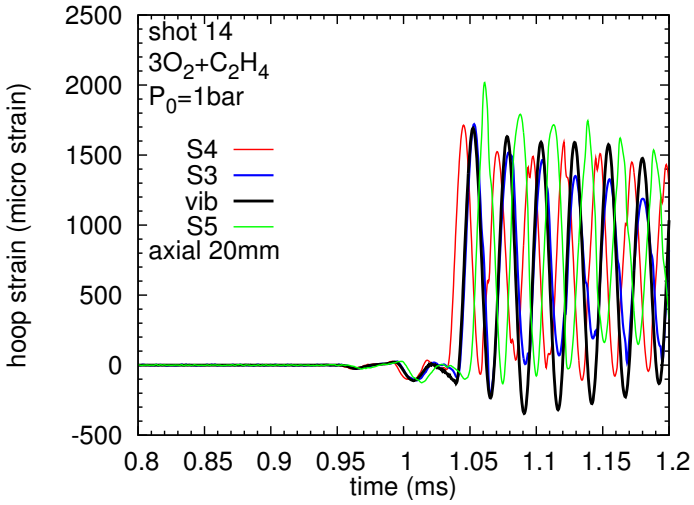

Figure E.14: Axial location hoop strain comparisons for shot 14.

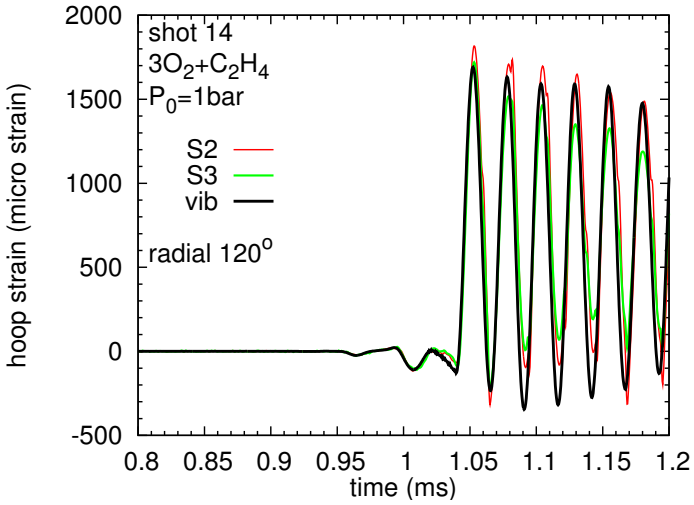

Figure E.15: Azimuthal location hoop strain comparisons for shot 14

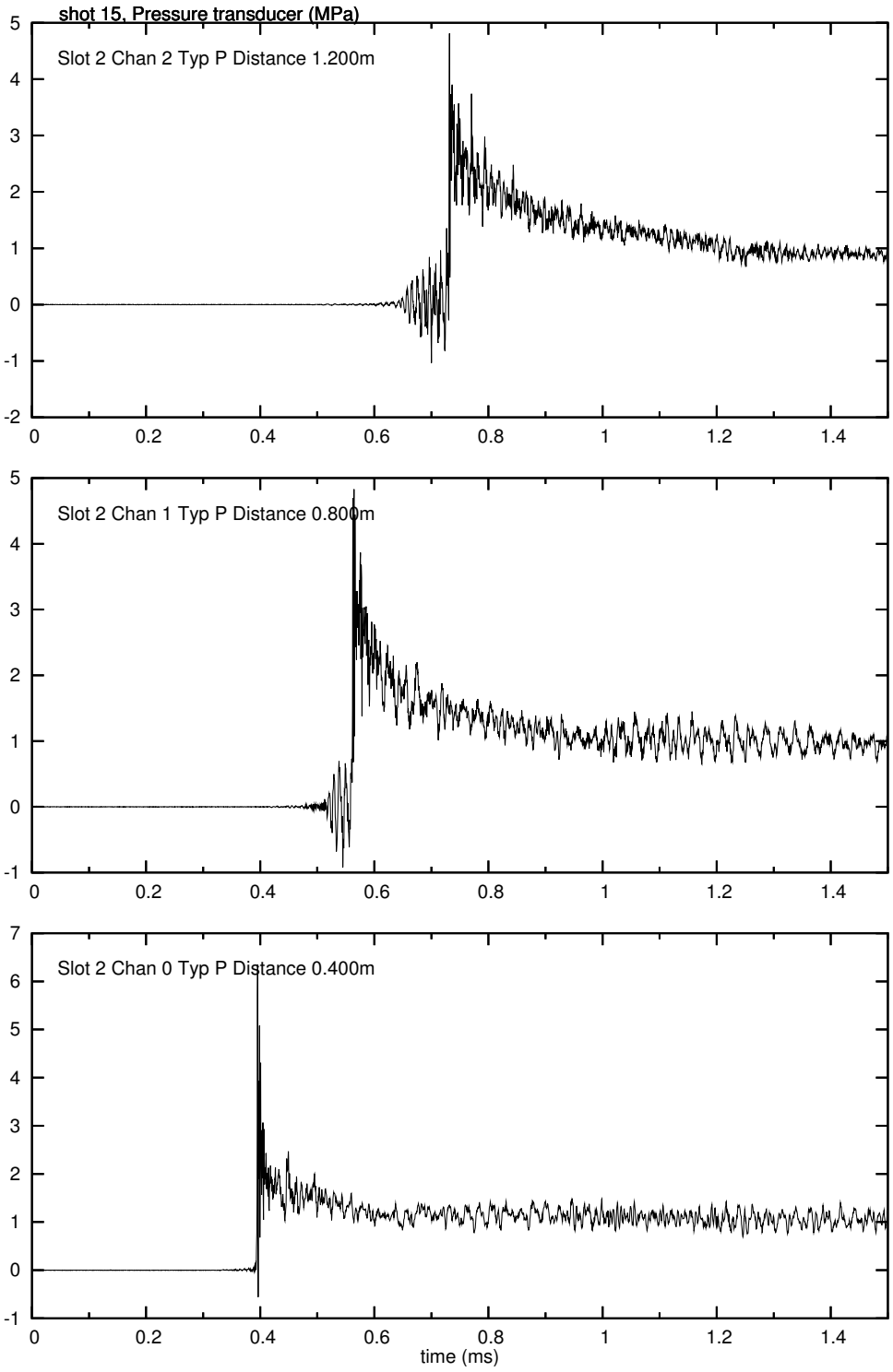

Figure E.16: Pressure traces for shot 15

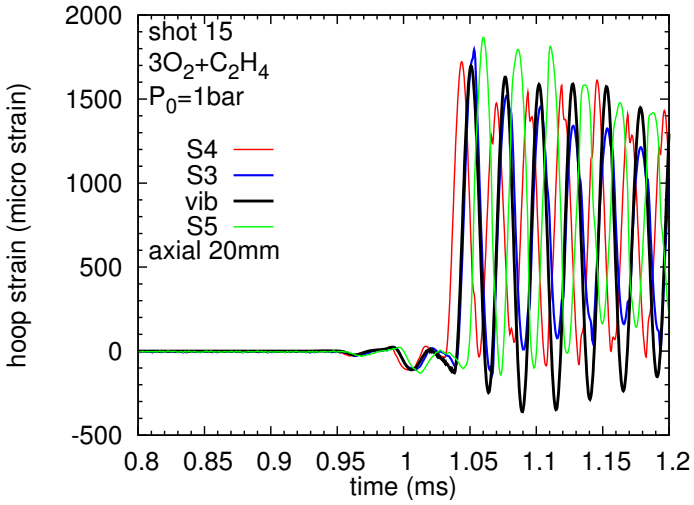

Figure E.17: Axial location hoop strain comparisons for shot 15.

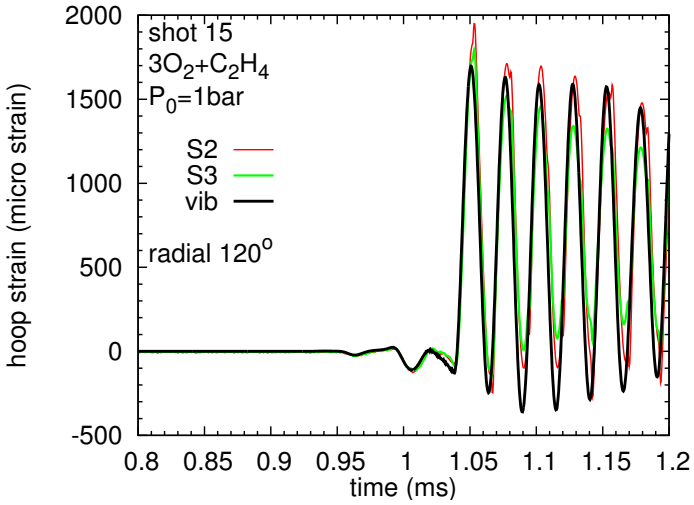

Figure E.18: Azimuthal location hoop strain comparisons for shot 15

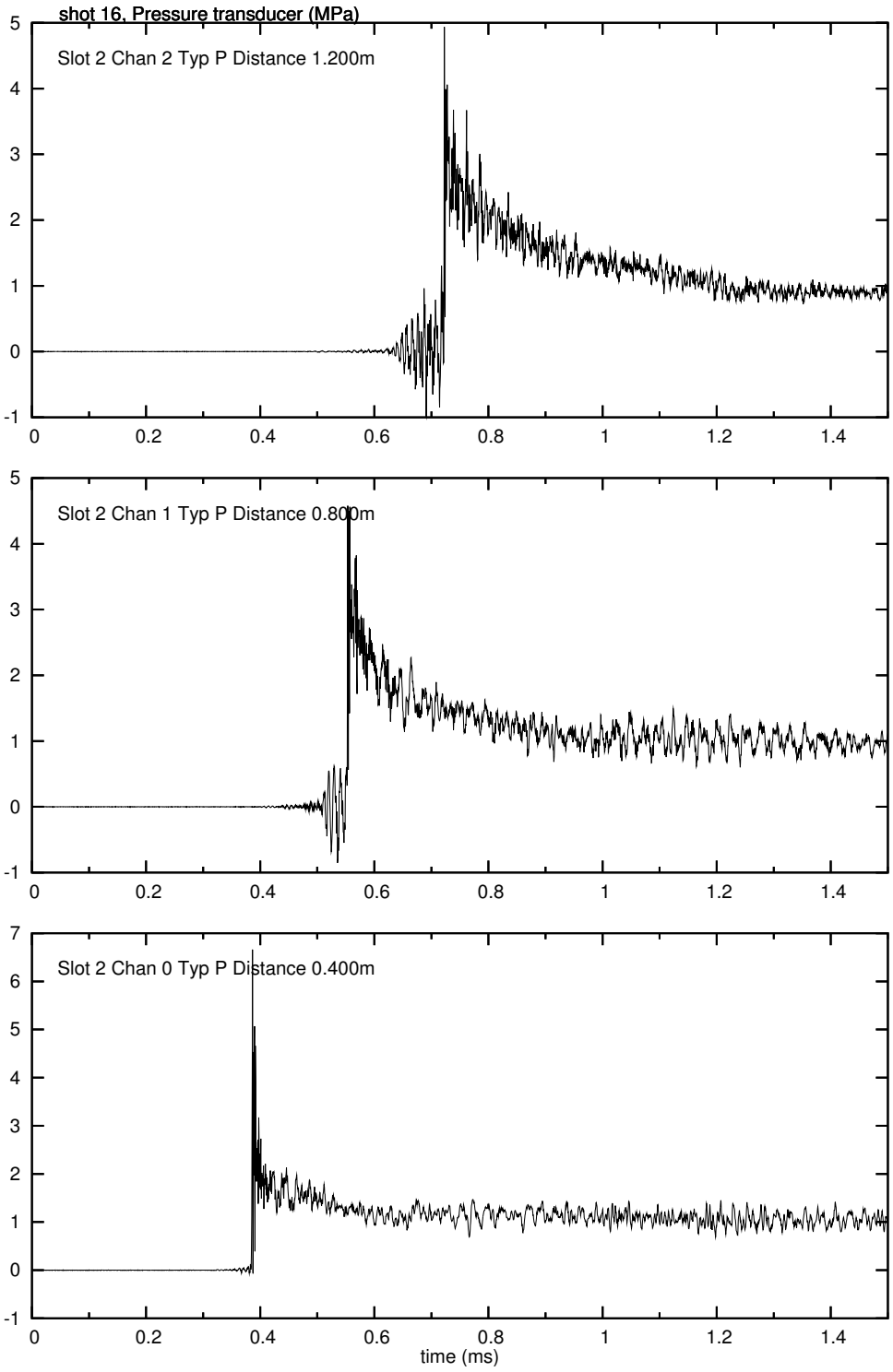

Figure E.19: Pressure traces for shot 16

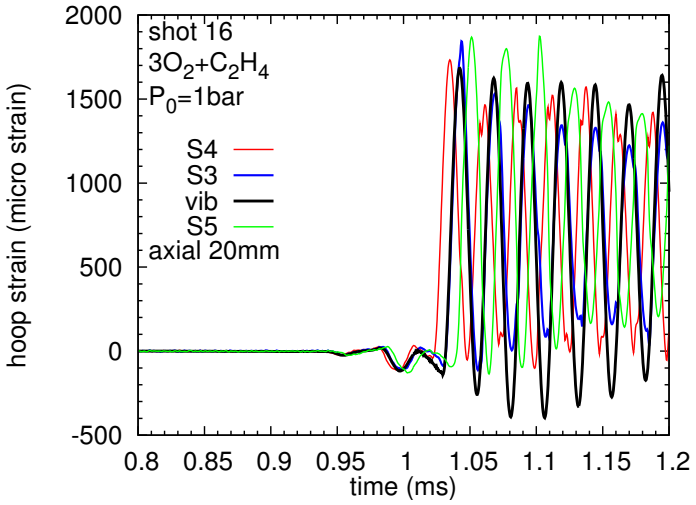

Figure E.20: Axial location hoop strain comparisons for shot 16.

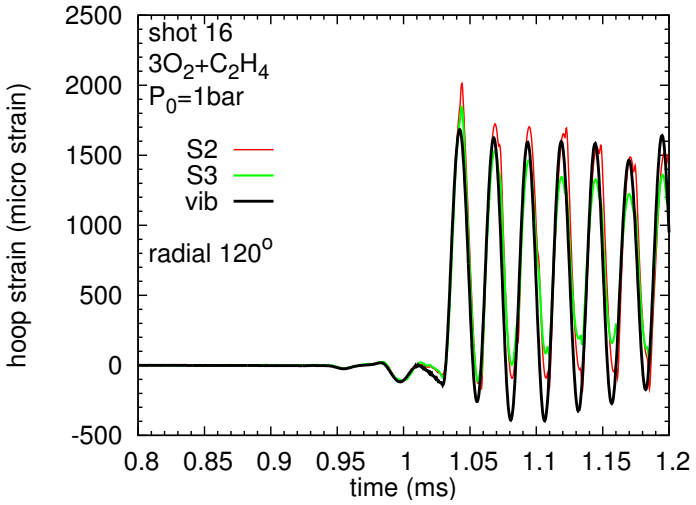

Figure E.21: Azimuthal location hoop strain comparisons for shot 16

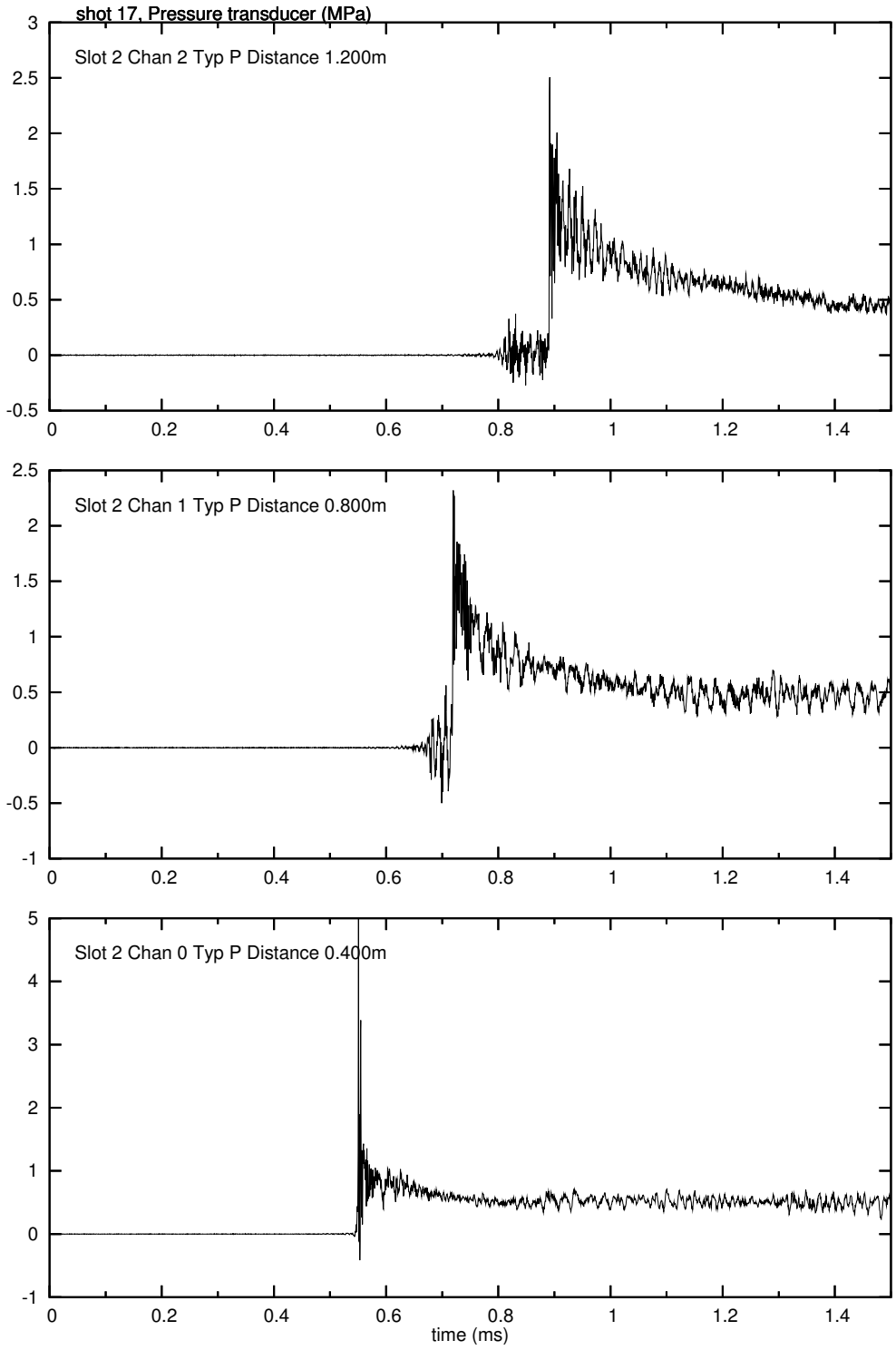

Figure E.22: Pressure traces for shot 17

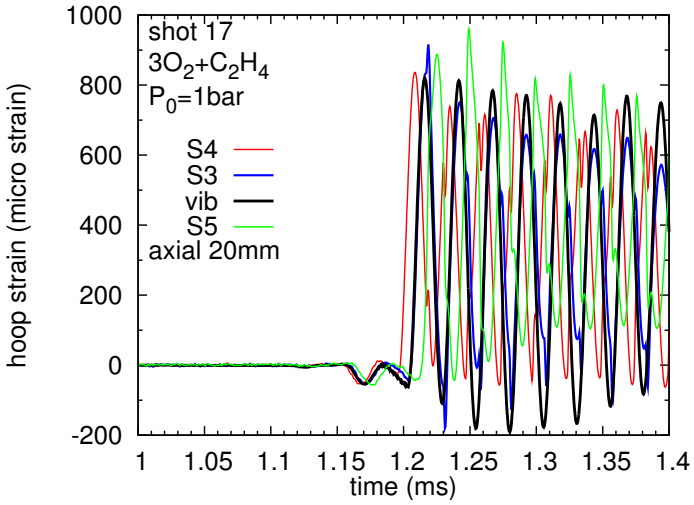

Figure E.23: Axial location hoop strain comparisons for shot 17.

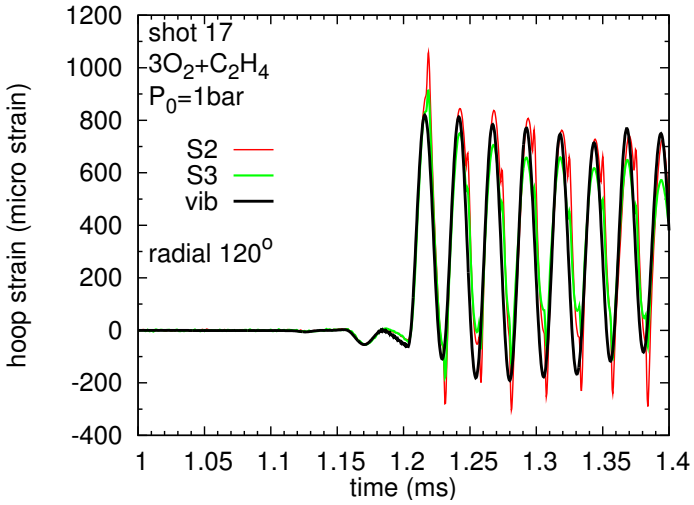

Figure E.24: Azimuthal location hoop strain comparisons for shot 17

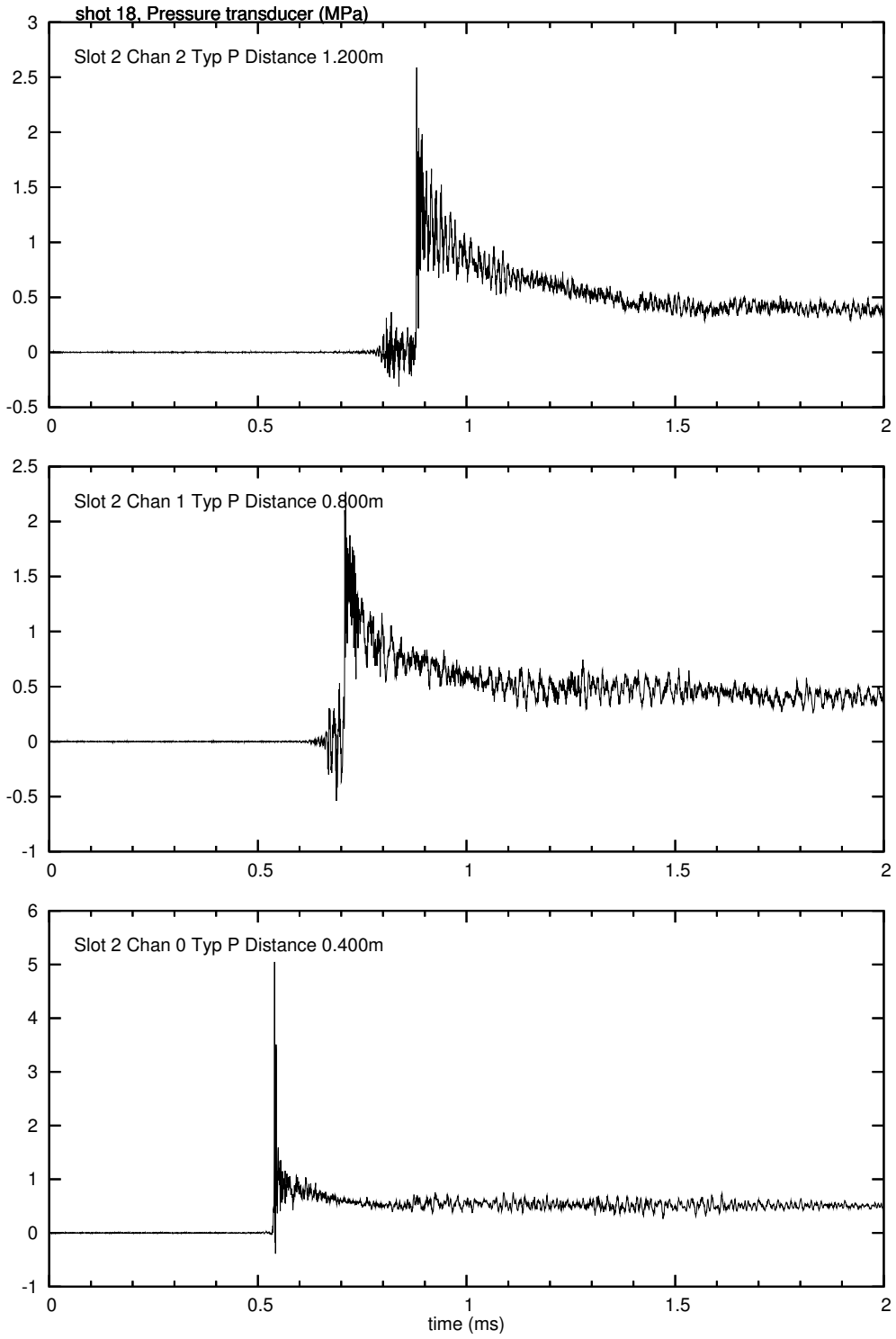

Figure E.25: Pressure traces for shot 18

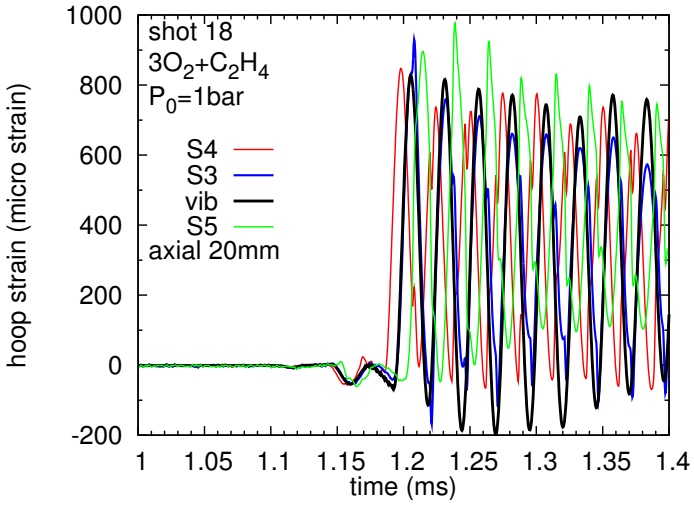

Figure E.26: Axial location hoop strain comparisons for shot 18.

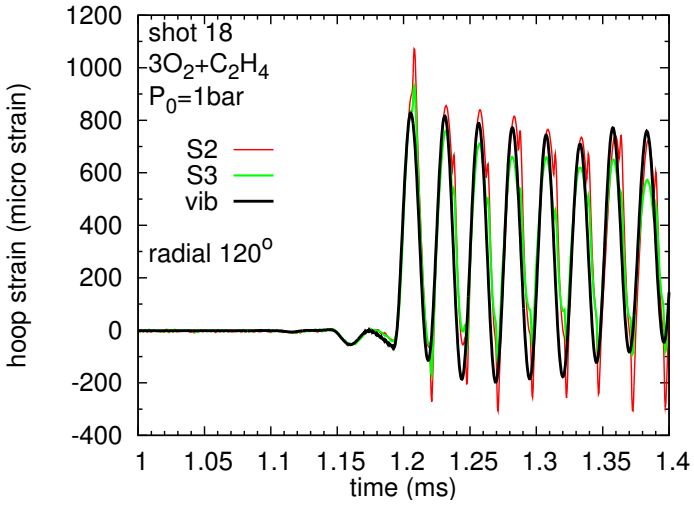

Figure E.27: Azimuthal location hoop strain comparisons for shot 18

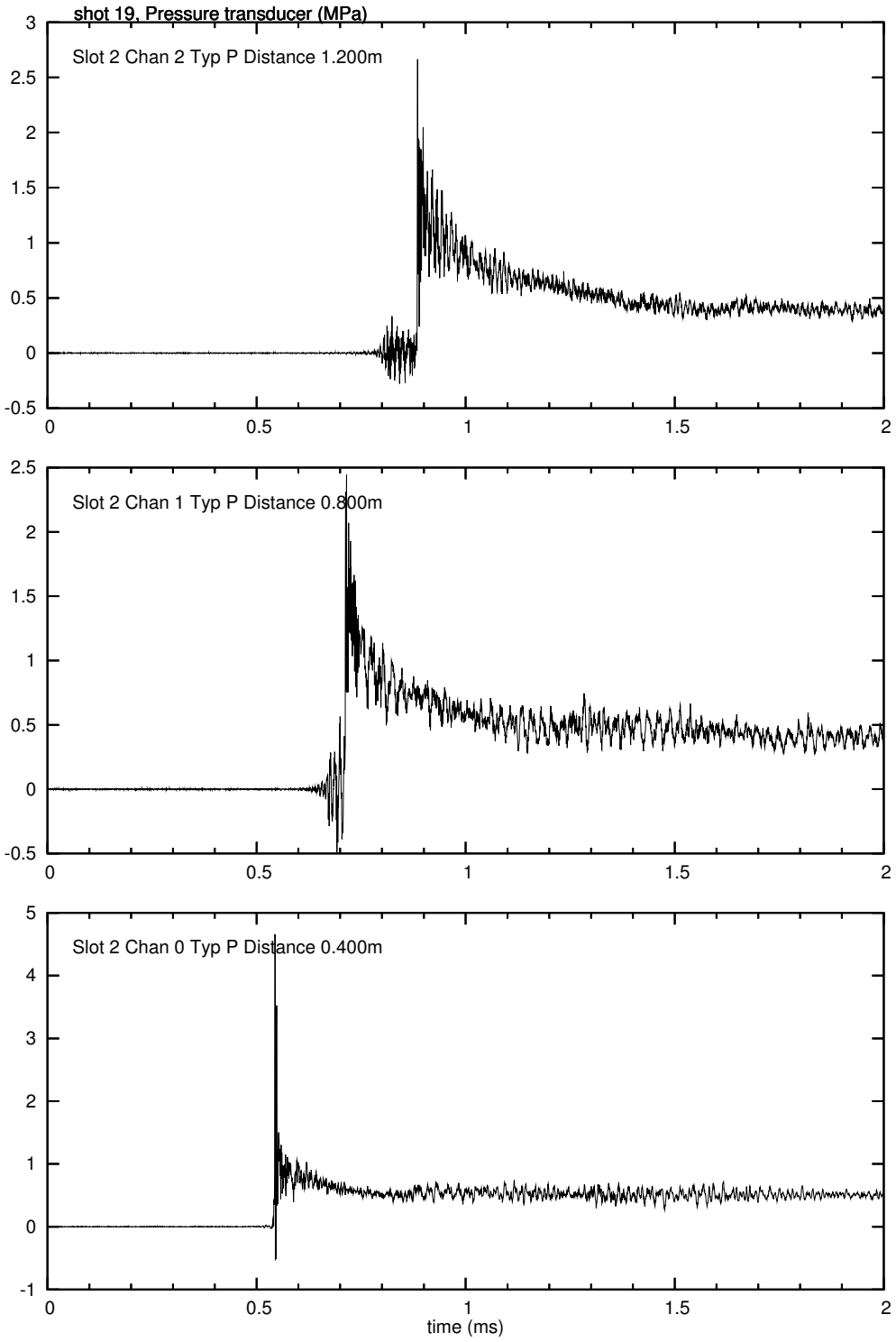

Figure E.28: Pressure traces for shot 19

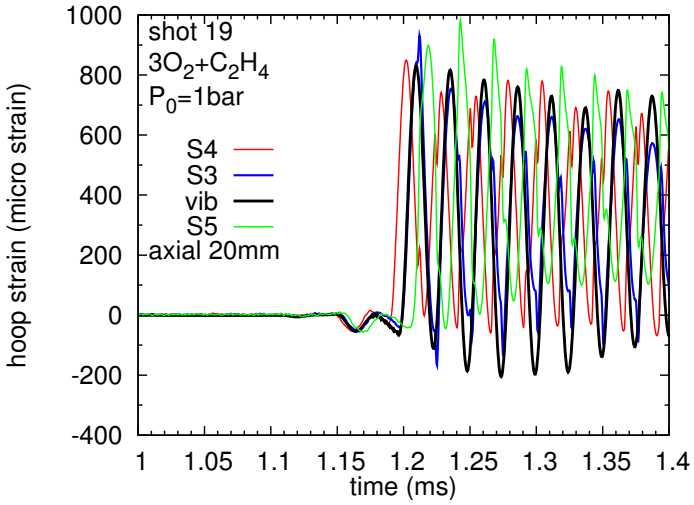

Figure E.29: Axial location hoop strain comparisons for shot 19.

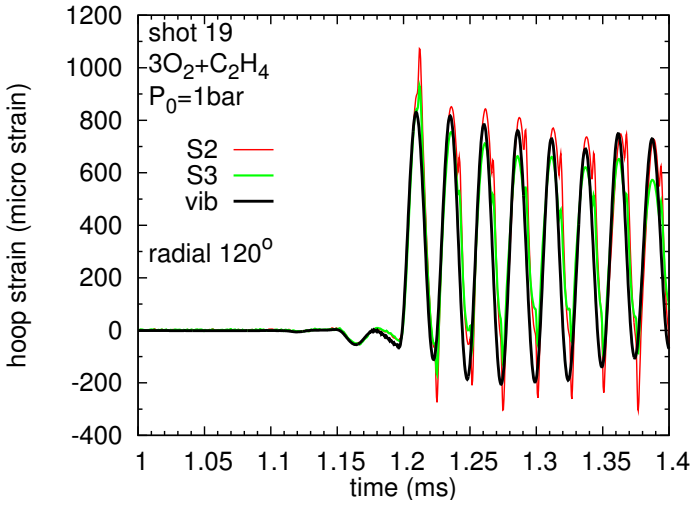

Figure E.30: Azimuthal location hoop strain comparisons for shot 19

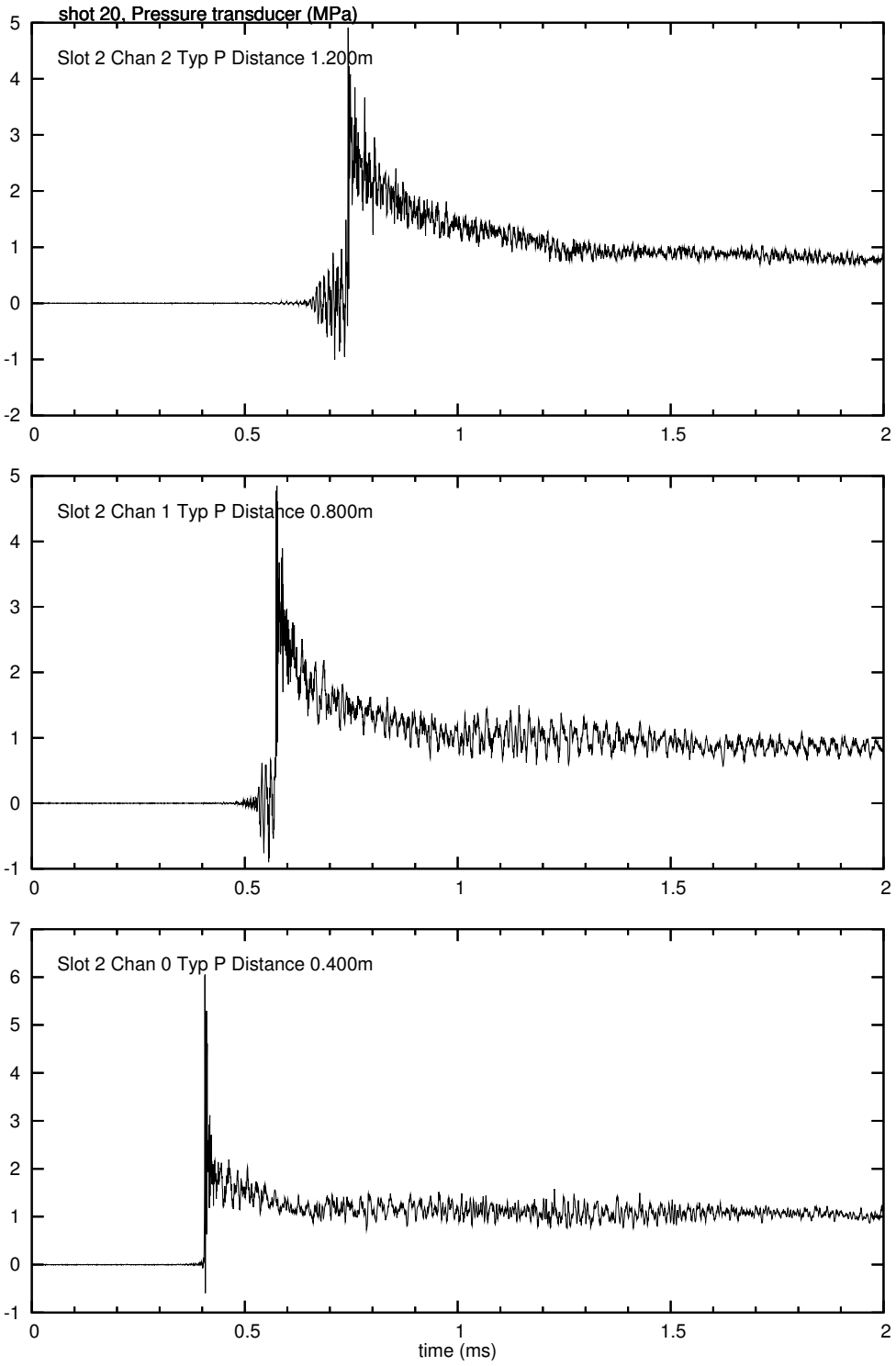

Figure E.31: Pressure traces for shot 20

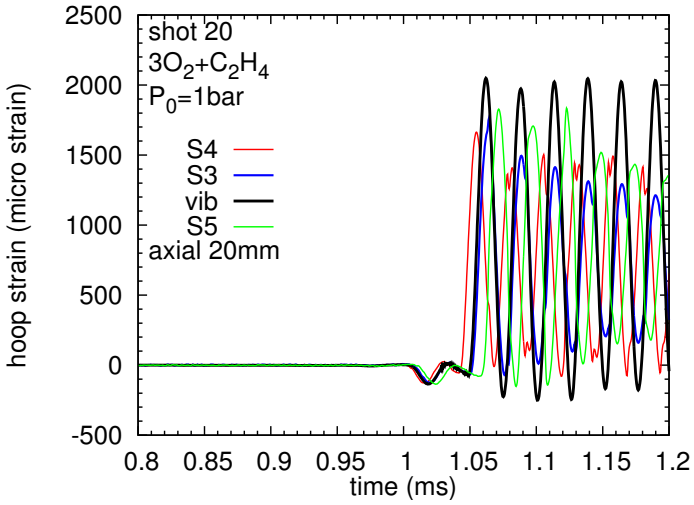

Figure E.32: Axial location hoop strain comparisons for shot 20.

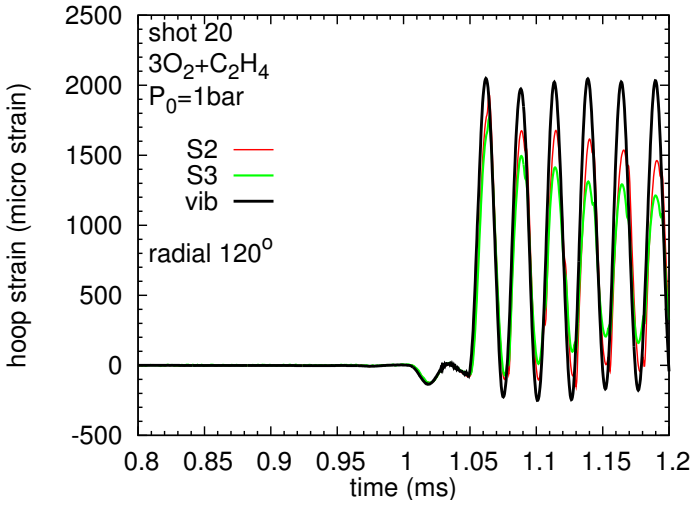

Figure E.33: Azimuthal location hoop strain comparisons for shot 20

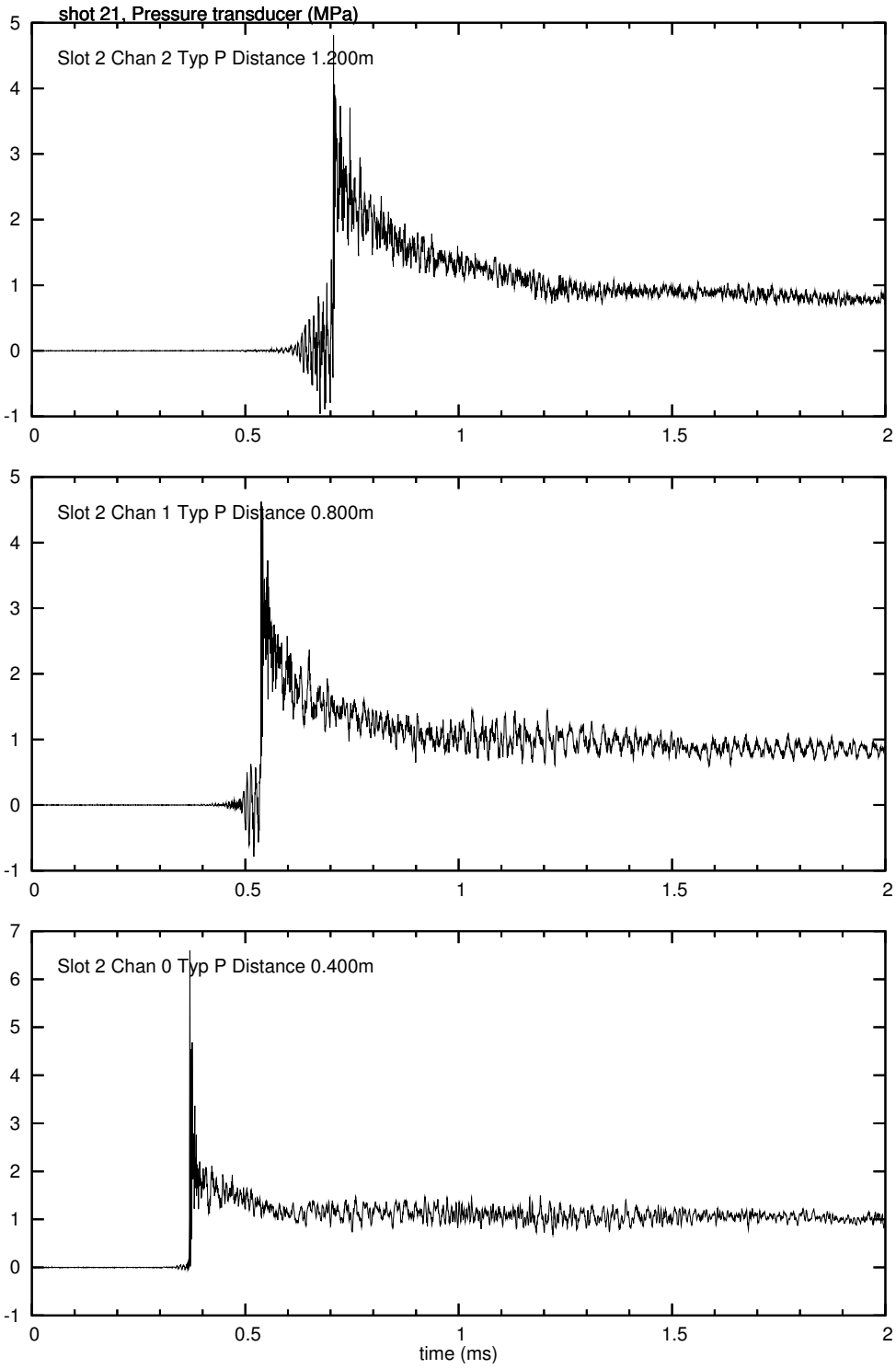

Figure E.34: Pressure traces for shot 21

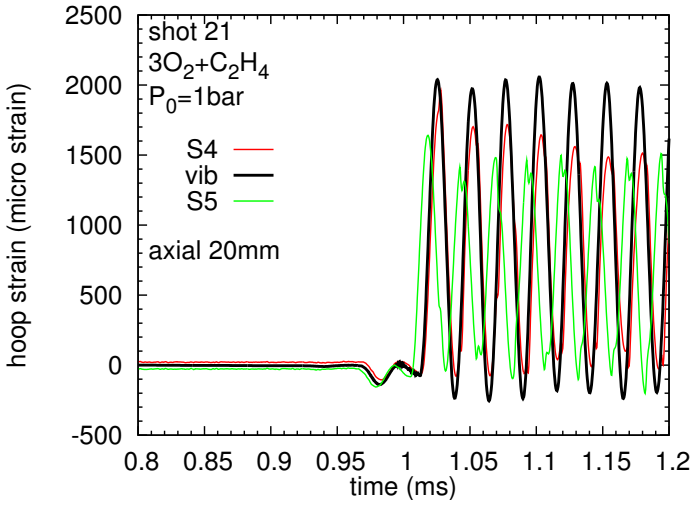

Figure E.35: Axial location hoop strain comparisons for shot 21.

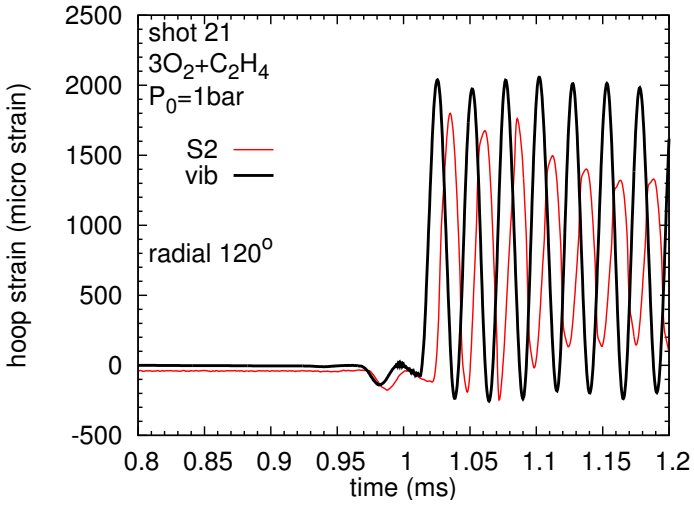

Figure E.36: Azimuthal location hoop strain comparisons for shot 21

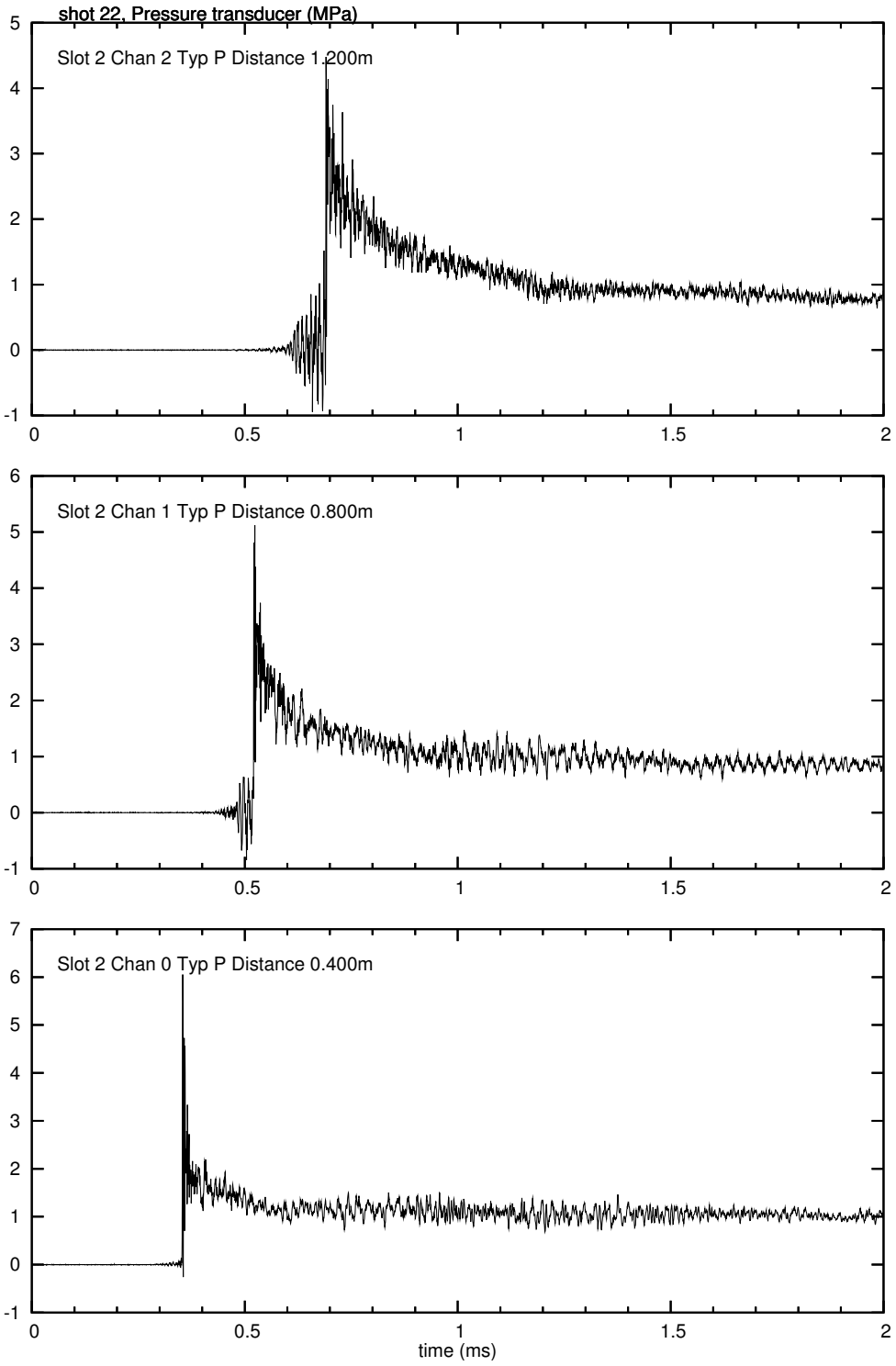

Figure E.37: Pressure traces for shot 22

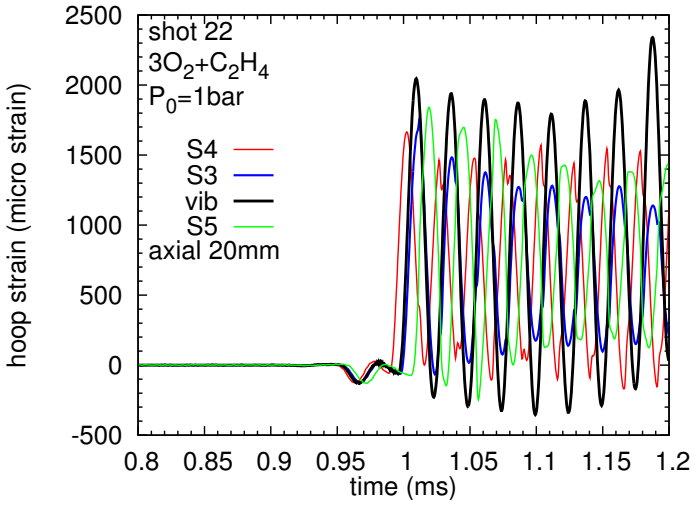

Figure E.38: Axial location hoop strain comparisons for shot 22.

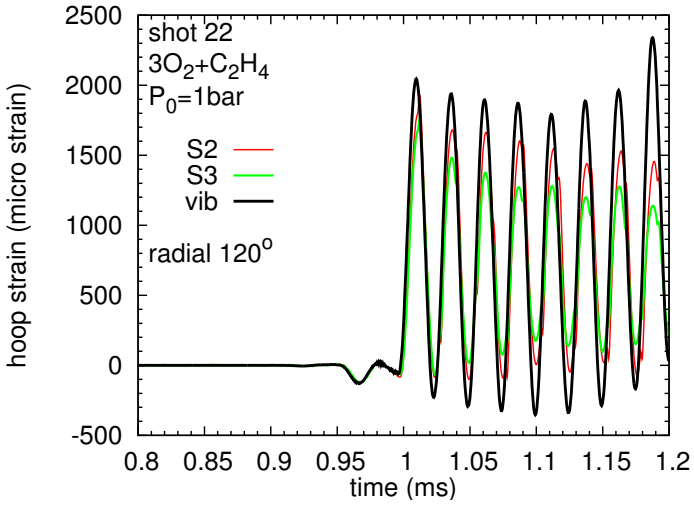

Figure E.39: Azimuthal location hoop strain comparisons for shot 22

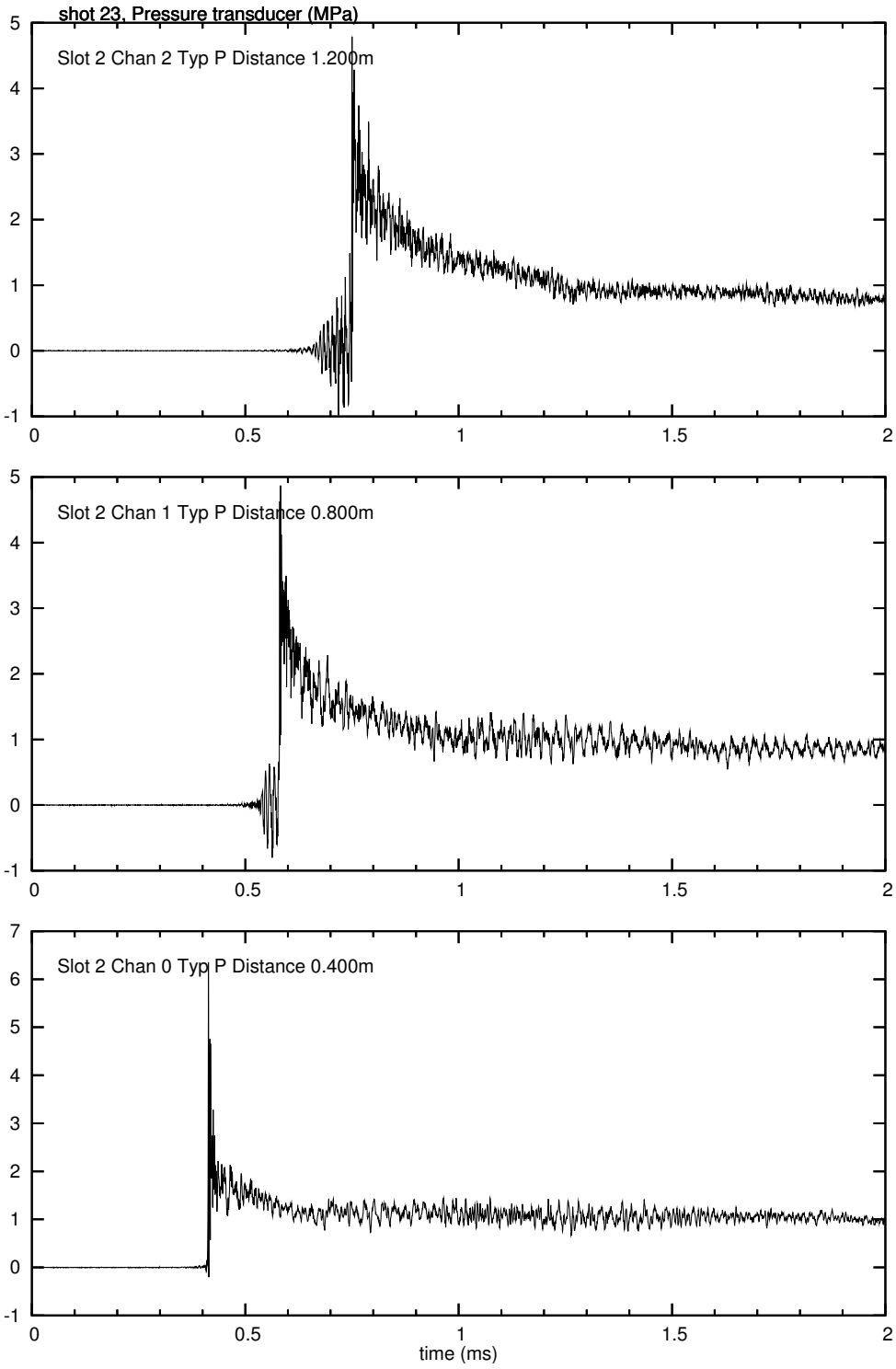

Figure E.40: Pressure traces for shot 23

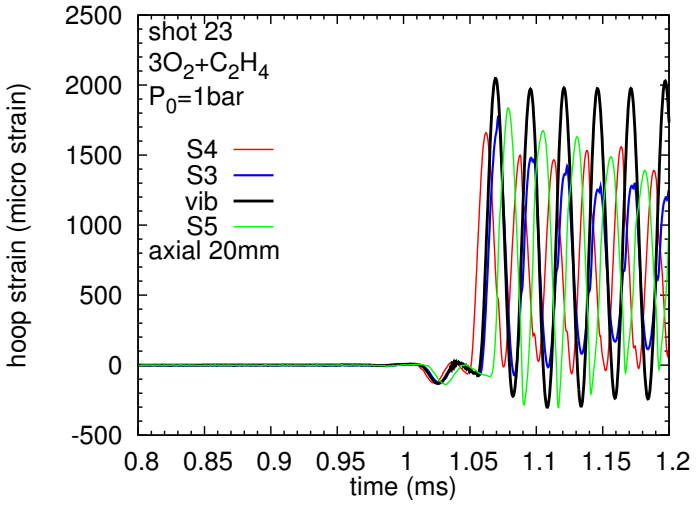

Figure E.41: Axial location hoop strain comparisons for shot 23.

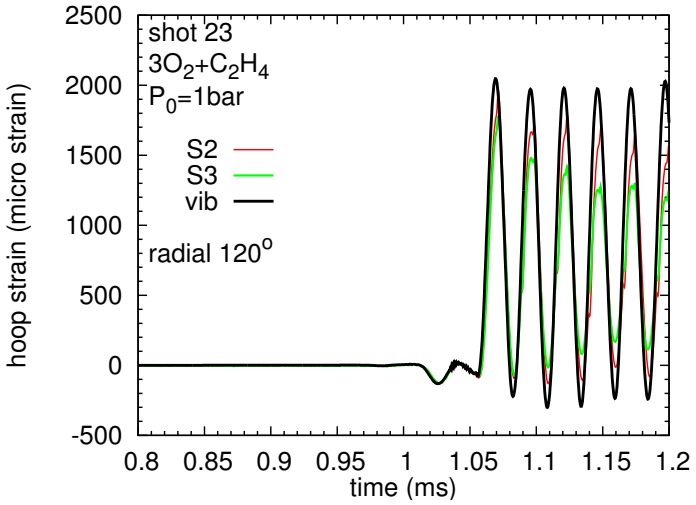

Figure E.42: Azimuthal location hoop strain comparisons for shot 23

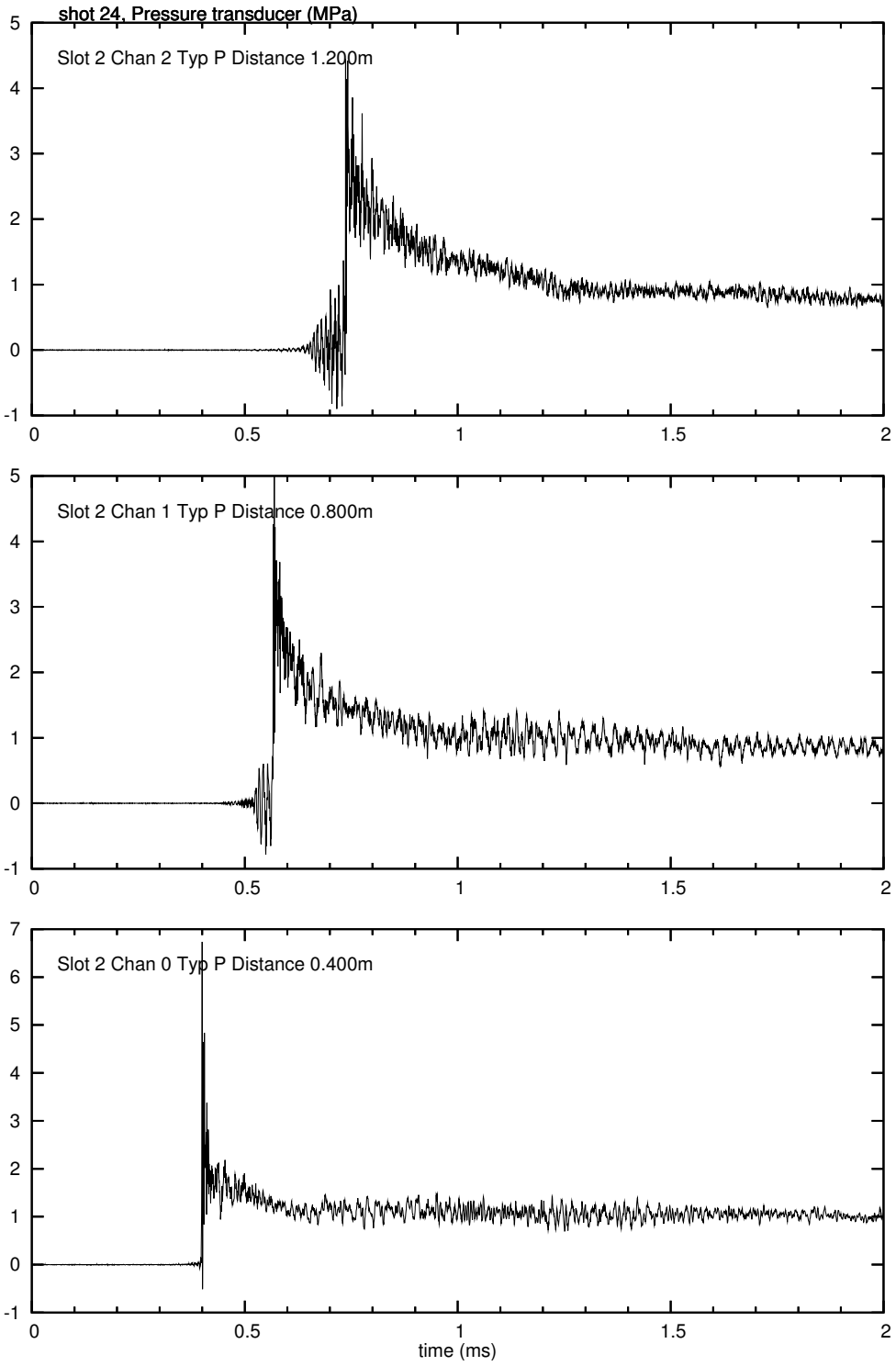

Figure E.43: Pressure traces for shot 24

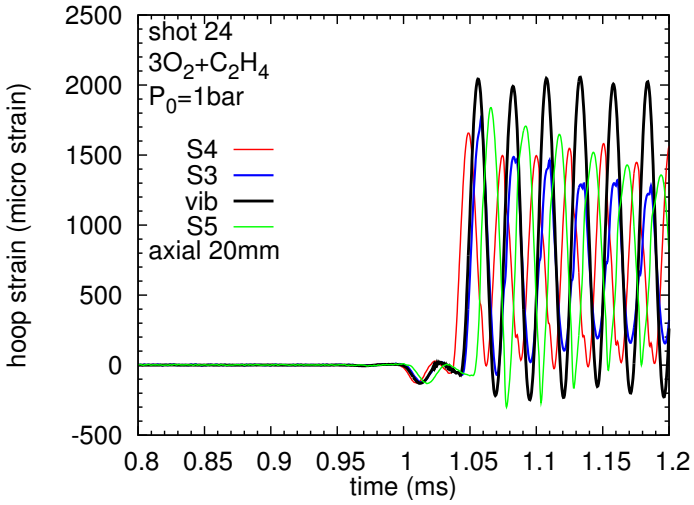

Figure E.44: Axial location hoop strain comparisons for shot 24.

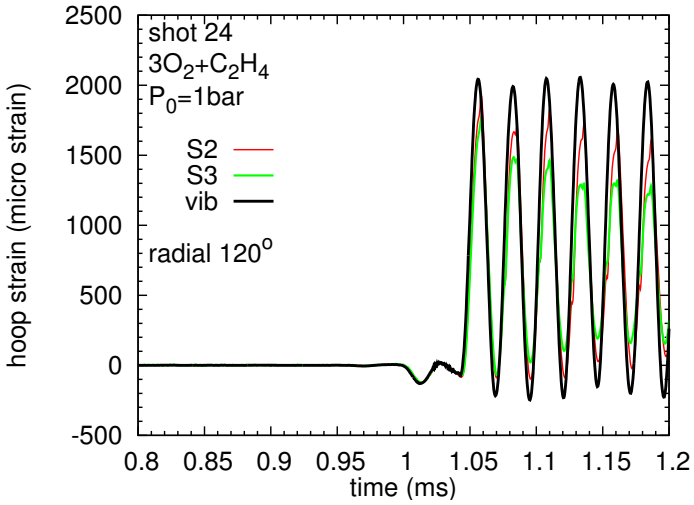

Figure E.45: Azimuthal location hoop strain comparisons for shot 24

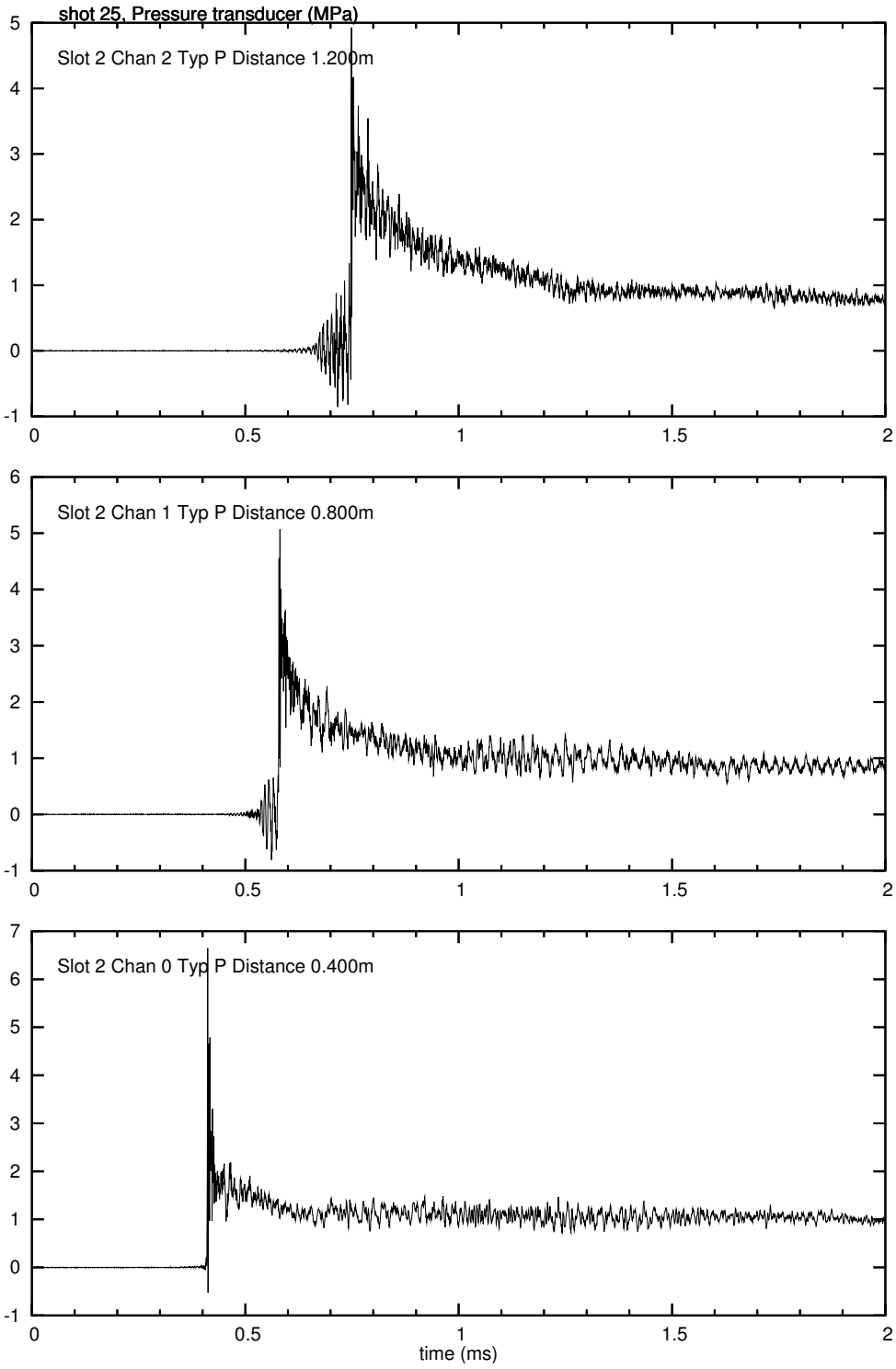

Figure E.46: Pressure traces for shot 25

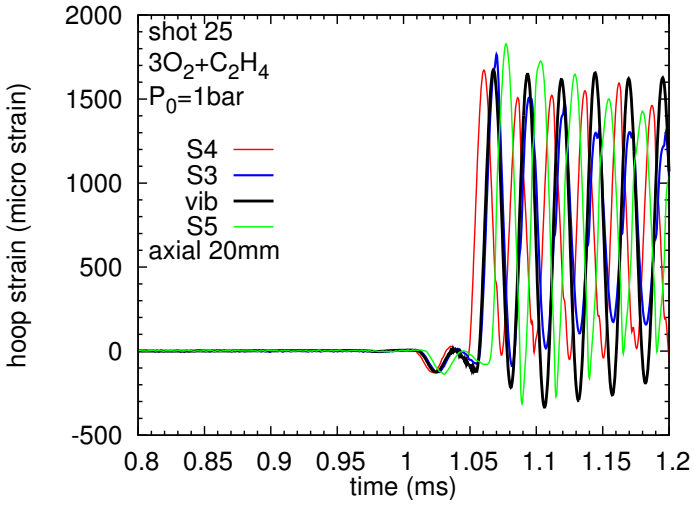

Figure E.47: Axial location hoop strain comparisons for shot 25.

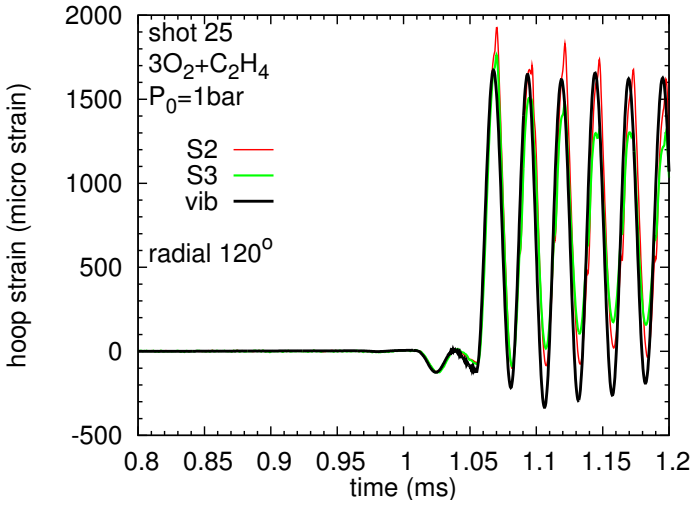

Figure E.48: Azimuthal location hoop strain comparisons for shot 25

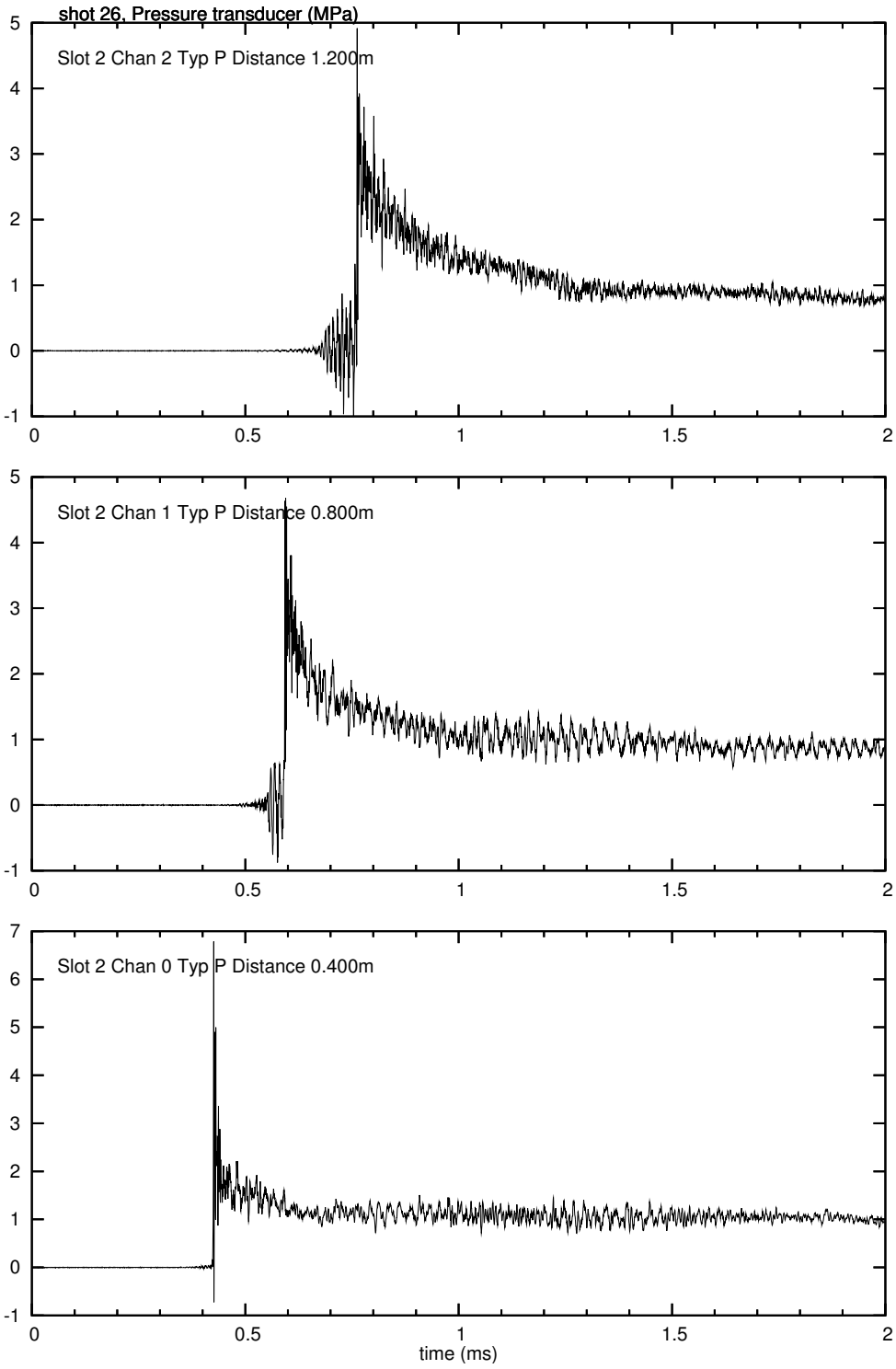

Figure E.49: Pressure traces for shot 26

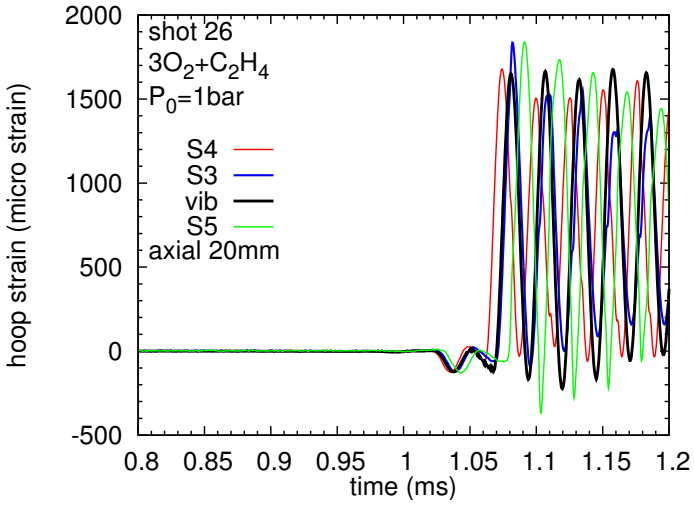

Figure E.50: Axial location hoop strain comparisons for shot 26.

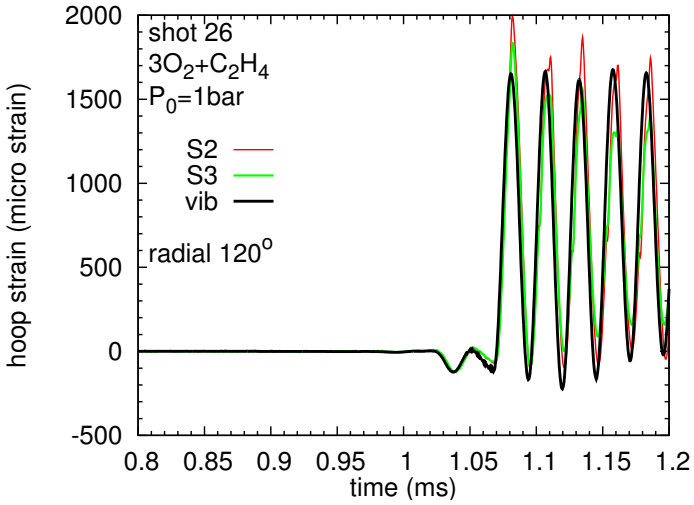

Figure E.51: Azimuthal location hoop strain comparisons for shot 26

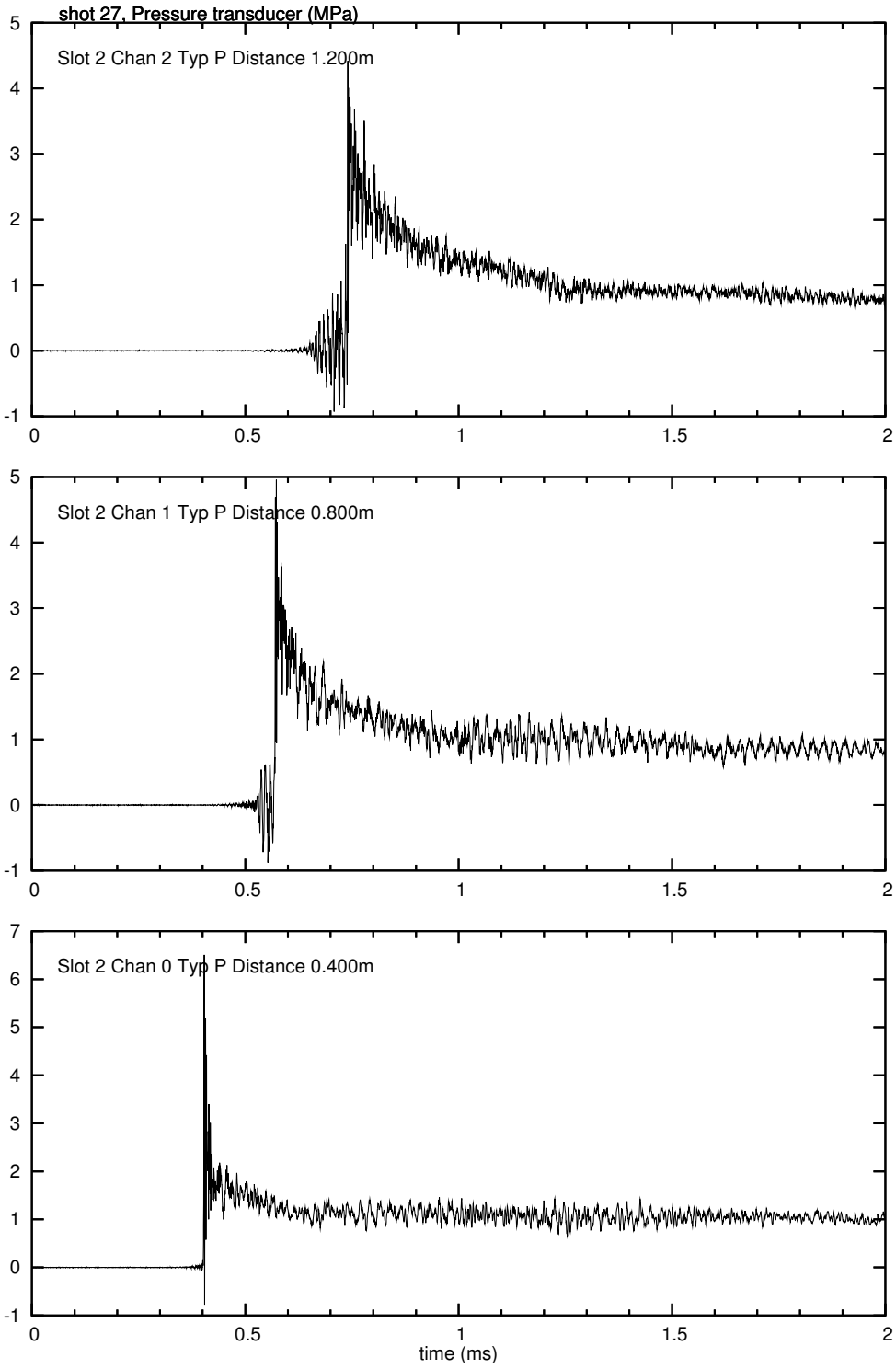

Figure E.52: Pressure traces for shot 27

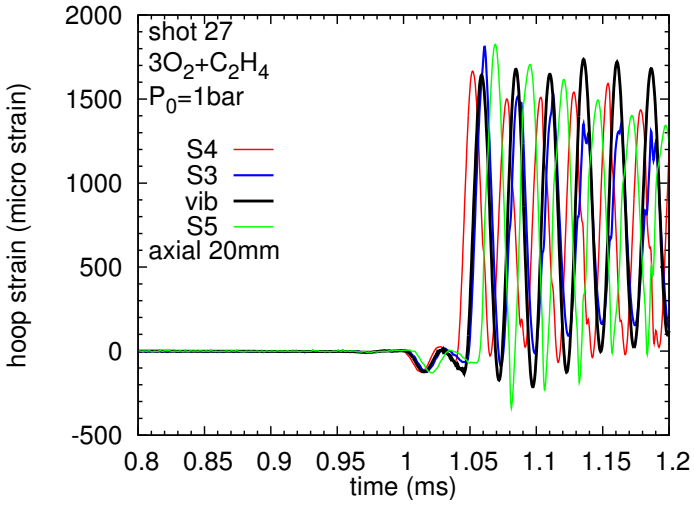

Figure E.53: Axial location hoop strain comparisons for shot 27.

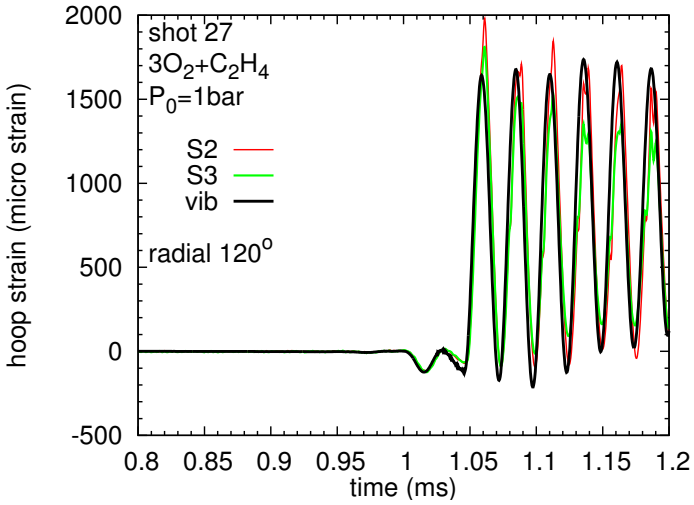

Figure E.54: Azimuthal location hoop strain comparisons for shot 27

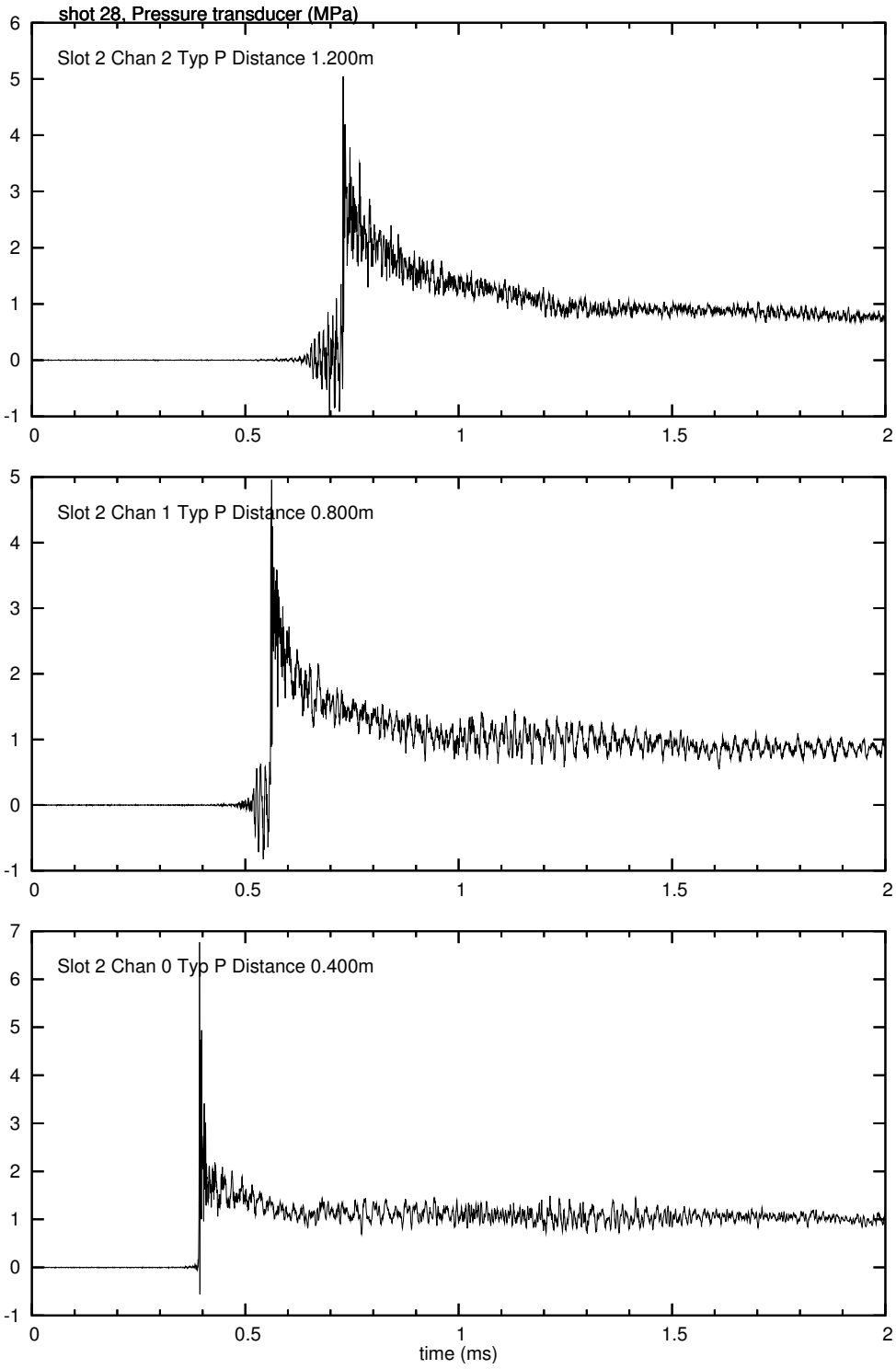

Figure E.55: Pressure traces for shot 28

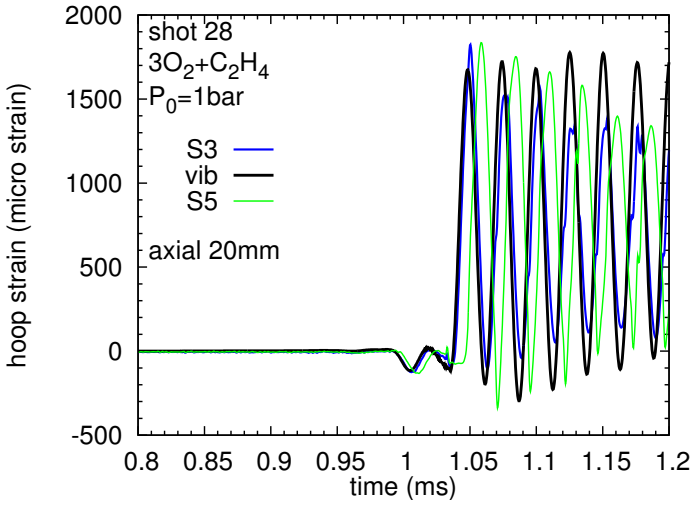

Figure E.56: Axial location hoop strain comparisons for shot 28.

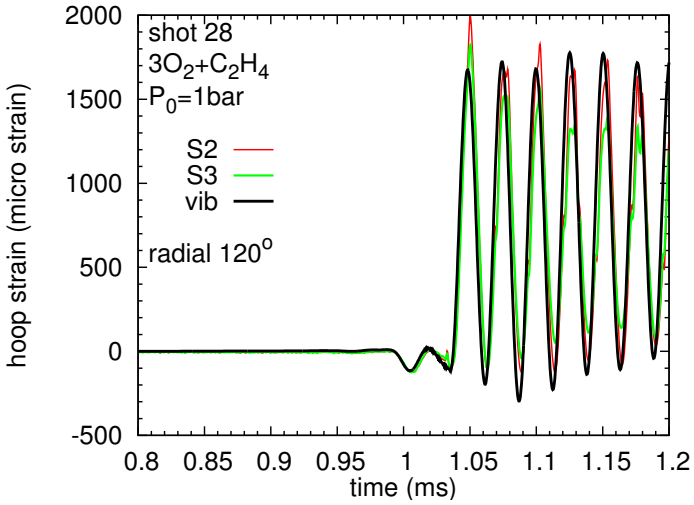

Figure E.57: Azimuthal location hoop strain comparisons for shot 28

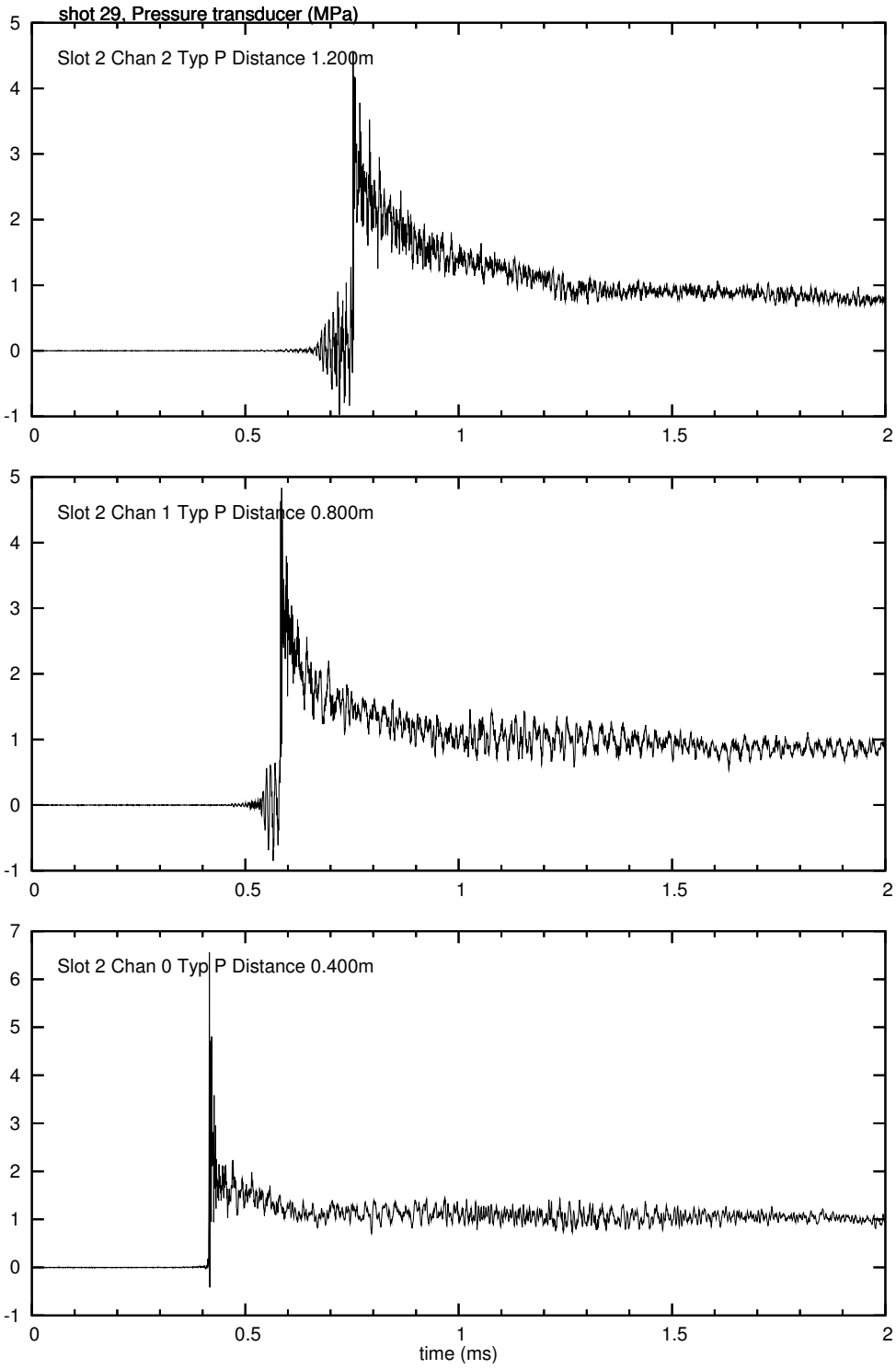

Figure E.58: Pressure traces for shot 29

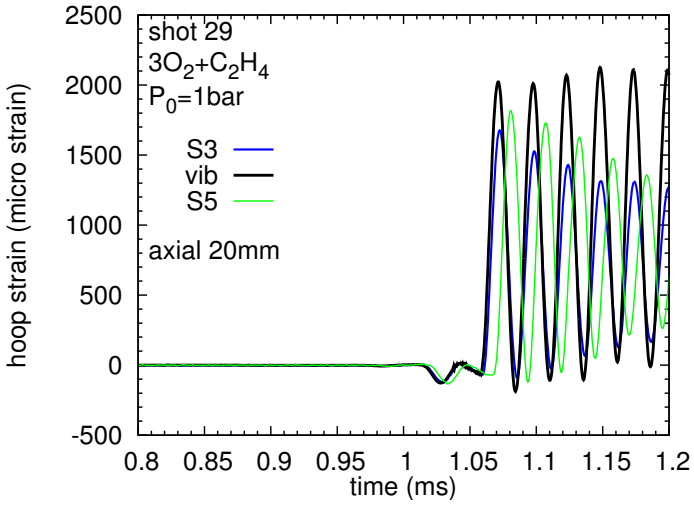

Figure E.59: Axial location hoop strain comparisons for shot 29.

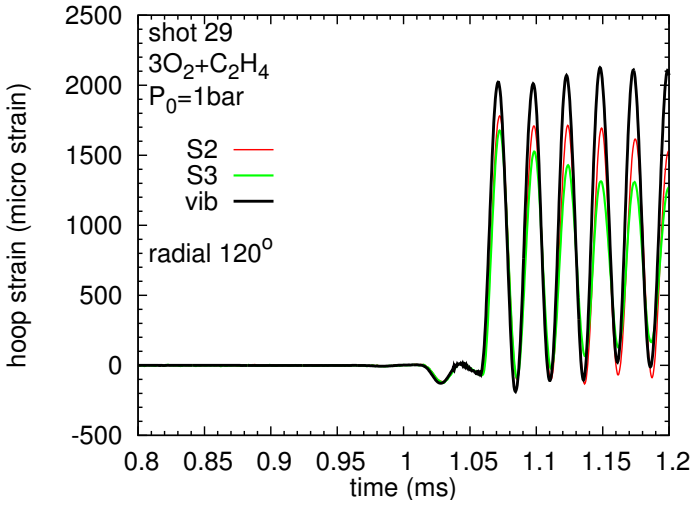

Figure E.60: Azimuthal location hoop strain comparisons for shot 29

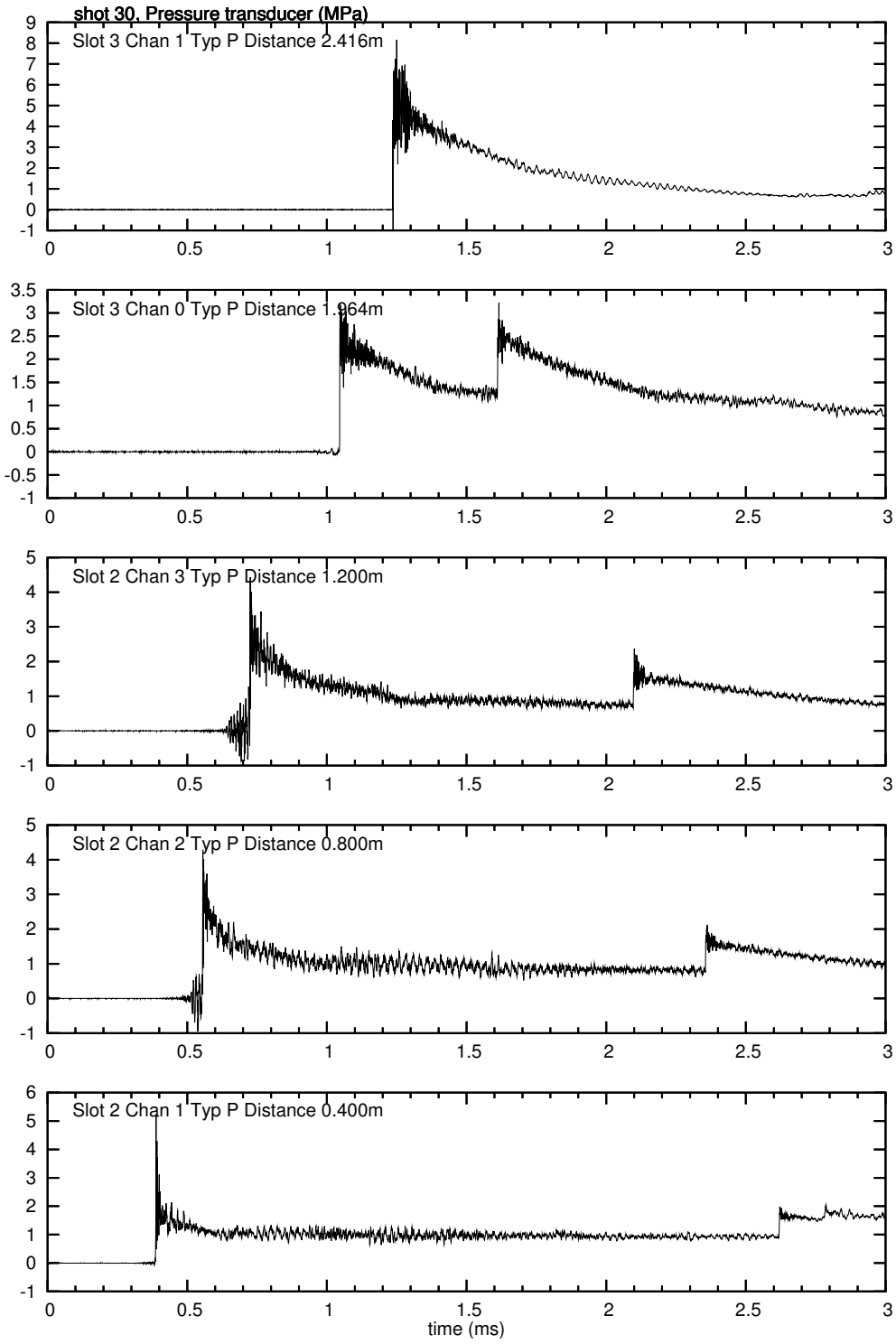

Figure E.61: Pressure signals of shot 30 with a short time scale.

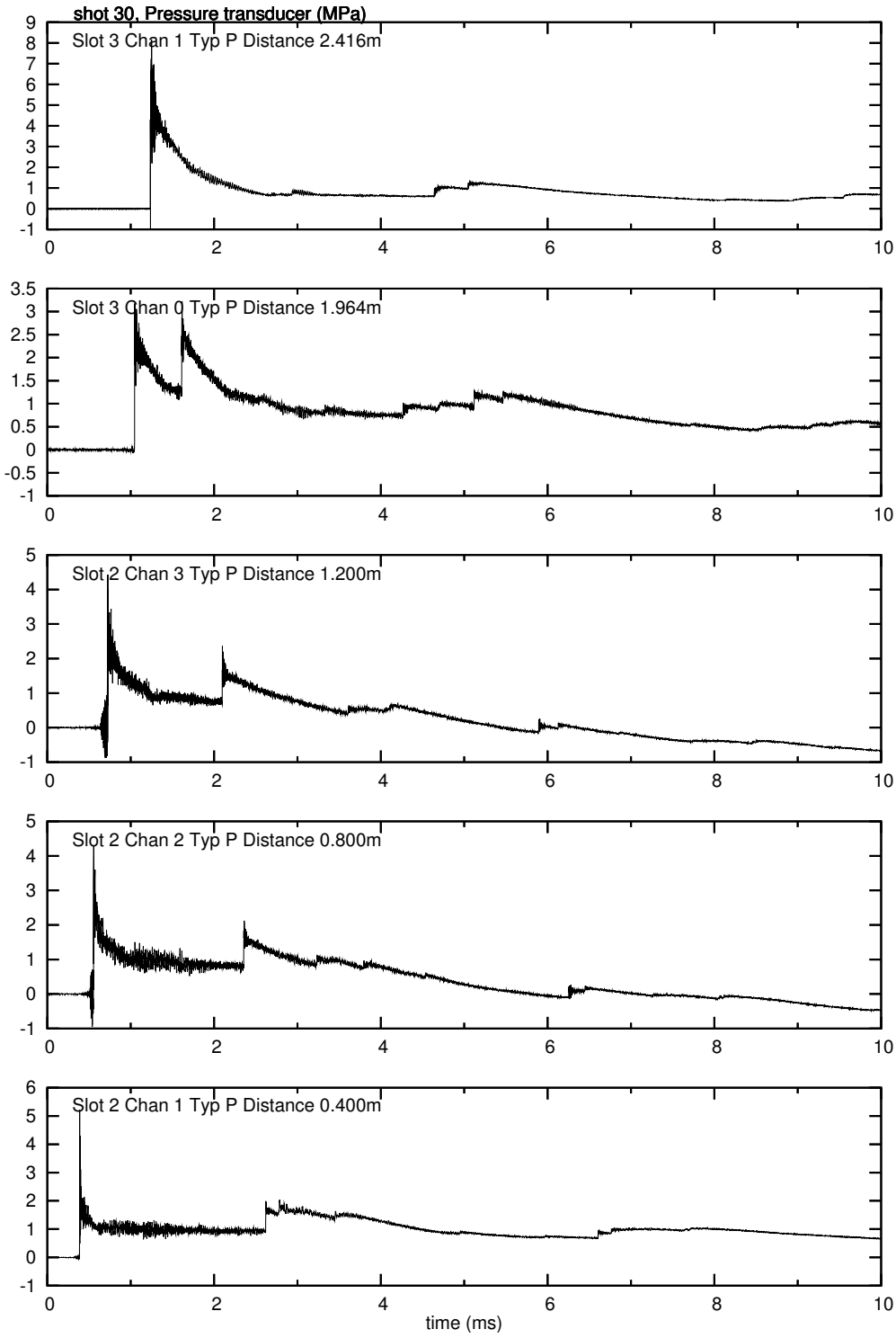

Figure E.62: Pressure signals of shot 30.

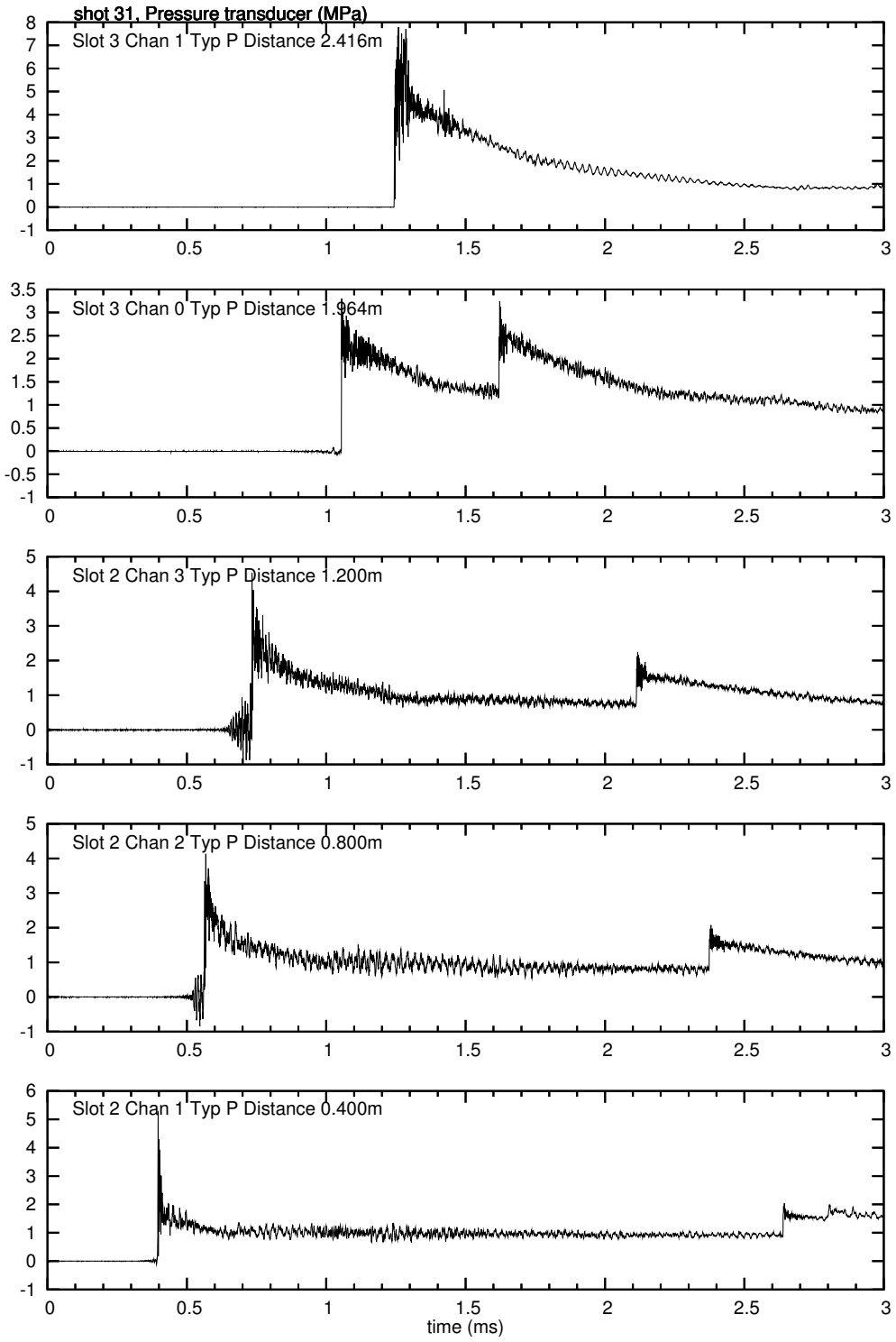

Figure E.63: Pressure signals of shot 31 with a short time scale.

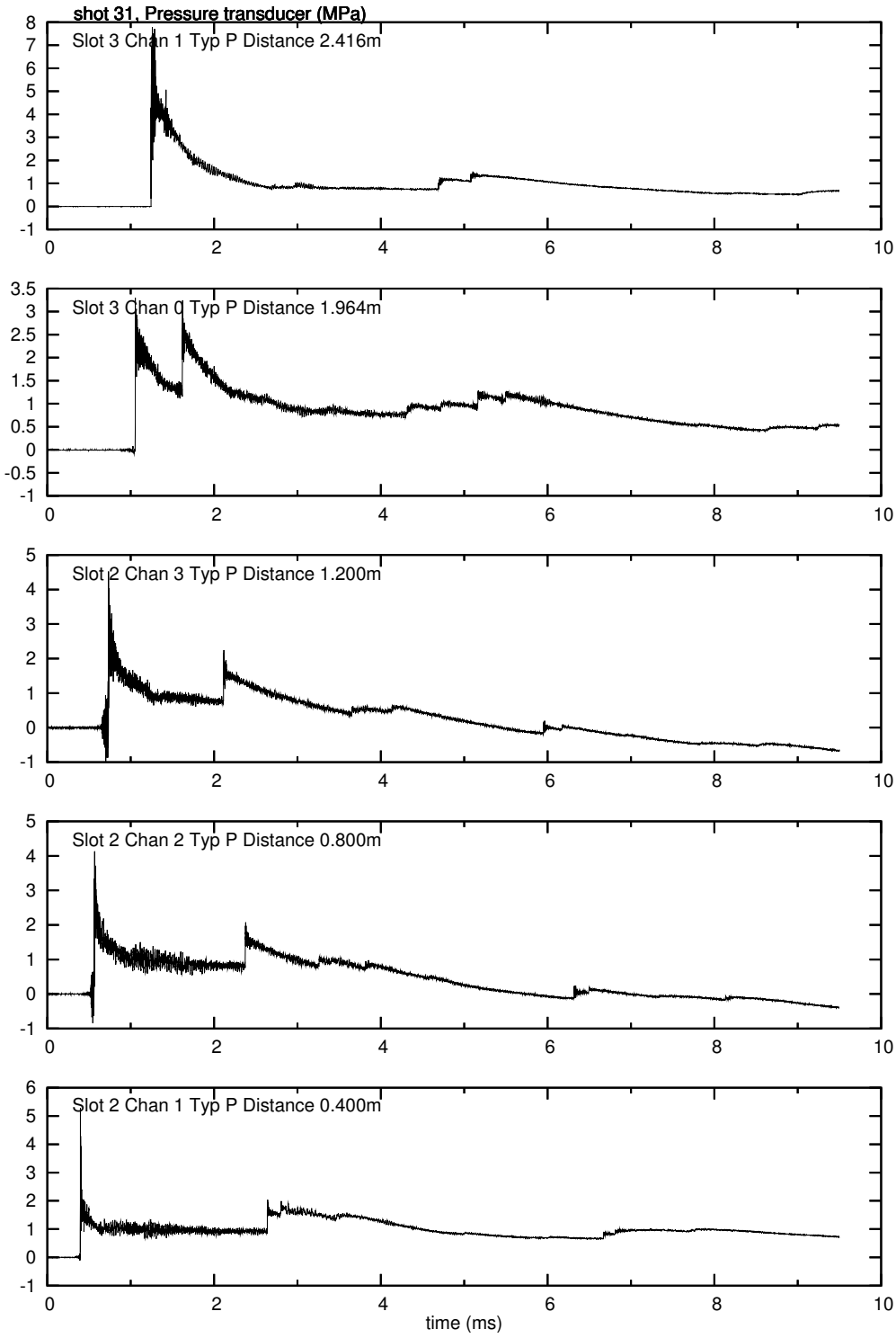

Figure E.64: Pressure signals of shot 31.

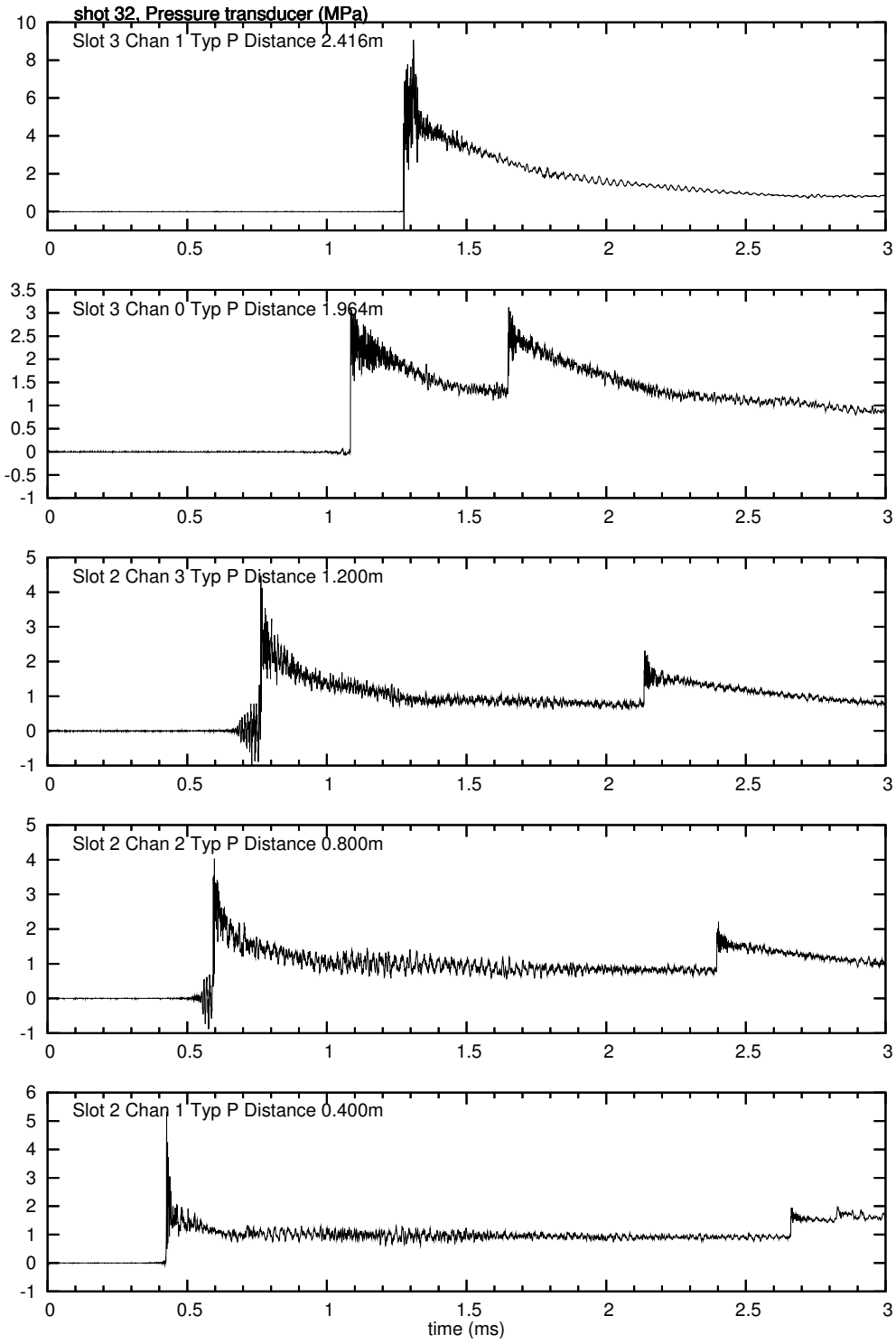

Figure E.65: Pressure signals of shot 32 with a short time scale.

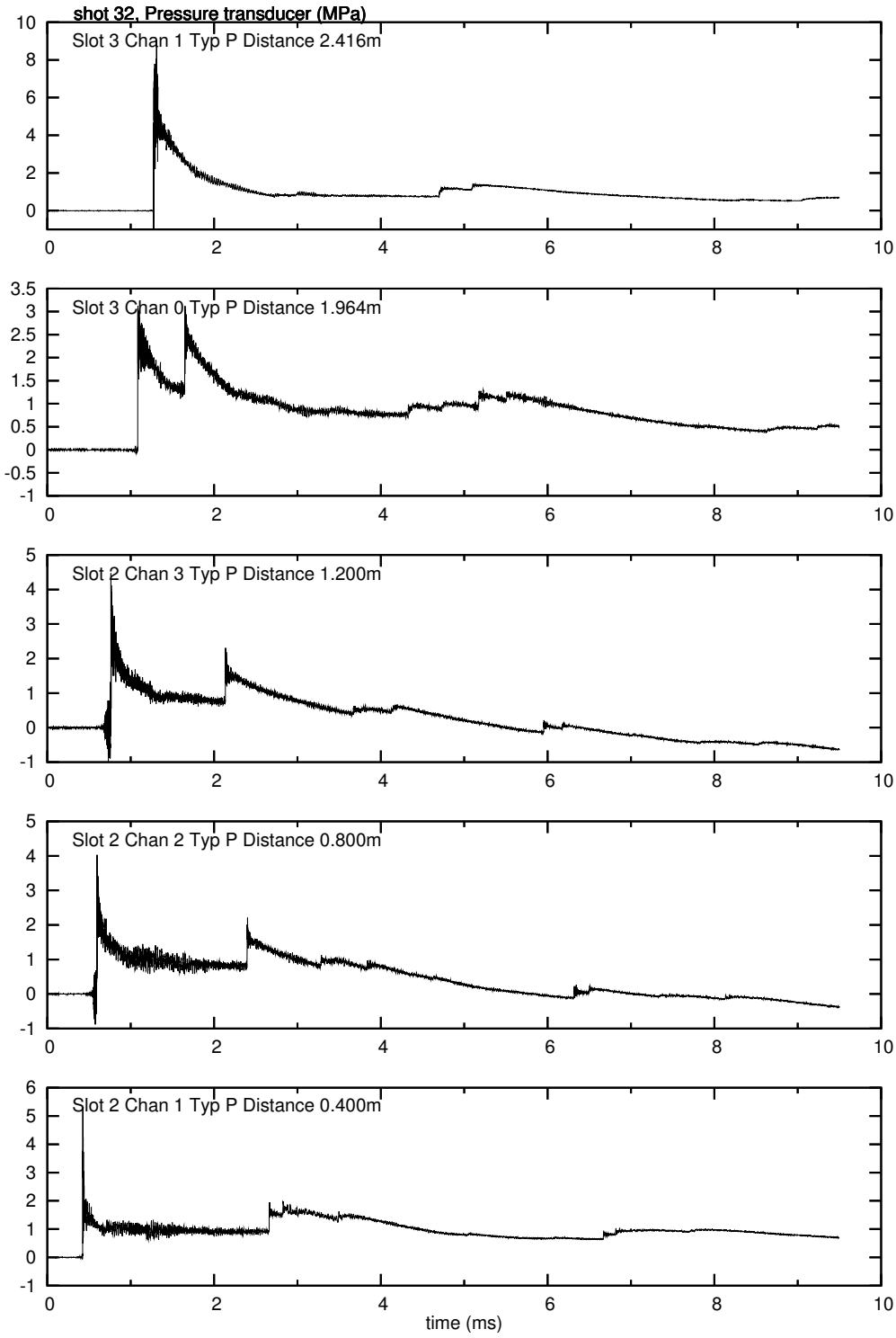

Figure E.66: Pressure signals of shot 32.

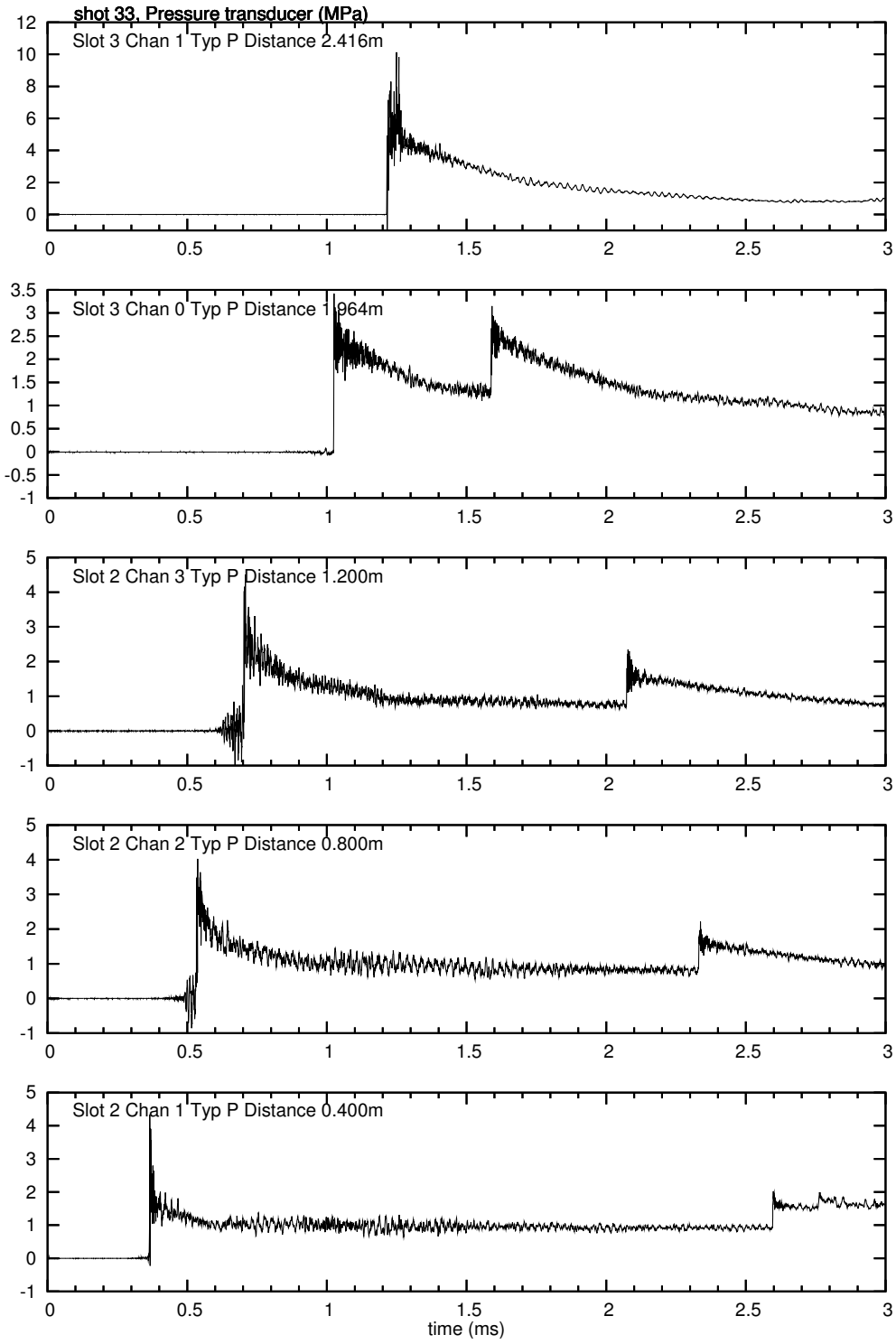

Figure E.67: Pressure signals of shot 33 with a short time scale.

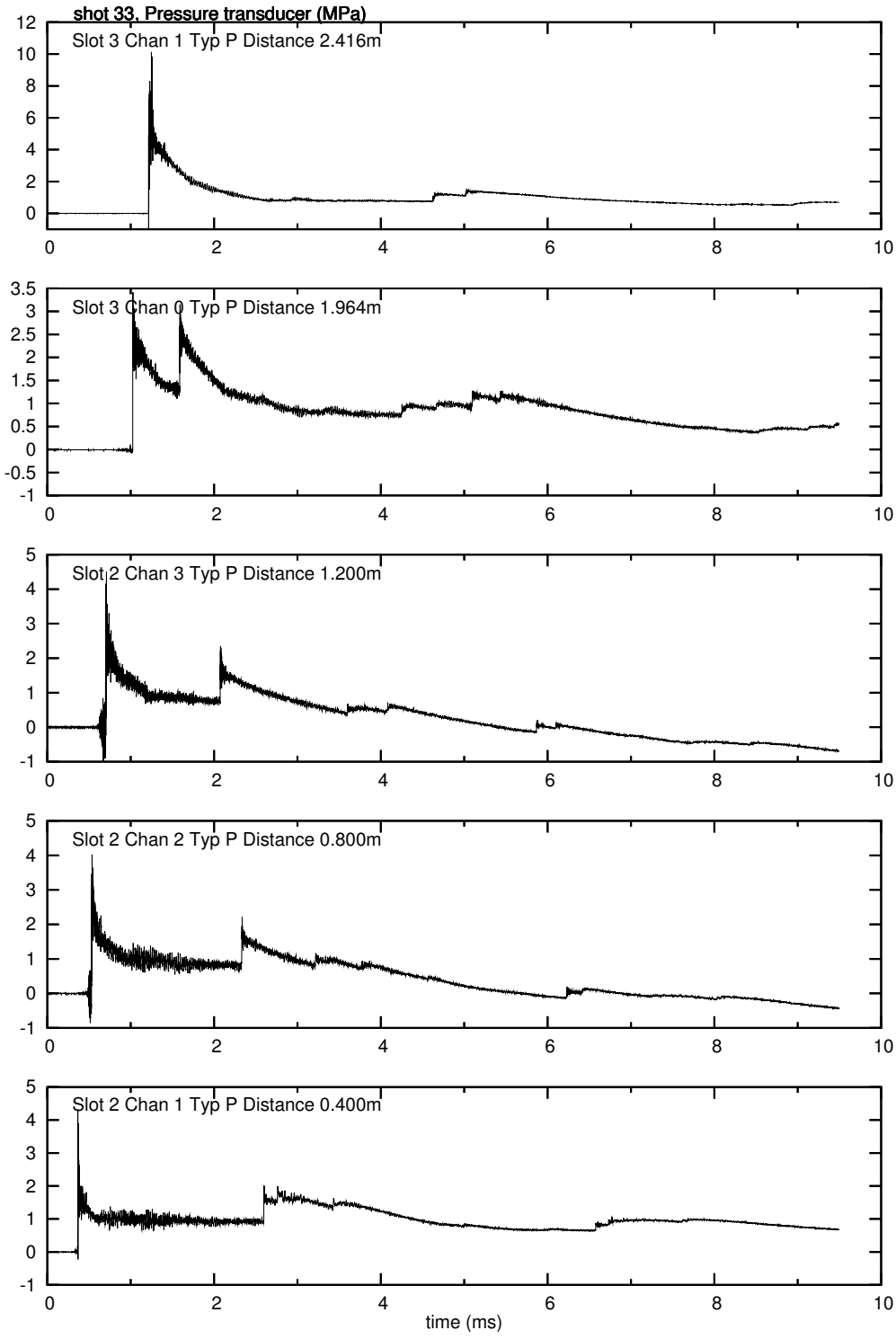

Figure E.68: Pressure signals of shot 33.

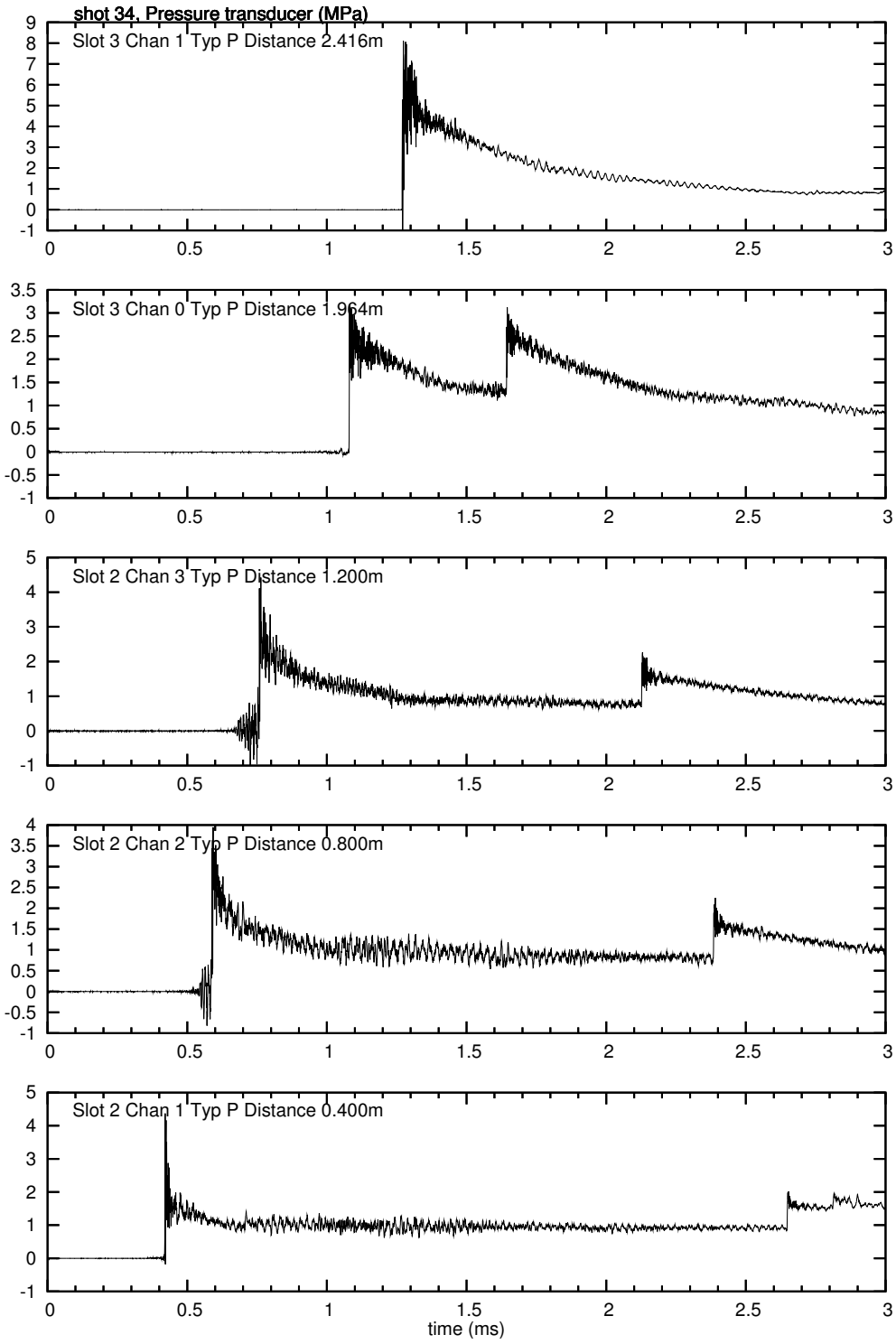

Figure E.69: Pressure signals of shot 34 with a short time scale.

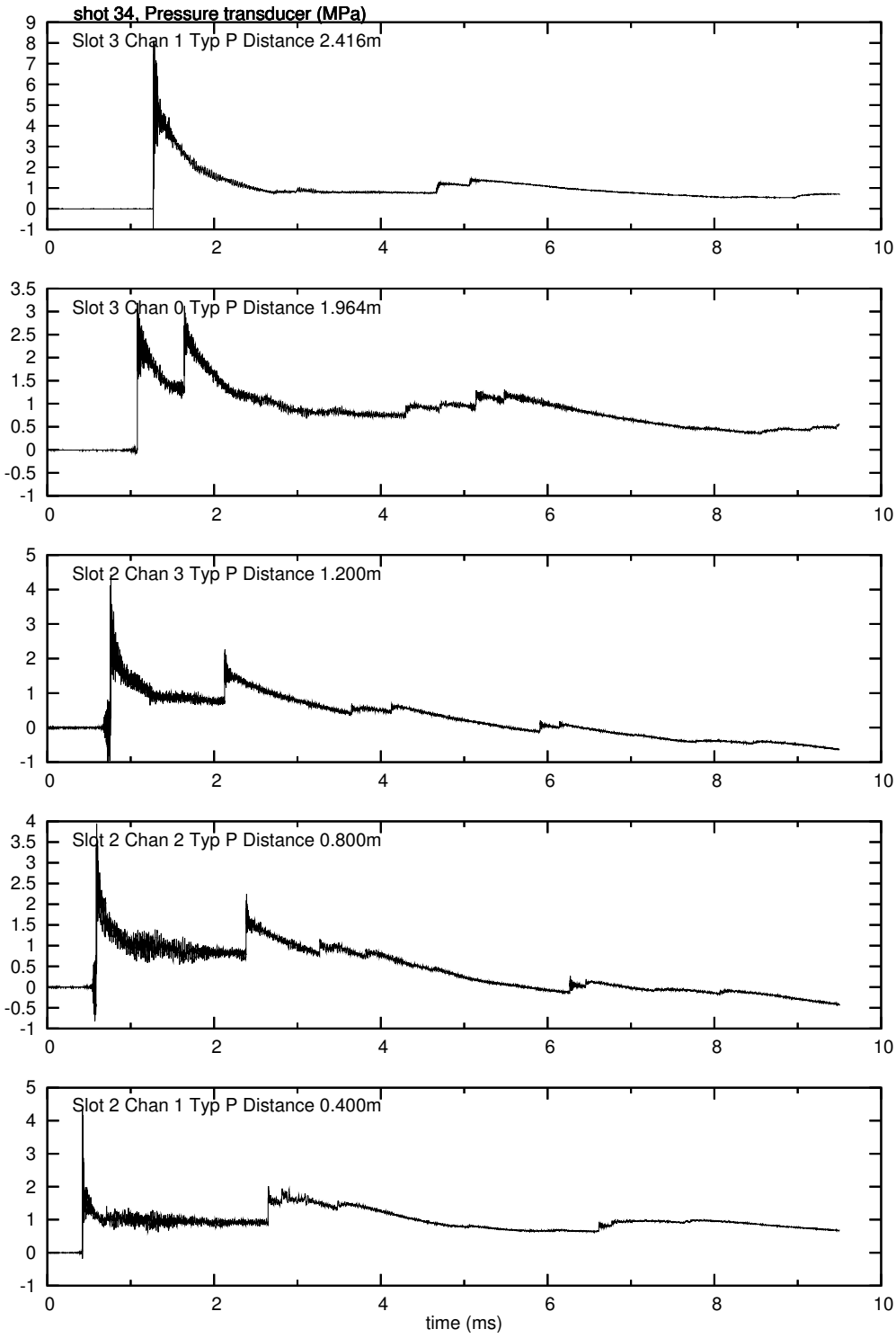

Figure E.70: Pressure signals of shot 34.

E.2 Series 2

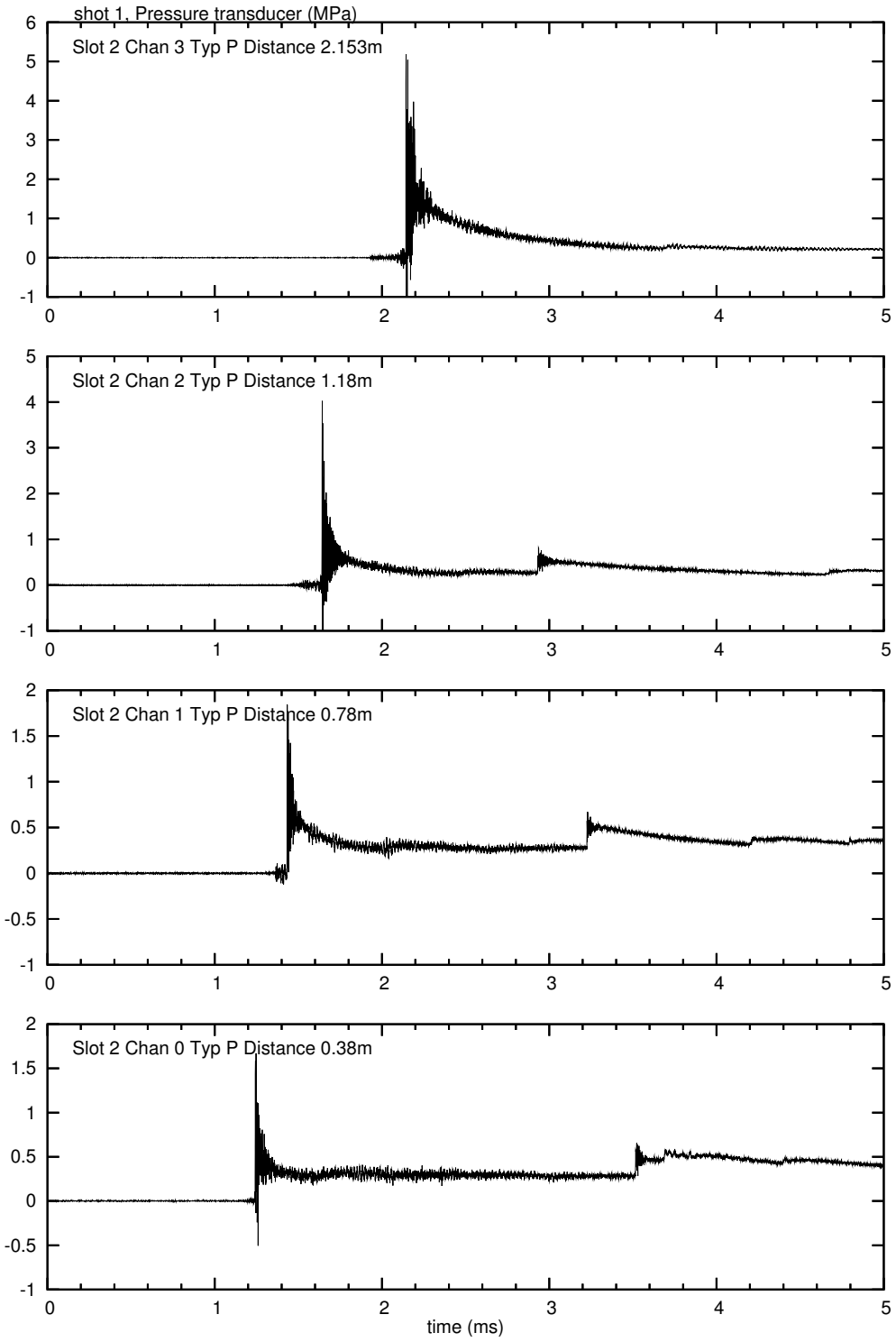

Figure E.71: Pressure signals of shot 1 with a short time scale.

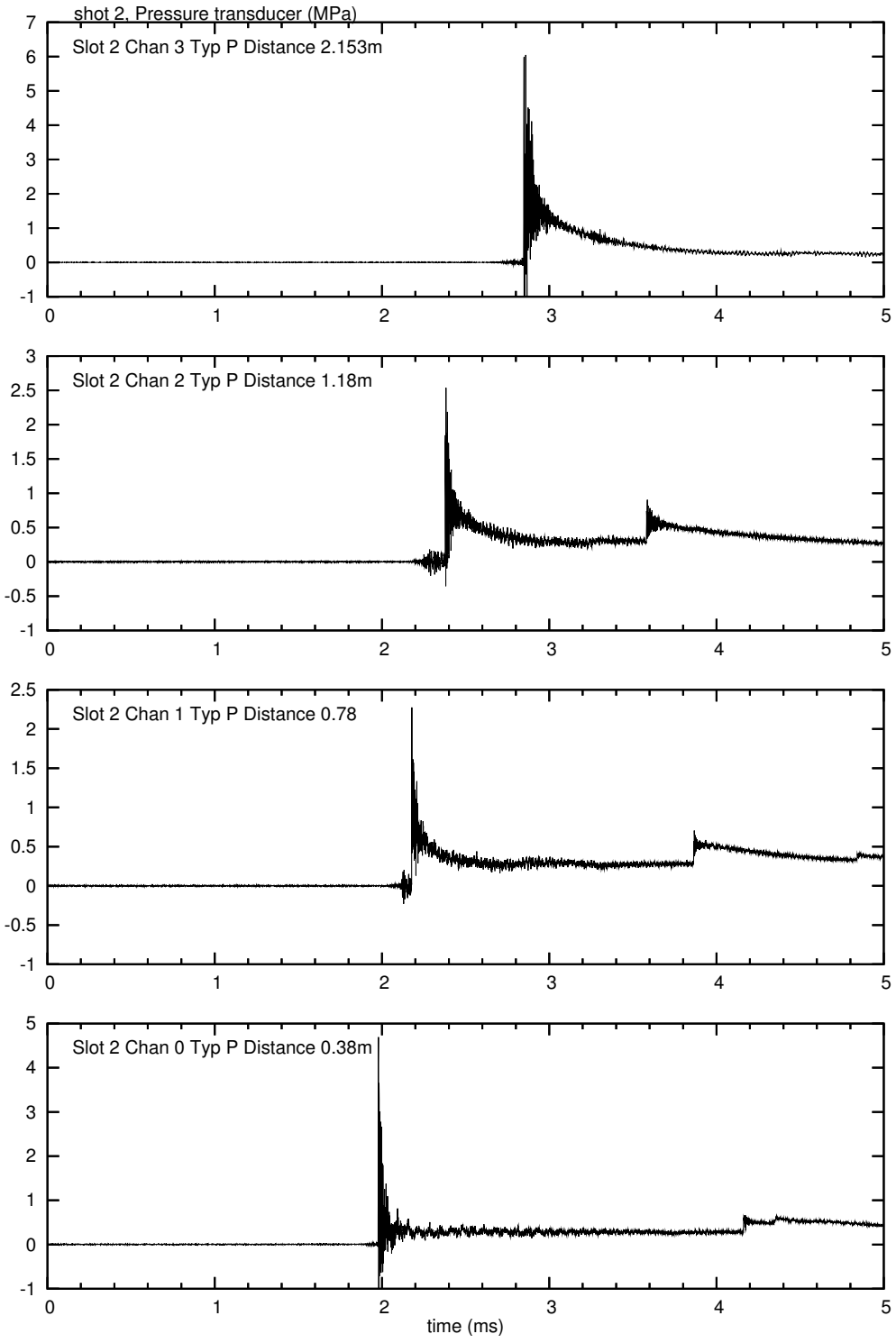

Figure E.72: Pressure signals of shot 2 with a short time scale.

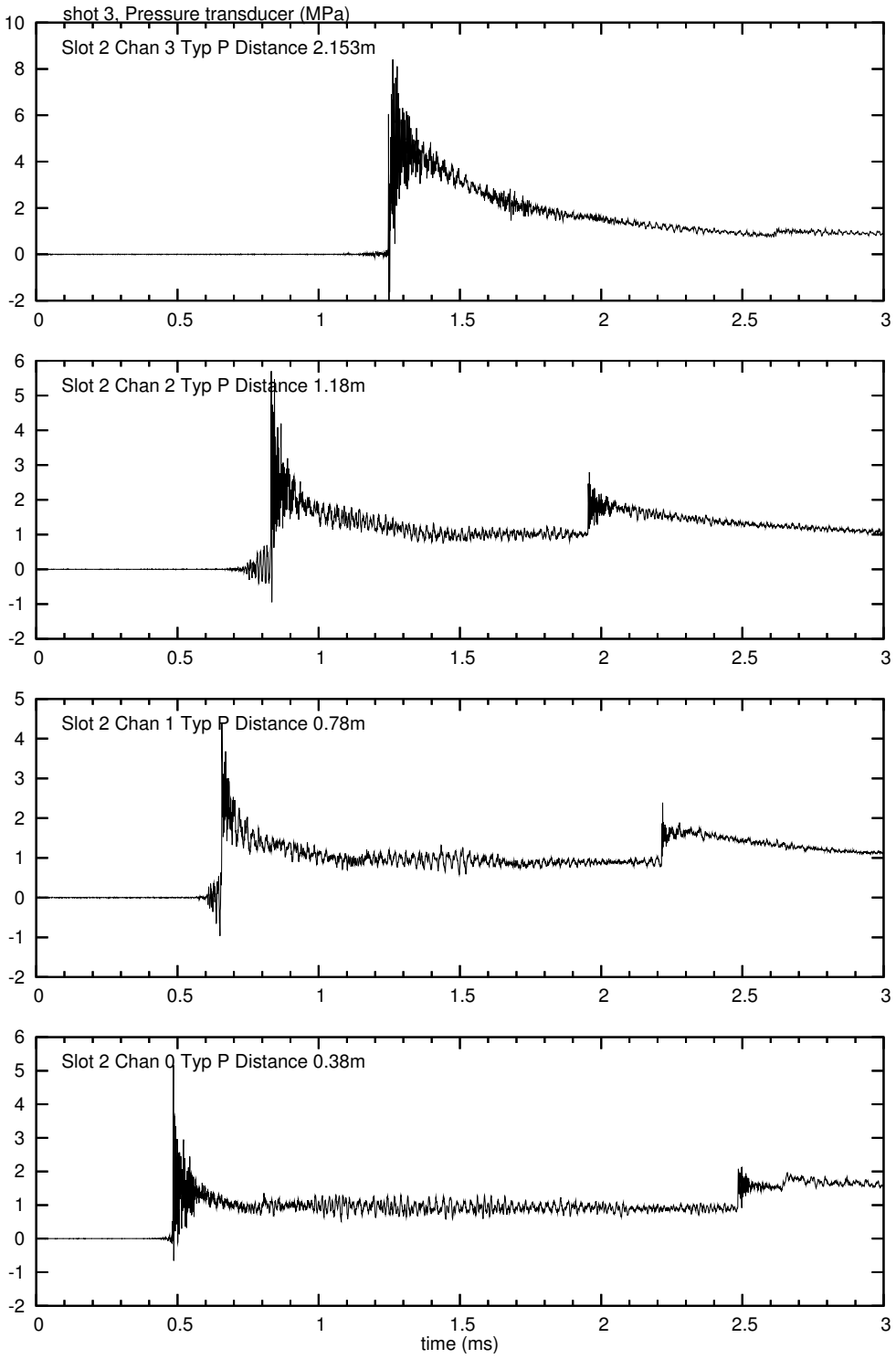

Figure E.73: Pressure signals of shot 3 with a short time scale.

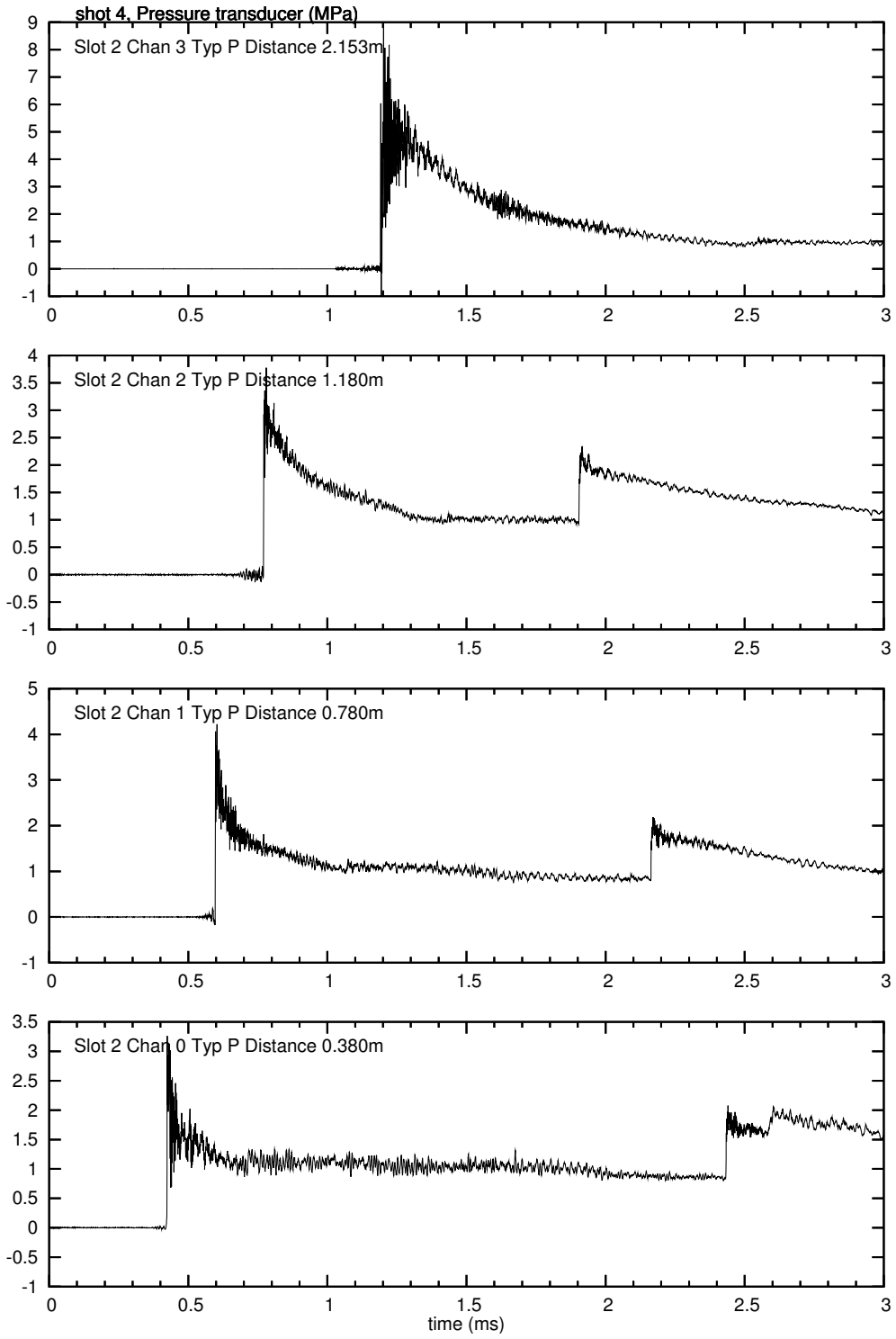

Figure E.74: Pressure signals of shot 4 with a short time scale.

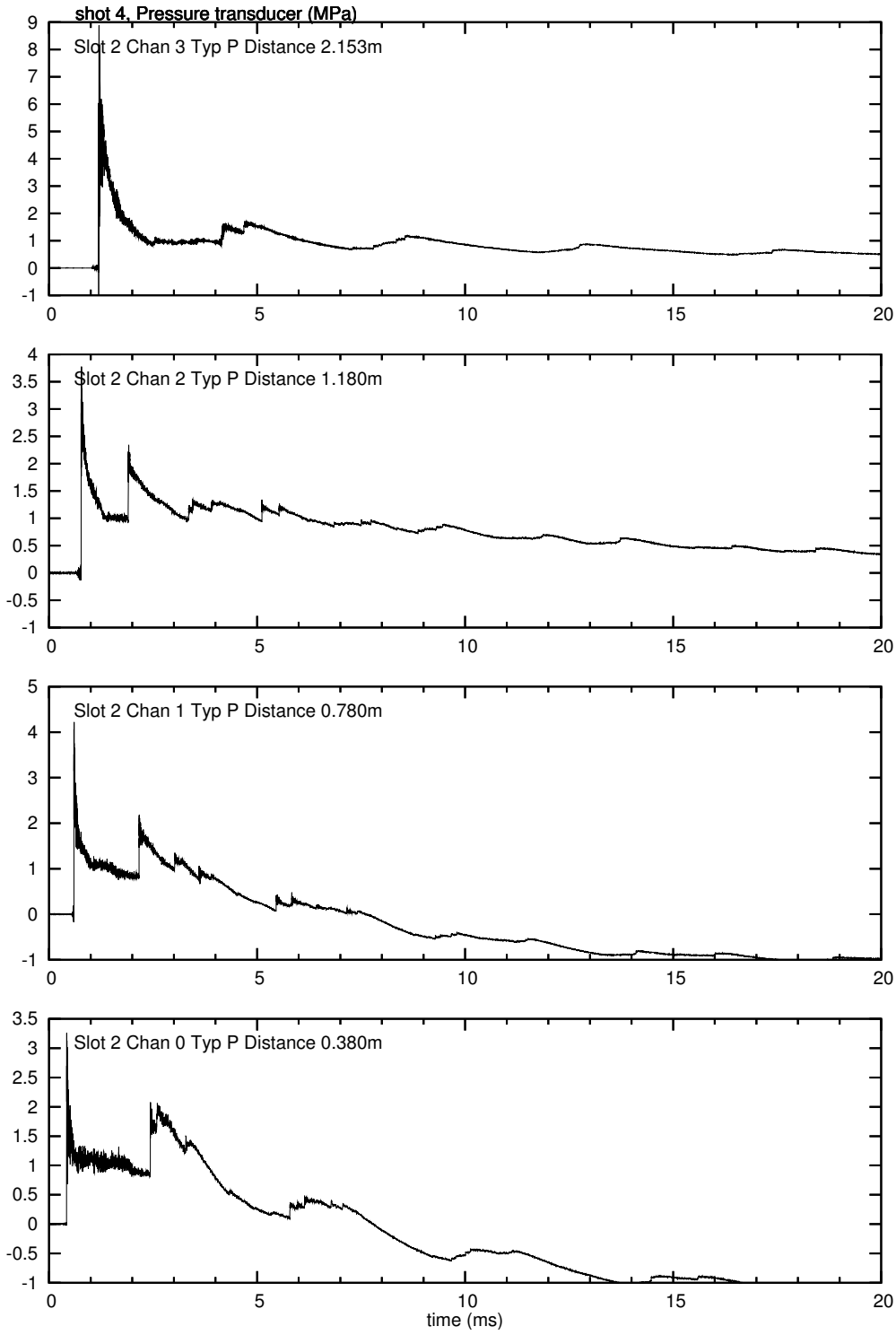

Figure E.75: Pressure signals of shot 4.

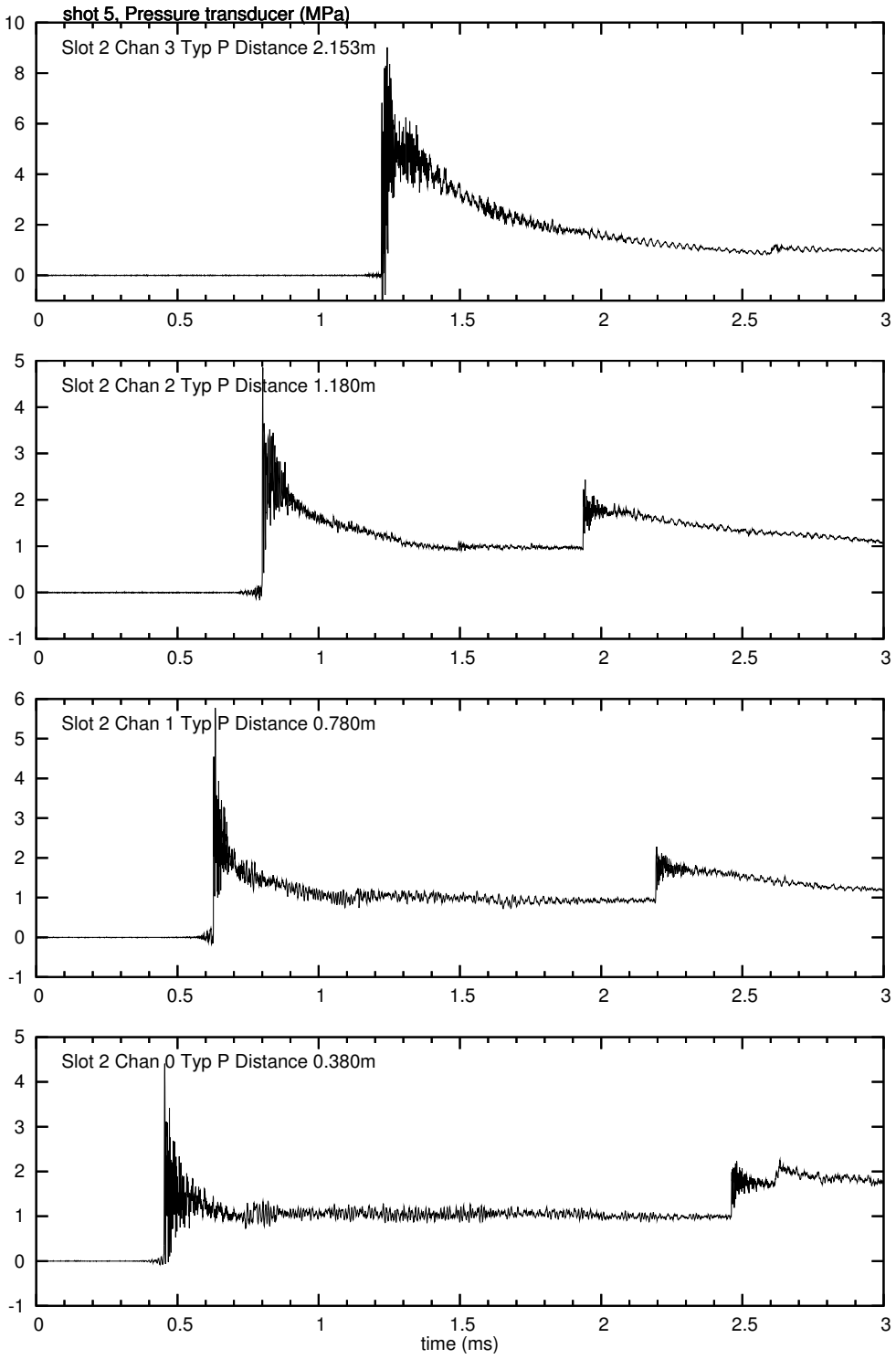

Figure E.76: Pressure signals of shot 5 with a short time scale.

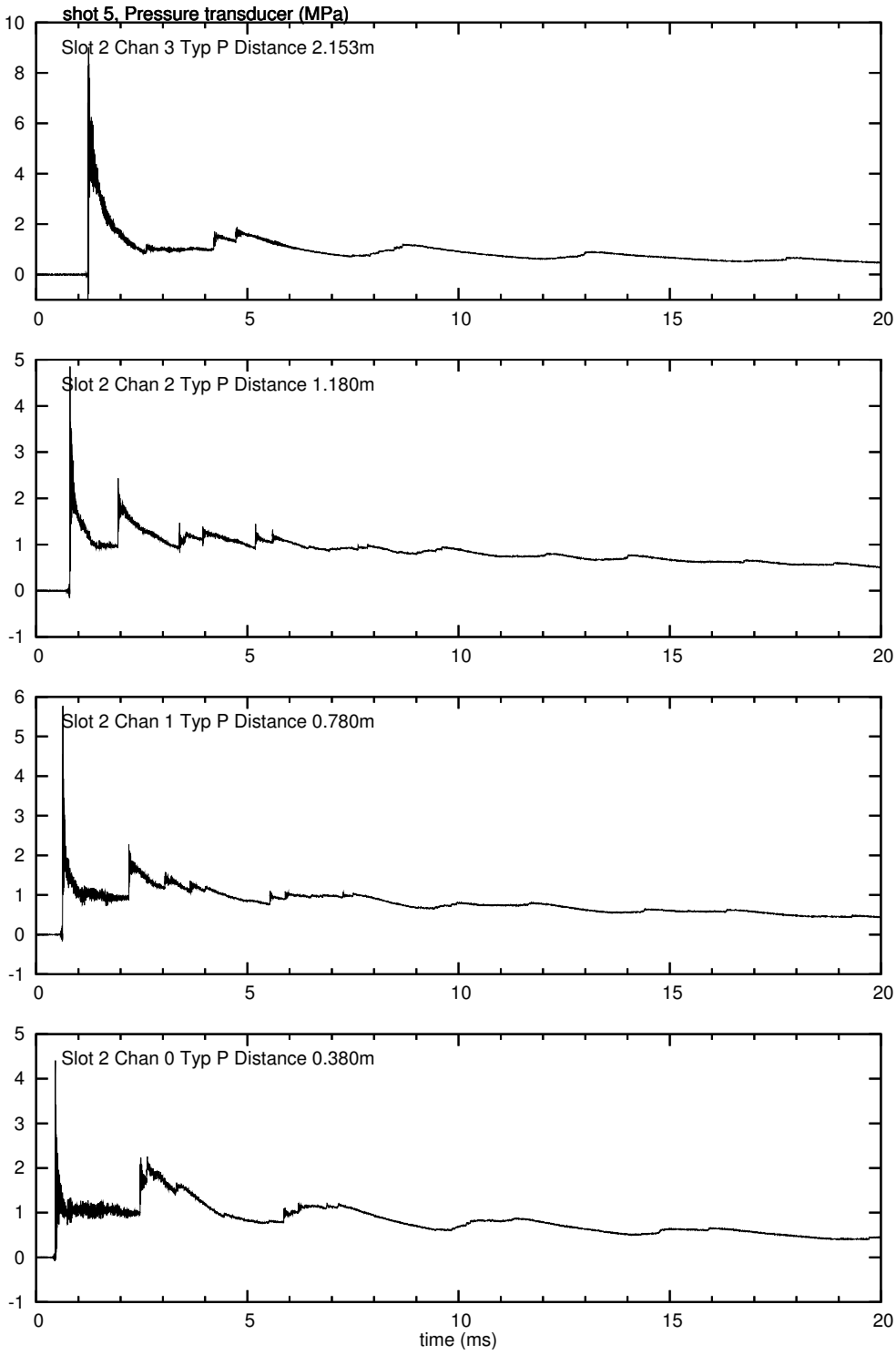

Figure E.77: Pressure signals of shot 5.

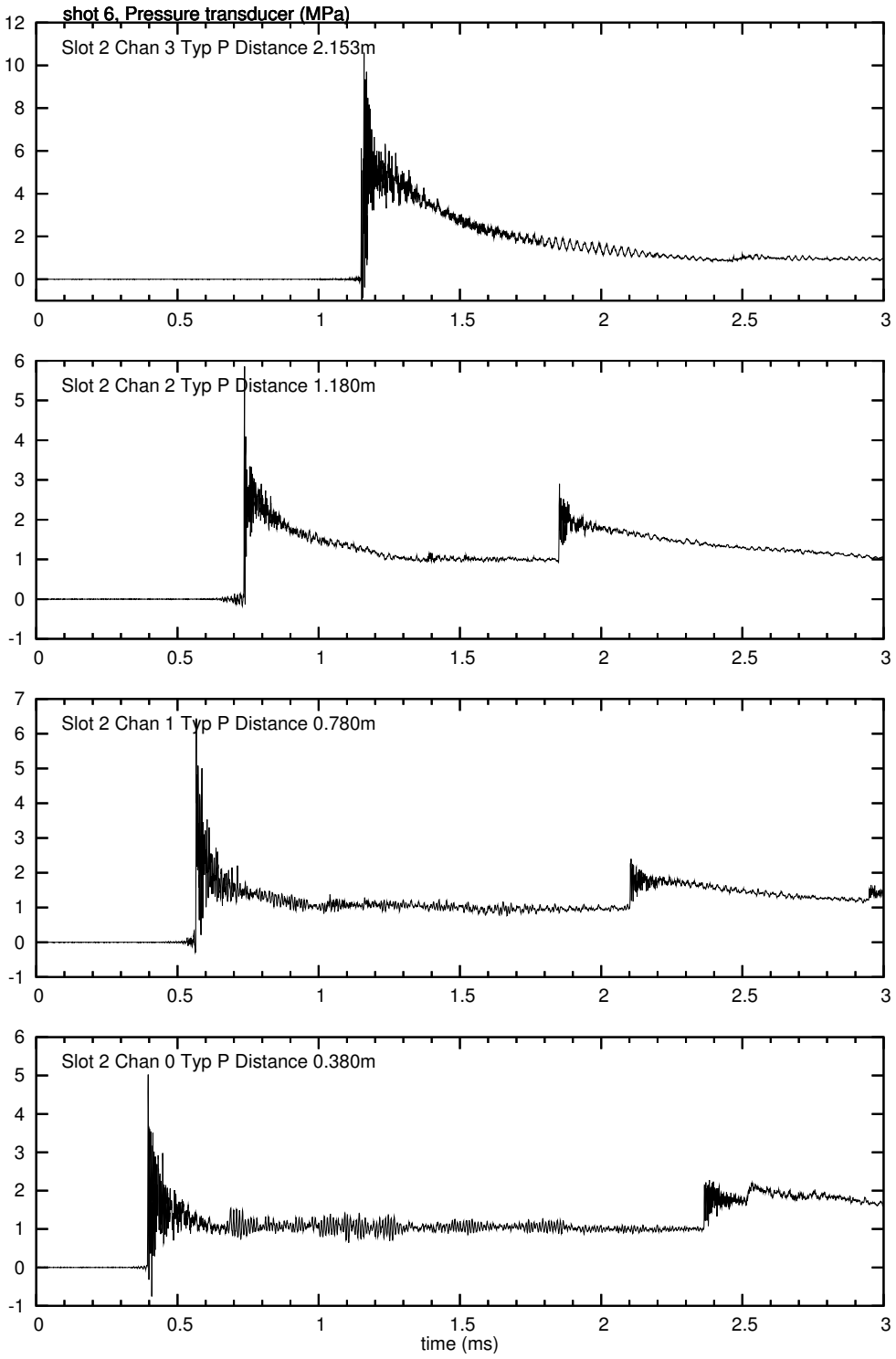

Figure E.78: Pressure signals of shot 6 with a short time scale.

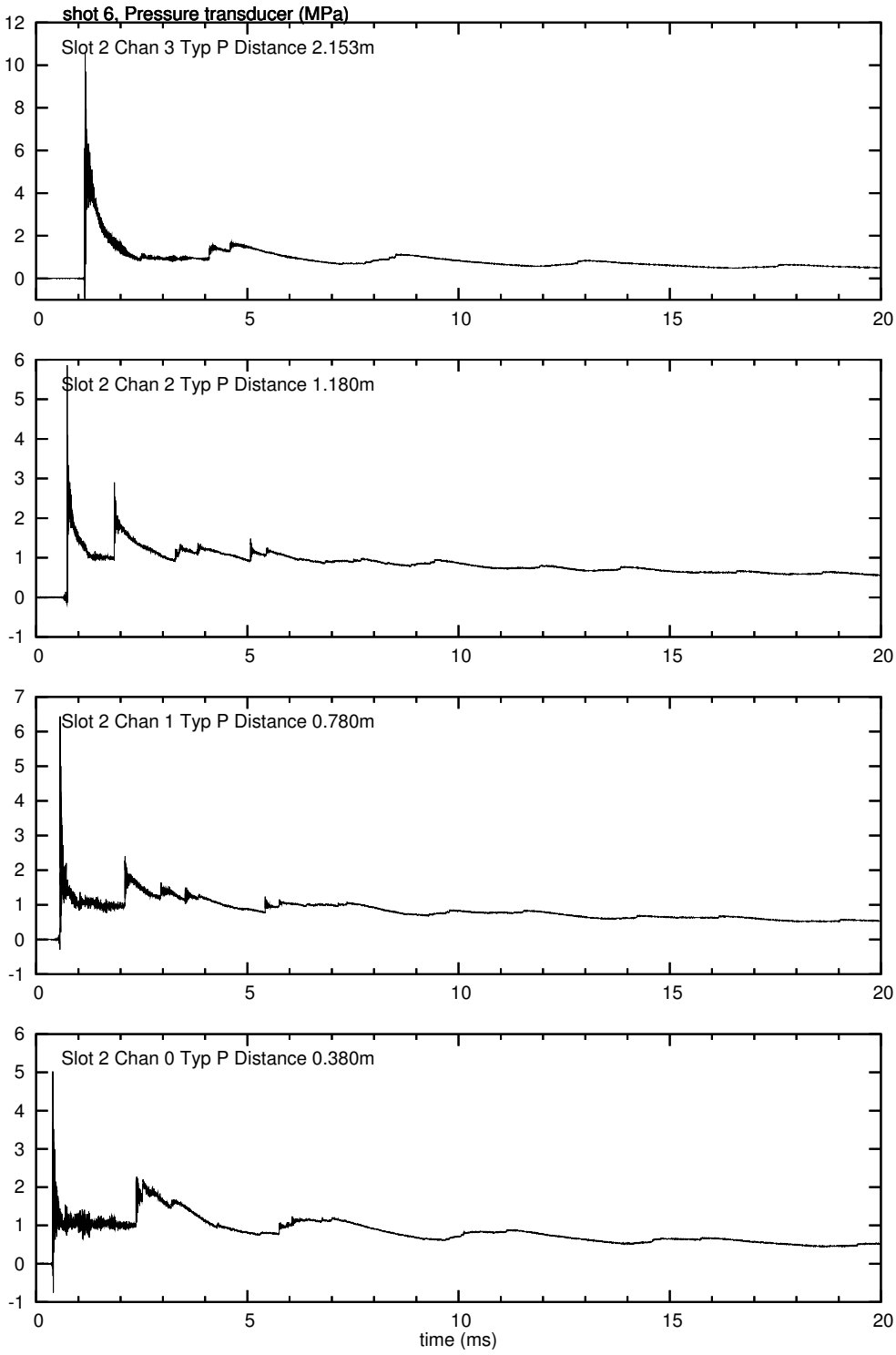

Figure E.79: Pressure signals of shot 6.

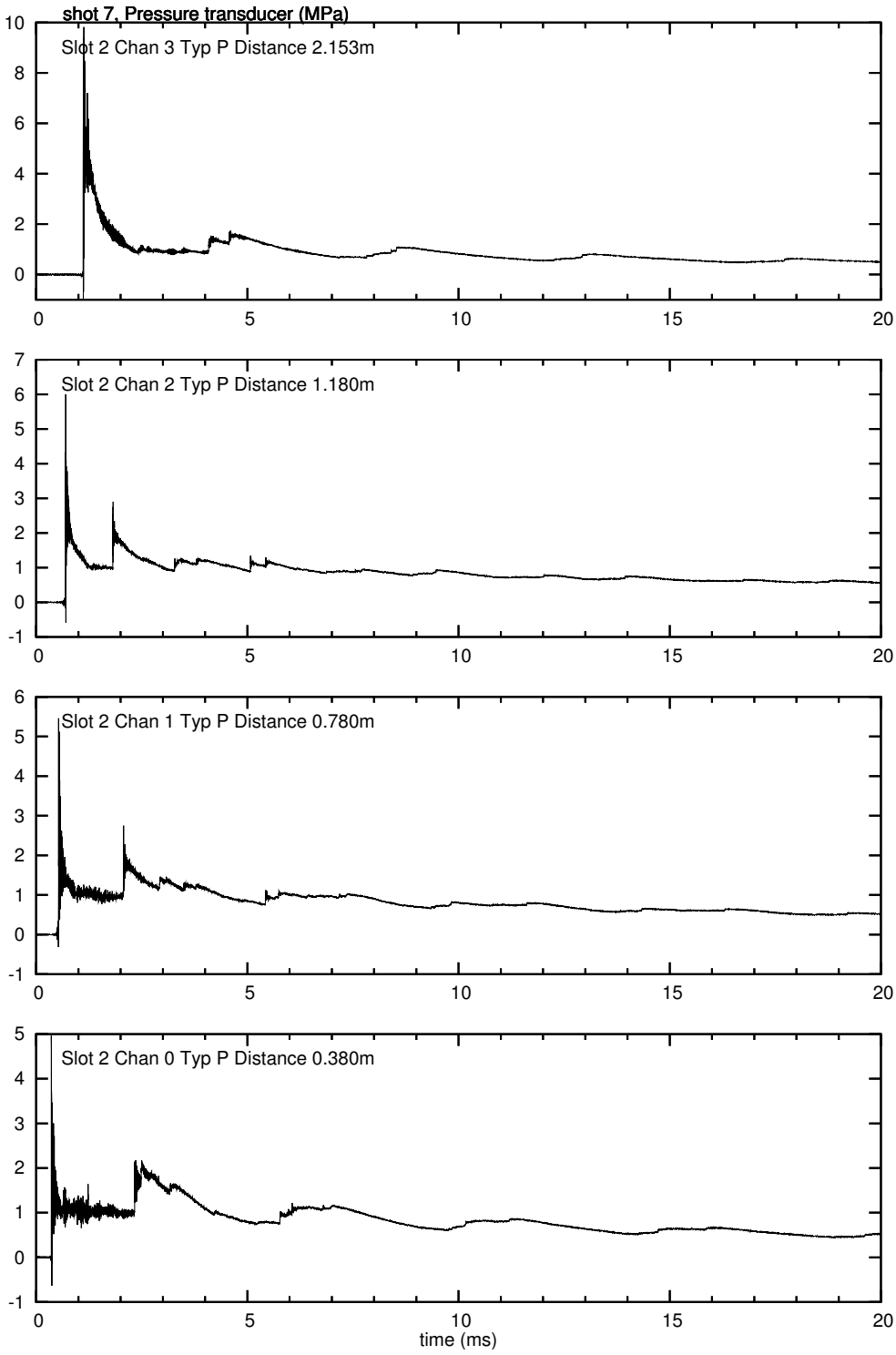

Figure E.80: Pressure signals of shot 7.

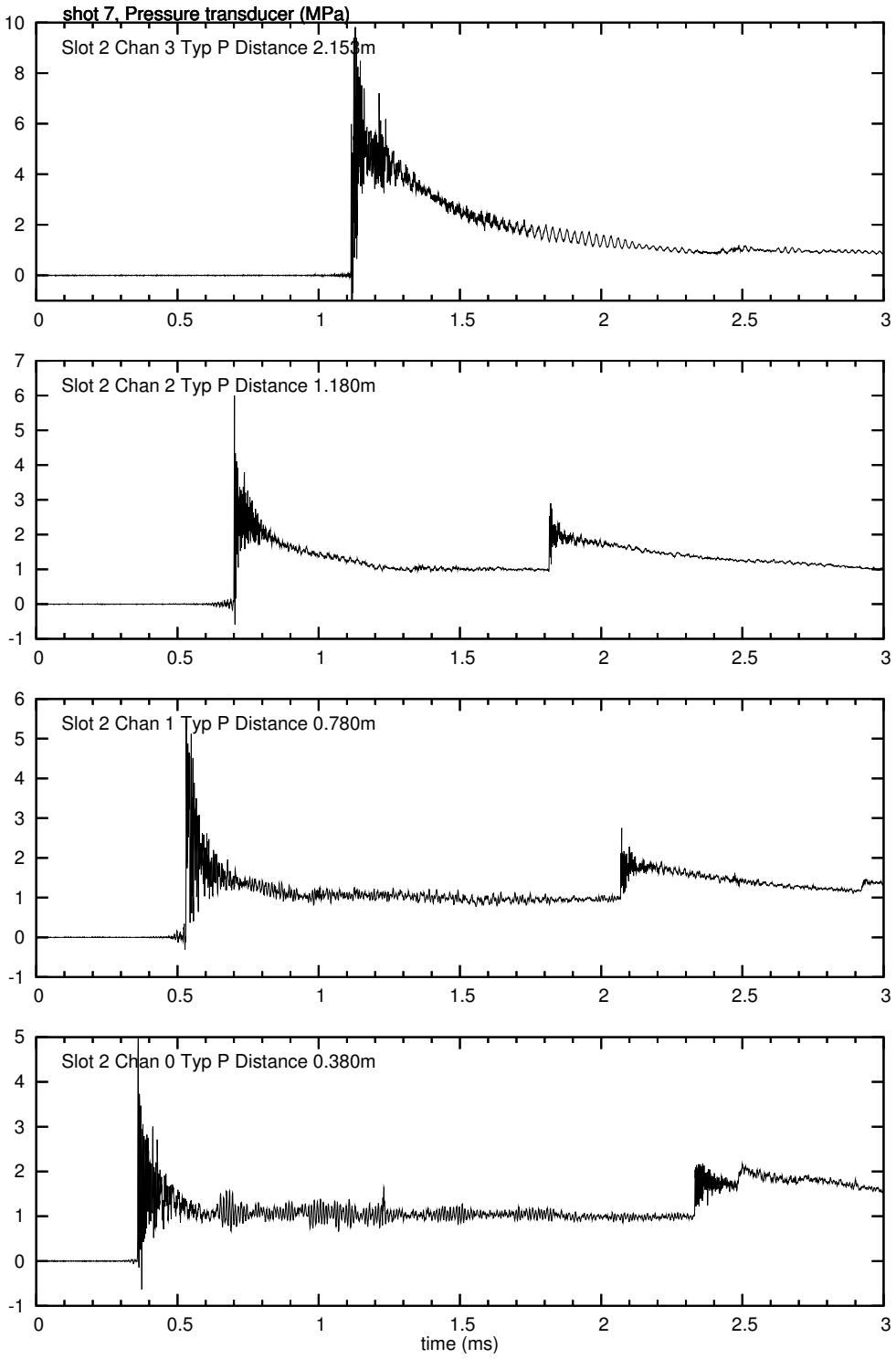

Figure E.81: Pressure signals of shot 7 with a short time scale.

Appendix F

Data for Driven Thin Tubes

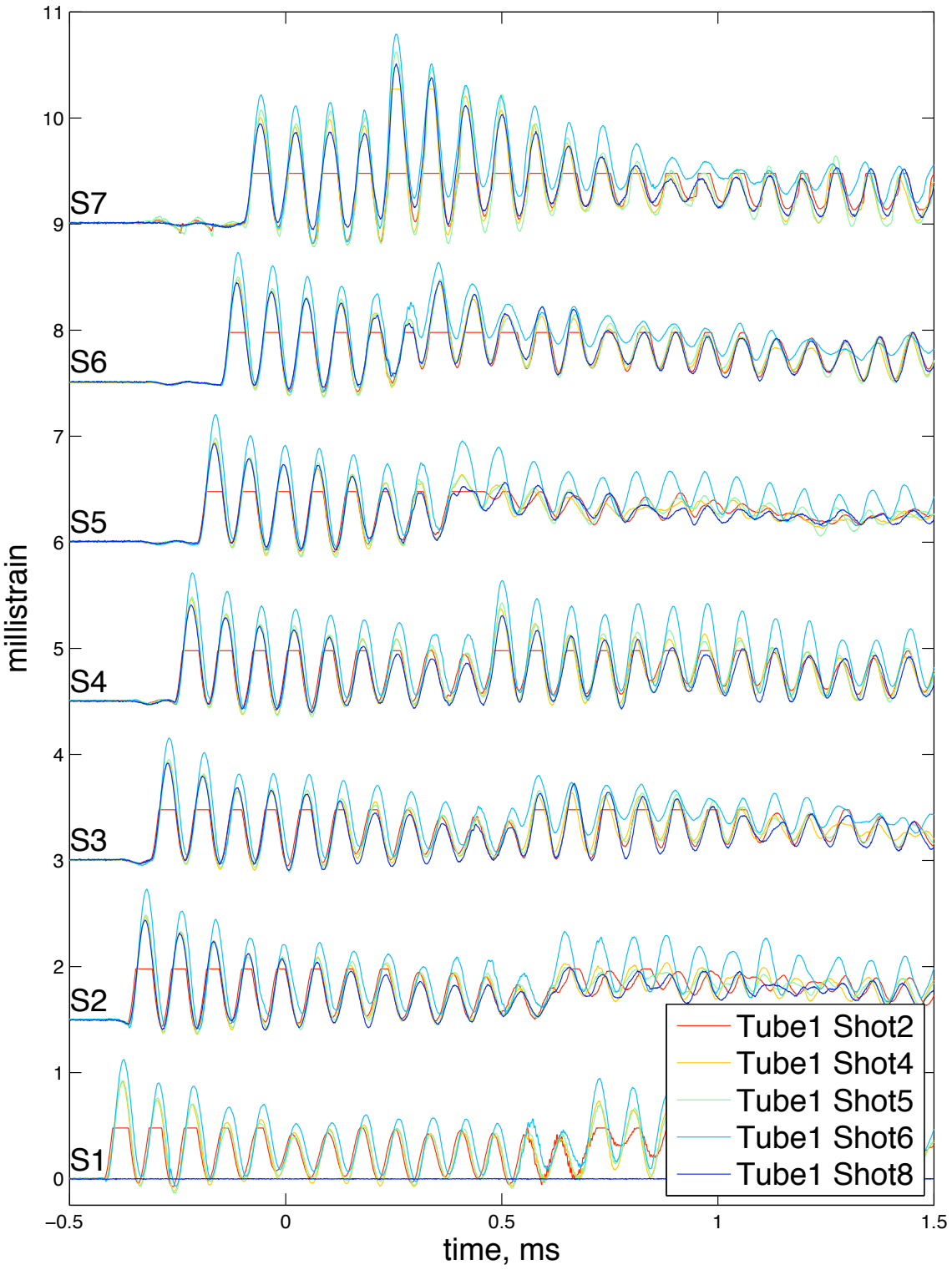

Figure F.1: Hoop strain data for elastic shots in tube 1.

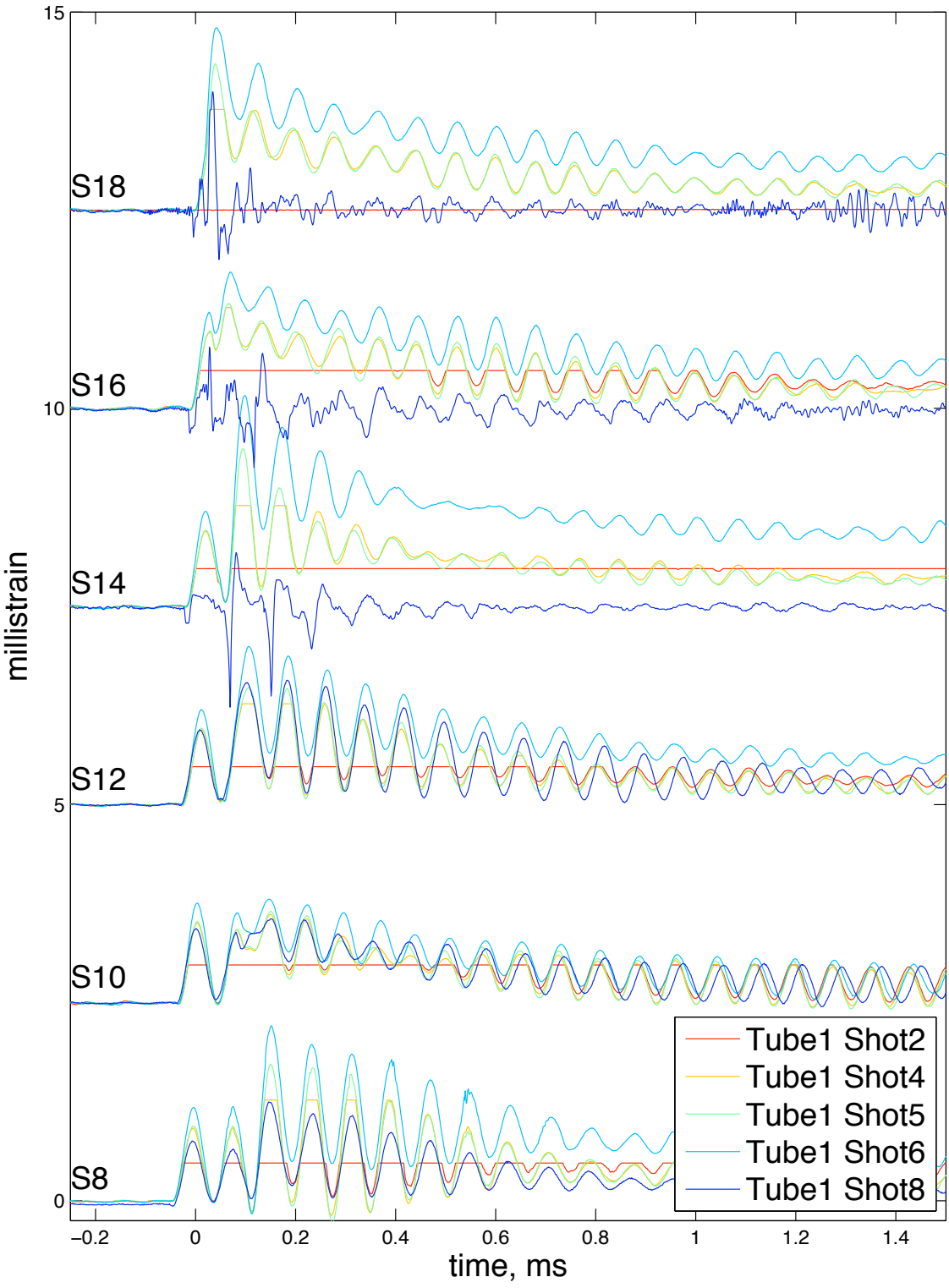

Figure F.2: Hoop strain data for elastic shots in tube 1.

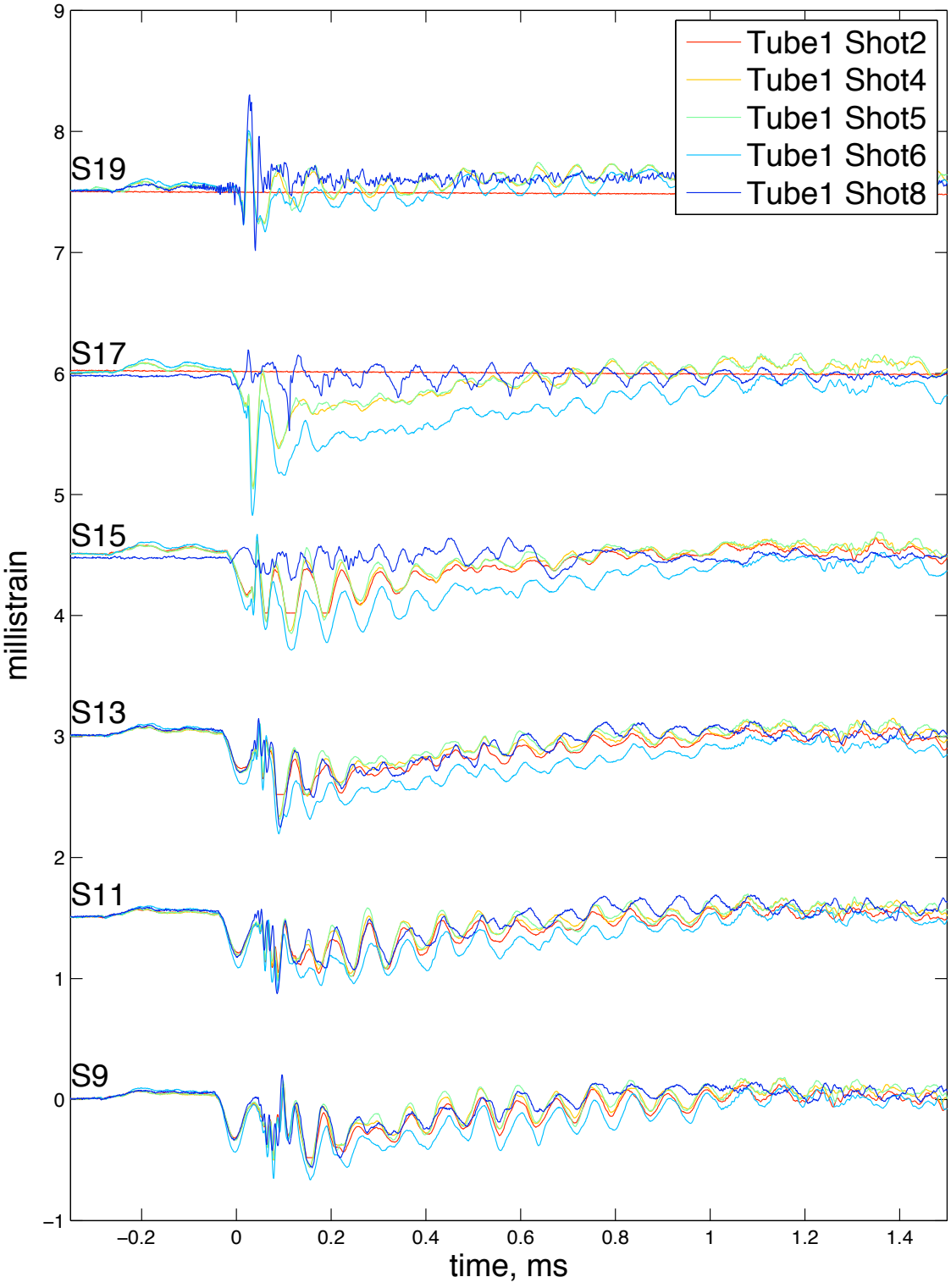

Figure F.3: Longitudinal strain data for elastic shots in tube 1.

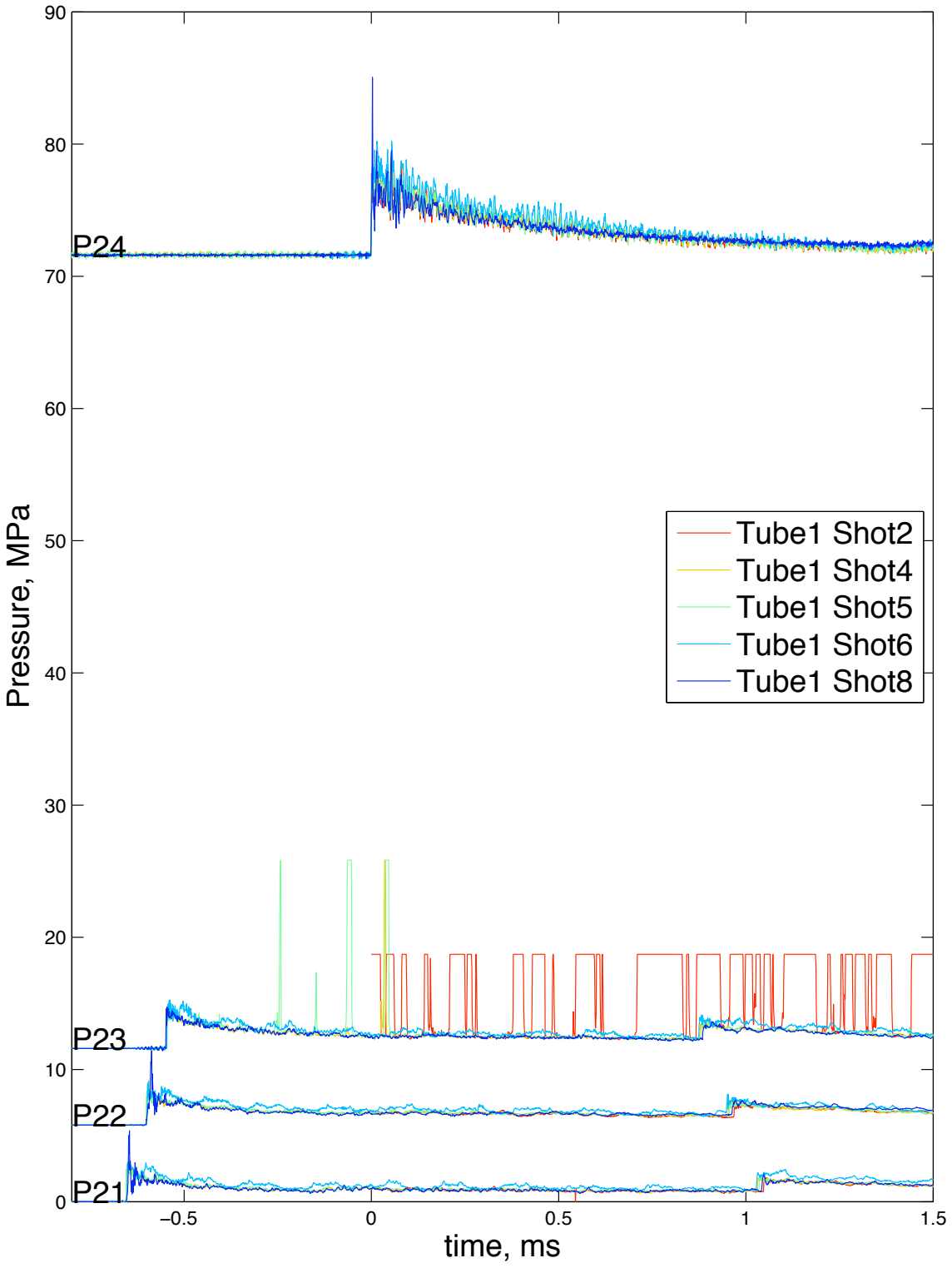

Figure F.4: Pressure data for elastic shots in tube 1.

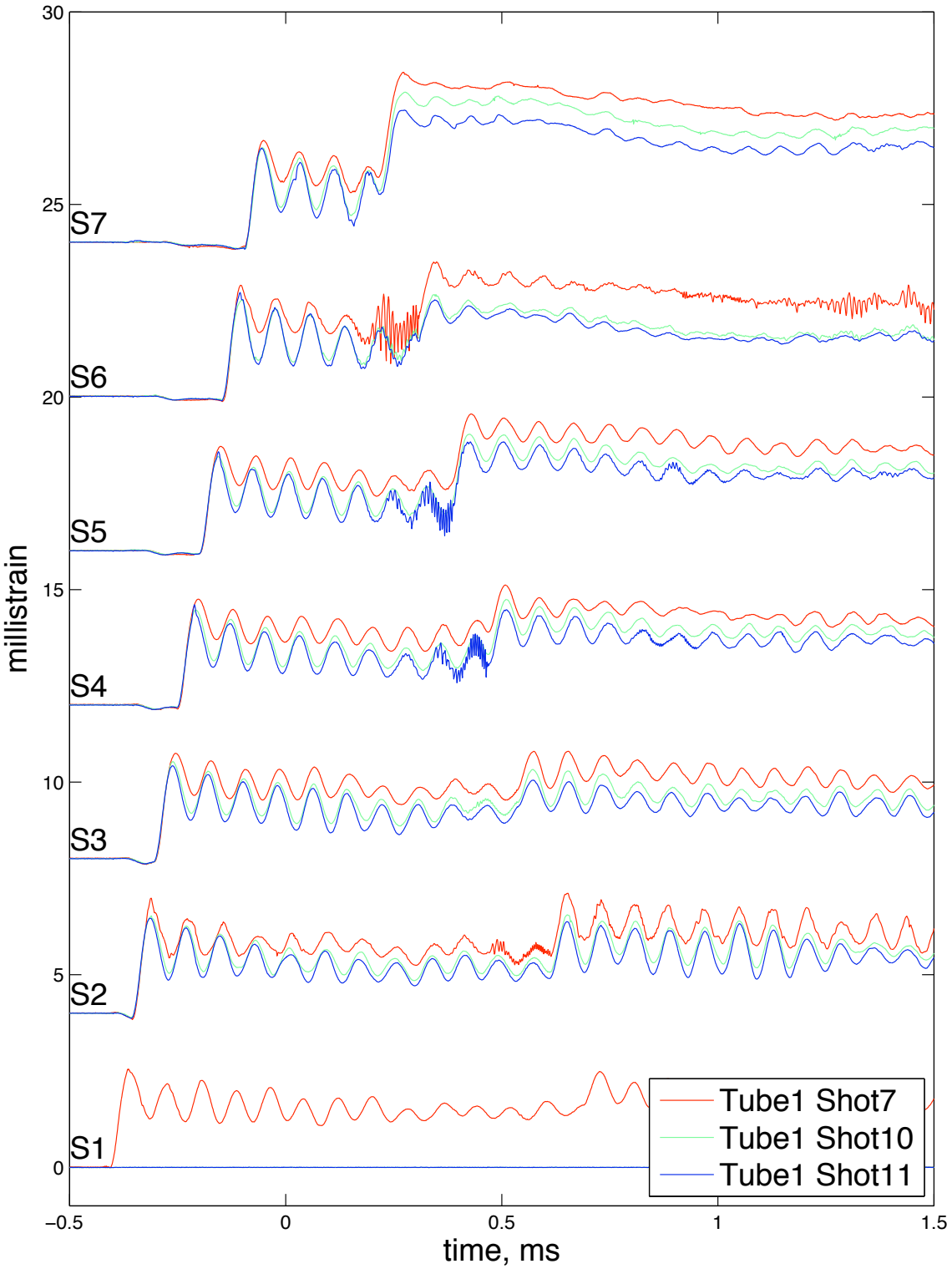

Figure F.5: Hoop strain data for plastic shots in tube 1.

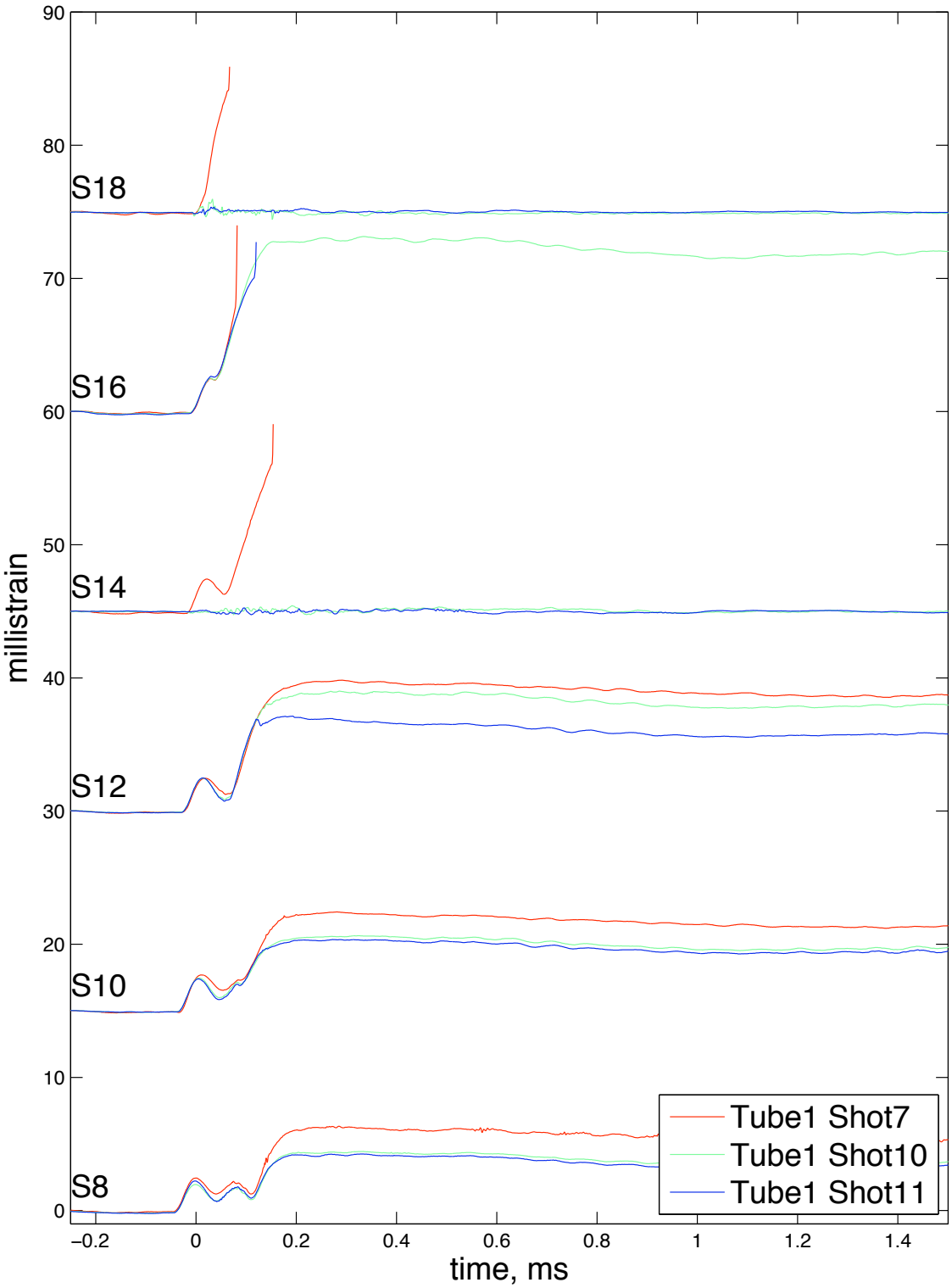

Figure F.6: Hoop strain data for plastic shots in tube 1.

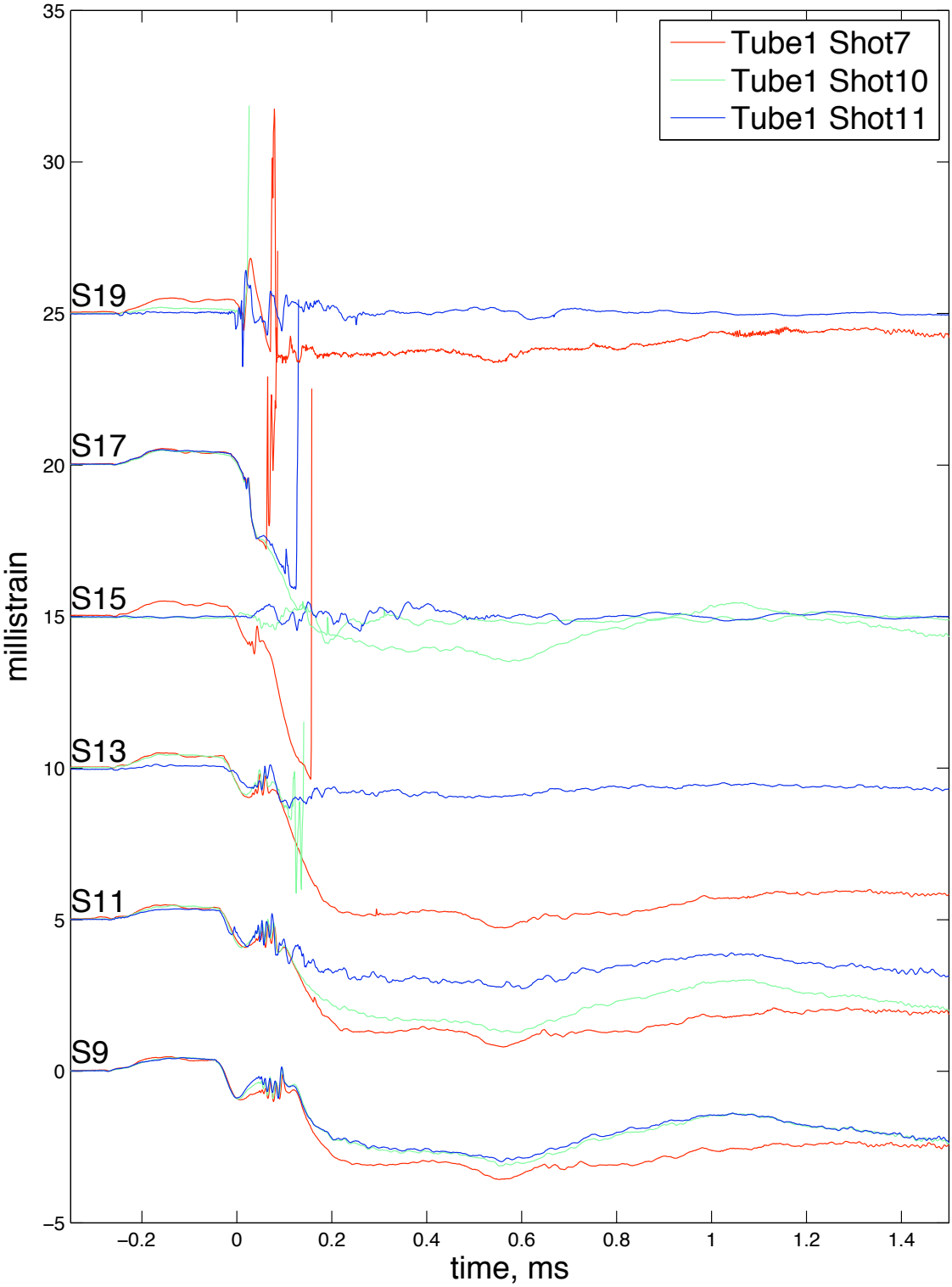

Figure F.7: Longitudinal strain data for plastic shots in tube 1.

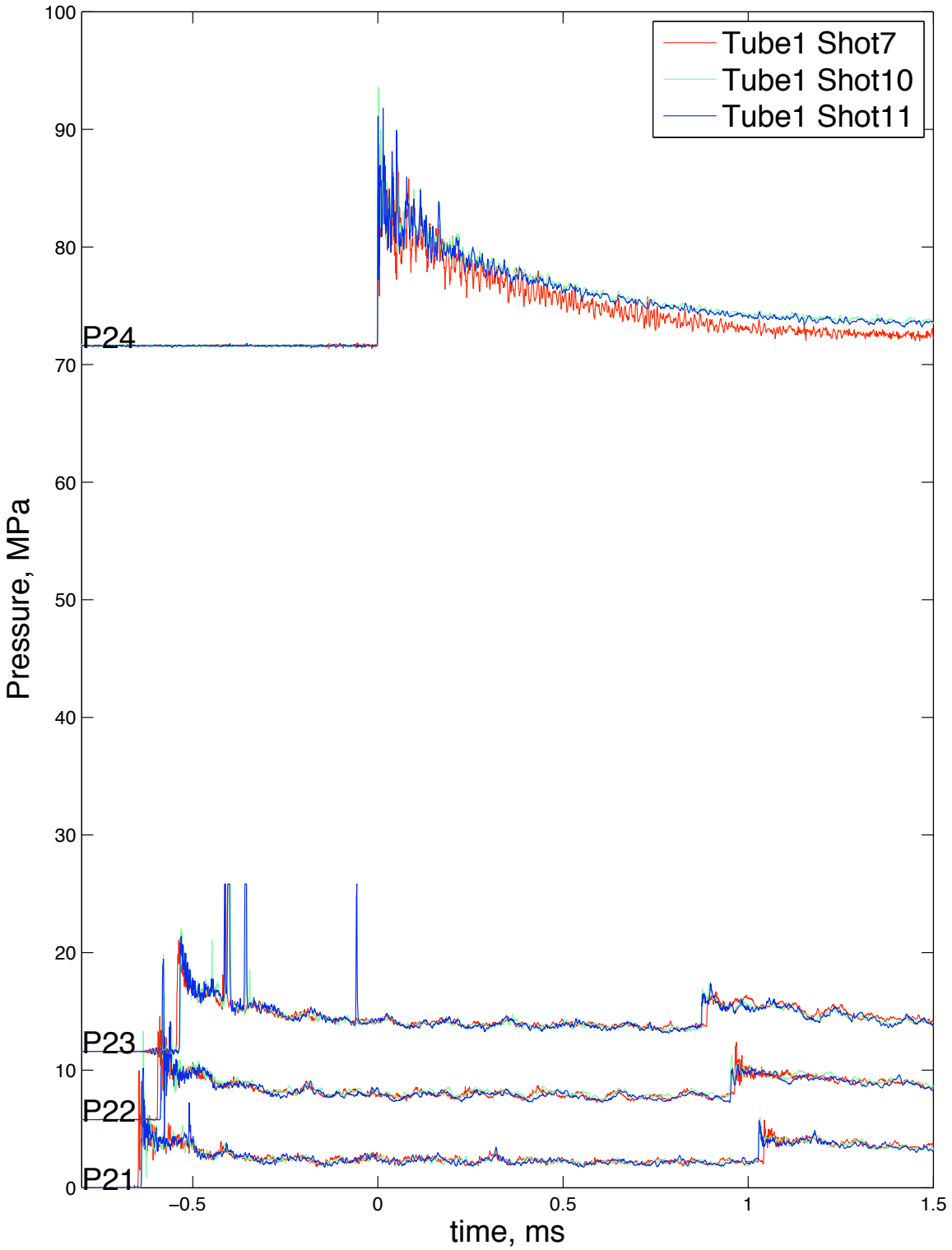

Figure F.8: Pressure data for plastic shots in tube 1.

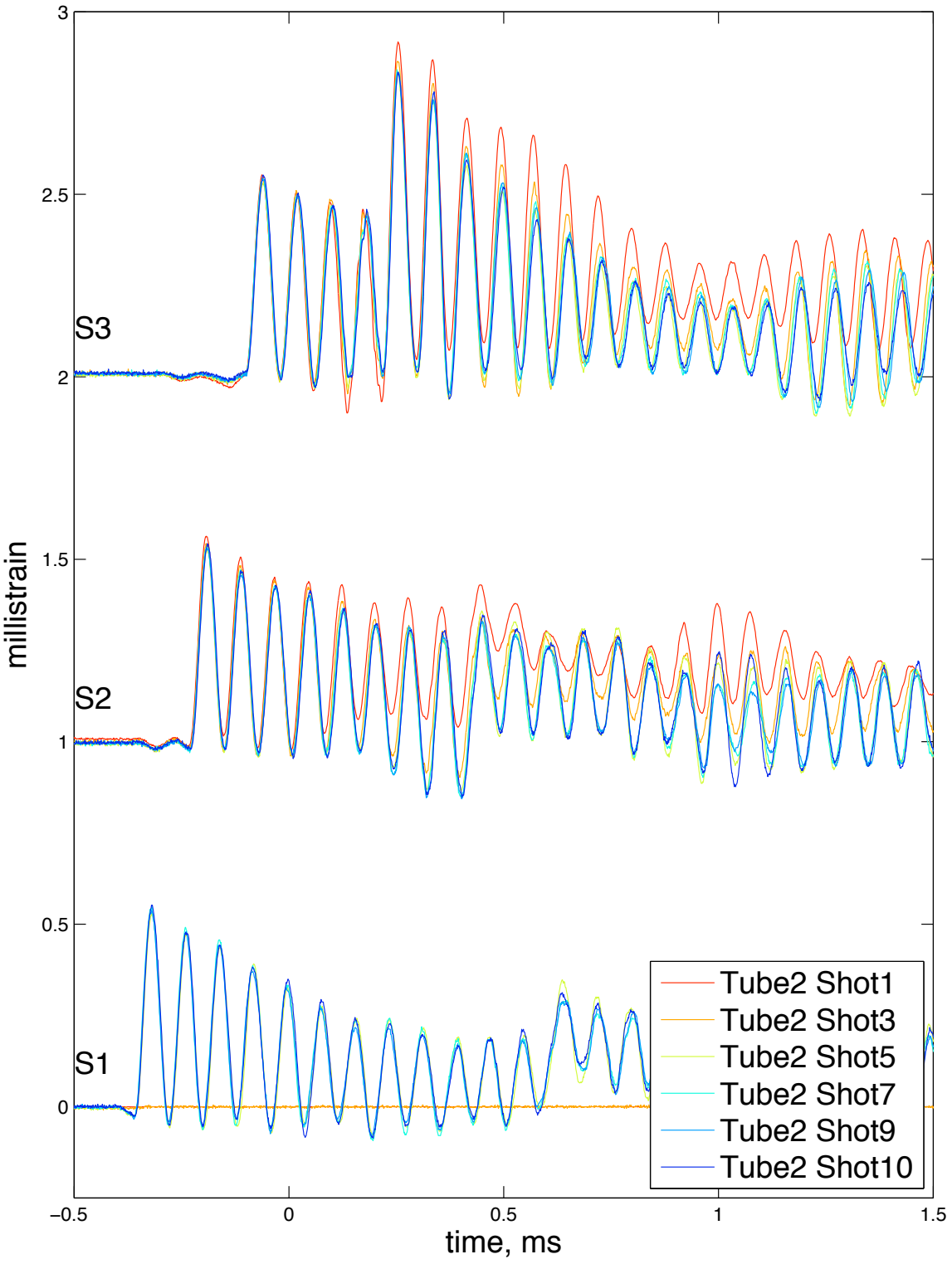

Figure F.9: Hoop strain data for elastic shots in tube 2.

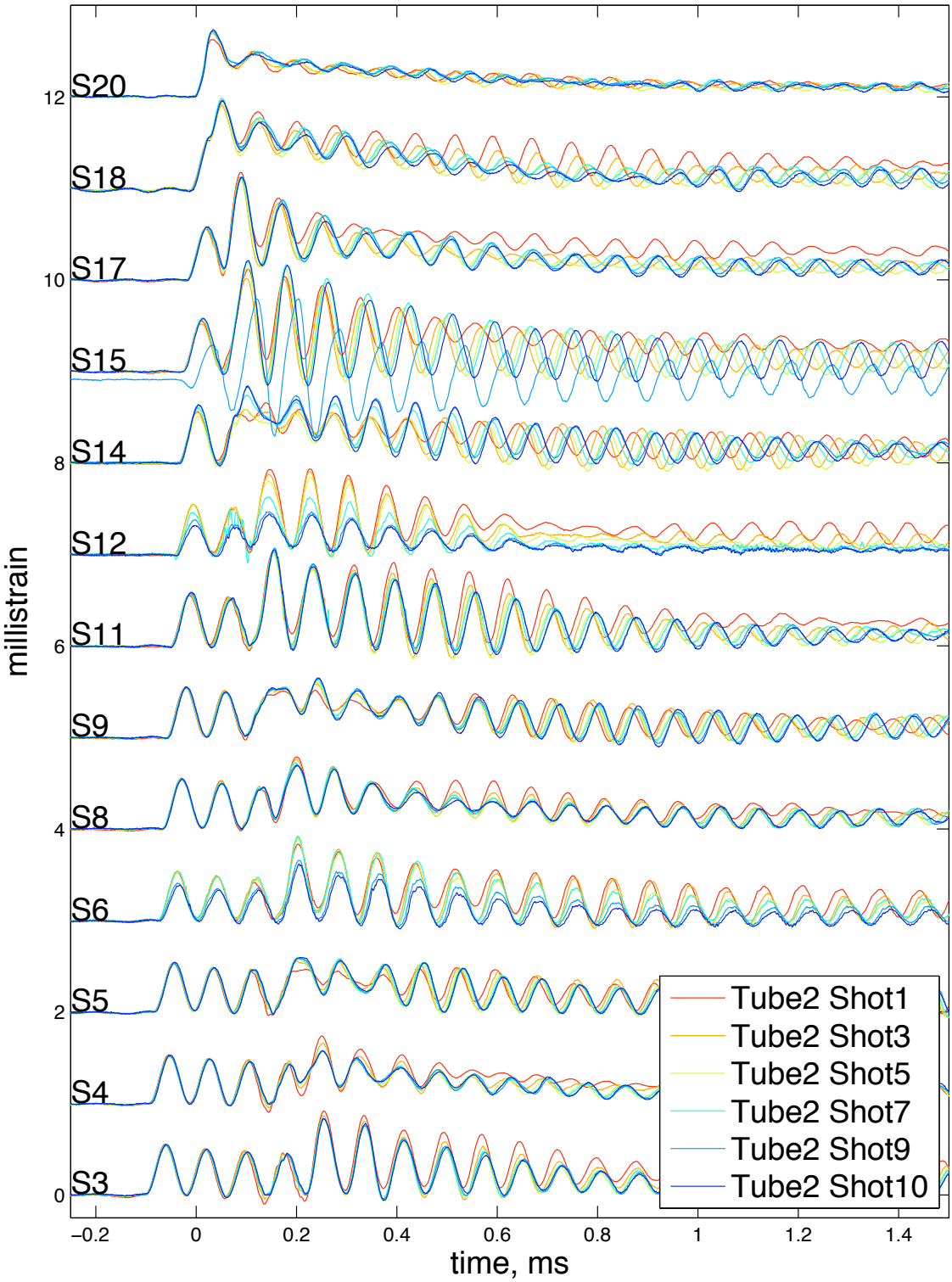

Figure F.10: Hoop strain data for elastic shots in tube 2.

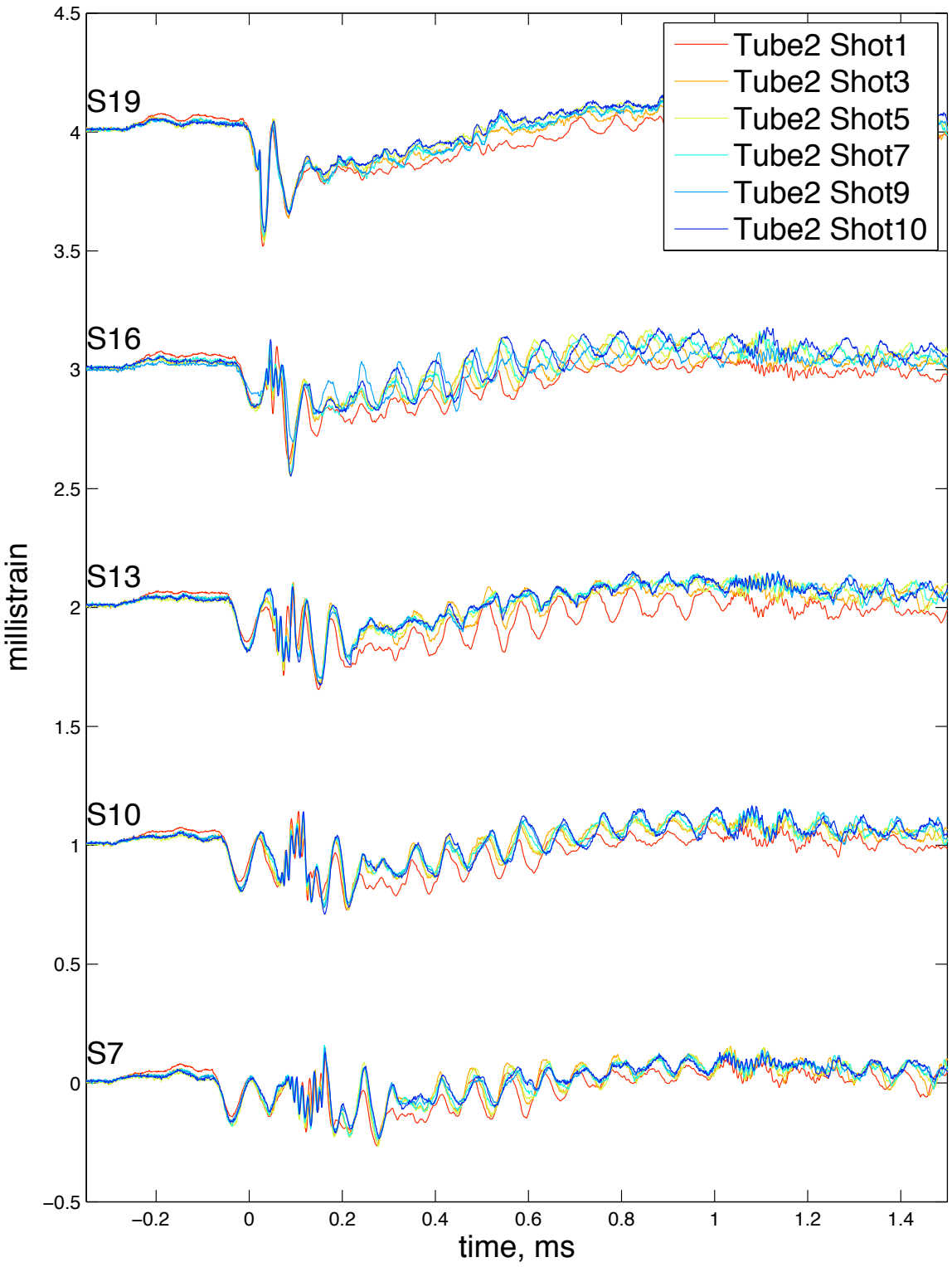

Figure F.11: Longitudinal strain data for elastic shots in tube 2.

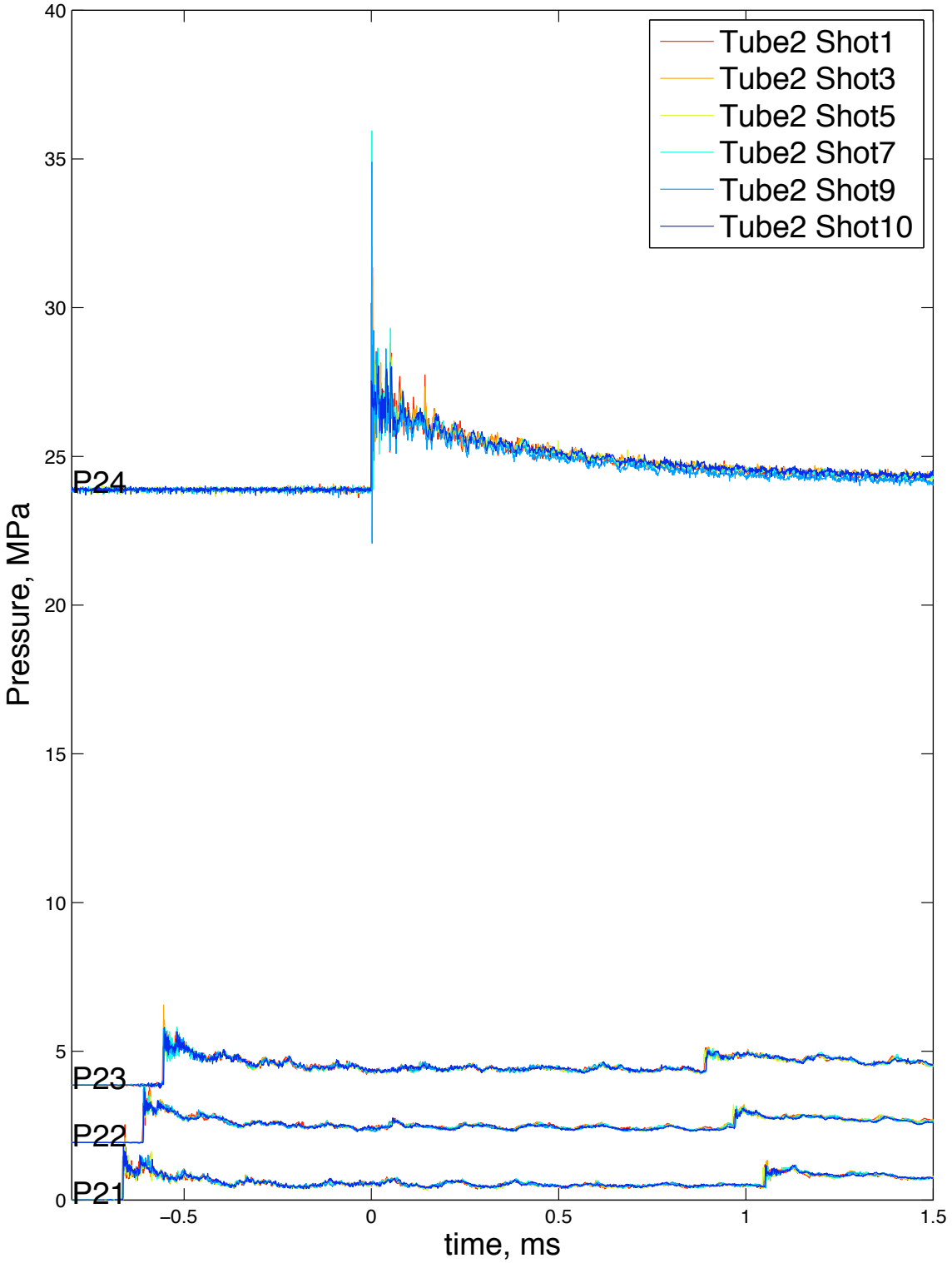

Figure F.12: Pressure data for elastic shots in tube 2.

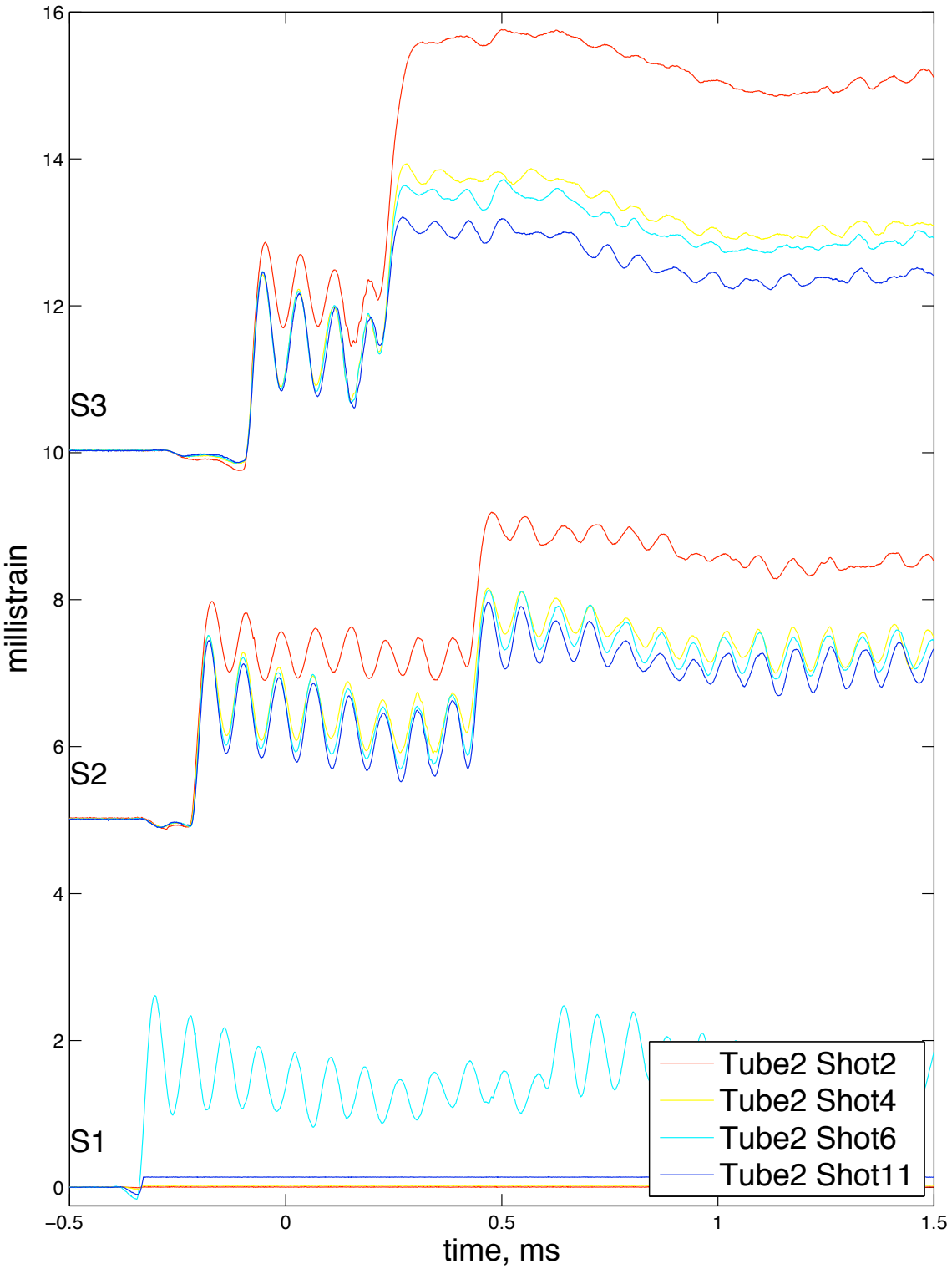

Figure F.13: Hoop strain data for plastic shots in tube 2.

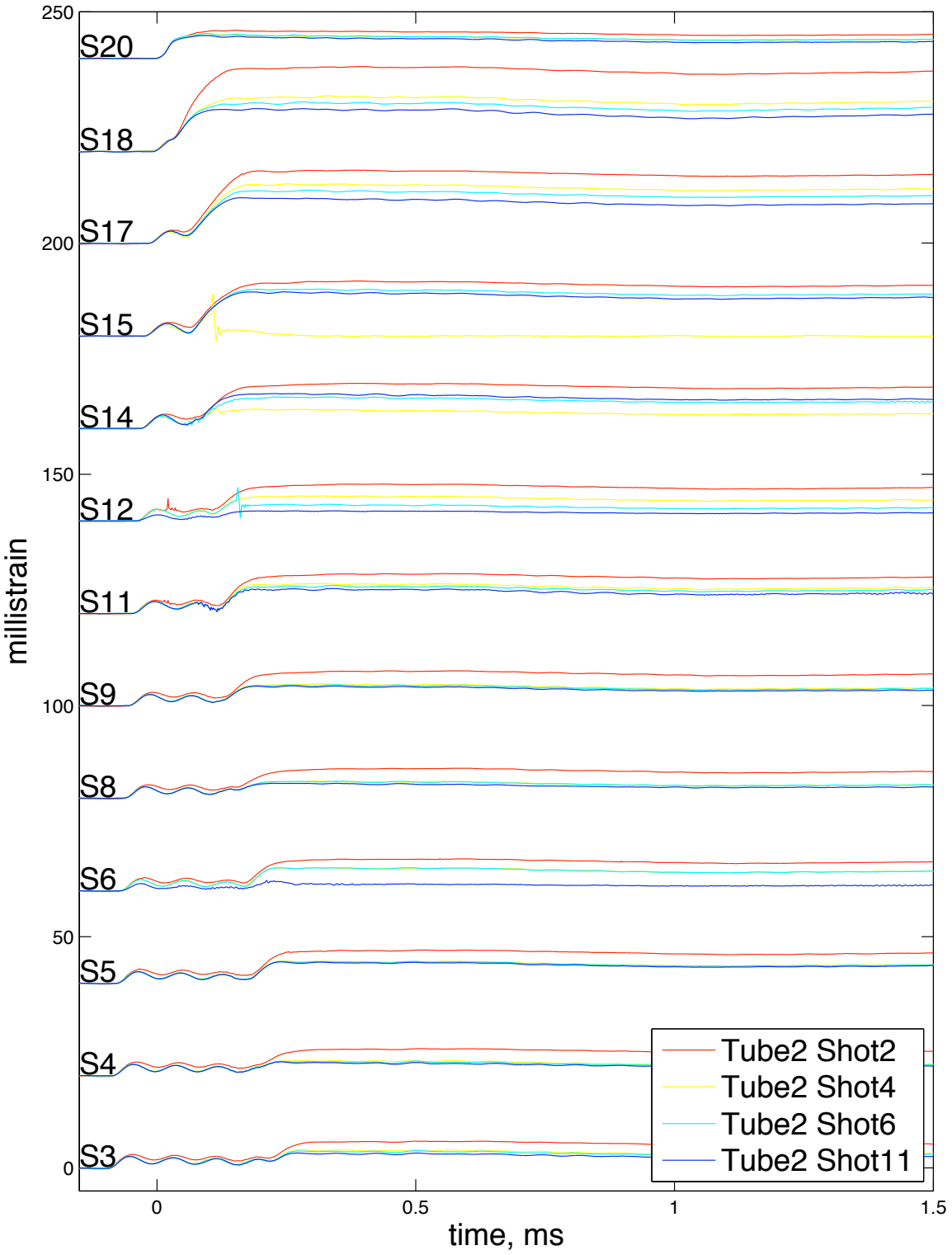

Figure F.14: Hoop strain data for plastic shots in tube 2.

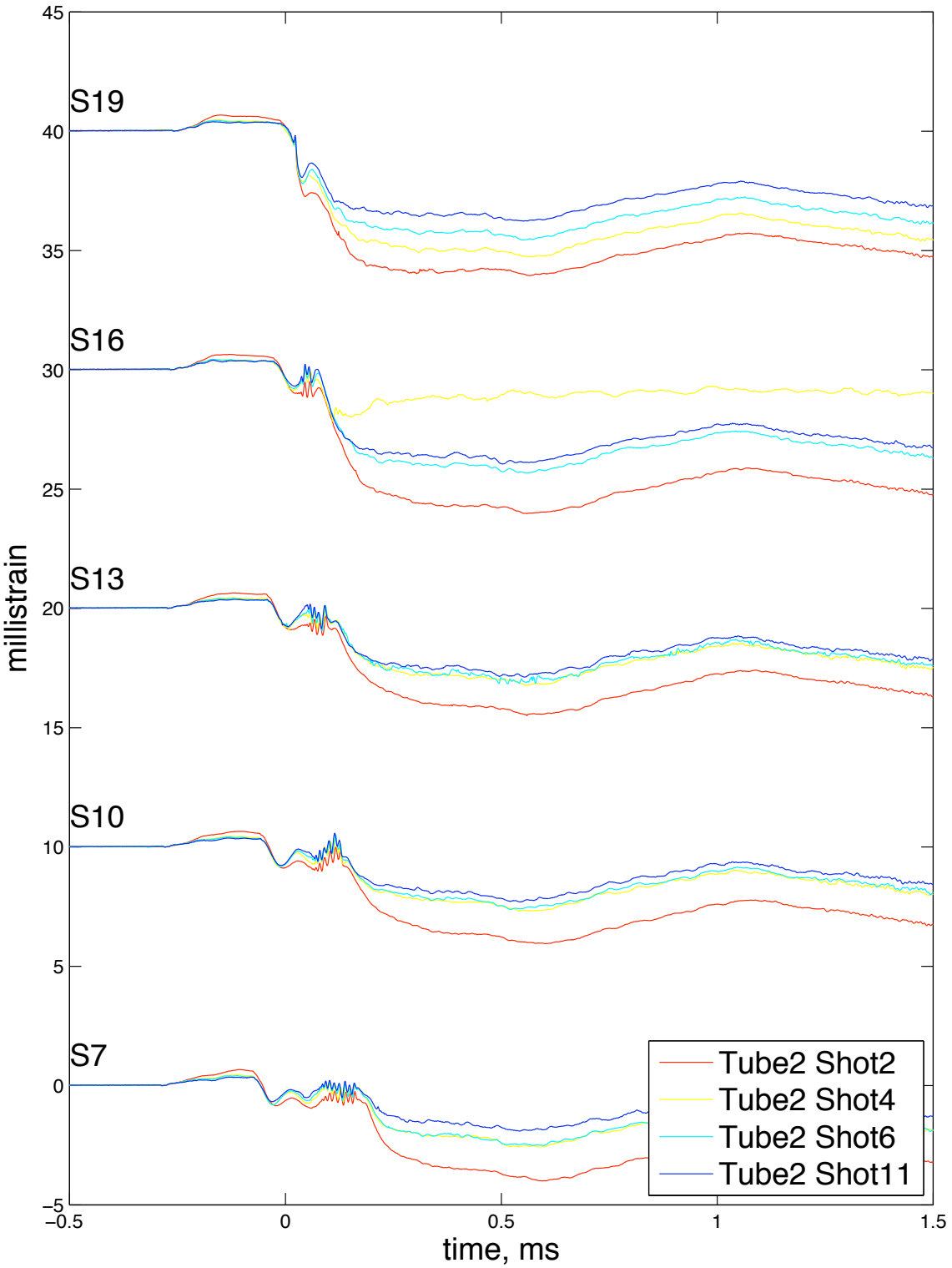

Figure F.15: Longitudinal strain data for plastic shots in tube 2.

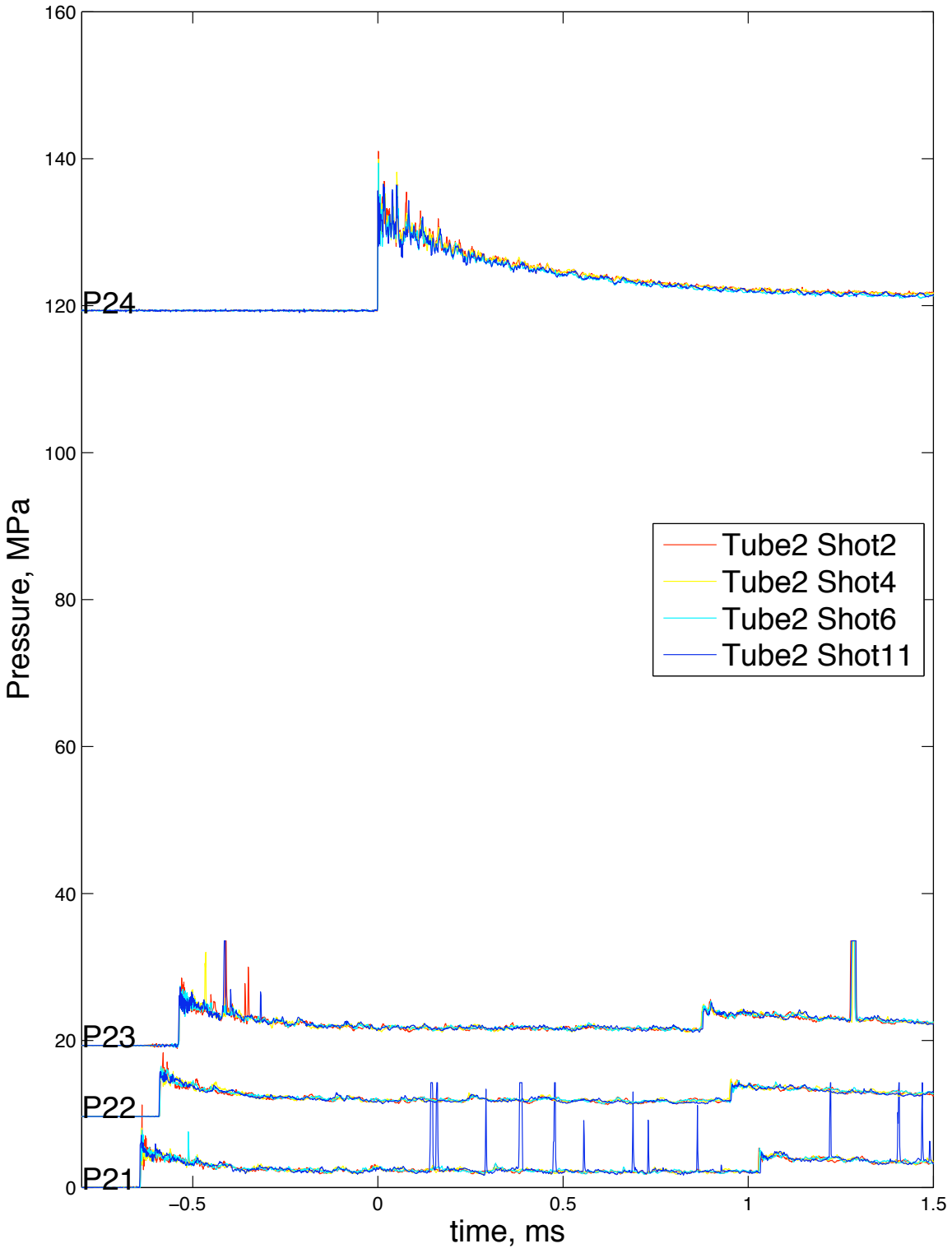

Figure F.16: Pressure data for plastic shots in tube 2.

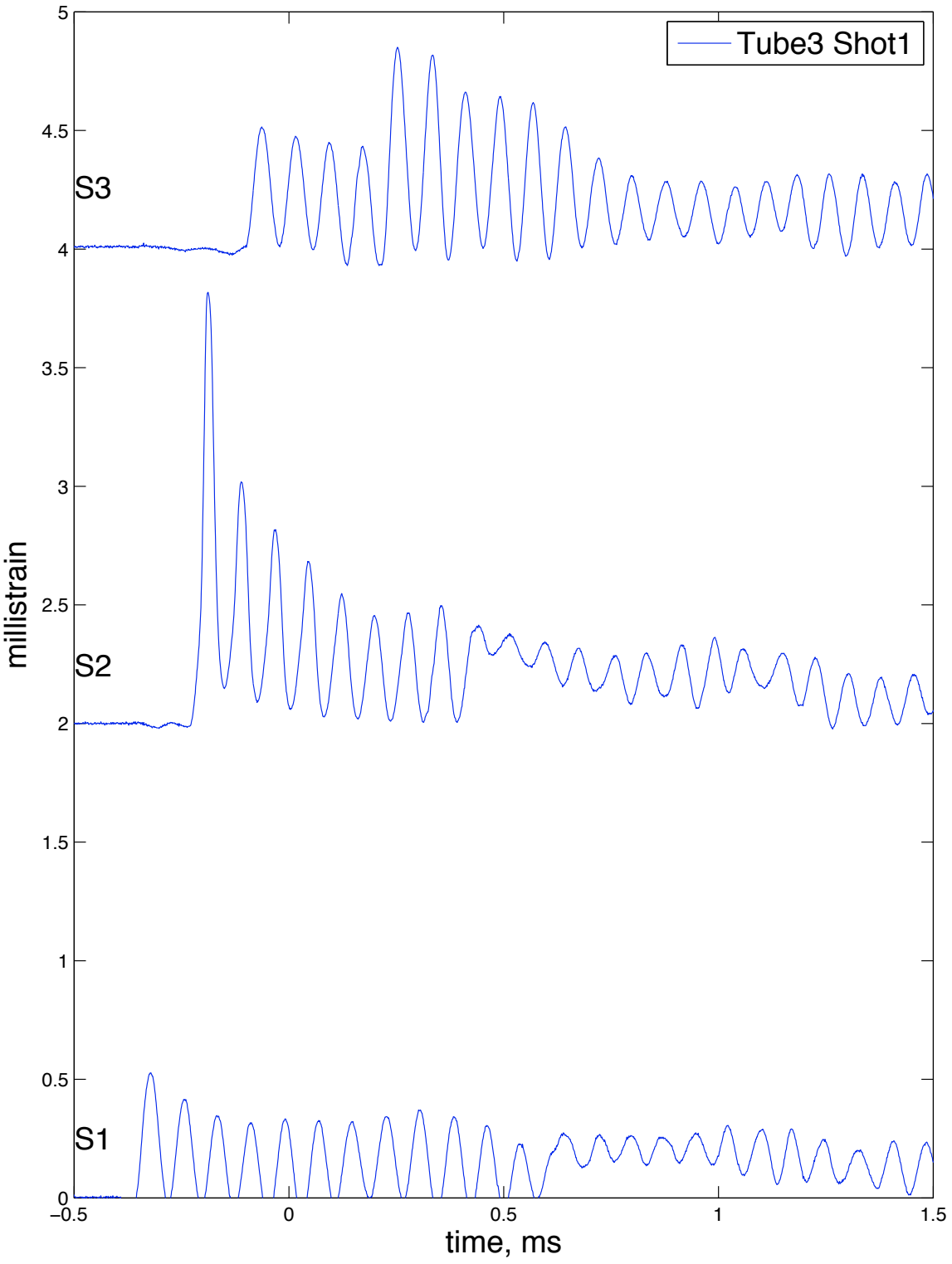

Figure F.17: Hoop strain data for elastic shots in tube 3.

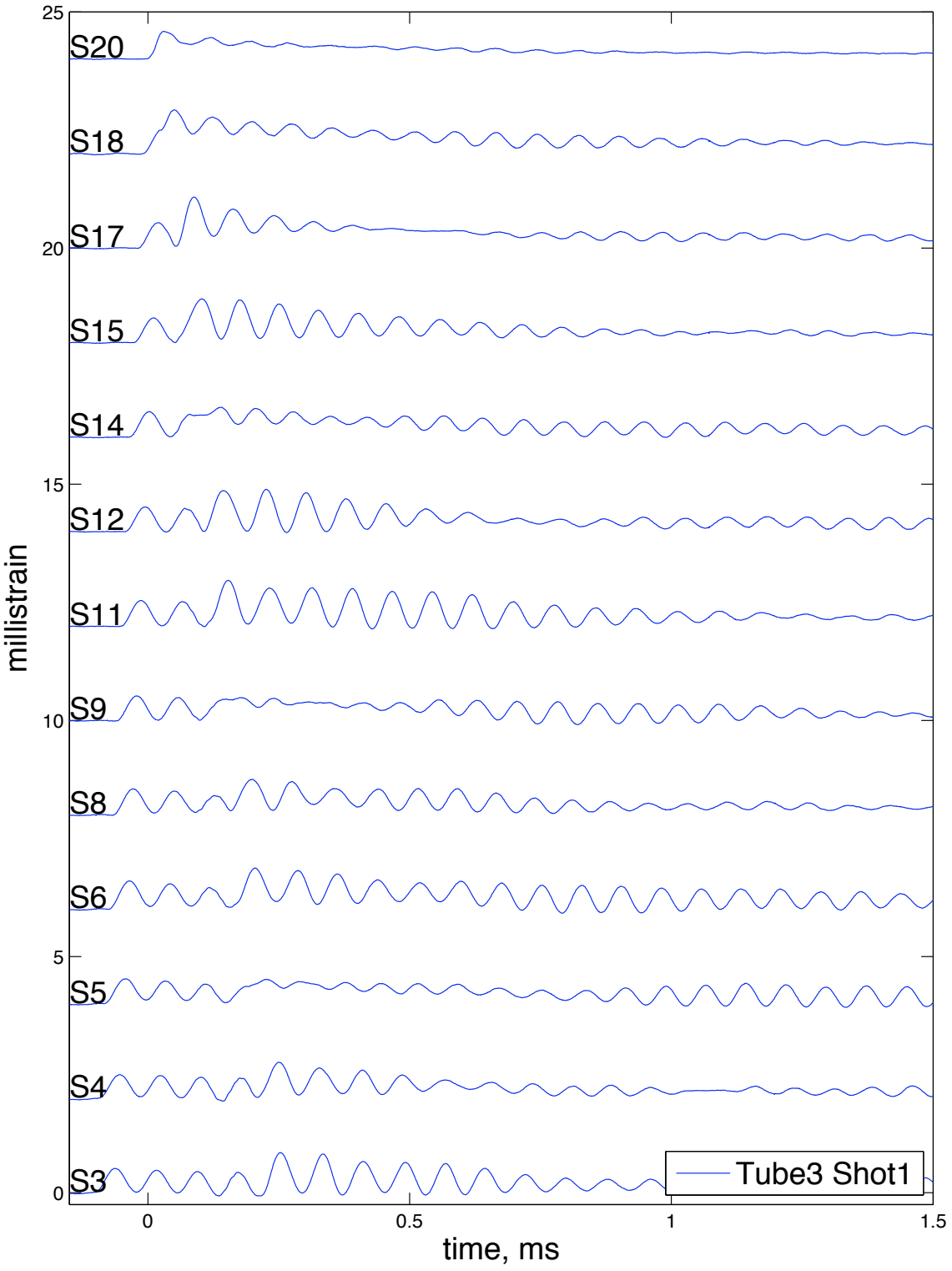

Figure F.18: Hoop strain data for elastic shots in tube 3.

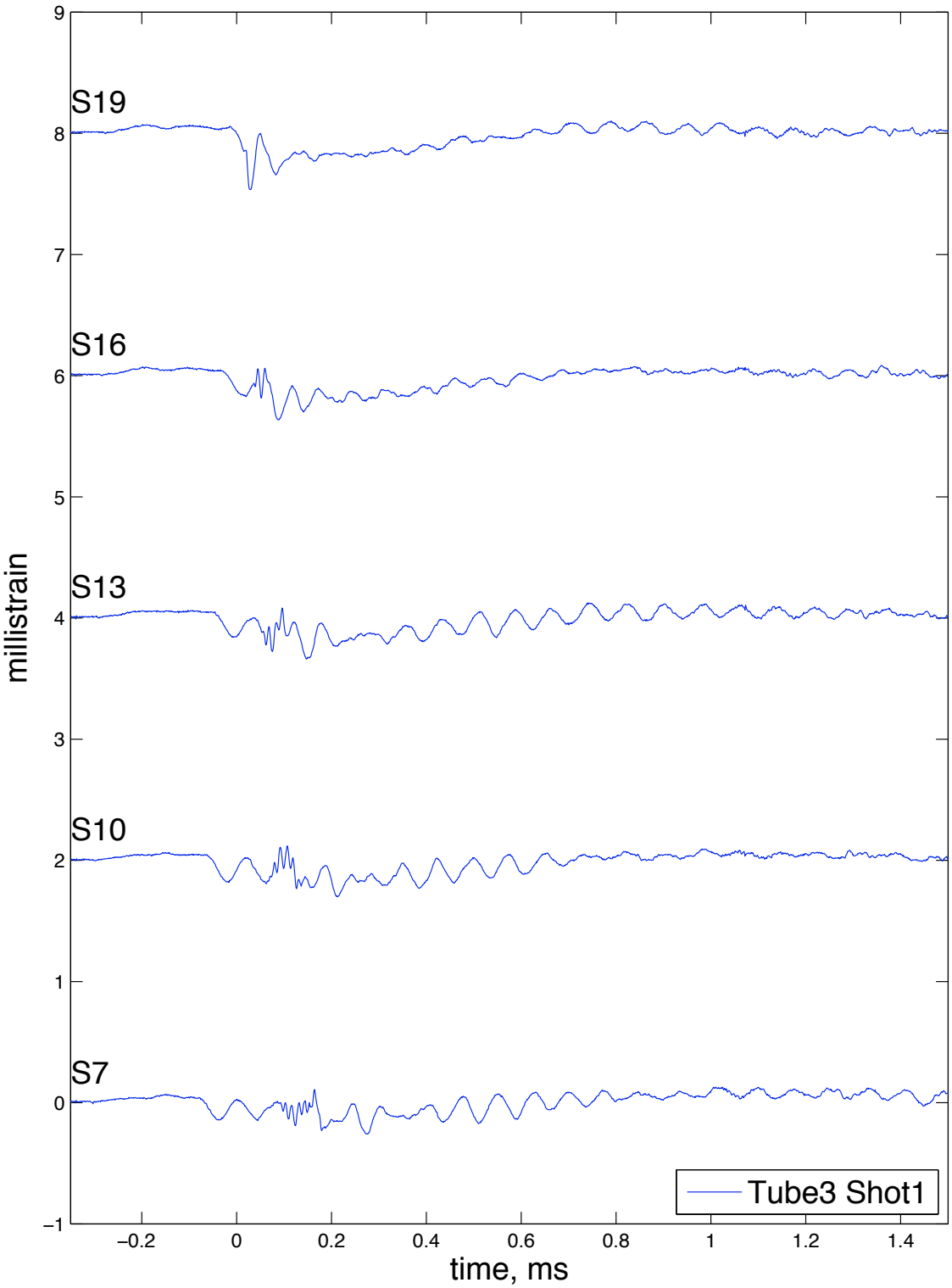

Figure F.19: Longitudinal strain data for elastic shots in tube 3.

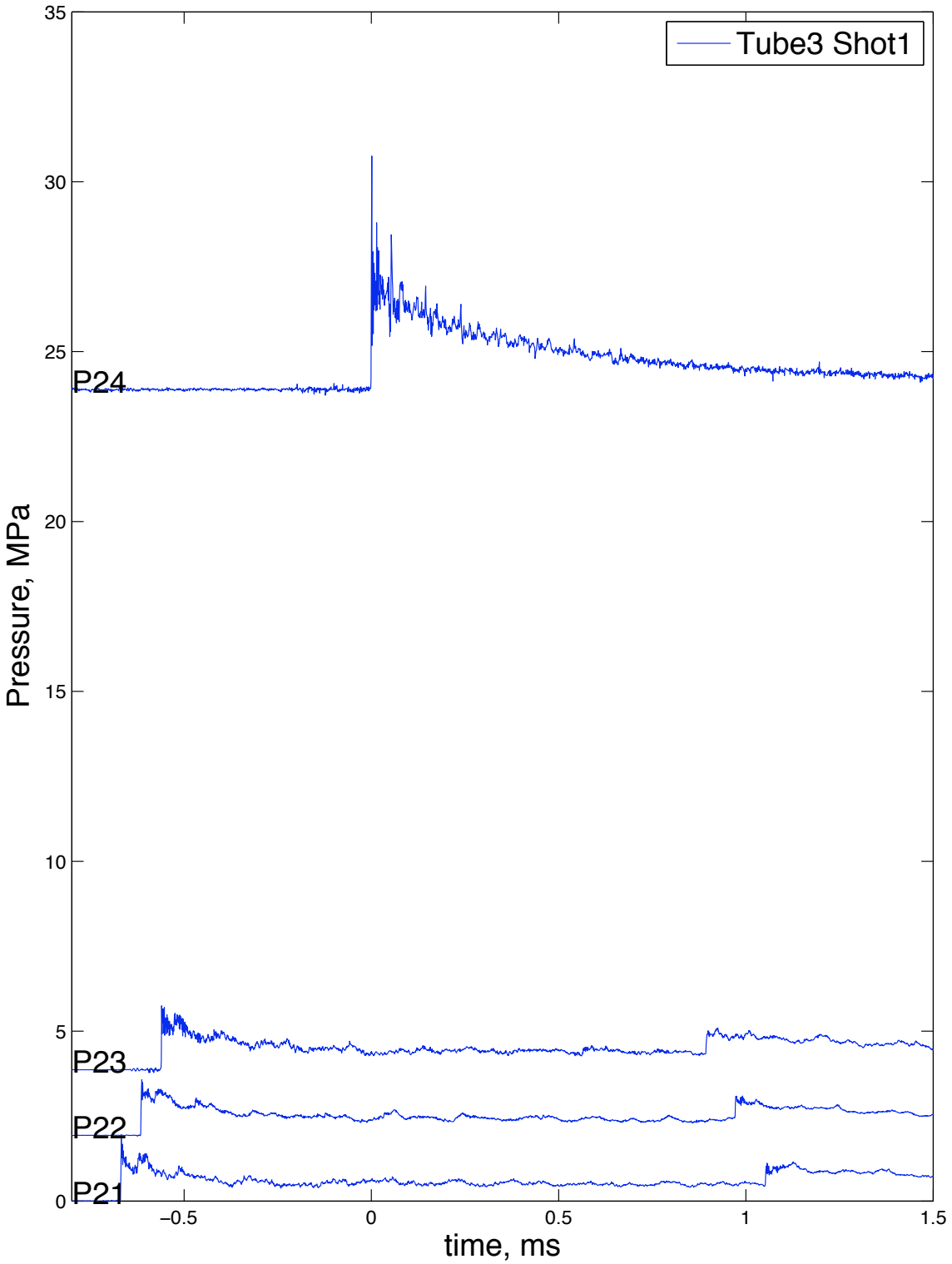

Figure F.20: Pressure data for elastic shots in tube 3.

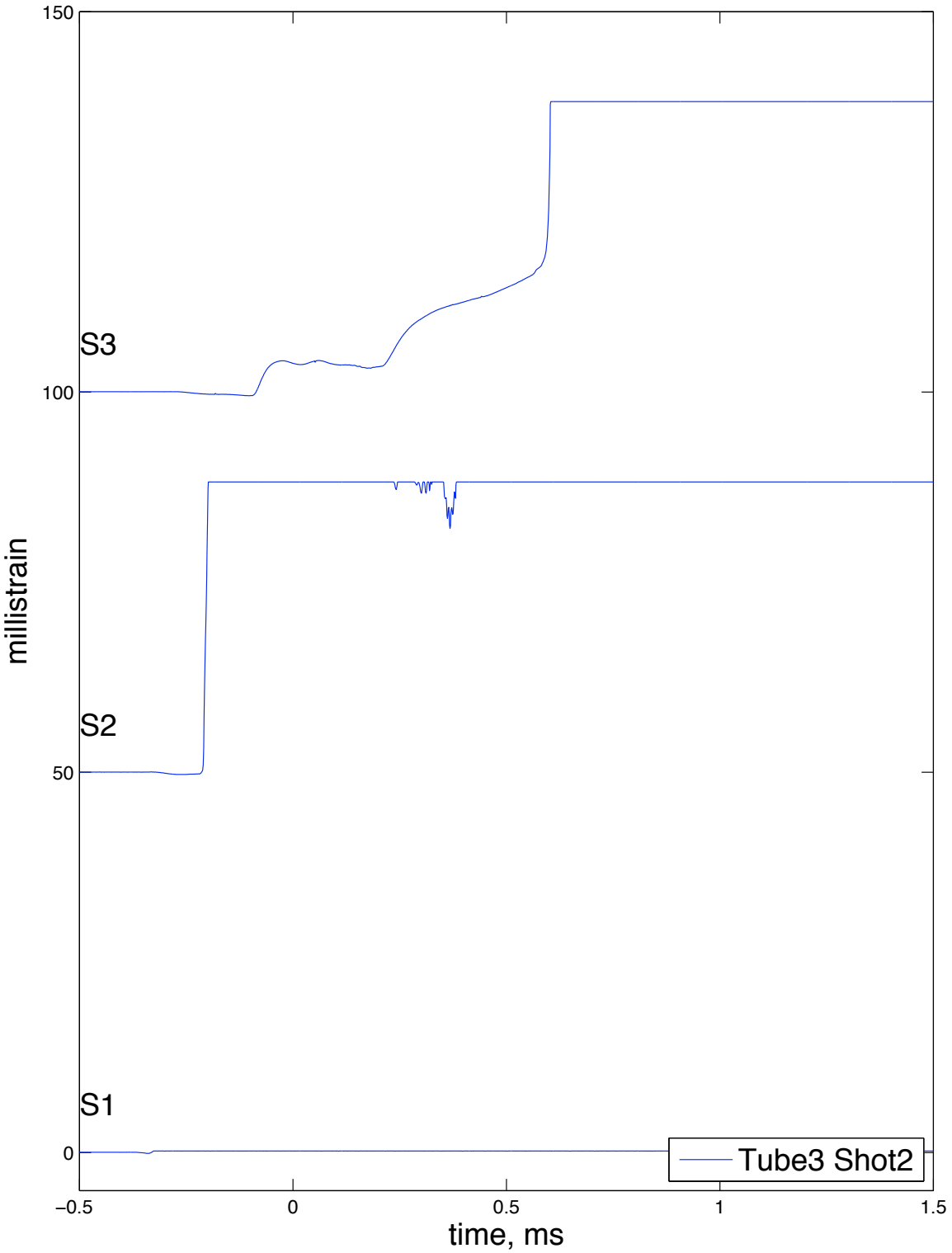

Figure F.21: Hoop strain data for plastic shots in tube 3.

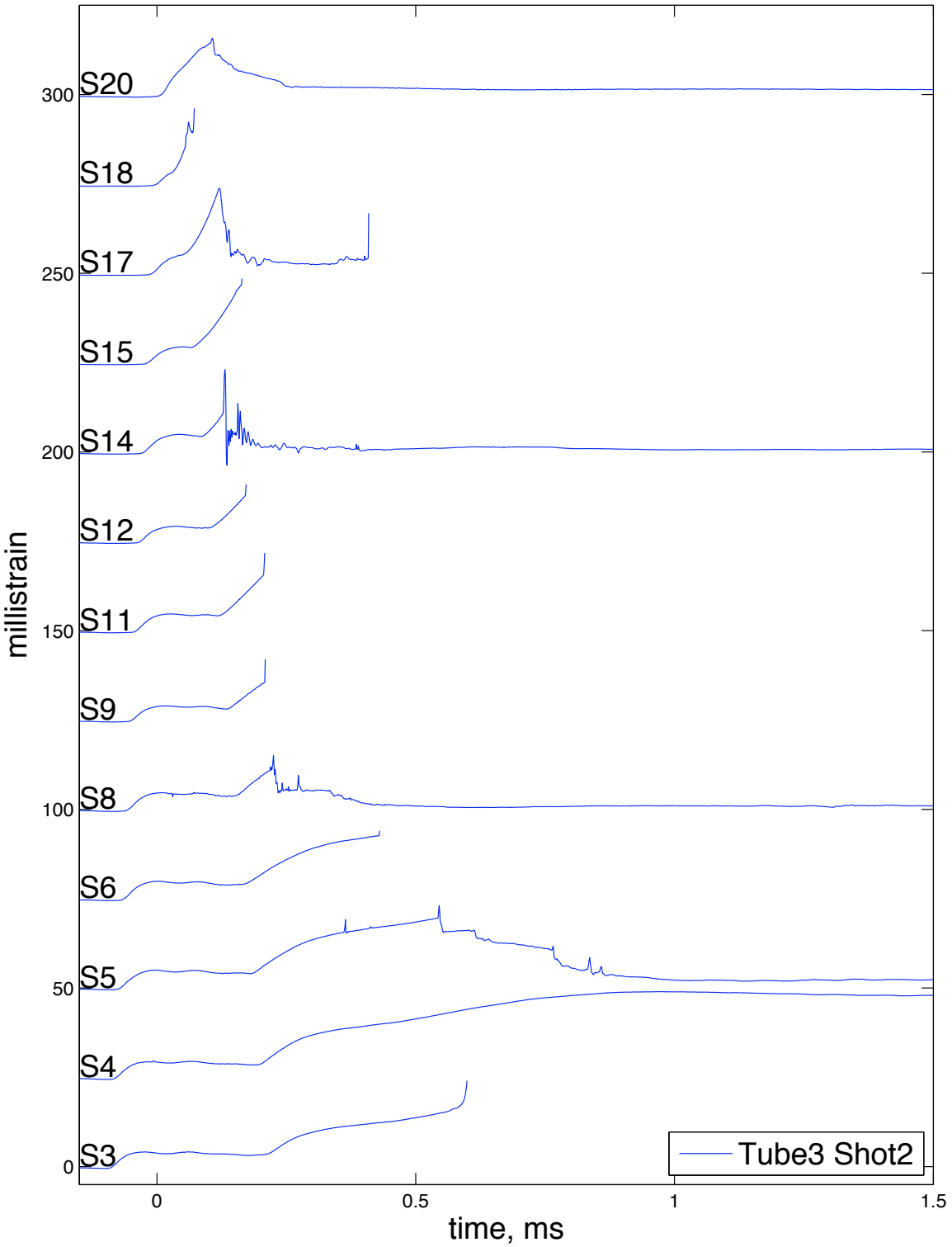

Figure F.22: Hoop strain data for plastic shots in tube 3.

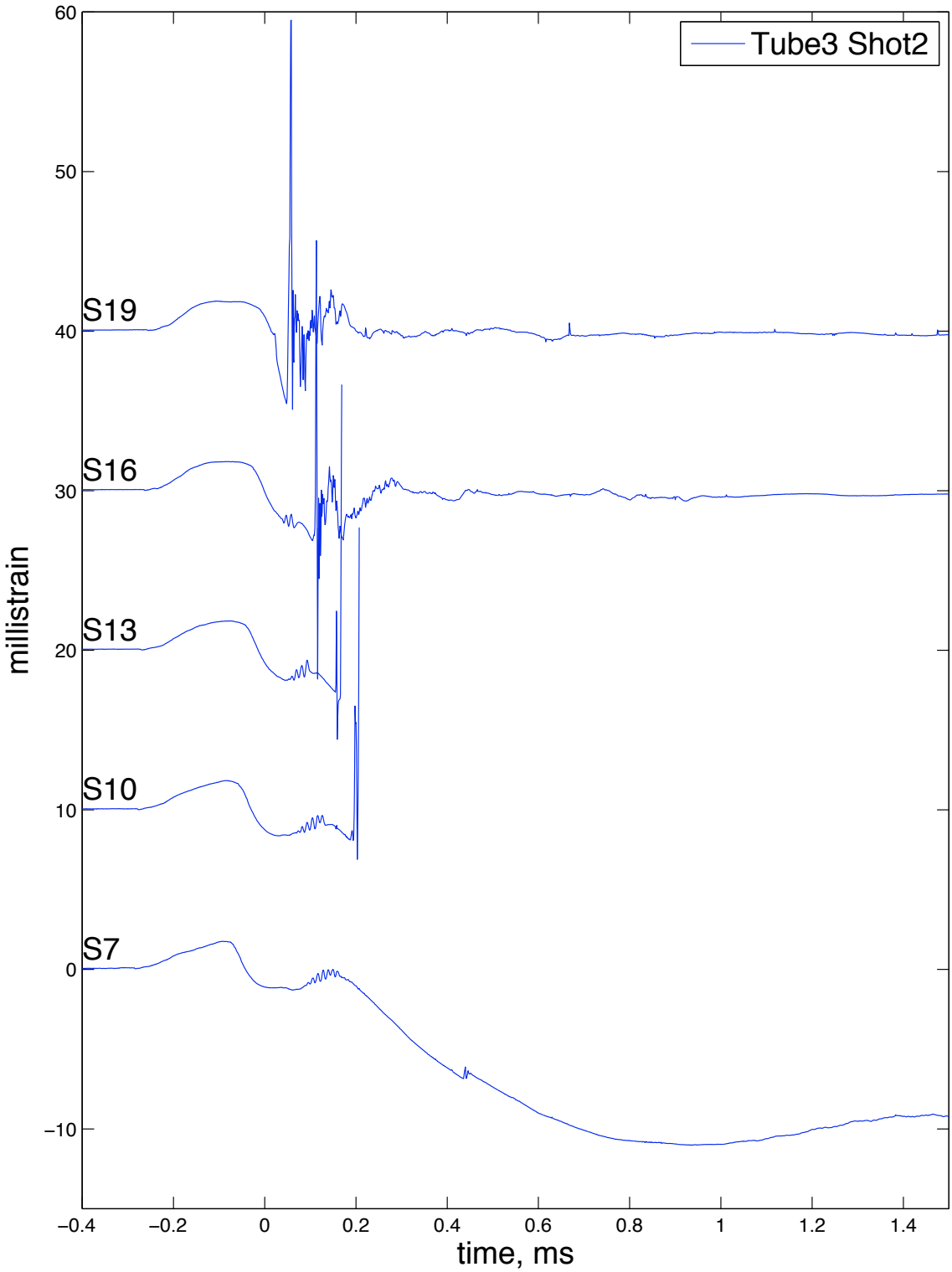

Figure F.23: Longitudinal strain data for plastic shots in tube 3.

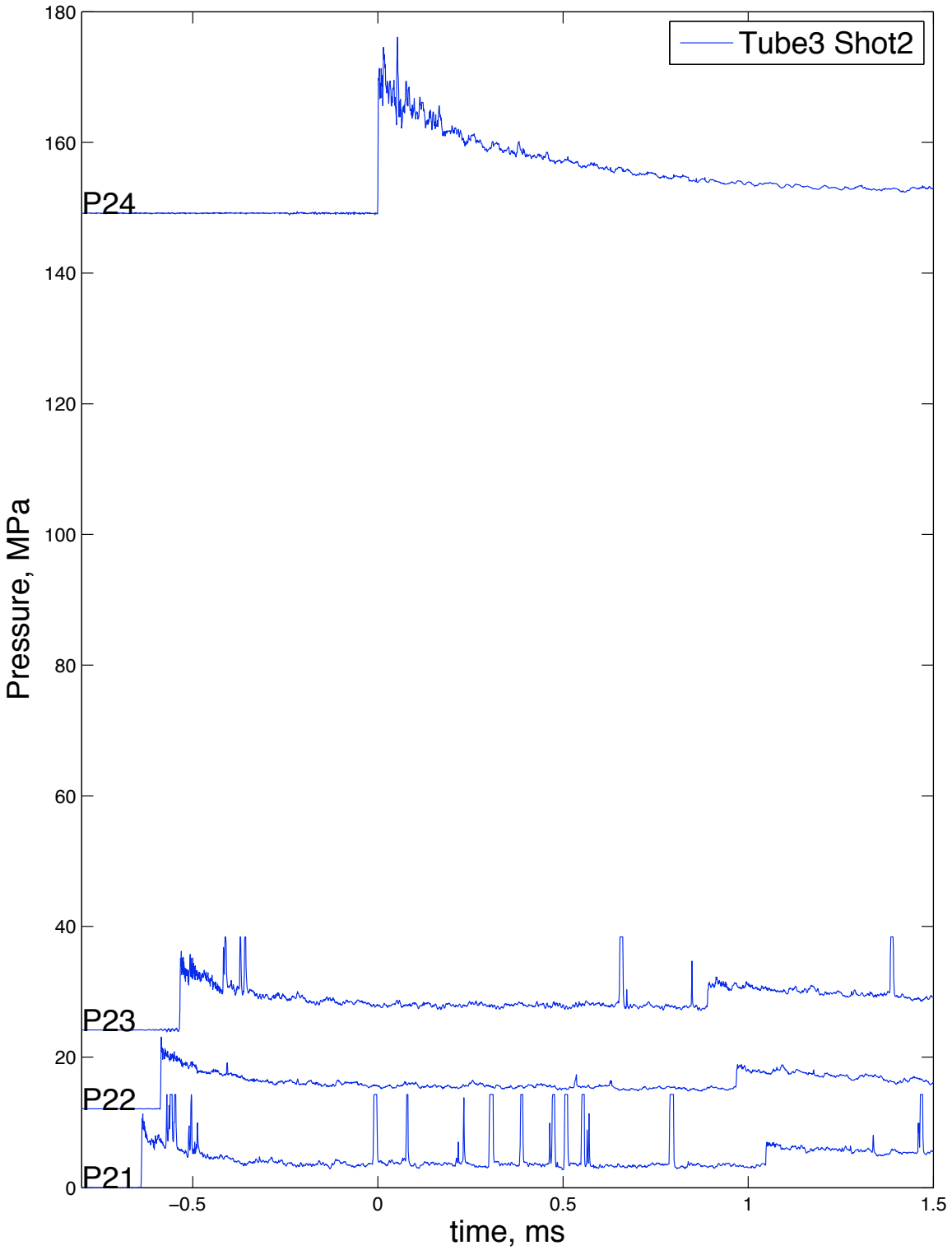

Figure F.24: Pressure data for plastic shots in tube 3.

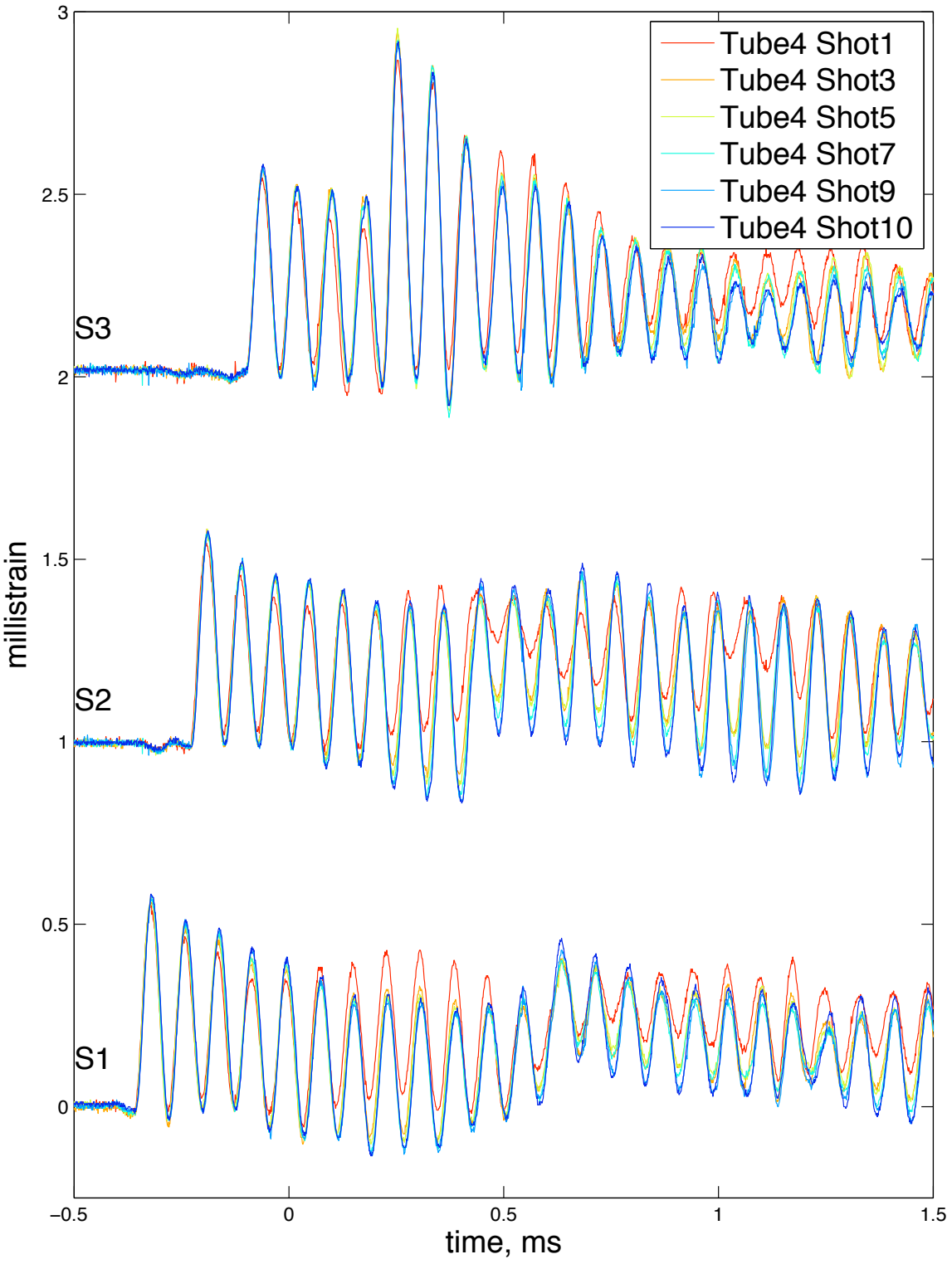

Figure F.25: Hoop strain data for elastic shots in tube 4.

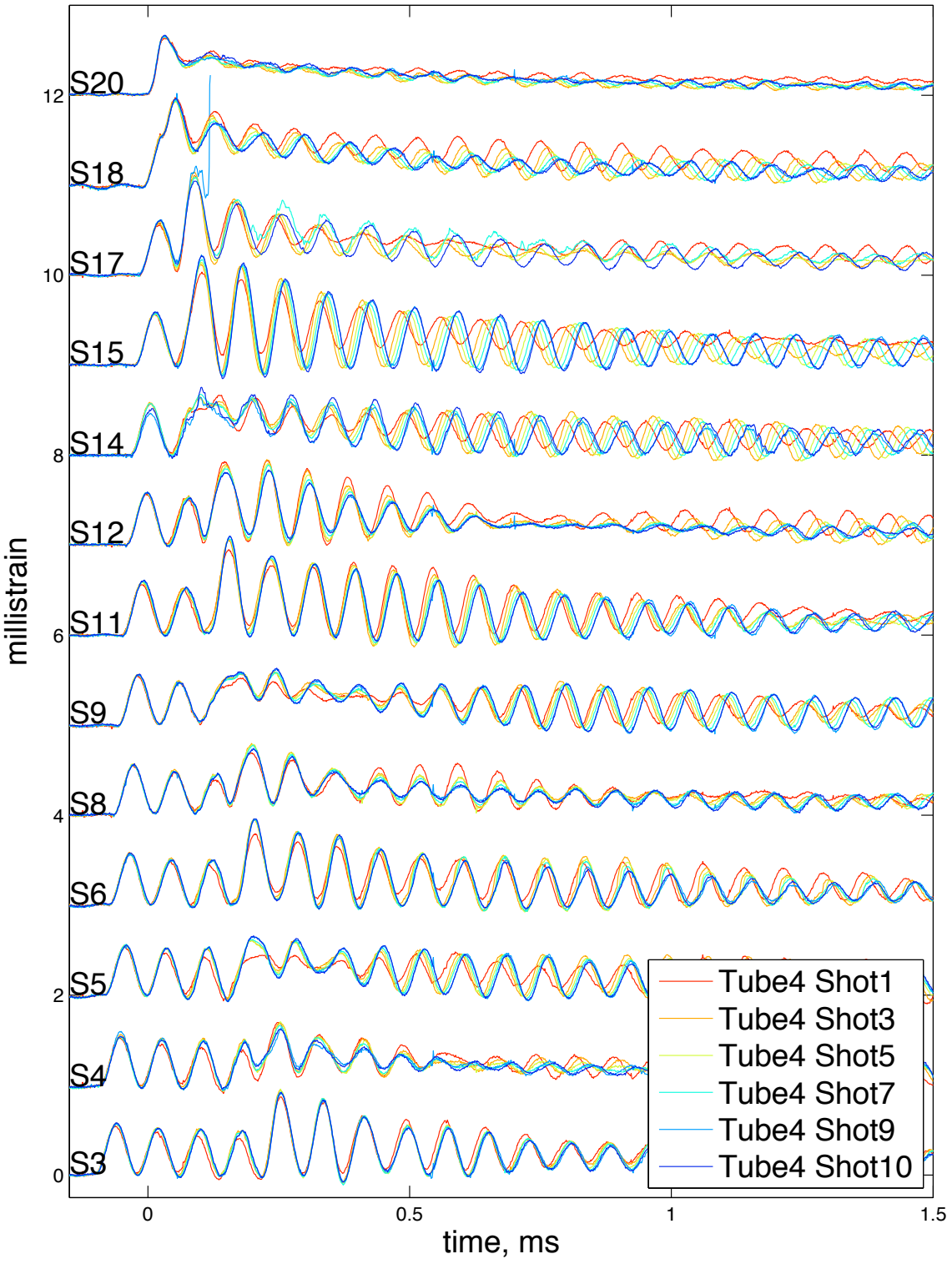

Figure F.26: Hoop strain data for elastic shots in tube 4.

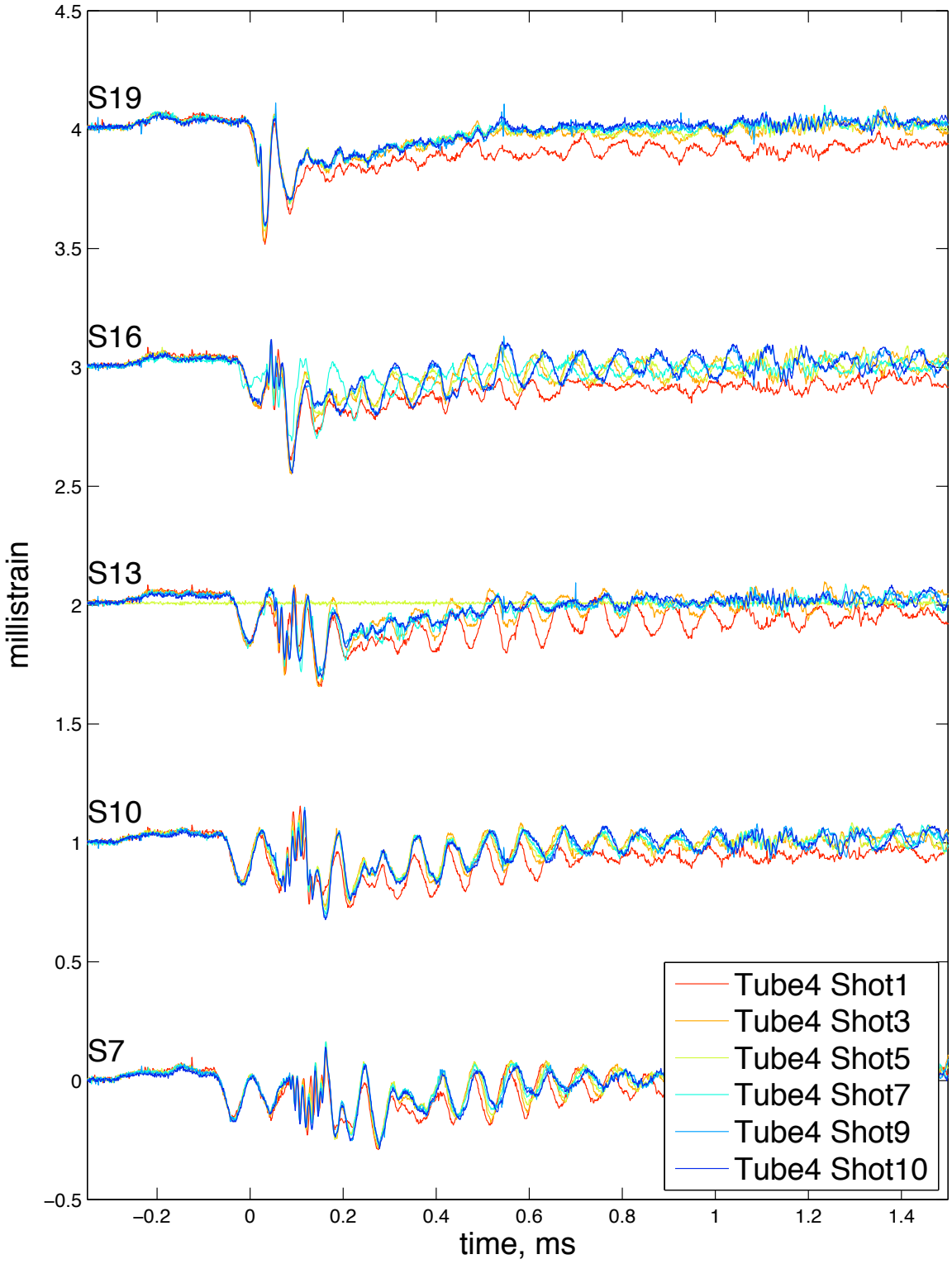

Figure F.27: Longitudinal strain data for elastic shots in tube 4.

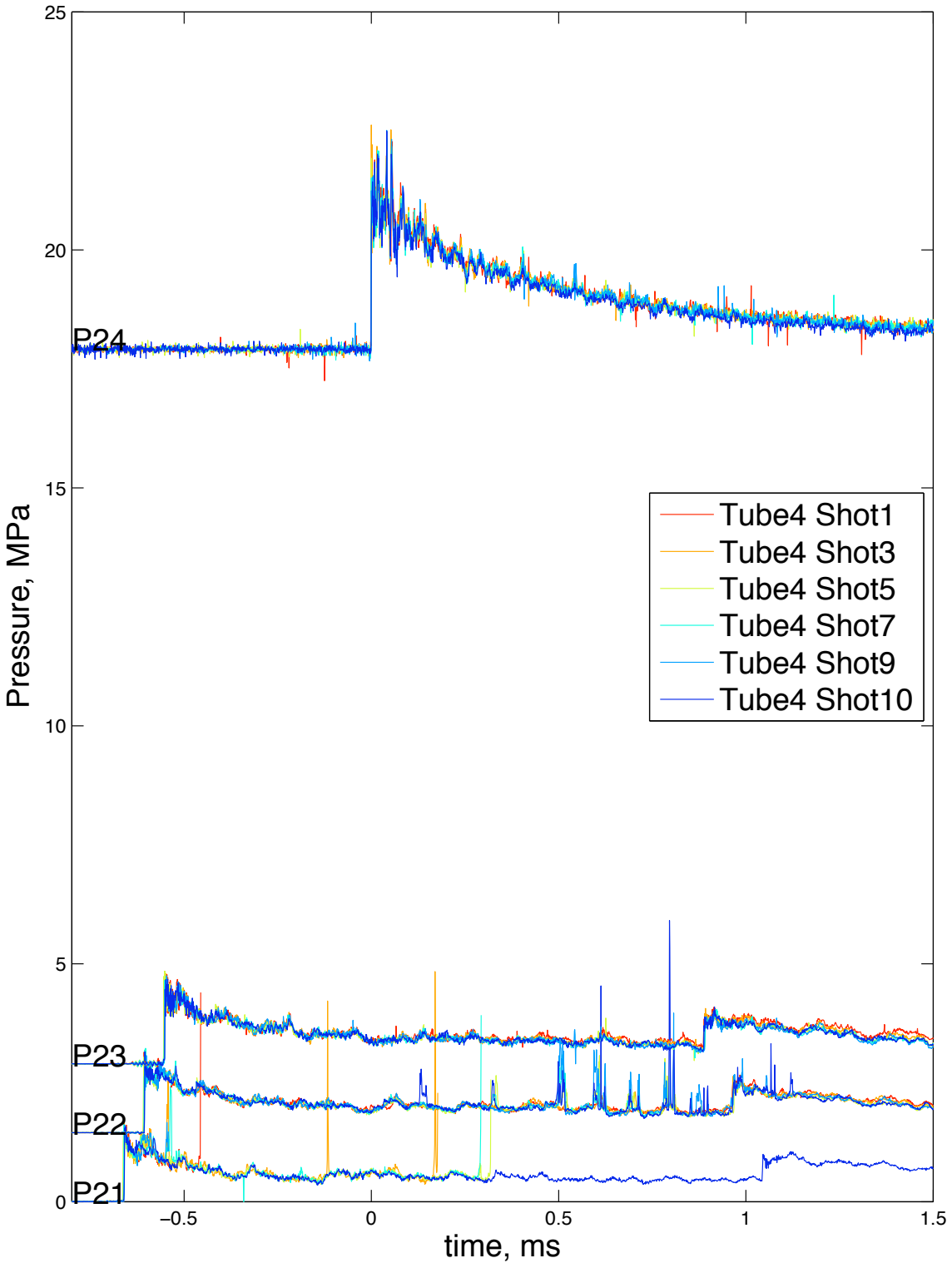

Figure F.28: Pressure data for elastic shots in tube 4.

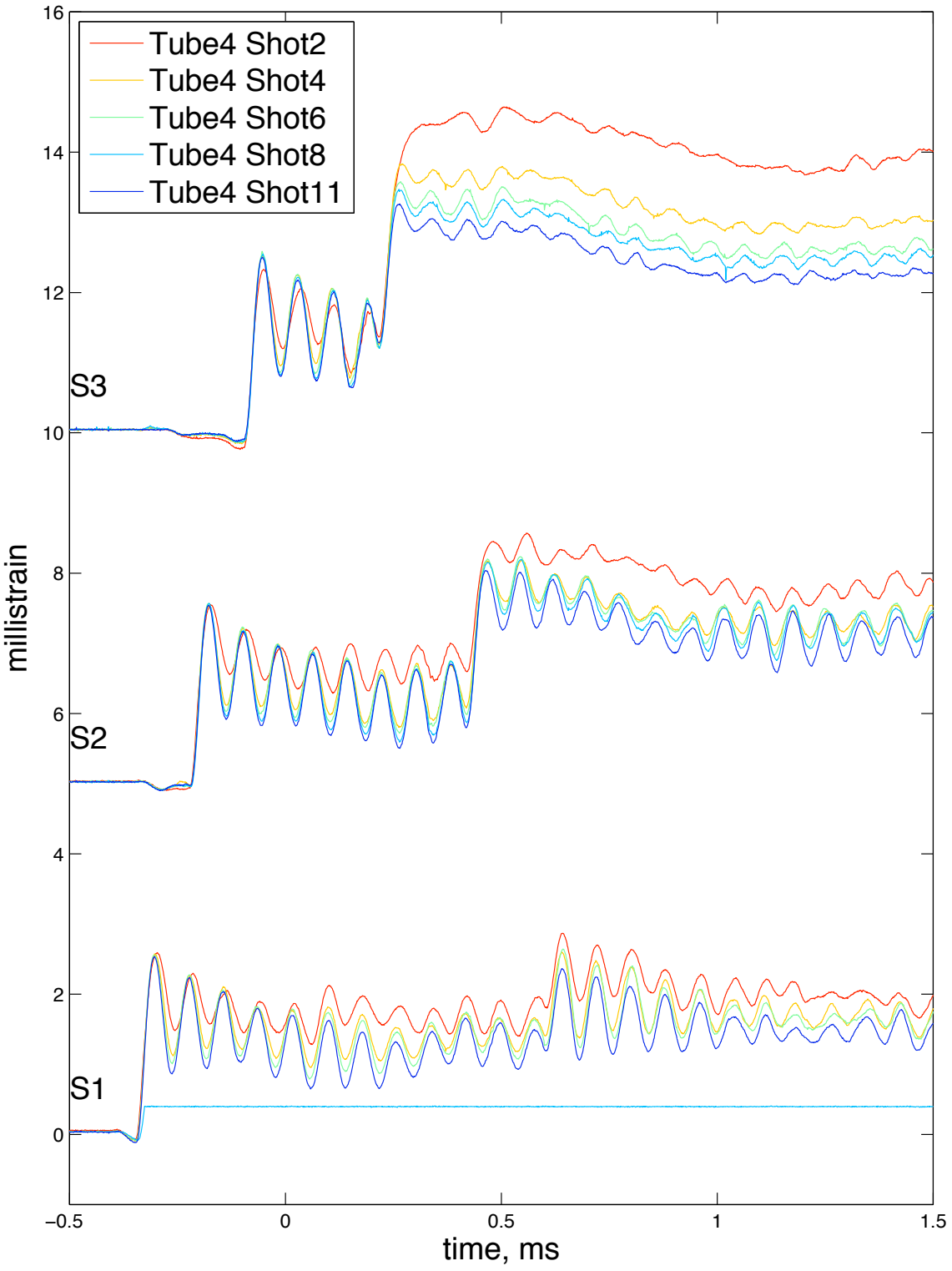

Figure F.29: Hoop strain data for plastic shots in tube 4.

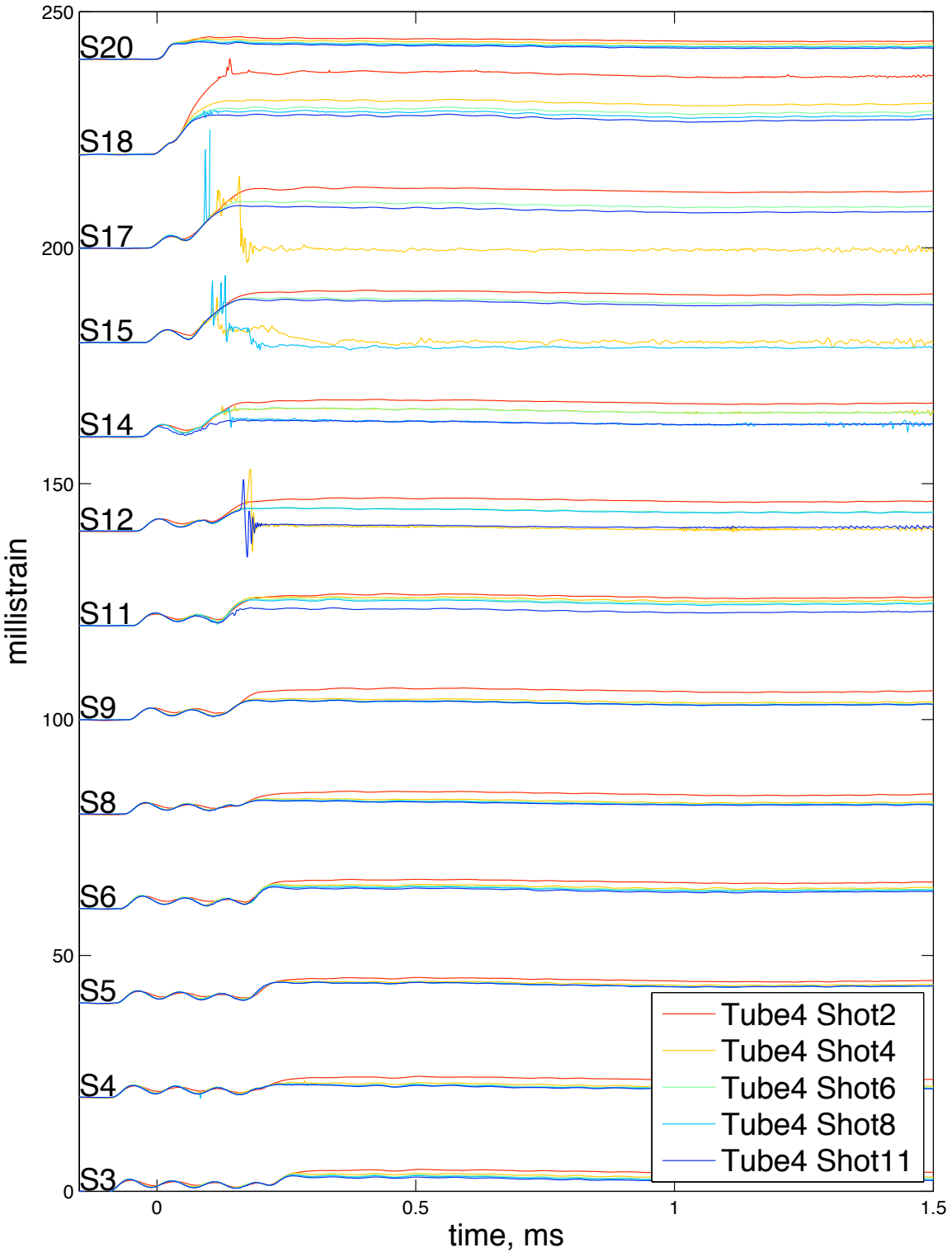

Figure F.30: Hoop strain data for plastic shots in tube 4.

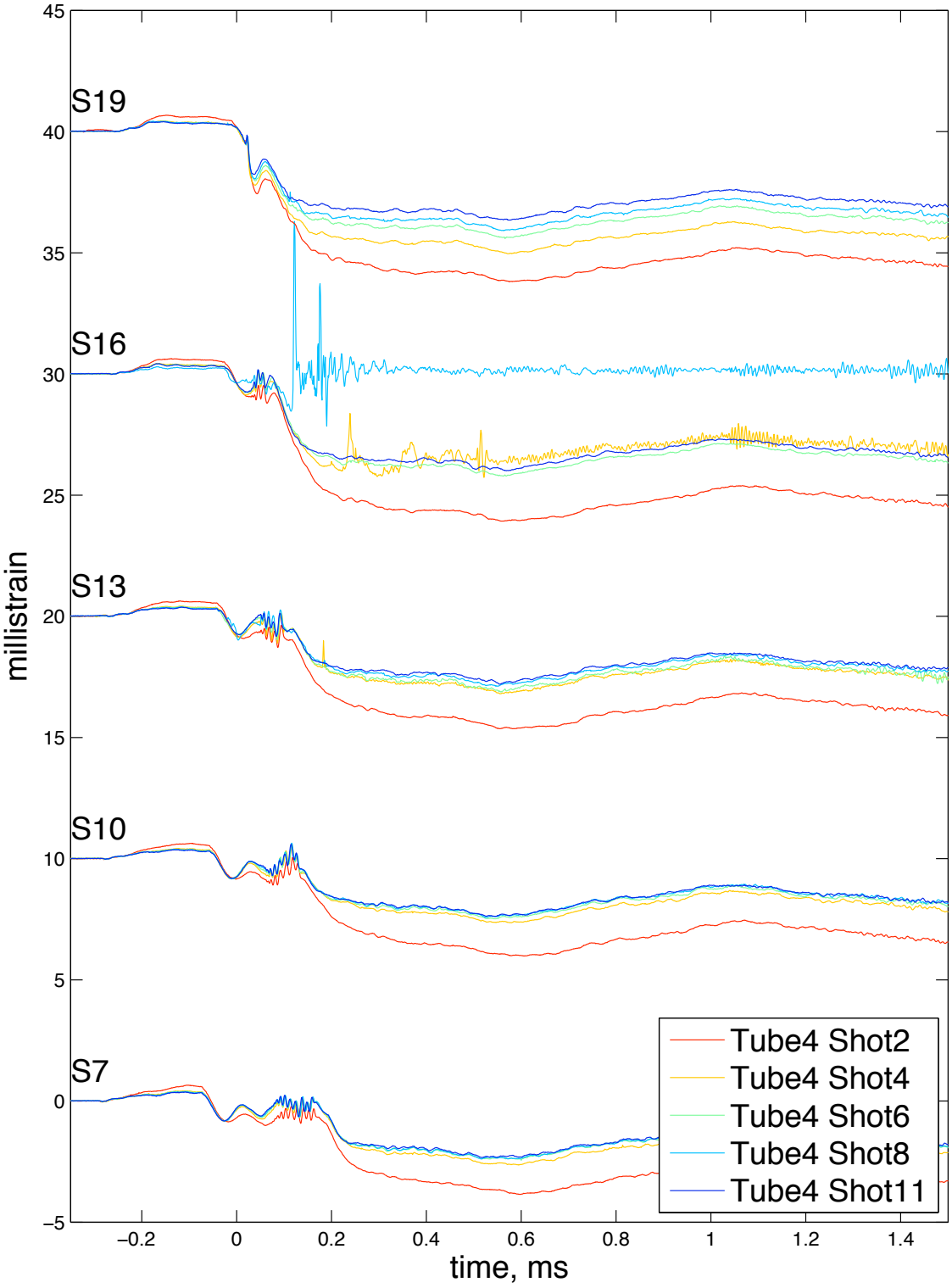

Figure F.31: Longitudinal strain data for plastic shots in tube 4.

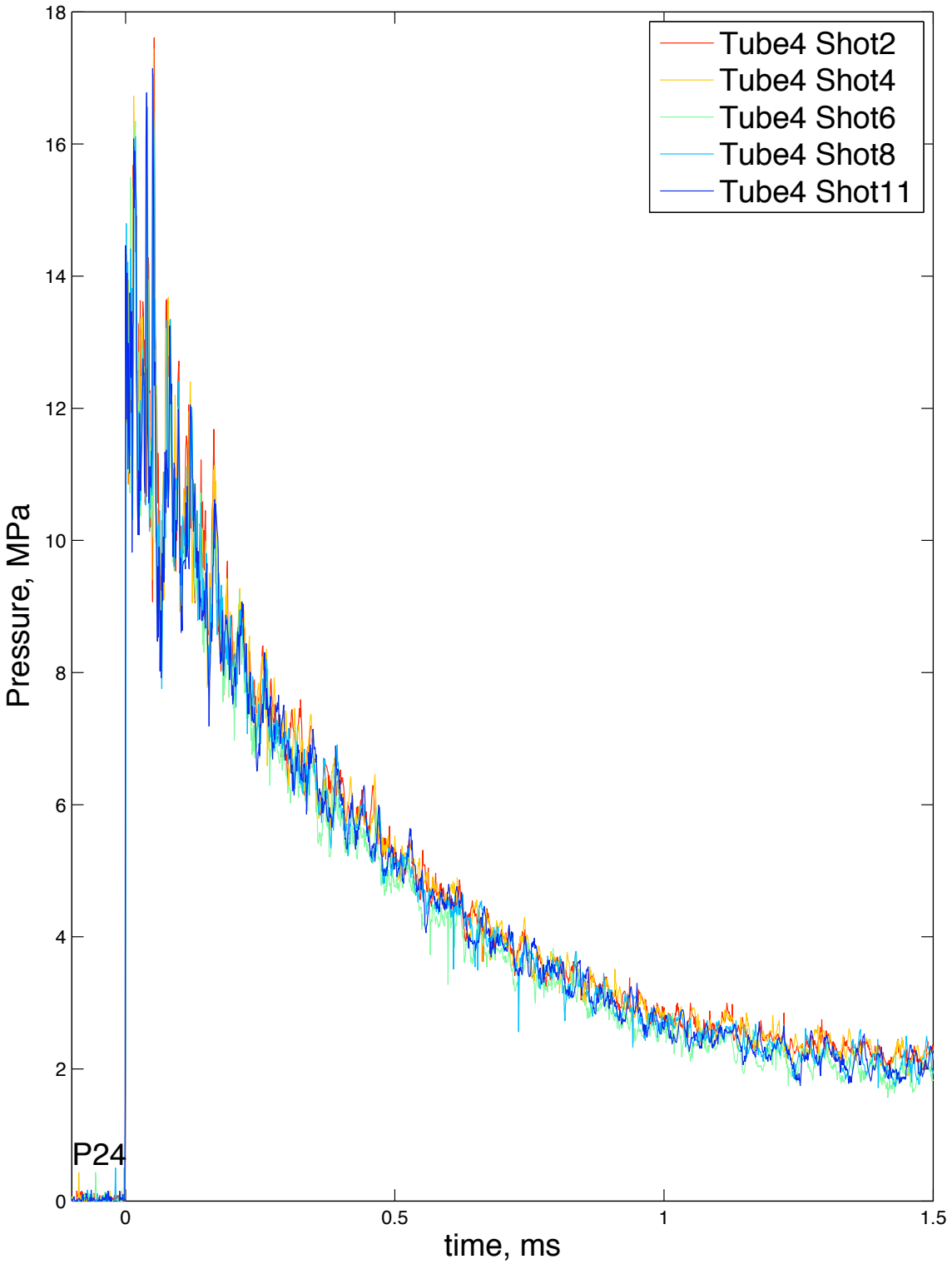

Figure F.32: Pressure data for plastic shots in tube 4.

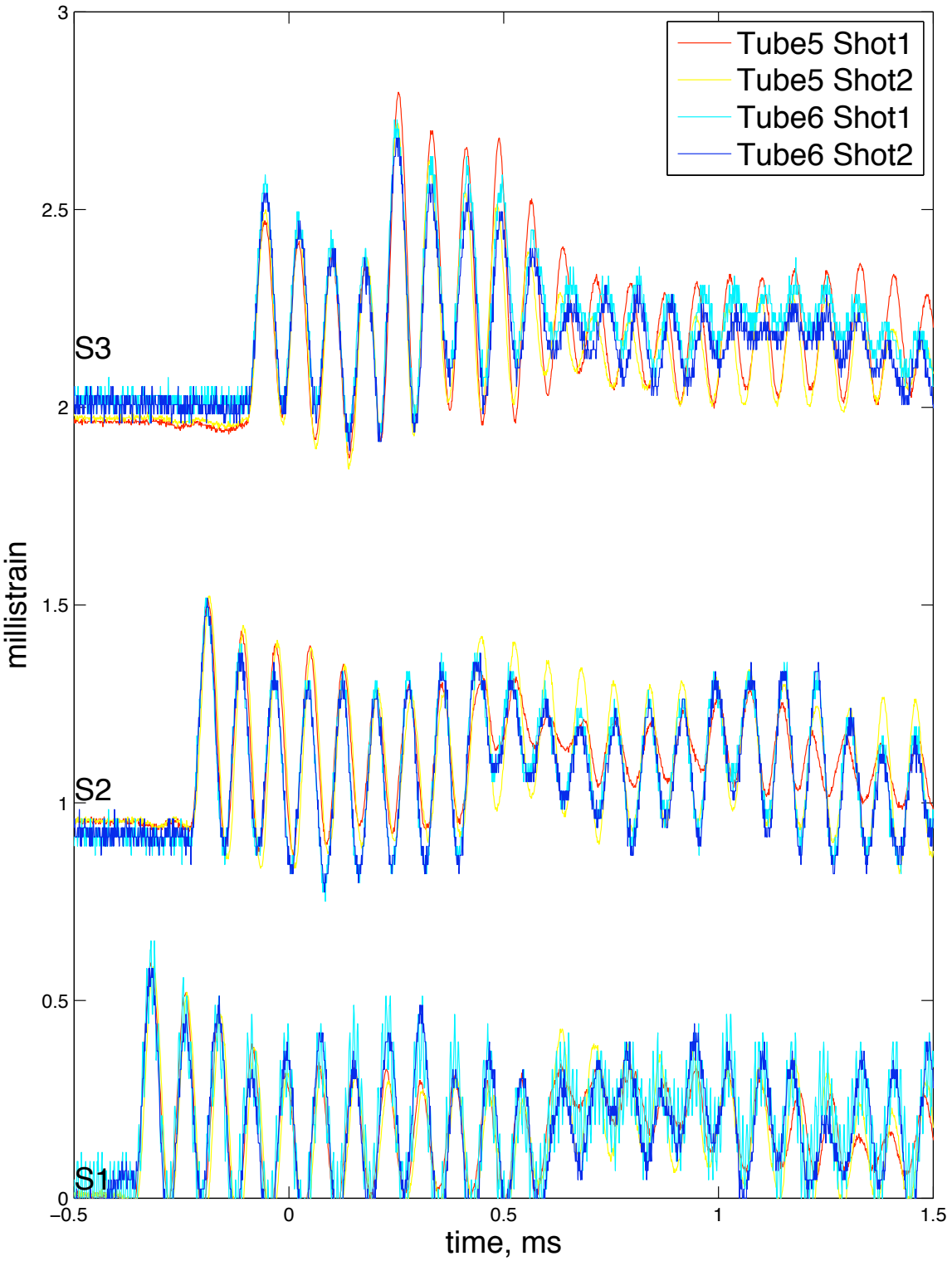

Figure F.33: Hoop strain data for elastic shots in tubes 5 and 6.

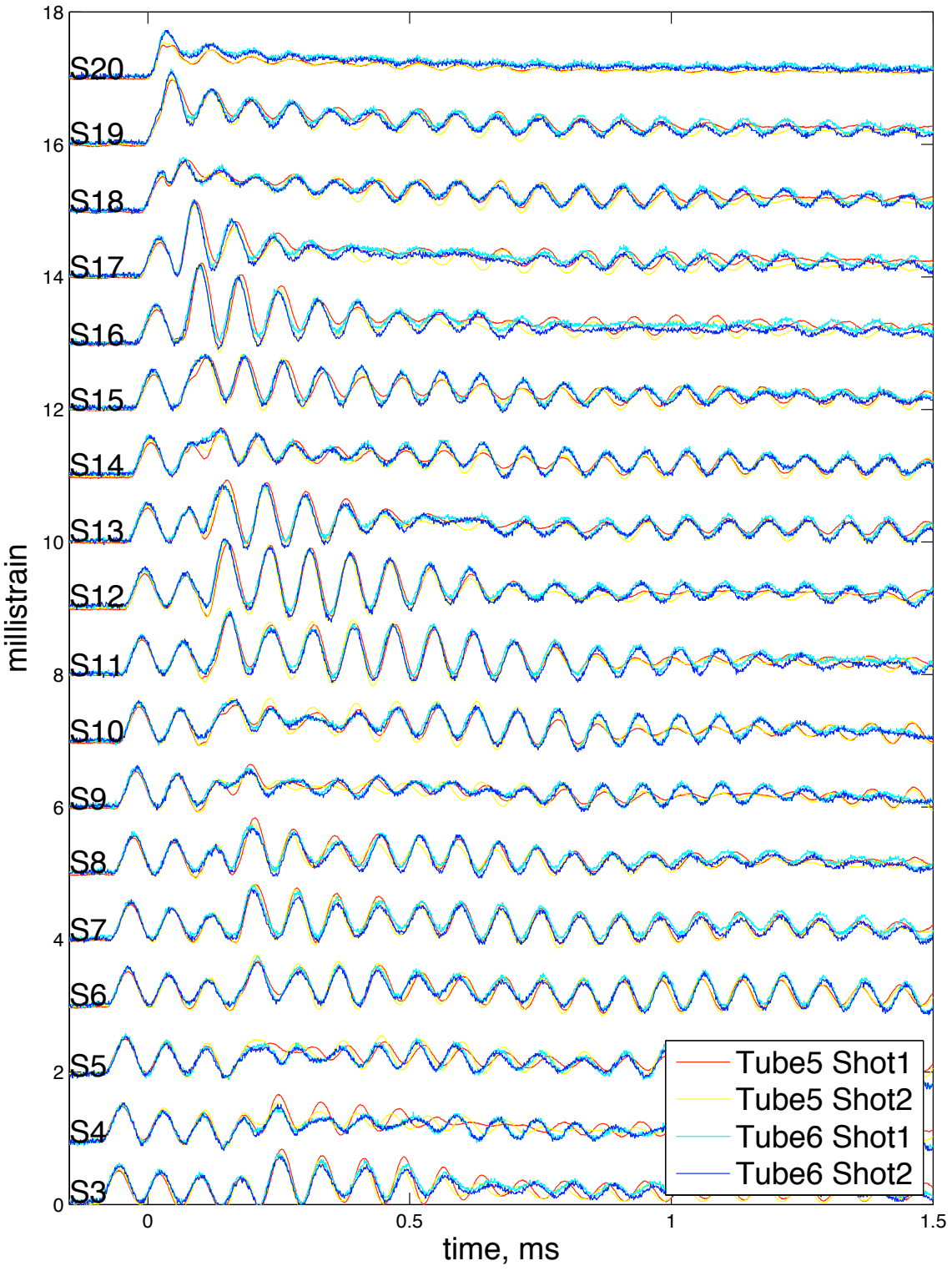

Figure F.34: Hoop strain data for elastic shots in tubes 5 and 6.

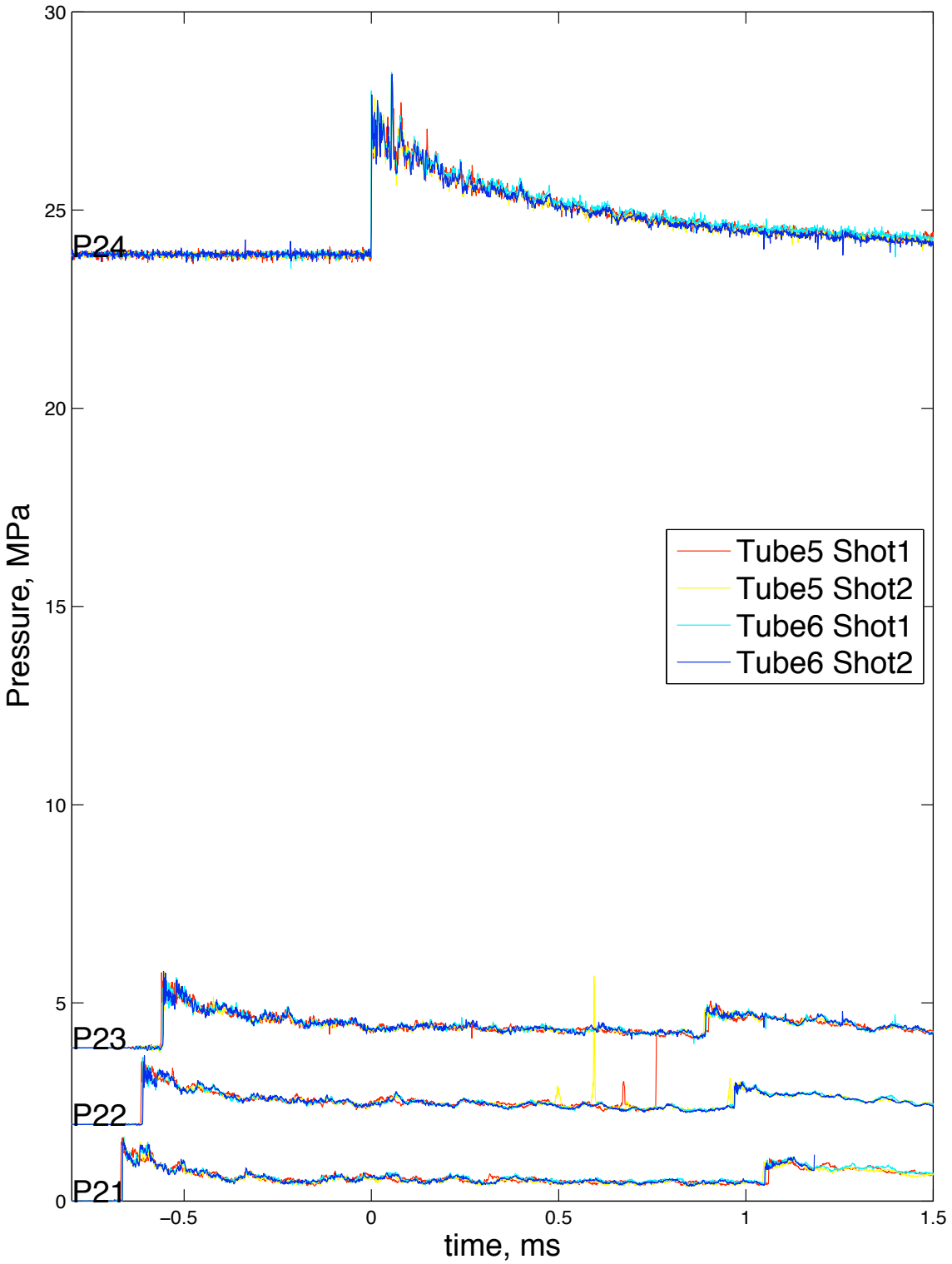

Figure F.35: Pressure data for elastic shots in tubes 5 and 6.

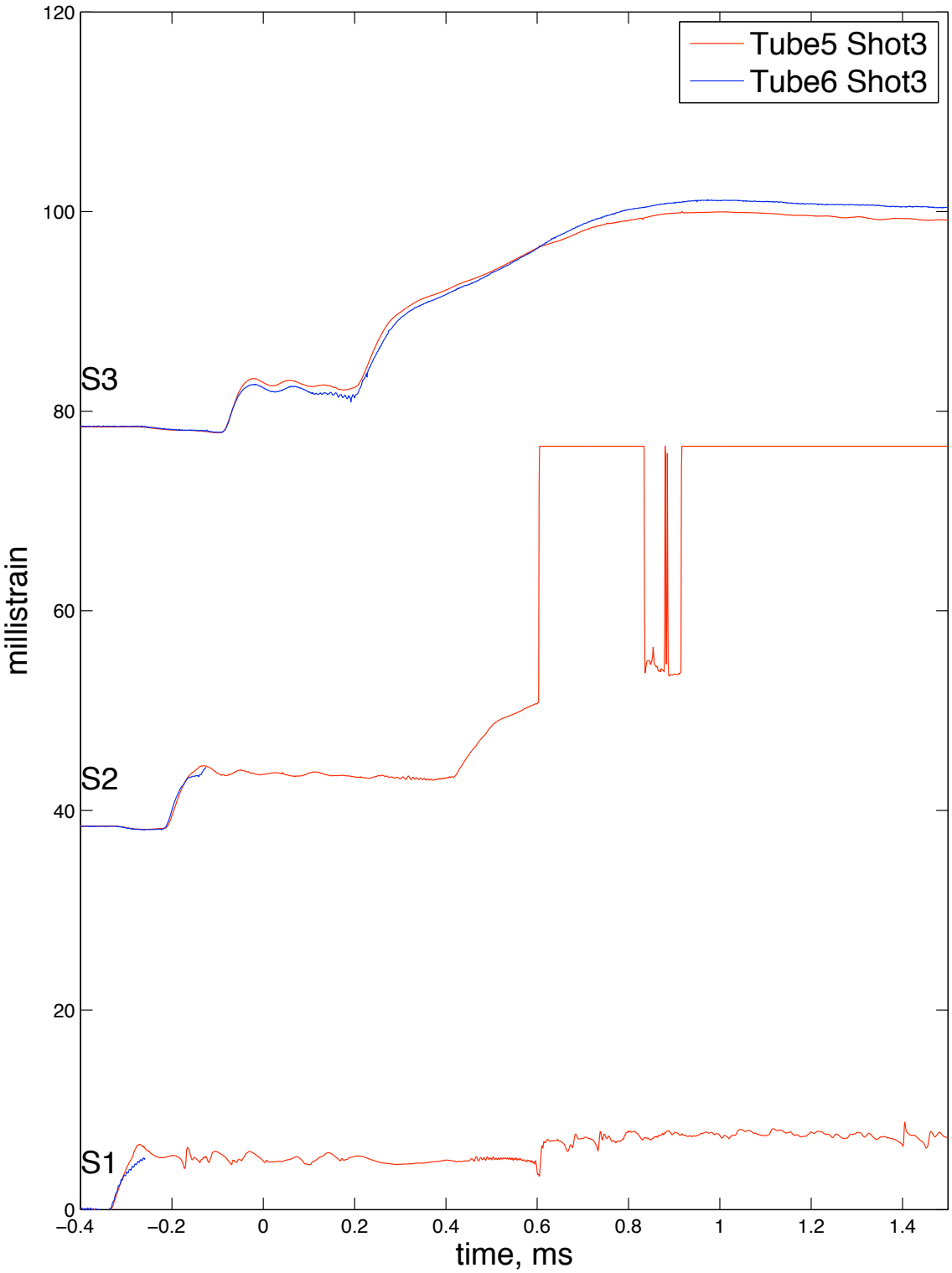

Figure F.36: Hoop strain data for plastic shots in tubes 5 and 6.

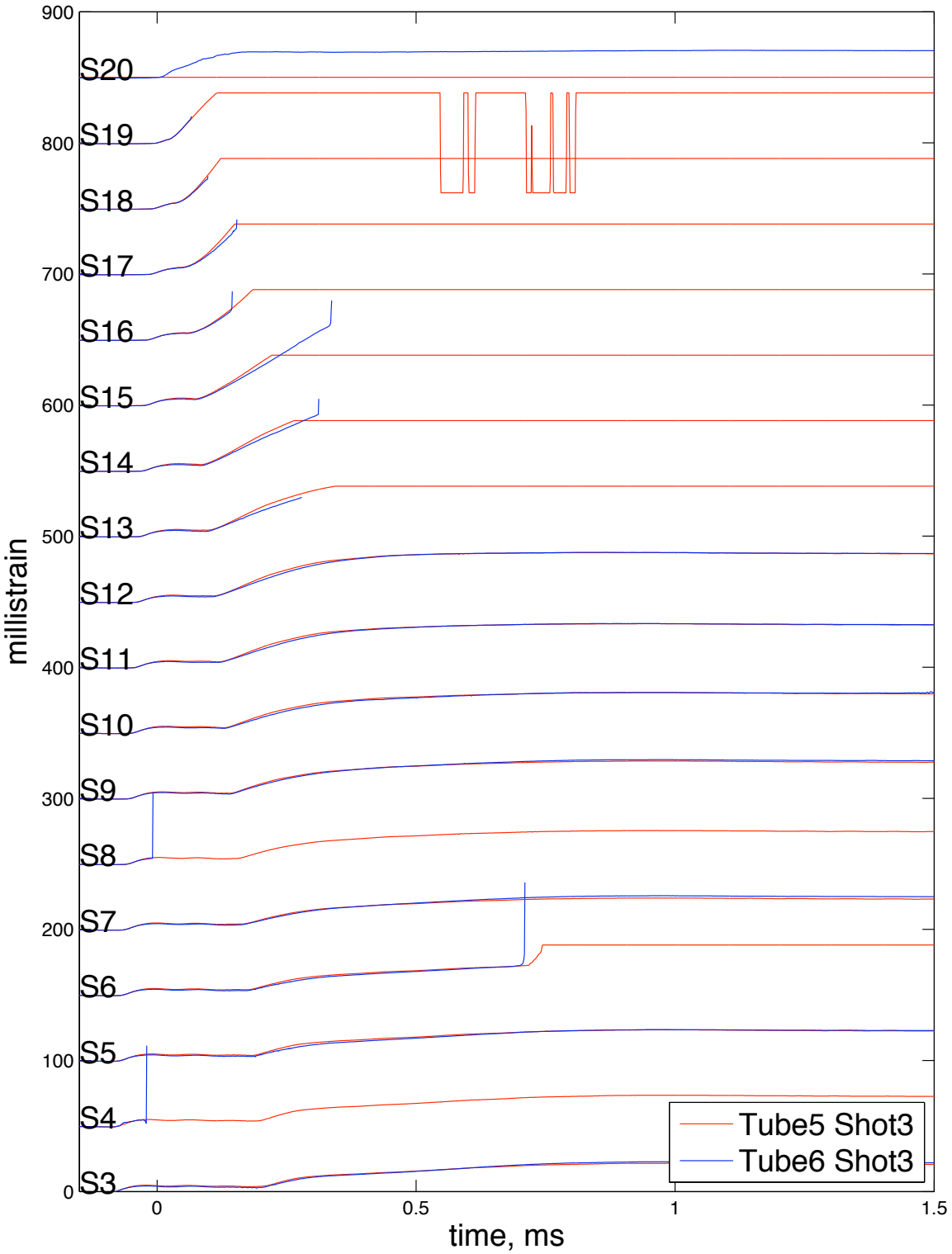

Figure F.37: Hoop strain data for plastic shots in tubes 5 and 6.

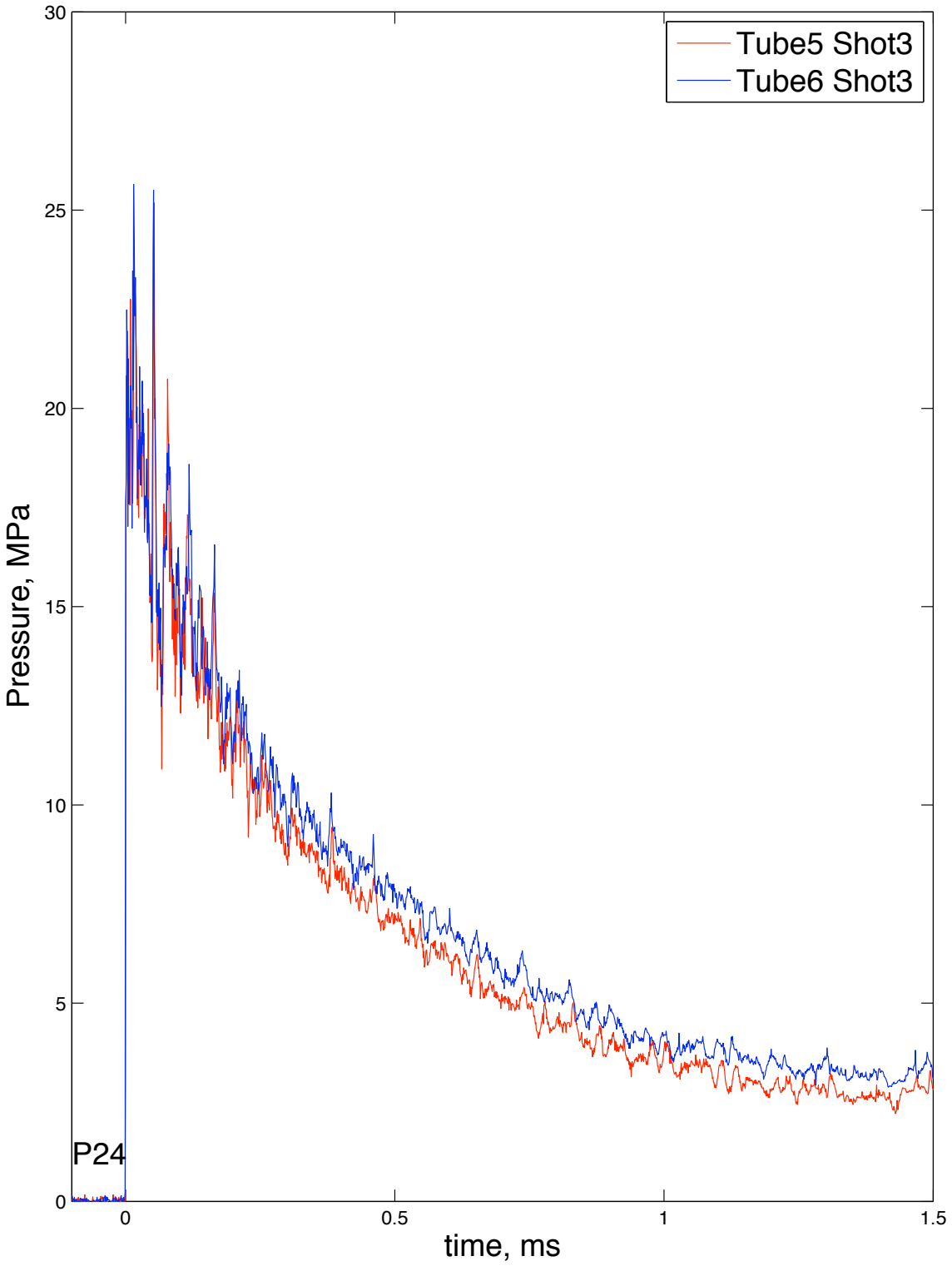

Figure F.38: Pressure data for plastic shots in tubes 5 and 6.

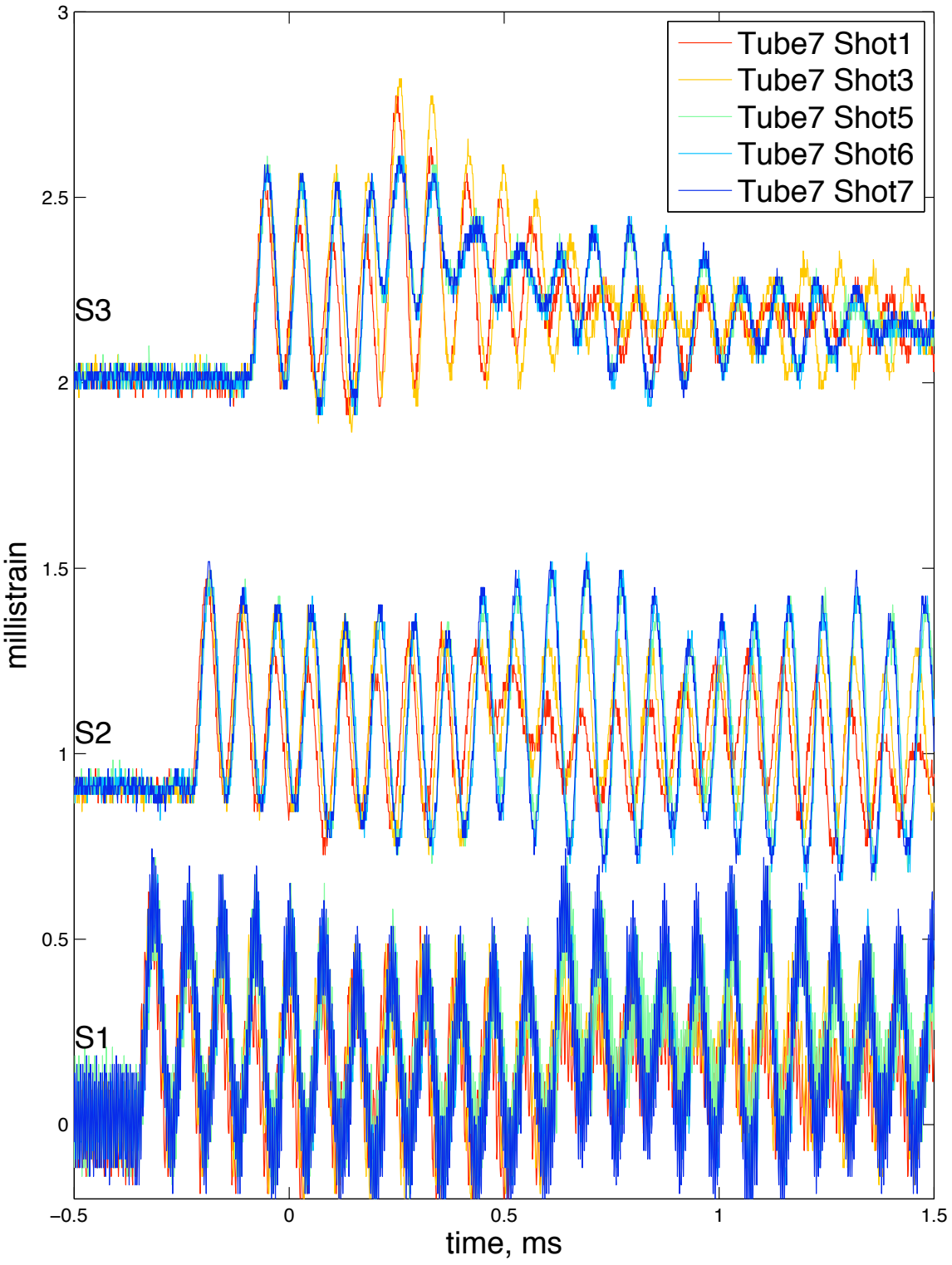

Figure F.39: Hoop strain data for elastic shots in tube 7.

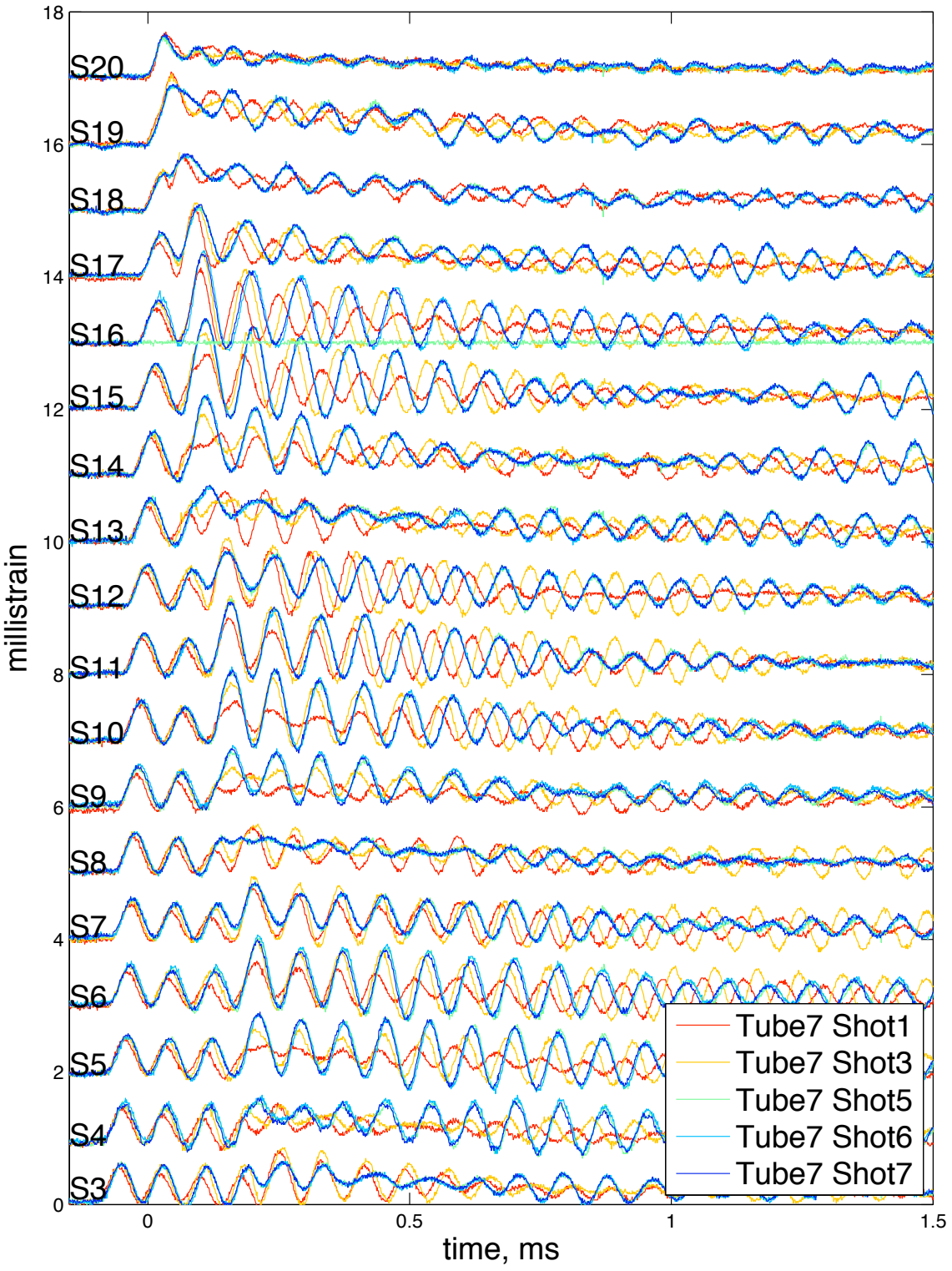

Figure F.40: Hoop strain data for elastic shots in tube 7.

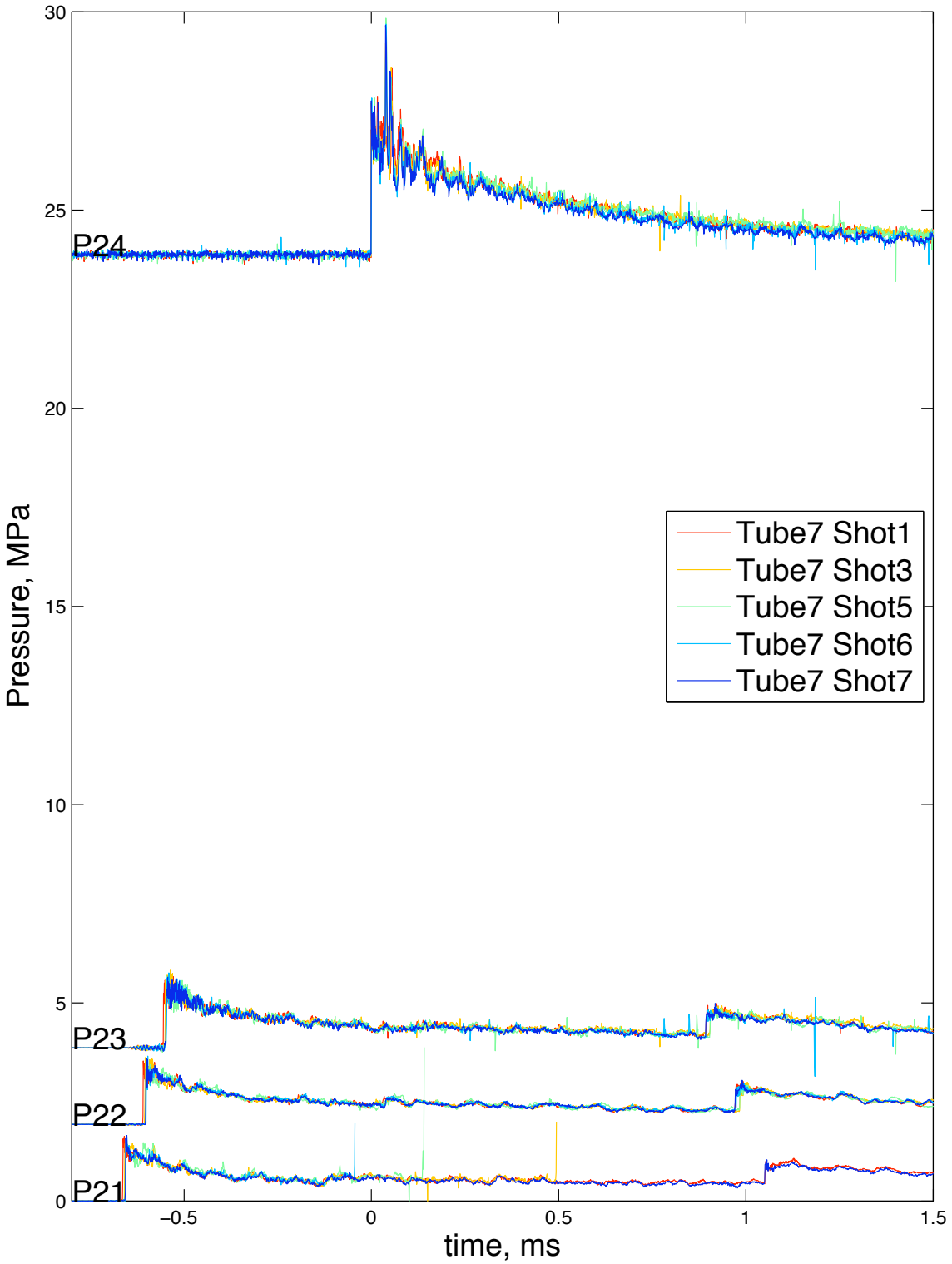

Figure F.41: data for lastic shots in tube 7.

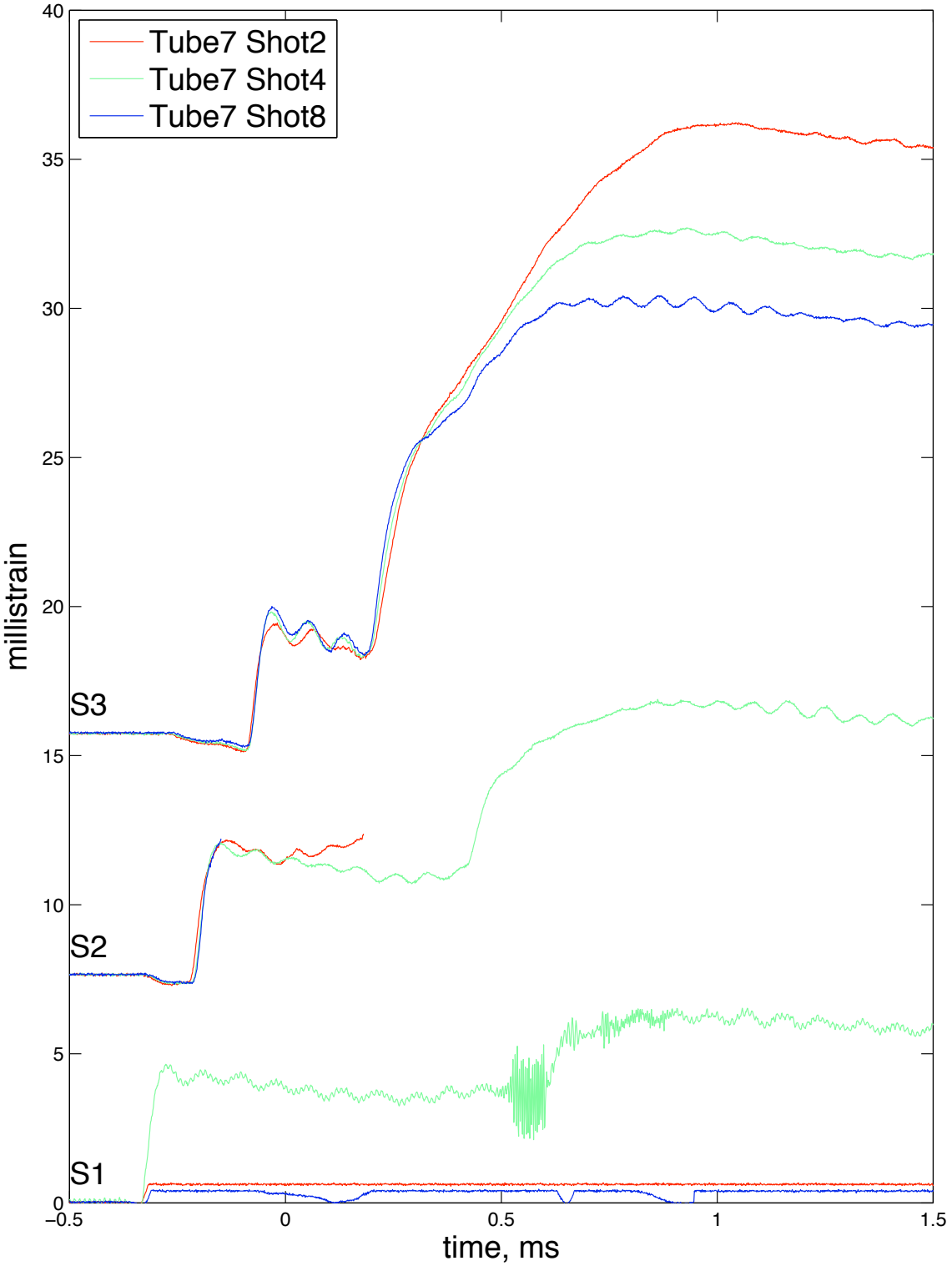

Figure F.42: Hoop strain data for plastic shots in tube 7.

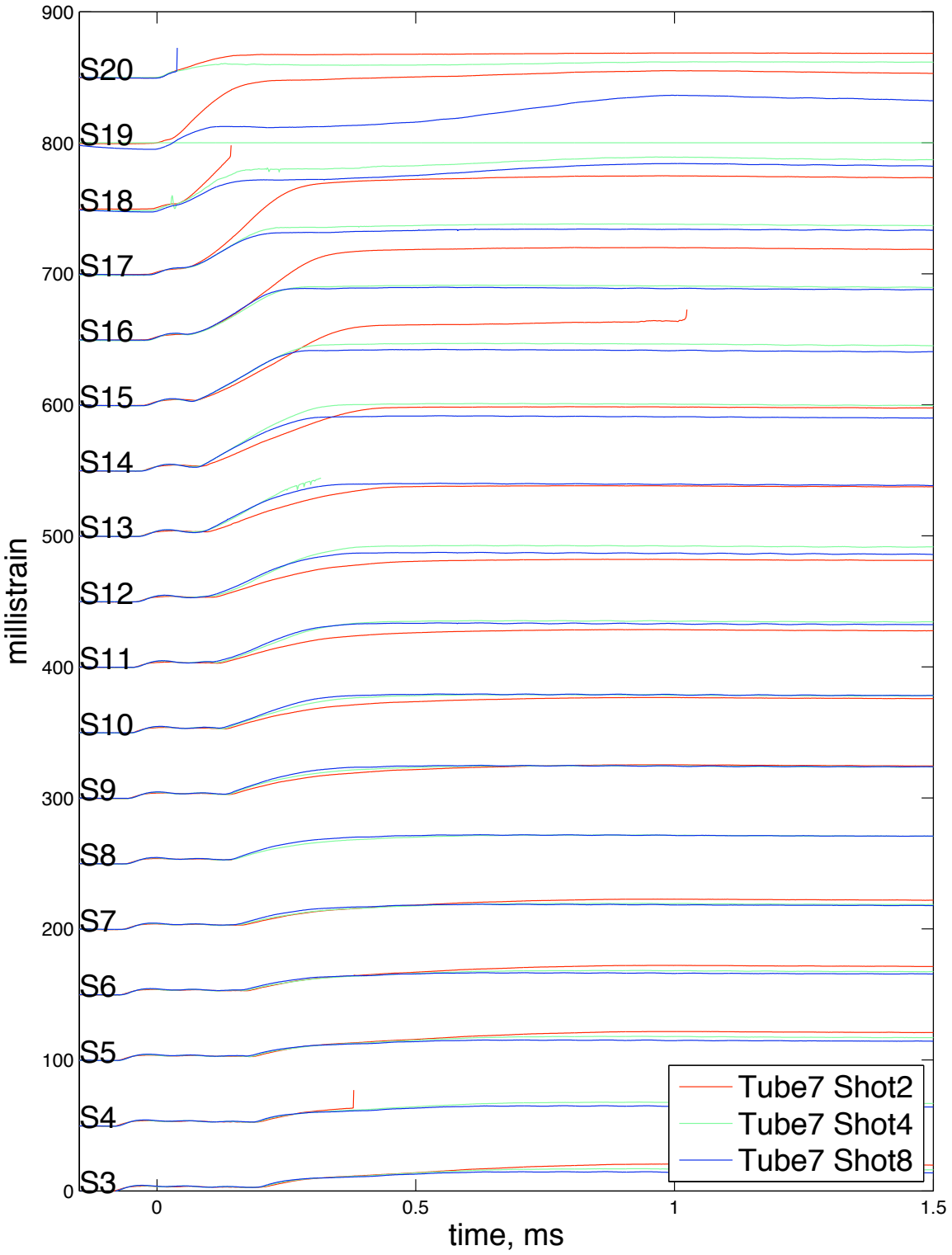

Figure F.43: Hoop strain data for plastic shots in tube 7.

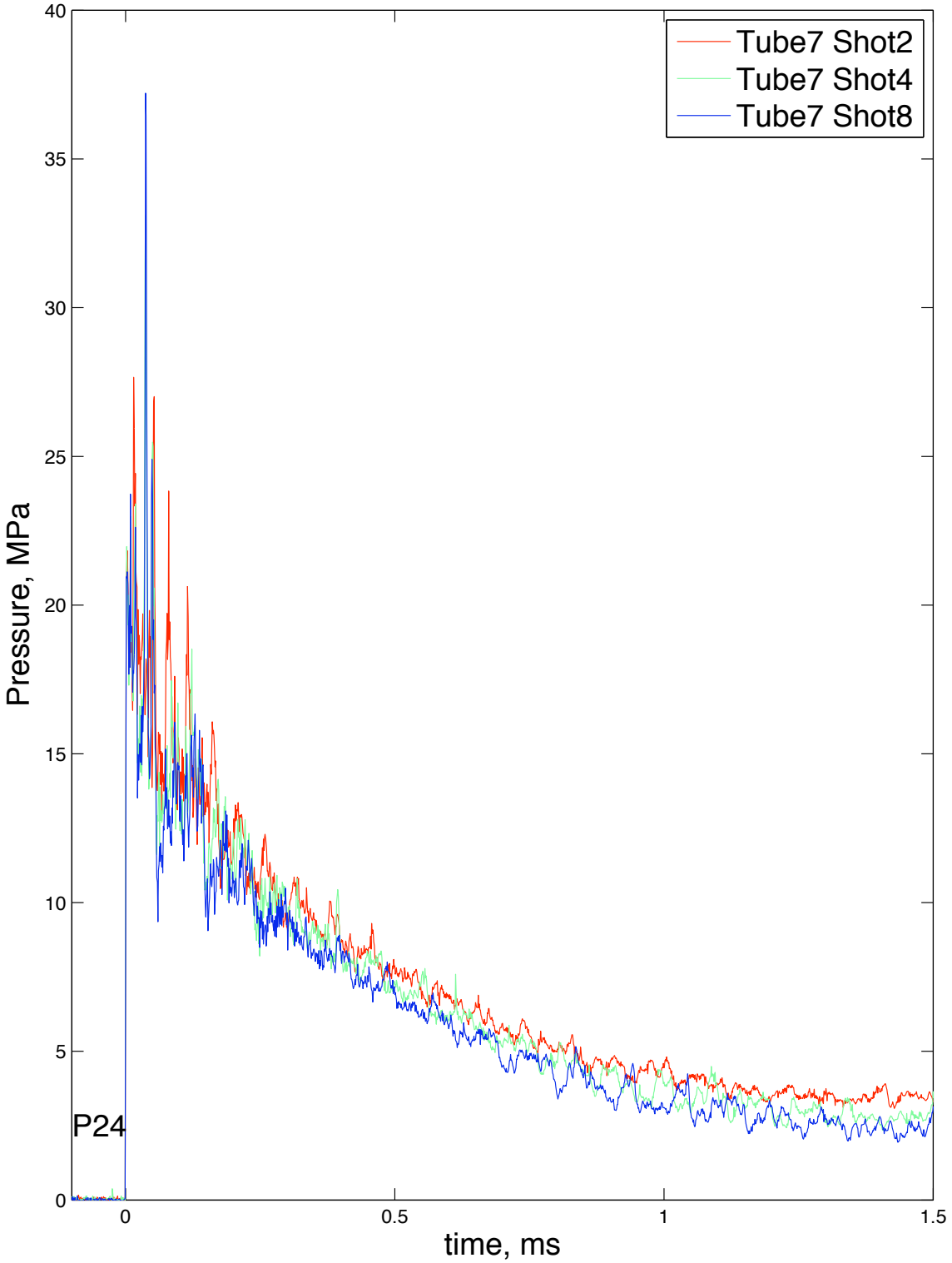

Figure F.44: Pressure data for plastic shots in tube 7.